

1993

A measurement of the branching ratio of long-lived neutral kaon going to positive muon negative muon

Michael Thomas Witkowski
College of William & Mary - Arts & Sciences

Follow this and additional works at: <https://scholarworks.wm.edu/etd>



Part of the [Physics Commons](#)

Recommended Citation

Witkowski, Michael Thomas, "A measurement of the branching ratio of long-lived neutral kaon going to positive muon negative muon" (1993). *Dissertations, Theses, and Masters Projects*. William & Mary. Paper 1539623833.

<https://dx.doi.org/doi:10.21220/s2-jd4c-jr33>

This Dissertation is brought to you for free and open access by the Theses, Dissertations, & Master Projects at W&M ScholarWorks. It has been accepted for inclusion in Dissertations, Theses, and Masters Projects by an authorized administrator of W&M ScholarWorks. For more information, please contact scholarworks@wm.edu.

INFORMATION TO USERS

This manuscript has been reproduced from the microfilm master. UMI films the text directly from the original or copy submitted. Thus, some thesis and dissertation copies are in typewriter face, while others may be from any type of computer printer.

The quality of this reproduction is dependent upon the quality of the copy submitted. Broken or indistinct print, colored or poor quality illustrations and photographs, print bleedthrough, substandard margins, and improper alignment can adversely affect reproduction.

In the unlikely event that the author did not send UMI a complete manuscript and there are missing pages, these will be noted. Also, if unauthorized copyright material had to be removed, a note will indicate the deletion.

Oversize materials (e.g., maps, drawings, charts) are reproduced by sectioning the original, beginning at the upper left-hand corner and continuing from left to right in equal sections with small overlaps. Each original is also photographed in one exposure and is included in reduced form at the back of the book.

Photographs included in the original manuscript have been reproduced xerographically in this copy. Higher quality 6" x 9" black and white photographic prints are available for any photographs or illustrations appearing in this copy for an additional charge. Contact UMI directly to order.

U·M·I

University Microfilms International
A Bell & Howell Information Company
300 North Zeeb Road, Ann Arbor, MI 48106-1346 USA
313/761-4700 800/521-0600

Order Number 9403276

A measurement of the branching ratio of $K_L^0 \rightarrow \mu^+ \mu^-$

Witkowski, Michael Thomas, Ph.D.

The College of William and Mary, 1993

U·M·I

300 N. Zeeb Rd.
Ann Arbor, MI 48106

A MEASUREMENT OF THE BRANCHING RATIO OF $K_L^0 \rightarrow \mu^+ \mu^-$

Michael Thomas Witkowski

April 1993

WMHEG-93-1

Supported in part by the
National Science Foundation
Grant PHY-8921480

A MEASUREMENT OF THE BRANCHING RATIO OF
 $K_L^0 \longrightarrow \mu^+ \mu^-$

A DISSERTATION
PRESENTED TO
THE FACULTY OF THE DEPARTMENT OF PHYSICS
THE COLLEGE OF WILLIAM AND MARY IN VIRGINIA

IN PARTIAL FULFILLMENT
OF THE REQUIREMENTS FOR THE DEGREE OF
DOCTOR OF PHILOSOPHY

by
Michael Thomas Witkowski
April 1993

APPROVAL SHEET

**This dissertation is submitted in partial fulfillment of
the requirements for the degree of
Doctor of Philosophy**



Michael Thomas Witkowski

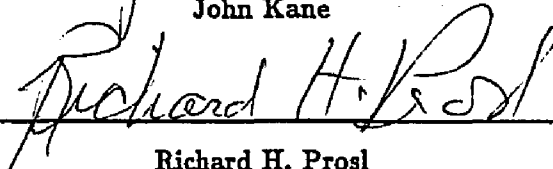
Approved, April 1993



Morton Eckhause

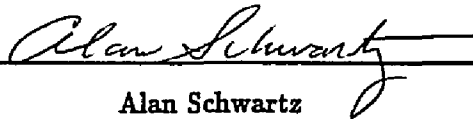


John Kane



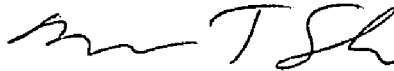
Richard H. Prosl

Department of Computer Science




Alan Schwartz

Department of Physics, Princeton University



Marc T. Sher



Robert E. Welsh

Dedication

To my wonderful wife:
Kathleen Elizabeth Witkowski

— and —

To our families:
The Witkowskis and The Kubats

Acknowledgements

All particle physics experiments are large, lengthy and collaborative. Without the effort of the E791 collaboration none of the work present in this dissertation would have been possible. Consequently, I wish to acknowledge the outstanding work and contributions of the E791 collaboration[1]. Above and beyond this general acknowledgement, there are several individuals with whom I have worked very closely who deserve particular acknowledgement:

Dr. John R. Kane, my advisor, as well as Dr. Morton Eckhause, Dr. Marc T. Sher, Dr. Robert E. Welsh and the late Dr. Rolf G. Winter for their advice, encouragement, patience, and general help during the experiment. They also deserve special acknowledged for the tedious task of proofreading this work and serving on my dissertation committee.

Dr. Richard Prosl for his services as a committee member and tolerance of this difficult cross disciplinary task.

Dr. Alan Schwartz, also a committee member, for his time, consideration and general tolerance of my *unique* personality. Also for the many long days and nights of work dedicated to the production of the best possible $\mu^+\mu^-$ result.

Dr. John Belz, Dr. Kurt Biery, Dr. Michael Chapman, Dr. Cedric Guss, Dr. Dayle Hancock, Dr. Ann Heinson, Dr. John Horvath, Dr. George Irwin, Dr. Steve Kettell and Dr. Yunan Kuang for their work and help in production analysis as well as all of the enlightening discussions and grunt work. As members of the analysis group, their efforts were vital to the completion of this dissertation.

My thanks to the staff of Brookhaven National Laboratory, especially that of the computer center and AGS. The services they provided, day and night, sun, rain, sleet and snow, were critical to the completion of the experiment and this dissertation.

Kathleen Elizabeth Witkowski, for her patience, Love and ...

My parents, Barbara Ann and Ronald Albert Witkowski for everything ...

And, Finally, to all others who assisted in the successful completion of the experiment and this dissertation but whom I have not named.

Contents

Approval Sheet	ii
Dedication	iii
Acknowledgements	iv
Table of Contents	v
List of Tables	ix
List of Figures	xi
Abstract	xxiii
1. Introduction	1
2. Theoretical Motivation	4
2.1 Overview	4
2.2 Neutral Kaon System	5
2.3 CP Violation	7
2.4 First Order	8
2.5 Imaginary Part of the Amplitude	11
2.6 Unitarity Bound	11
2.7 Real Part of the Amplitude	11
2.8 Radiative Corrections	12
3. The E791 Detector	16
3.1 Overview	16

3.2	B5 Beamline	18
3.2.1	The Proton Beam	18
3.2.2	The Target	18
3.2.3	The Neutral Beamline	19
3.2.4	The Vacuum Decay Region	21
3.3	Spectrometer	24
3.3.1	Overview	24
3.3.2	The Spectrometer Magnets	24
3.3.3	The Drift Chambers	26
3.3.4	The Trigger Scintillation Counters	28
3.4	Electron Identification Elements	29
3.4.1	Overview	29
3.4.2	The Čerenkov Counters	29
3.4.3	The Lead Glass Array	31
3.5	Finger Counters	32
3.6	Muon Identification Elements	33
3.6.1	Overview	33
3.6.2	The Muon Hodoscope	33
3.6.3	The Muon Rangefinder	34
4.	The Data Acquisition System	39
4.1	Overview	39
4.2	Level 0 Trigger	41
4.3	Level 1 Trigger	42
4.4	Digitization	44
4.4.1	Overview	44
4.4.2	The 6-Bit Time-To-Digital Converters	47
4.4.3	The 8-Bit Fine-Binned Time-To-Digital Converters	47
4.4.4	The Amplitude-To-Digital Converters	47
4.4.5	The Latch Modules	48
4.5	Level 2 Trigger	48
4.6	Readout	49
4.7	Level 3 Trigger	50

4.8	Running Conditions	52
5	The Offline Code	54
5.1	Overview	54
5.2	Generation of Monte Carlo Events	56
5.3	Processing of Raw Data	57
5.4	Pattern Recognition	57
5.5	Track Fitting Algorithms	62
5.6	Track Counter Association	65
5.6.1	The Čerenkov Counter	66
5.6.2	The Lead Glass	66
5.6.3	The Muon Hodoscope	66
5.6.4	The Muon Rangefinder	67
6.	The Production Analysis	69
6.1	Overview	69
6.2	Pass 0	70
6.3	Pass 1	70
6.4	Pass 2	71
6.5	Pass 3	73
6.6	Generation of Monte Carlo Samples	73
6.7	Pass 4	76
7.	Event Selection and Efficiency Calculations	79
7.1	Overview	79
7.2	$K_L^0 \rightarrow \mu^+ \mu^-$ Sample	79
7.3	$K_L^0 \rightarrow \pi^+ \pi^-$ Sample	81
7.4	Calculation of Acceptances	82
7.5	Level 1 Efficiency Calculation	82
7.6	Level 3 Efficiencies	82
7.7	$\mu^+ \mu^-$ Particle Identification Efficiency	84
7.8	$\pi^+ \pi^-$ Interaction Correction	84

8. Results	93
8.1 Overview	93
8.2 $\mu^+\mu^-$ Counting Results.	93
8.3 $\pi^+\pi^-$ Counting Results.	95
8.4 Acceptance Calculation Results.	97
8.5 Level 1 Efficiency Results.	98
8.6 Level 3 Efficiency Results.	100
8.7 $\mu^+\mu^-$ Particle Identification Efficiency Results.	102
8.8 $\pi^+\pi^-$ Interaction Correction Results.	103
8.9 Branching Ratio Calculation Results.	103
9. Conclusion	106
Appendices	
A. Corrections to the Monte Carlo Data Set	109
B. Correction for K_S^0 Contamination	116
C. Analysis Cuts	119
D. Combination of Data Sets	139
E. $\mu^+\mu^-$ and $\pi^+\pi^-$ Systematic Studies	143
F. Acceptance Systematic Studies	156
G. L1 Efficiency Systematic Studies	169
H. Branching Ratio Systematic Studies	176
Bibliography	183
Vita	189

List of Tables

1.1	Previous experimental results for $K_L^0 \rightarrow \mu^+ \mu^-$	3
2.1	CP violation parameters for K_L^0 processes.	8
4.1	Summary of Level 1 physics trigger requirements.	44
4.2	Summary of trigger rates.	51
4.3	Breakdown of 1989 and 1990 events by trigger type.	53
5.1	QT degrees of freedom.	64
6.1	Physics events out of pass 1 in 1989 and 1990.	71
6.2	Summary of the pass 3 output for 1989 and 1990.	73
6.3	Summary of Monte Carlo generation output.	75
8.1	Electron efficiency and extrapolation constants for the $\mu^+ \mu^-$ sample.	94
8.2	$\mu^+ \mu^-$ counting results.	94
8.3	$\pi^+ \pi^-$ counting results used for background subtraction.	96
8.4	$\pi^+ \pi^-$ counting results.	96
8.5	Acceptance calculation results.	99
8.6	Systematic errors on acceptance ratio results.	99
8.7	L1 efficiency calculation results.	101
8.8	L3 efficiency calculation results.	101
8.9	$\mu^+ \mu^-$ particle identification efficiency results.	102
8.10	Branching ratio calculation results from data.	104
8.11	Branching ratio calculation results from maximum likelihood.	104
B.1	Factors used in calculation of K_S^0 contamination correction.	117

C.1	Event identification cuts.	120
C.2	Runs removed from event stream.	120
C.3	Aperture cuts.	122
C.4	Kinematic cuts.	123
C.5	Particle identification cuts.	124
C.6	Divisions used in the systematic studies.	126
C.7	Muon PID cuts used in the systematic studies.	126
C.8	Cut values used in the systematic studies.	127

List of Figures

2.1	Observed (a) and suppressed (b) K-decays.	9
2.2	$K_L^0 \rightarrow \ell^+\ell^-$ via a two photon intermediate state.	10
2.3	$K_L^0 \rightarrow \ell^+\ell^-$ via virtual two photon intermediate state.	12
2.4	Short distance contributions to $K_L^0 \rightarrow \ell^+\ell^-$	13
2.5	Radiative corrections to $K_L^0 \rightarrow \ell^+\ell^-$ decays.	14
3.1	Schematic view of the BNL E791 detector and beamline.	17
3.2	The target holder used in 1989.	20
3.3	The target holder used in 1990.	20
3.4	The upstream end of the E791 beamline.	21
3.5	Beamline shielding diagram.	22
3.6	Vacuum window used in 1989.	23
3.7	Vacuum window used in 1990.	23
3.8	Schematic of the E791 spectrometer.	25
3.9	Geometry of drift chamber wires.	27
3.10	The design of the drift chamber frames.	27
3.11	The x measuring trigger scintillation counters.	28
3.12	Top view of a Čerenkov counter.	30
3.13	Side view of a Čerenkov counter.	30
3.14	The lead glass array.	32
3.15	Illustration of the MHO and iron filter.	34
3.16	Top and side views of the muon rangefinder.	35
3.17	Cross sectional view of an extrusion.	36
3.18	Illustration of an x measuring plane.	37
3.19	Schematic of the gas distribution system.	38

4.1	Schematic of the E791 acquisition system.	40
4.2	Logic to the L0 trigger.	41
4.3	Drift chamber inputs to the level 1 trigger.	42
4.4	Muon Hodoscope inputs to the Level 1 trigger.	43
4.5	Level 1 physics trigger.	45
4.6	Final stage of Level 1 logic.	46
4.7	Definition of colinearity θ_c	51
5.1	Offline analysis flowchart.	55
5.2	Schematic of the Monte Carlo generation stage.	58
5.3	Schematic of the Monte Carlo swimming stage.	58
5.4	Illustration of a good time sum triple.	60
5.5	Illustration of a good time sum pair.	60
5.6	Schematic of 2-D track finding.	61
5.7	Illustration of the ambiguity in a good time sum pair.	62
6.1	Flow of the pass 1 analysis.	72
6.2	Flow of the pass 2 production.	74
6.3	Flow of the pass 4 production	77
7.1	θ_c^2 vs. mass plot for the combined 1989 and 1990 $\mu^+\mu^-$ sample.	86
7.2	Mass histogram for the combined 1989 and 1990 $\mu^+\mu^-$ sample.	87
7.3	θ_c^2 histogram for the combined 1989 and 1990 $\mu^+\mu^-$ sample.	87
7.4	θ_c^2 histogram for the combined 1989 and 1990 $\mu^+\mu^-$ sample (e).	88
7.5	θ_c^2 histogram for the combined 1989 and 1990 $\mu^+\mu^-$ sample (no e).	88
7.6	θ_c^2 for a sample of K_{e3} events without $\mu^+\mu^-$ PID.	89
7.7	θ_c^2 histogram for the combined 1989 and 1990 $\mu^+\mu^-$ sample (no e).	89
7.8	θ_c^2 vs. mass plot for a prescale of the combined 1989 and 1990 $\pi^+\pi^-$ sample.	90
7.9	Mass histogram for the combined 1989 and 1990 $\pi^+\pi^-$ sample.	91
7.10	θ_c^2 histogram for the combined 1989 and 1990 $\pi^+\pi^-$ sample.	91
7.11	θ_c^2 for a sample of Monte Carlo K_{e3} events.	92
7.12	θ_c^2 for a sample of Monte Carlo $K_{\mu3}$ events.	92
A.1	Data and Monte Carlo $\pi^+\pi^-$ sample as a function of run number in 1989.	113
A.2	Data and Monte Carlo $\pi^+\pi^-$ sample as a function of run number in 1990.	113

A.3	Data and Monte Carlo $\pi^+\pi^-$ sample as a function of kaon momentum. . . .	114
A.4	Data and Monte Carlo $\pi^+\pi^-$ sample as a function of vertex z position. . . .	114
A.5	Data and Monte Carlo $\pi^+\pi^-$ sample as a function of vertex x/z	115
A.6	Data and Monte Carlo $\pi^+\pi^-$ sample as a function of vertex y/z	115
C.1	Data and Monte Carlo histogram for vacuum window cut in 1989.	128
C.2	Data and Monte Carlo histogram for vacuum window cut in 1990.	128
C.3	Data and Monte Carlo histogram for PbG inner x edge cut in 1989.	129
C.4	Data and Monte Carlo histogram for PbG inner x edge cut in 1990.	129
C.5	Data and Monte Carlo histogram as a function of track momentum.	130
C.6	Data and Monte Carlo histogram as a function of momentum asymmetry. . . .	130
C.7	Data and Monte Carlo histogram as a function of FT $P_F - P_B$ match. . . .	131
C.8	Data and Monte Carlo histogram as a function of QT $P_F - P_B$ match. . . .	131
C.9	Data and Monte Carlo histogram as a function of reconstructed mass. . . .	132
C.10	Data and Monte Carlo histogram as a function of colinearity.	132
C.11	Data and Monte Carlo histogram as a function of track χ^2 cut (FT).	133
C.12	Data and Monte Carlo histogram as a function of vertex χ^2 cut (FT). . . .	133
C.13	Data and Monte Carlo histogram as a function of x track χ^2 cut (QT). . . .	134
C.14	Data and Monte Carlo histogram as a function of y track χ^2 cut (QT). . . .	134
C.15	Data and Monte Carlo histogram as a function of vertex χ^2 cut (QT). . . .	135
C.16	Histogram of L3 reconstructed mass.	135
C.17	Histogram of TSC time.	136
C.18	Histogram of MRG actual-expected cut for the $\mu^+\mu^-$ sample.	136
C.19	Illustration of the PbG contour cut (pions, muons and electrons).	137
C.20	Illustration of the PbG contour cut (pions and muons).	137
C.21	Illustration of the PbG contour cut (electrons).	138
E.1	$\mu^+\mu^-$ count (FT).	144
E.2	$\mu^+\mu^-$ count as a function of run number (FT).	144
E.3	$\mu^+\mu^-$ count as a function of charge location (FT).	144
E.4	$\mu^+\mu^-$ count as a function of kaon momentum (FT).	144
E.5	$\mu^+\mu^-$ count as a function of vertex z position (FT).	144
E.6	$\mu^+\mu^-$ count as a function of MHO confidence level cut (FT).	144
E.7	$\mu^+\mu^-$ count as a function of vacuum flange cut in 1989 (FT).	144

E.8	$\mu^+\mu^-$ count as a function of vacuum flange cut in 1990 (FT).	144
E.9	$\mu^+\mu^-$ count as a function of mass window width cut (FT).	145
E.10	$\mu^+\mu^-$ count as a function of mass window center cut (FT).	145
E.11	$\mu^+\mu^-$ count as a function of vertex z position cut (FT).	145
E.12	$\mu^+\mu^-$ count as a function of vertex x/z position cut (FT).	145
E.13	$\mu^+\mu^-$ count as a function of vertex y/z position cut (FT).	145
E.14	$\mu^+\mu^-$ count as a function of low track momentum cut (FT).	145
E.15	$\mu^+\mu^-$ count as a function of momentum imbalance cut (FT).	145
E.16	$\mu^+\mu^-$ count as a function of front-back momentum match cut (FT).	145
E.17	$\mu^+\mu^-$ count as a function of event time cut (FT).	146
E.18	$\mu^+\mu^-$ count as a function of 1989 PbG inner x position cut (FT).	146
E.19	$\mu^+\mu^-$ count as a function of 1990 PbG inner x position cut (FT).	146
E.20	$\mu^+\mu^-$ count as a function of track χ^2 cut (FT).	146
E.21	$\mu^+\mu^-$ count as a function of vertex χ^2 cut (FT).	146
E.22	$\mu^+\mu^-$ count as a function of θ_c^2 cut (FT).	146
E.23	$\mu^+\mu^-$ count as a function of MRG actual – expected stop gap cut (FT).	146
E.24	$\mu^+\mu^-$ count (QT).	147
E.25	$\mu^+\mu^-$ count as a function of run number (QT).	147
E.26	$\mu^+\mu^-$ count as a function of charge location (QT).	147
E.27	$\mu^+\mu^-$ count as a function of kaon momentum (QT).	147
E.28	$\mu^+\mu^-$ count as a function of vertex z position (QT).	147
E.29	$\mu^+\mu^-$ count as a function of MHO confidence level cut (QT).	147
E.30	$\mu^+\mu^-$ count as a function of vacuum flange cut in 1989 (QT).	147
E.31	$\mu^+\mu^-$ count as a function of vacuum flange cut in 1990 (QT).	147
E.32	$\mu^+\mu^-$ count as a function of mass window width cut (QT).	148
E.33	$\mu^+\mu^-$ count as a function of mass window center cut (QT).	148
E.34	$\mu^+\mu^-$ count as a function of vertex z position cut (QT).	148
E.35	$\mu^+\mu^-$ count as a function of vertex x/z position cut (QT).	148
E.36	$\mu^+\mu^-$ count as a function of vertex y/z position cut (QT).	148
E.37	$\mu^+\mu^-$ count as a function of low track momentum cut (QT).	148
E.38	$\mu^+\mu^-$ count as a function of momentum imbalance cut (QT).	148
E.39	$\mu^+\mu^-$ count as a function of front-back momentum match cut (QT).	148
E.40	$\mu^+\mu^-$ count as a function of event time cut (QT).	149

E.41 $\mu^+\mu^-$ count as a function of 1989 PbG inner x position cut (QT).	149
E.42 $\mu^+\mu^-$ count as a function of 1990 PbG inner x position cut (QT).	149
E.43 $\mu^+\mu^-$ count as a function of track χ^2 cut (QT).	149
E.44 $\mu^+\mu^-$ count as a function of vertex χ^2 cut (QT).	149
E.45 $\mu^+\mu^-$ count as a function of θ_c^2 cut (QT).	149
E.46 $\mu^+\mu^-$ count as a function of MRG actual – expected stop gap cut (QT).	149
E.47 $\pi^+\pi^-$ count (FT).	150
E.48 $\pi^+\pi^-$ count as a function of run number (FT).	150
E.49 $\pi^+\pi^-$ count as a function of charge location (FT).	150
E.50 $\pi^+\pi^-$ count as a function of kaon momentum (FT).	150
E.51 $\pi^+\pi^-$ count as a function of vertex z position (FT).	150
E.52 $\pi^+\pi^-$ count as a function of MHO confidence level cut (FT).	150
E.53 $\pi^+\pi^-$ count as a function of vacuum flange cut in 1989 (FT).	150
E.54 $\pi^+\pi^-$ count as a function of vacuum flange cut in 1990 (FT).	150
E.55 $\pi^+\pi^-$ count as a function of mass window width cut (FT).	151
E.56 $\pi^+\pi^-$ count as a function of mass window center cut (FT).	151
E.57 $\pi^+\pi^-$ count as a function of vertex z position cut (FT).	151
E.58 $\pi^+\pi^-$ count as a function of vertex x/z position cut (FT).	151
E.59 $\pi^+\pi^-$ count as a function of vertex y/z position cut (FT).	151
E.60 $\pi^+\pi^-$ count as a function of low track momentum cut (FT).	151
E.61 $\pi^+\pi^-$ count as a function of momentum imbalance cut (FT).	151
E.62 $\pi^+\pi^-$ count as a function of front-back momentum match cut (FT).	151
E.63 $\pi^+\pi^-$ count as a function of event time cut (FT).	152
E.64 $\pi^+\pi^-$ count as a function of 1989 PbG inner x position cut (FT).	152
E.65 $\pi^+\pi^-$ count as a function of 1990 PbG inner x position cut (FT).	152
E.66 $\pi^+\pi^-$ count as a function of track χ^2 cut (FT).	152
E.67 $\pi^+\pi^-$ count as a function of vertex χ^2 cut (FT).	152
E.68 $\pi^+\pi^-$ count as a function of θ_c^2 cut (FT).	152
E.69 $\pi^+\pi^-$ count as a function of MRG actual – expected stop gap cut (FT).	152
E.70 $\pi^+\pi^-$ count (QT).	153
E.71 $\pi^+\pi^-$ count as a function of run number (QT).	153
E.72 $\pi^+\pi^-$ count as a function of charge location (QT).	153
E.73 $\pi^+\pi^-$ count as a function of kaon momentum (QT).	153

E.74	$\pi^+\pi^-$ count as a function of vertex z position (QT).	153
E.75	$\pi^+\pi^-$ count as a function of MHO confidence level cut (QT).	153
E.76	$\pi^+\pi^-$ count as a function of vacuum flange cut in 1989 (QT).	153
E.77	$\pi^+\pi^-$ count as a function of vacuum flange cut in 1990 (QT).	153
E.78	$\pi^+\pi^-$ count as a function of mass window width cut (QT).	154
E.79	$\pi^+\pi^-$ count as a function of mass window center cut (QT).	154
E.80	$\pi^+\pi^-$ count as a function of vertex z position cut (QT).	154
E.81	$\pi^+\pi^-$ count as a function of vertex x/z position cut (QT).	154
E.82	$\pi^+\pi^-$ count as a function of vertex y/z position cut (QT).	154
E.83	$\pi^+\pi^-$ count as a function of low track momentum cut (QT).	154
E.84	$\pi^+\pi^-$ count as a function of momentum imbalance cut (QT).	154
E.85	$\pi^+\pi^-$ count as a function of front-back momentum match cut (QT).	154
E.86	$\pi^+\pi^-$ count as a function of event time cut (QT).	155
E.87	$\pi^+\pi^-$ count as a function of 1989 PbG inner x position cut (QT).	155
E.88	$\pi^+\pi^-$ count as a function of 1990 PbG inner x position cut (QT).	155
E.89	$\pi^+\pi^-$ count as a function of track χ^2 cut (QT).	155
E.90	$\pi^+\pi^-$ count as a function of vertex χ^2 cut (QT).	155
E.91	$\pi^+\pi^-$ count as a function of θ_c^2 cut (QT).	155
E.92	$\pi^+\pi^-$ count as a function of MRG actual – expected stop gap cut (QT).	155
F.1	$\mu^+\mu^-$ acceptance (FT).	157
F.2	$\mu^+\mu^-$ acceptance as a function of run number (FT).	157
F.3	$\mu^+\mu^-$ acceptance as a function of charge location (FT).	157
F.4	$\mu^+\mu^-$ acceptance as a function of kaon momentum (FT).	157
F.5	$\mu^+\mu^-$ acceptance as a function of vertex z position (FT).	157
F.6	$\mu^+\mu^-$ acceptance as a function of MHO confidence level cut (FT).	157
F.7	$\mu^+\mu^-$ acceptance as a function of vacuum flange cut in 1989 (FT).	157
F.8	$\mu^+\mu^-$ acceptance as a function of vacuum flange cut in 1990 (FT).	157
F.9	$\mu^+\mu^-$ acceptance as a function of mass window width cut (FT).	158
F.10	$\mu^+\mu^-$ acceptance as a function of mass window center cut (FT).	158
F.11	$\mu^+\mu^-$ acceptance as a function of vertex z position cut (FT).	158
F.12	$\mu^+\mu^-$ acceptance as a function of vertex x/z position cut (FT).	158
F.13	$\mu^+\mu^-$ acceptance as a function of vertex y/z position cut (FT).	158

F.14 $\mu^+\mu^-$ acceptance as a function of low track momentum cut (FT).	158
F.15 $\mu^+\mu^-$ acceptance as a function of momentum imbalance cut (FT).	158
F.16 $\mu^+\mu^-$ acceptance as a function of front-back momentum match cut (FT). . .	158
F.17 $\mu^+\mu^-$ acceptance as a function of event time cut (FT).	159
F.18 $\mu^+\mu^-$ acceptance as a function of 1989 PbG inner x position cut (FT). . . .	159
F.19 $\mu^+\mu^-$ acceptance as a function of 1990 PbG inner x position cut (FT). . . .	159
F.20 $\mu^+\mu^-$ acceptance as a function of track χ^2 cut (FT).	159
F.21 $\mu^+\mu^-$ acceptance as a function of vertex χ^2 cut (FT).	159
F.22 $\mu^+\mu^-$ acceptance as a function of θ_c^2 cut (FT).	159
F.23 $\mu^+\mu^-$ acceptance as a function of MRG actual – expected stop gap cut (FT).159	
F.24 $\mu^+\mu^-$ acceptance (QT).	160
F.25 $\mu^+\mu^-$ acceptance as a function of run number (QT).	160
F.26 $\mu^+\mu^-$ acceptance as a function of charge location (QT).	160
F.27 $\mu^+\mu^-$ acceptance as a function of kaon momentum (QT).	160
F.28 $\mu^+\mu^-$ acceptance as a function of vertex z position (QT).	160
F.29 $\mu^+\mu^-$ acceptance as a function of MHO confidence level cut (QT).	160
F.30 $\mu^+\mu^-$ acceptance as a function of vacuum flange cut in 1989 (QT).	160
F.31 $\mu^+\mu^-$ acceptance as a function of vacuum flange cut in 1990 (QT).	160
F.32 $\mu^+\mu^-$ acceptance as a function of mass window width cut (QT).	161
F.33 $\mu^+\mu^-$ acceptance as a function of mass window center cut (QT).	161
F.34 $\mu^+\mu^-$ acceptance as a function of vertex z position cut (QT).	161
F.35 $\mu^+\mu^-$ acceptance as a function of vertex x/z position cut (QT).	161
F.36 $\mu^+\mu^-$ acceptance as a function of vertex y/z position cut (QT).	161
F.37 $\mu^+\mu^-$ acceptance as a function of low track momentum cut (QT).	161
F.38 $\mu^+\mu^-$ acceptance as a function of momentum imbalance cut (QT).	161
F.39 $\mu^+\mu^-$ acceptance as a function of front-back momentum match cut (QT). . .	161
F.40 $\mu^+\mu^-$ acceptance as a function of event time cut (QT).	162
F.41 $\mu^+\mu^-$ acceptance as a function of 1989 PbG inner x position cut (QT). . .	162
F.42 $\mu^+\mu^-$ acceptance as a function of 1990 PbG inner x position cut (QT). . .	162
F.43 $\mu^+\mu^-$ acceptance as a function of track χ^2 cut (QT).	162
F.44 $\mu^+\mu^-$ acceptance as a function of vertex χ^2 cut (QT).	162
F.45 $\mu^+\mu^-$ acceptance as a function of θ_c^2 cut (QT).	162
F.46 $\mu^+\mu^-$ acceptance as a function of MRG actual – expected stop gap cut (QT).162	

F.47 $\pi^+\pi^-$ acceptance (FT).	163
F.48 $\pi^+\pi^-$ acceptance as a function of run number (FT).	163
F.49 $\pi^+\pi^-$ acceptance as a function of charge location (FT).	163
F.50 $\pi^+\pi^-$ acceptance as a function of kaon momentum (FT).	163
F.51 $\pi^+\pi^-$ acceptance as a function of vertex z position (FT).	163
F.52 $\pi^+\pi^-$ acceptance as a function of MHO confidence level cut (FT).	163
F.53 $\pi^+\pi^-$ acceptance as a function of vacuum flange cut in 1989 (FT).	163
F.54 $\pi^+\pi^-$ acceptance as a function of vacuum flange cut in 1990 (FT).	163
F.55 $\pi^+\pi^-$ acceptance as a function of mass window width cut (FT).	164
F.56 $\pi^+\pi^-$ acceptance as a function of mass window center cut (FT).	164
F.57 $\pi^+\pi^-$ acceptance as a function of vertex z position cut (FT).	164
F.58 $\pi^+\pi^-$ acceptance as a function of vertex x/z position cut (FT).	164
F.59 $\pi^+\pi^-$ acceptance as a function of vertex y/z position cut (FT).	164
F.60 $\pi^+\pi^-$ acceptance as a function of low track momentum cut (FT).	164
F.61 $\pi^+\pi^-$ acceptance as a function of momentum imbalance cut (FT).	164
F.62 $\pi^+\pi^-$ acceptance as a function of front-back momentum match cut (FT).	164
F.63 $\pi^+\pi^-$ acceptance as a function of event time cut (FT).	165
F.64 $\pi^+\pi^-$ acceptance as a function of 1989 PbG inner x position cut (FT).	165
F.65 $\pi^+\pi^-$ acceptance as a function of 1990 PbG inner x position cut (FT).	165
F.66 $\pi^+\pi^-$ acceptance as a function of track χ^2 cut (FT).	165
F.67 $\pi^+\pi^-$ acceptance as a function of vertex χ^2 cut (FT).	165
F.68 $\pi^+\pi^-$ acceptance as a function of θ_c^2 cut (FT).	165
F.69 $\pi^+\pi^-$ acceptance as a function of MRG actual – expected stop gap cut (FT).	165
F.70 $\pi^+\pi^-$ acceptance (QT).	166
F.71 $\pi^+\pi^-$ acceptance as a function of run number (QT).	166
F.72 $\pi^+\pi^-$ acceptance as a function of charge location (QT).	166
F.73 $\pi^+\pi^-$ acceptance as a function of kaon momentum (QT).	166
F.74 $\pi^+\pi^-$ acceptance as a function of vertex z position (QT).	166
F.75 $\pi^+\pi^-$ acceptance as a function of MHO confidence level cut (QT).	166
F.76 $\pi^+\pi^-$ acceptance as a function of vacuum flange cut in 1989 (QT).	166
F.77 $\pi^+\pi^-$ acceptance as a function of vacuum flange cut in 1990 (QT).	166
F.78 $\pi^+\pi^-$ acceptance as a function of mass window width cut (QT).	167
F.79 $\pi^+\pi^-$ acceptance as a function of mass window center cut (QT).	167

F.80	$\pi^+\pi^-$ acceptance as a function of vertex z position cut (QT).	167
F.81	$\pi^+\pi^-$ acceptance as a function of vertex x/z position cut (QT).	167
F.82	$\pi^+\pi^-$ acceptance as a function of vertex y/z position cut (QT).	167
F.83	$\pi^+\pi^-$ acceptance as a function of low track momentum cut (QT).	167
F.84	$\pi^+\pi^-$ acceptance as a function of momentum imbalance cut (QT).	167
F.85	$\pi^+\pi^-$ acceptance as a function of front-back momentum match cut (QT).	167
F.86	$\pi^+\pi^-$ acceptance as a function of event time cut (QT).	168
F.87	$\pi^+\pi^-$ acceptance as a function of 1989 PbG inner x position cut (QT).	168
F.88	$\pi^+\pi^-$ acceptance as a function of 1990 PbG inner x position cut (QT).	168
F.89	$\pi^+\pi^-$ acceptance as a function of track χ^2 cut (QT).	168
F.90	$\pi^+\pi^-$ acceptance as a function of vertex χ^2 cut (QT).	168
F.91	$\pi^+\pi^-$ acceptance as a function of θ_c^2 cut (QT).	168
F.92	$\pi^+\pi^-$ acceptance as a function of MRG actual – expected stop gap cut (QT).	168
G.1	L1 efficiency (FT).	170
G.2	L1 efficiency as a function of run number (FT).	170
G.3	L1 efficiency as a function of charge location (FT).	170
G.4	L1 efficiency as a function of kaon momentum (FT).	170
G.5	L1 efficiency as a function of vertex z position (FT).	170
G.6	L1 efficiency as a function of MHO confidence level cut (FT).	170
G.7	L1 efficiency as a function of vacuum flange cut in 1989 (FT).	170
G.8	L1 efficiency as a function of vacuum flange cut in 1990 (FT).	170
G.9	L1 efficiency as a function of mass window width cut (FT).	171
G.10	L1 efficiency as a function of mass window center cut (FT).	171
G.11	L1 efficiency as a function of vertex z position cut (FT).	171
G.12	L1 efficiency as a function of vertex x/z position cut (FT).	171
G.13	L1 efficiency as a function of vertex y/z position cut (FT).	171
G.14	L1 efficiency as a function of low track momentum cut (FT).	171
G.15	L1 efficiency as a function of momentum imbalance cut (FT).	171
G.16	L1 efficiency as a function of front-back momentum match cut (FT).	171
G.17	L1 efficiency as a function of event time cut (FT).	172
G.18	L1 efficiency as a function of 1989 PbG inner x position cut (FT).	172
G.19	L1 efficiency as a function of 1990 PbG inner x position cut (FT).	172

G.20	L1 efficiency as a function of track χ^2 cut (FT).	172
G.21	L1 efficiency as a function of vertex χ^2 cut (FT).	172
G.22	L1 efficiency as a function of θ_c^2 cut (FT).	172
G.23	L1 efficiency as a function of MRG actual – expected stop gap cut (FT).	172
G.24	L1 efficiency (QT).	173
G.25	L1 efficiency as a function of run number (QT).	173
G.26	L1 efficiency as a function of charge location (QT).	173
G.27	L1 efficiency as a function of kaon momentum (QT).	173
G.28	L1 efficiency as a function of vertex z position (QT).	173
G.29	L1 efficiency as a function of MHO confidence level cut (QT).	173
G.30	L1 efficiency as a function of vacuum flange cut in 1989 (QT).	173
G.31	L1 efficiency as a function of vacuum flange cut in 1990 (QT).	173
G.32	L1 efficiency as a function of mass window width cut (QT).	174
G.33	L1 efficiency as a function of mass window center cut (QT).	174
G.34	L1 efficiency as a function of vertex z position cut (QT).	174
G.35	L1 efficiency as a function of vertex x/z position cut (QT).	174
G.36	L1 efficiency as a function of vertex y/z position cut (QT).	174
G.37	L1 efficiency as a function of low track momentum cut (QT).	174
G.38	L1 efficiency as a function of momentum imbalance cut (QT).	174
G.39	L1 efficiency as a function of front-back momentum match cut (QT).	174
G.40	L1 efficiency as a function of event time cut (QT).	175
G.41	L1 efficiency as a function of 1989 PbG inner x position cut (QT).	175
G.42	L1 efficiency as a function of 1990 PbG inner x position cut (QT).	175
G.43	L1 efficiency as a function of track χ^2 cut (QT).	175
G.44	L1 efficiency as a function of vertex χ^2 cut (QT).	175
G.45	L1 efficiency as a function of θ_c^2 cut (QT).	175
G.46	L1 efficiency as a function of MRG actual – expected stop gap cut (QT).	175
H.1	$B(K_L^0 \rightarrow \mu^+ \mu^-)$ (FT).	177
H.2	$B(K_L^0 \rightarrow \mu^+ \mu^-)$ as a function of run number (FT).	177
H.3	$B(K_L^0 \rightarrow \mu^+ \mu^-)$ as a function of charge location (FT).	177
H.4	$B(K_L^0 \rightarrow \mu^+ \mu^-)$ as a function of kaon momentum (FT).	177
H.5	$B(K_L^0 \rightarrow \mu^+ \mu^-)$ as a function of vertex z position (FT).	177

H.6	$B(K_L^0 \rightarrow \mu^+ \mu^-)$ as a function of MHO confidence level cut (FT).	177
H.7	$B(K_L^0 \rightarrow \mu^+ \mu^-)$ as a function of vacuum flange cut in 1989 (FT).	177
H.8	$B(K_L^0 \rightarrow \mu^+ \mu^-)$ as a function of vacuum flange cut in 1990 (FT).	177
H.9	$B(K_L^0 \rightarrow \mu^+ \mu^-)$ as a function of mass window width cut (FT).	178
H.10	$B(K_L^0 \rightarrow \mu^+ \mu^-)$ as a function of mass window center cut (FT).	178
H.11	$B(K_L^0 \rightarrow \mu^+ \mu^-)$ as a function of vertex z position cut (FT).	178
H.12	$B(K_L^0 \rightarrow \mu^+ \mu^-)$ as a function of vertex x/z position cut (FT).	178
H.13	$B(K_L^0 \rightarrow \mu^+ \mu^-)$ as a function of vertex y/z position cut (FT).	178
H.14	$B(K_L^0 \rightarrow \mu^+ \mu^-)$ as a function of low track momentum cut (FT).	178
H.15	$B(K_L^0 \rightarrow \mu^+ \mu^-)$ as a function of momentum imbalance cut (FT).	178
H.16	$B(K_L^0 \rightarrow \mu^+ \mu^-)$ as a function of front-back momentum match cut (FT).	178
H.17	$B(K_L^0 \rightarrow \mu^+ \mu^-)$ as a function of event time cut (FT).	179
H.18	$B(K_L^0 \rightarrow \mu^+ \mu^-)$ as a function of 1989 PbG inner x position cut (FT).	179
H.19	$B(K_L^0 \rightarrow \mu^+ \mu^-)$ as a function of 1990 PbG inner x position cut (FT).	179
H.20	$B(K_L^0 \rightarrow \mu^+ \mu^-)$ as a function of track χ^2 cut (FT).	179
H.21	$B(K_L^0 \rightarrow \mu^+ \mu^-)$ as a function of vertex χ^2 cut (FT).	179
H.22	$B(K_L^0 \rightarrow \mu^+ \mu^-)$ as a function of θ_c^2 cut (FT).	179
H.23	$B(K_L^0 \rightarrow \mu^+ \mu^-)$ as a function of MRG actual – expected stop gap cut (FT).	179
H.24	$B(K_L^0 \rightarrow \mu^+ \mu^-)$ (QT).	180
H.25	$B(K_L^0 \rightarrow \mu^+ \mu^-)$ as a function of run number (QT).	180
H.26	$B(K_L^0 \rightarrow \mu^+ \mu^-)$ as a function of charge location (QT).	180
H.27	$B(K_L^0 \rightarrow \mu^+ \mu^-)$ as a function of kaon momentum (QT).	180
H.28	$B(K_L^0 \rightarrow \mu^+ \mu^-)$ as a function of vertex z position (QT).	180
H.29	$B(K_L^0 \rightarrow \mu^+ \mu^-)$ as a function of MHO confidence level cut (QT).	180
H.30	$B(K_L^0 \rightarrow \mu^+ \mu^-)$ as a function of vacuum flange cut in 1989 (QT).	180
H.31	$B(K_L^0 \rightarrow \mu^+ \mu^-)$ as a function of vacuum flange cut in 1990 (QT).	180
H.32	$B(K_L^0 \rightarrow \mu^+ \mu^-)$ as a function of mass window width cut (QT).	181
H.33	$B(K_L^0 \rightarrow \mu^+ \mu^-)$ as a function of mass window center cut (QT).	181
H.34	$B(K_L^0 \rightarrow \mu^+ \mu^-)$ as a function of vertex z position cut (QT).	181
H.35	$B(K_L^0 \rightarrow \mu^+ \mu^-)$ as a function of vertex x/z position cut (QT).	181
H.36	$B(K_L^0 \rightarrow \mu^+ \mu^-)$ as a function of vertex y/z position cut (QT).	181
H.37	$B(K_L^0 \rightarrow \mu^+ \mu^-)$ as a function of low track momentum cut (QT).	181
H.38	$B(K_L^0 \rightarrow \mu^+ \mu^-)$ as a function of momentum imbalance cut (QT).	181

H.39	$B(K_L^0 \rightarrow \mu^+ \mu^-)$ as a function of front-back momentum match cut (QT).	181
H.40	$B(K_L^0 \rightarrow \mu^+ \mu^-)$ as a function of event time cut (QT).	182
H.41	$B(K_L^0 \rightarrow \mu^+ \mu^-)$ as a function of 1989 PbG inner x position cut (QT).	182
H.42	$B(K_L^0 \rightarrow \mu^+ \mu^-)$ as a function of 1990 PbG inner x position cut (QT).	182
H.43	$B(K_L^0 \rightarrow \mu^+ \mu^-)$ as a function of track χ^2 cut (QT).	182
H.44	$B(K_L^0 \rightarrow \mu^+ \mu^-)$ as a function of vertex χ^2 cut (QT).	182
H.45	$B(K_L^0 \rightarrow \mu^+ \mu^-)$ as a function of θ_c^2 cut (QT).	182
H.46	$B(K_L^0 \rightarrow \mu^+ \mu^-)$ as a function of MRG actual – expected stop gap cut (QT).	182

Abstract

The branching ratio $B(K_L^0 \rightarrow \mu^+\mu^-)$ has been measured using data obtained during running periods in 1988, 1989 and 1990. The data obtained in the 1990 running period are the latest and last from BNL experiment E791. During the three running periods, 87, 274 and 346 respective candidate events were observed, forming an overall sample of 707 $\mu^+\mu^-$ events. This number represents the largest sample to-date of $K_L^0 \rightarrow \mu^+\mu^-$ events. The result for the branching fraction using the total data set is $B(K_L^0 \rightarrow \mu^+\mu^-) = (6.86 \pm 0.37) \times 10^{-9}$. This result is very near the unitarity bound of 6.81×10^{-9} and is consistent with earlier measurements.

A MEASUREMENT OF THE BRANCHING RATIO OF

$$K_L^0 \longrightarrow \mu^+ \mu^-$$

Chapter 1

Introduction

From data sets recorded in 1988, 1989 and 1990, the branching ratio for $K_L^0 \rightarrow \mu^+\mu^-$ has been measured. The results for the data sets taken in 1988 and 1989 have been previously reported[2][3]. The data recorded in 1989 have been reanalyzed along with the most recent 1990 data set under a common analysis described in this work. The yields of $\mu^+\mu^-$ candidate events were 87, 274 and 346, respectively, yielding a total sample of 707 $\mu^+\mu^-$ events. This represents the largest sample to-date of $K_L^0 \rightarrow \mu^+\mu^-$ events.

The experiment, E791, was performed in the B5 beamline at the Alternating Gradient Synchrotron of Brookhaven National Laboratory. In addition to the $K_L^0 \rightarrow \mu^+\mu^-$ channel, E791 also searched for $K_L^0 \rightarrow \mu^\pm e^\mp$ and $K_L^0 \rightarrow e^+e^-$ decays, although results for only the $K_L^0 \rightarrow \mu^+\mu^-$ decay will be presented in this dissertation[4][5][6][7]. Normalization was done to the $K_L^0 \rightarrow \pi^+\pi^-$ decay, of which over 57,000 events were observed during all three running periods. Adjusted for the prescaling of events, this corresponded to over 275×10^6 accepted $K_L^0 \rightarrow \pi^+\pi^-$ events and over 3×10^{12} K_L^0 decays.

The standard model of weak interactions, which governs K_L^0 decays, has been highly successful in understanding the behavior of elementary particles. Kaon physics has been instrumental in the development of that theory[8][9]. Most notably, the prediction of the existence of the charm quark via the GIM mechanism and the first observation of CP violation were made in the kaon system[10][11]. In spite of the ability of the standard model to bring order to the apparent chaos of the particle world, there are still problems with the theory. No explanation for the division of fermions into families arises from the theory. The masses of the constituent fermions, leptons and quarks, are not predicted and appear to be arbitrary. The theory also contains a large number of parameters which seems

unnatural. These are serious problems for a so-called fundamental theory. Given the fact that kaon physics was instrumental in the development of the theory, it is only natural to look first to kaon systems for violations of the theory. The theoretical side of particle physics - or lack thereof - is the driving force behind experimental particle physics. It is, in a very significant sense, the essence of the experiment described here.

The experimental aspect of particle physics seems to be somewhat overlooked. While the results of experiments are significant and sometimes considered profound, the heart of any experiment is the equipment used to make measurements. Many Nobel prizes have been awarded for development of theories and experimental discoveries that have fundamentally changed the way nature is thought about. There is, however, another class of Nobel awards in physics. These awards were for development of equipment that fundamentally changed the way we live and work as well as for allowing observations that made the previous two classes possible. Awards for the inventions of the cyclotron, of a photographic method of studying nuclei, of the transistor, of bubble chambers and, in 1992, of multi-wire proportional counters for tracking charged particles are prime examples. The experiment described in this dissertation is possible only because of these developments. The detector is, in fact, the heart and body of an experiment.

The final part of particle physics experiments is the analysis of data. Since modern particle physics experiments are plagued with too much data rather than too little, the use of high speed computing devices is essential to interpreting the data. Again, this area is sometimes forgotten even though it is a critical part of the experiment. The analysis described in this dissertation was based upon nearly 6000 raw data tapes with, each containing about 150 Mbyte of data. The first production pass reduced the initial data by a factor of approximately 30. Subsequent passes have a lesser reduction effect but offer a higher level of detail in the analysis. Pass 2 was performed on 200 cartridges with about 180 Meg each and pass 4 was performed on about 100 cartridges with the same density of data. Pass 3 had only a minimal CPU use but was necessary to organize the data into useful subsets.

Based upon these observations, it is clear that the description of a particle physics experiment involves a description of the essence, body and brains of the experiment. Of course, the actual areas in this dissertation will be titled in a more appropriate manner; however, the concept remains the same. Thus, this dissertation is organized into eight chapters of which this is the first. Chapter 2 will survey the motivation and historical development associated with the $K_L^0 \rightarrow \mu^+ \mu^-$ decay. The experimental apparatus and

Authors	Year	Events	$B(K_L^0 \rightarrow \mu^+ \mu^-)$
Carithers <i>et al.</i>	1973	6	$12_{-4}^{+8} \times 10^{-9}$
Fukushima <i>et al.</i>	1976	3	$8.8_{-5.5}^{+10.7} \times 10^{-9}$
Shochet <i>et al.</i>	1979	15	$8.1_{-1.8}^{+2.8} \times 10^{-9}$
Inagaki <i>et al.</i> (KEK 137)	1989	54	$(8.4 \pm 1.1) \times 10^{-9}$
Mathiazhagen <i>et al.</i> (BNL 791)	1989	87	$(5.8 \pm 0.6 \pm 0.4) \times 10^{-9}$
Inagaki <i>et al.</i> (KEK 137)	1991	178	$(7.9 \pm 0.6 \pm 0.3) \times 10^{-9}$
Heinson <i>et al.</i> (BNL 791)	1991	281	$(7.6 \pm 0.5 \pm 0.4) \times 10^{-9}$
Arisaka <i>et al.</i> (BNL 791)	1993	707	$(6.86 \pm 0.37) \times 10^{-9}$

Table 1.1: Previous experimental results for $K_L^0 \rightarrow \mu^+ \mu^-$.

data acquisition are described in chapters 3 and 4. Chapter 5 will present a description of the offline code while chapter 6 will describe the production analysis. Chapters 7 and 8 describe the final analysis and present a summary of the results. The final chapter concludes the work presented in this dissertation and discusses implications for the future. Several appendices are also included. The material presented in them is important to the work described in the chapters, however they represent topics that do not fit naturally into the structure of the main body of this text.

Finally, table 1.1 lists the results of previous $K_L^0 \rightarrow \mu^+ \mu^-$ experiments [2][3][12][13][14][15][16][17]. The final result for BNL 791 represents the work presented in this dissertation and includes the previous measurements from the 1989 and 1988 running periods. The table clearly illustrates that the research performed by E791 has significantly increased the accuracy of the measurement. At the time of submission of this dissertation the final result from E791 is unpublished.

Chapter 2

Theoretical Motivation

2.1 Overview

Kaons have provided the theoretical and experimental particle physics community with rich developments over the past 45 years. In 1947, strange particles were first observed by Rochester and Butler in the decay of a neutral kaon into two charged pions[18]. It was not until years later, however, that the kaons themselves were identified. The particles were assigned a quantum number called strangeness due to the unusual way in which they behaved. They were produced copiously through strong interactions yet had relatively long lifetimes. Further research into strange particles led to the associated production hypothesis in 1952[19]. This hypothesis explained this unusual nature of strange particles by asserting that strong interactions conserved strangeness by producing the particles in complimentary pairs. The individual strange particles could then decay into final nonstrange states only via the weak interaction which did not conserve strangeness.

In 1956, two important developments occurred. First, Lee and Yang postulated that weak interactions were not invariant under space inversion, or were parity violating[20]. Secondly, a long-lived neutral kaon was discovered by two groups in addition to the observed short-lived kaon[21][22]. In 1957, the prediction of parity nonconservation in weak interactions was confirmed in an experiment by Wu et al observing the decay of ^{60}Co [23]. Next, in 1964, an experiment by Christenson et al, demonstrated that the combined operation of charge conjugation and space inversion (CP) was violated in the long lived neutral kaon system[11]. It was previously believed that CP would be a conserved quantity even though parity or P alone was not. To date, the neutral kaon system is the only system in

which CP violation has been observed to occur.

By 1967-1968, Weinberg and Salam had proposed a gauge theory that unified the electromagnetic and weak interactions[8][9]. This work was the first attempt to formulate a theory now known as the standard model. The theory was not determined to be renormalizable until 1971[24]. Even before this, however, the theory was exhibiting problems. The decay $K_L^0 \rightarrow \mu^+ \mu^-$ did not proceed at the expected rate. Apparently the decay was suppressed for reasons not contained in the theory. In 1970, Glashow, Iliopoulos and Majani (GIM) postulated the existence of a second quark doublet containing a charm quark[10]. This addition forced the contributions to the $K_L^0 \rightarrow \mu^+ \mu^-$ rate to cancel at first order, thus explaining the apparent suppression.

In 1974 the detection of the J/ψ particle by two independent groups, required if the charm quark existed, reinforced the theory and the GIM postulate[25][26]. The theory has been extended further to incorporate a third doublet of quarks. One member of this doublet, the top quark, has not yet been detected but is expected to exist. The other member, the bottom quark, was detected in 1977 by the observation of the Υ (Upsilon) meson[27]. This followed the detection of a third lepton class in 1975[28]. Later, in 1983, the gauge bosons, W and Z, were observed, again reinforcing the theory[29].

Clearly the information from kaon physics has been instrumental in the development of the standard model. Given this, it is reasonable to search the system for anomalies that would cause further modification of the theory. This chapter discusses some of the theory behind the neutral kaon. Much, unfortunately, is left out. The field is too rich for a through treatment to be given in one short chapter. Consequently, only the areas needed to justify this experimental search and interpret its results are presented. Detailed theoretical considerations of the neutral kaon system can be found in references [30] and [31]. Additionally, this chapter is focused on the $K_L^0 \rightarrow \mu^+ \mu^-$ decay. Since the $K_L^0 \rightarrow e^+ e^-$ decay is essentially identical, both are considered together wherever possible. When the two are considered, they are referred to as $K_L^0 \rightarrow \ell^+ \ell^-$ decays.

2.2 Neutral Kaon System

A neutral kaon, K^0 , is a meson that consists of a d quark and an \bar{s} anti-quark. The antiparticle to the neutral kaon, \bar{K}^0 , consists of a \bar{d} anti-quark and an s quark. The mass of the particle is (497.671 ± 0.031) MeV [32]. It has zero spin and a strangeness of -1 ($+1$

for the anti-particle).

On the surface, neutral kaons seem to be rather uninteresting creatures. Fortunately, the neutral kaon is very interesting. As noted in the introduction, it has been instrumental in the development of the standard model. In order to reveal some of its interesting properties of the neutral kaon, consider the discrete symmetries charge conjugation (C), parity or space inversion (P), and their product (CP). Using conventional phase definitions, C, P, and CP operating on neutral kaons yield:

$$C|K^0\rangle = -|\bar{K}^0\rangle \quad \text{and} \quad C|\bar{K}^0\rangle = -|K^0\rangle \quad (2.1)$$

$$P|K^0\rangle = -|K^0\rangle \quad \text{and} \quad P|\bar{K}^0\rangle = -|\bar{K}^0\rangle \quad (2.2)$$

$$CP|K^0\rangle = |\bar{K}^0\rangle \quad \text{and} \quad CP|\bar{K}^0\rangle = |K^0\rangle \quad (2.3)$$

Neutral kaons can decay into a 2π or 3π final state. The 2π state can be either $\pi^0\pi^0$ or $\pi^+\pi^-$. The 3π state can be $3\pi^0$ or $\pi^+\pi^-\pi^0$. The 2π final state is an even eigenstate of CP while the 3π final state, although also an eigenstate, is CP odd. Since the weak interaction conserves CP^1 and the final states are eigenstates of CP, the initial state must also be an eigenstate of CP. Clearly, K^0 and \bar{K}^0 are not eigenstates of CP. CP eigenstates can be easily constructed if the neutral kaon system is considered to be a mixture of K^0 and \bar{K}^0 :

$$|K_1^0\rangle = \frac{1}{\sqrt{2}} [|K^0\rangle + |\bar{K}^0\rangle] \quad (2.4)$$

$$|K_2^0\rangle = \frac{1}{\sqrt{2}} [|K^0\rangle - |\bar{K}^0\rangle] \quad (2.5)$$

K_1^0 is CP even and is therefore expected to decay into the 2π mode with the 3π mode forbidden. K_2^0 , on the other hand, is CP odd and is expected to permit the 3π mode but not the 2π mode. In addition, since much more of the available phase space is used in the decay to the 3π state, K_2^0 is expected to have a much longer lifetime than K_1^0 .

Experimentally, two neutral kaons with distinct lifetimes are observed[22][21]. The short-lived kaon, K_S^0 , is observed to decay into the 2π mode with a lifetime of about 9×10^{-10} sec. The long-lived kaon, K_L^0 , is observed to decay into the 3π mode with a lifetime of about 5×10^{-8} sec. It seems that K_L^0 should be associated with K_2^0 and K_S^0 with K_1^0 . The idea that the observed neutral kaons, K_1^0 and K_2^0 , were mixtures of the particle/anti-particle pair, K^0 and \bar{K}^0 , was introduced by Gell-Mann and Pais in 1955[33].

¹CP is conserved only to a good approximation as will be shown shortly.

2.3 CP Violation

In 1964, Christenson, Cronin, Fitch and Turlay discovered a decay of the long-lived neutral kaon into the $\pi^+\pi^-$ mode. This contradicted the developments of Gell-Mann and Pais. The neutral kaons, K_1^0 and K_2^0 , were constructed of mixtures of K^0 and \bar{K}^0 in order that they would be CP eigenstates. This 1964 observation showed that K_L^0 did not conserve CP in its decay and, thus, was not an eigenstate of CP. Since the long lived neutral kaon was able to decay into both CP even and CP odd modes, the conclusion was that K_L^0 and K_S^0 had to be ad-mixtures of K_1^0 and K_2^0 :

$$|K_S^0\rangle = \frac{1}{(1 + |\epsilon|^2)^{1/2}} \left[|K_1^0\rangle + \epsilon |K_2^0\rangle \right] \quad (2.6)$$

$$|K_L^0\rangle = \frac{1}{(1 + |\epsilon|^2)^{1/2}} \left[|K_2^0\rangle + \epsilon |K_1^0\rangle \right]. \quad (2.7)$$

This can also be written in terms of K^0 and \bar{K}^0 :

$$|K_S^0\rangle = \frac{1}{(2(1 + |\epsilon|^2))^{1/2}} \left[(1 + \epsilon)|K^0\rangle + (1 - \epsilon)|\bar{K}^0\rangle \right] \quad (2.8)$$

$$|K_L^0\rangle = \frac{1}{(2(1 + |\epsilon|^2))^{1/2}} \left[(1 + \epsilon)|K^0\rangle - (1 - \epsilon)|\bar{K}^0\rangle \right] \quad (2.9)$$

where ϵ is a complex parameter related to the degree of CP violation.

Prior to this observation of CP nonconservation, it was believed that all interactions conserved CP. Parity violation had been observed several years earlier but the interactions conserved the combined CP quantity. Work after this discovery of CP violation led to the famous CPT theorem[34]. This theorem states that all interactions conserve the combined quantities CP and T (time reversal). The direct extension of this to the neutral kaon system is that kaon decay also violates the separate symmetry T. Kaons, in one sense, act as arrows that define the direction of time. As mentioned previously, CP violation has only been observed in the K_L^0 system.

CP violation in the K_L^0 system occurs in the decays $K_L^0 \rightarrow \pi^+\pi^-$, $K_L^0 \rightarrow \pi^0\pi^0$, $K_L^0 \rightarrow \pi^\pm e^\mp \nu$ (called K_{e3}) and $K_L^0 \rightarrow \pi^\pm \mu^\mp \nu$ (called $K_{\mu3}$). The violation that occurs in K_{e3} and $K_{\mu3}$ is a bit subtle. The rates for the decays $K_L^0 \rightarrow \pi^+ e^- \bar{\nu}_e$ and $K_L^0 \rightarrow \pi^+ \mu^- \bar{\nu}_\mu$ are slightly different from those for $K_L^0 \rightarrow \pi^- e^+ \nu_e$ and $K_L^0 \rightarrow \pi^- \mu^+ \nu_\mu$. This asymmetry is a violation of CP conservation. Other possible modes that are CP violating have been searched for but none has yet been found. The amount of CP violation in K_L^0 is small,

Parameter	Accepted Value	Error
δ	0.00327	0.0012
$ \eta_{+-} $	2.268×10^{-3}	0.023×10^{-3}
ϕ_{+-}	46.6 deg	1.2 deg
$ \eta_{00} $	2.253×10^{-3}	0.024×10^{-3}
ϕ_{00}	46.6 deg	2.0 deg

Table 2.1: CP violation parameters for K_L^0 processes.

only about 0.3%. The quantification of the CP violation is usually quoted in terms of two complex numbers and one real number and are defined:

$$\delta(\ell) = \frac{\Gamma(K_L^0 \rightarrow \pi^- \ell^+ \nu_\ell) - \Gamma(K_L^0 \rightarrow \pi^+ \ell^- \nu_\ell)}{\Gamma(K_L^0 \rightarrow \pi^- \ell^+ \nu_\ell) + \Gamma(K_L^0 \rightarrow \pi^+ \ell^- \nu_\ell)} \quad (2.10)$$

$$\eta_{+-} = \frac{A(K_L^0 \rightarrow \pi^+ \pi^-)}{A(K_S^0 \rightarrow \pi^+ \pi^-)} \quad (2.11)$$

$$\eta_{00} = \frac{A(K_L^0 \rightarrow \pi^0 \pi^0)}{A(K_S^0 \rightarrow \pi^0 \pi^0)} \quad (2.12)$$

Experimentally, δ is measured for K_{e3} and $K_{\mu 3}$ separately. These values are called $\delta(e)$ and $\delta(\mu)$ with δ being the weighted average of the two. δ is real; however, η_{00} and η_{+-} are generally complex and consist of a magnitude $|\eta|$ and a phase ϕ . There is one additional quantity that needs mentioning. This parameter, ϵ' , is related to the asymmetry in decays into the 2π mode but different isospin states. Note that the pion has an isospin of 1, so the final 2π state can have an isospin of 0 or 2. Any asymmetry in the decay into these two isospin states is further evidence of CP violation. The usefulness of this parameter is that it allows a relation between ϵ and the other parameters to be developed. These numbers will be useful in a later discussion. The accepted values of these parameters are shown in table 2.1[32].

2.4 First Order

The decay illustrated in figure 2.1(a) is an allowed first order decay of a charged kaon. This diagram contributes nearly 65% of the decay rate for charged kaons. The decay proceeds

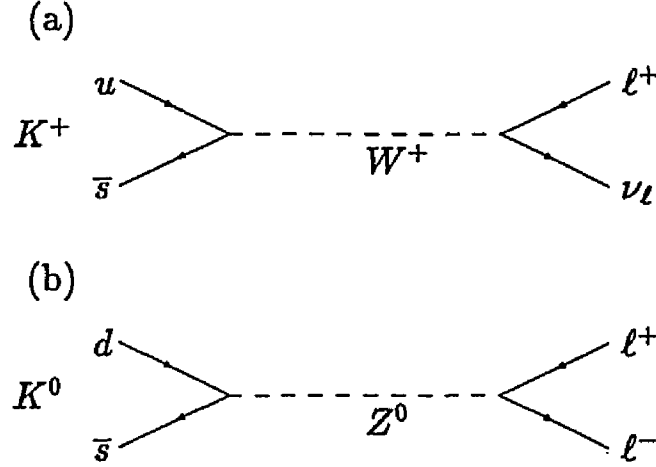


Figure 2.1: Observed (a) and suppressed (b) K-decays.

at first order via a flavor changing charged current. By analogy to this case, one would expect the decay illustrated in figure 2.1(b) to occur similarly via a flavor changing neutral current (FCNC)[35]. Although historically much of this information was unavailable, the lack of observation of the decay at the then expected rate led to the GIM postulate. Since there is now a third generation of quarks, the lack of a rate needs to be considered at the Cabibbo-Kobayashi-Maskawa (CKM) mixing matrix level[35][36]. First, notice that the amplitude will be proportional to:

$$V_{ud}^* V_{us} + V_{cd}^* V_{cs} + V_{td}^* V_{ts} \quad (2.13)$$

where the individual matrix elements are given by the CKM matrix under a standard parameterization[32][36]:

$$\begin{pmatrix} V_{ud} & V_{us} & V_{ub} \\ V_{cd} & V_{cs} & V_{cb} \\ V_{td} & V_{ts} & V_{tb} \end{pmatrix} = \begin{pmatrix} c_{12}c_{13} & s_{12}c_{13} & s_{13}e^{-i\delta_{13}} \\ -s_{12}c_{23} - c_{12}s_{23}s_{13}e^{i\delta_{13}} & c_{12}c_{23} - s_{12}s_{23}s_{13}e^{i\delta_{13}} & s_{23}c_{13} \\ s_{12}s_{23} - c_{12}c_{23}s_{13}e^{i\delta_{13}} & -c_{12}s_{23} - s_{12}c_{23}s_{13}e^{i\delta_{13}} & c_{23}c_{13} \end{pmatrix} \quad (2.14)$$

A simple bit of algebra shows that this term is identically zero. In the case of two quark generations, the original postulate of the GIM mechanism, equation 2.14 becomes:

$$\begin{pmatrix} V_{ud} & V_{us} \\ V_{cd} & V_{cs} \end{pmatrix} = \begin{pmatrix} \cos \theta_c & \sin \theta_c \\ -\sin \theta_c & \cos \theta_c \end{pmatrix} \quad (2.15)$$

where θ_c is the Cabibbo angle and is determined experimentally. By analogy to equation 2.13, it is clear that there is no contribution at first order. The $K_L^0 \rightarrow \mu^+ \mu^-$ decay is,

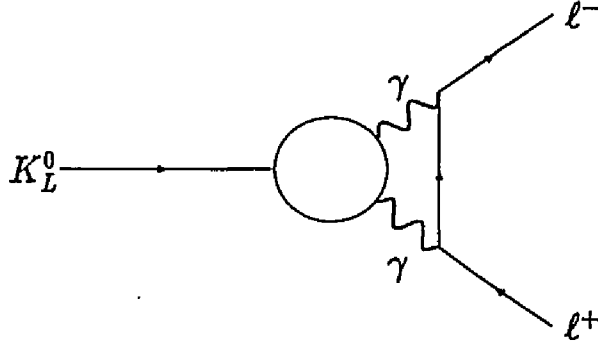


Figure 2.2: $K_L^0 \rightarrow l^+ l^-$ via a two photon intermediate state.

thus, a higher order process and GIM suppression was valid not only for two generations of quarks but also for three. FCNC's are, consequently, strictly forbidden in the standard model.

A second level of suppression arises from helicity considerations. First, as will be discussed later, the expected rate for $K_L^0 \rightarrow e^+ e^-$ is smaller than that for $K_L^0 \rightarrow \mu^+ \mu^-$ by a factor of a few times 10^{-4} . Since the electron is much lighter than the muon, this difference is not apparent from simple phase space arguments. Secondly, the neutral kaon is a spin zero particle. Consequently, the decay products must have opposite spins or the same helicities in order to conserve angular momentum. In the limit of massless leptons, particles and anti-particles must have opposite helicities. This automatically eliminates the possibility of the kaon decaying into a di-neutrino mode, assuming that neutrinos are massless. In the limit of the energy of a massive lepton much greater than its mass, the particle and anti-particle must have opposite helicities. Since the electron and muon are not strictly massless, they can be forced into an incorrect helicity state with a coupling on the order of m_l . Thus, the $K_L^0 \rightarrow l^+ l^-$ rate is suppressed by the leptons being forced into wrong helicity states. The ratio m_e^2/m_μ^2 yields the relative suppression of the $K_L^0 \rightarrow e^+ e^-$ decay compared to $K_L^0 \rightarrow \mu^+ \mu^-$. This value, 2.34×10^{-5} , clearly indicates that the $K_L^0 \rightarrow e^+ e^-$ rate would be larger than the $K_L^0 \rightarrow \mu^+ \mu^-$ rate in the absence of helicity constraints. Finally, the expected rate for $K_L^0 \rightarrow l^+ l^-$ decays as the mass of the lepton approaches zero is zero from the unitarity bound discussed in the next sections.

2.5 Imaginary Part of the Amplitude

Treating the decay $K_L^0 \rightarrow \ell^+ \ell^-$ at second order requires a consideration of the imaginary and real parts of the amplitude. Figure 2.2 is a diagram of the contribution of the imaginary part of the amplitude. Other intermediate states ($\pi\gamma$, $\pi\pi$, etc.) yield exceedingly small contributions and are not considered. It is believed that this diagram represents the dominant contribution to the $K_L^0 \rightarrow \ell^+ \ell^-$ rate. The diagram can be used to calculate the unitarity bound, the minimum rate at which $K_L^0 \rightarrow \ell^+ \ell^-$ is expected to occur. If the real part of the amplitude is zero, the unitarity rate should be consistent with the experimentally measured rate. Any difference between the measured rate and the unitarity rate is either an indication of new physics or a measure of the contribution of the real part of the amplitude.

2.6 Unitarity Bound

The unitarity bound can be calculated by relating the rates for $K_L^0 \rightarrow \gamma\gamma$ and $K_L^0 \rightarrow \ell^+ \ell^-$. This was calculated by L. Sehgal in 1969 and found to be [37]:

$$B(K_L^0 \rightarrow \gamma\gamma \rightarrow \ell^+ \ell^-) = B(K_L^0 \rightarrow \gamma\gamma) \times \frac{\alpha^2}{2} \left(\frac{m_\ell}{m_K} \right)^2 \frac{1}{\beta} \left(\ln \frac{1+\beta}{1-\beta} \right)^2 \quad (2.16)$$

where α is the fine structure constant and

$$\beta \equiv \left(1 - \frac{4m_\ell^2}{m_K^2} \right)^{1/2}. \quad (2.17)$$

Taking the best measurement of the $K_L^0 \rightarrow \gamma\gamma$ branching ratio of $(5.70 \pm 0.27) \times 10^{-4}$ [32], Equation 2.16 implies lower limits on the branching ratios:

$$B(K_L^0 \rightarrow \gamma\gamma \rightarrow \mu^+ \mu^-) \geq (6.81 \pm 0.32) \times 10^{-9} \quad (2.18)$$

and

$$B(K_L^0 \rightarrow \gamma\gamma \rightarrow e^+ e^-) \geq (3.03 \pm 0.14) \times 10^{-12}. \quad (2.19)$$

2.7 Real Part of the Amplitude

The real part of the amplitude contains two parts: long- and short-distance contributions. The diagram for the long-distance contribution is illustrated in figure 2.3. As in the case

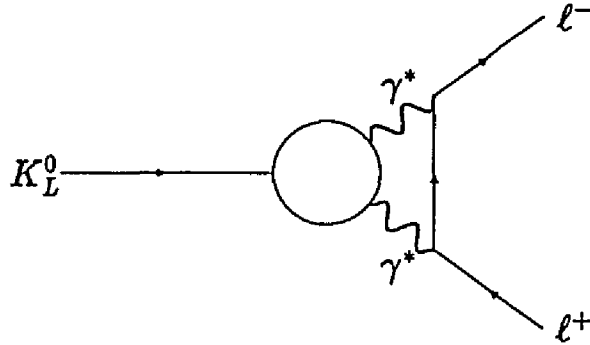


Figure 2.3: $K_L^0 \longrightarrow \ell^+ \ell^-$ via virtual two photon intermediate state.

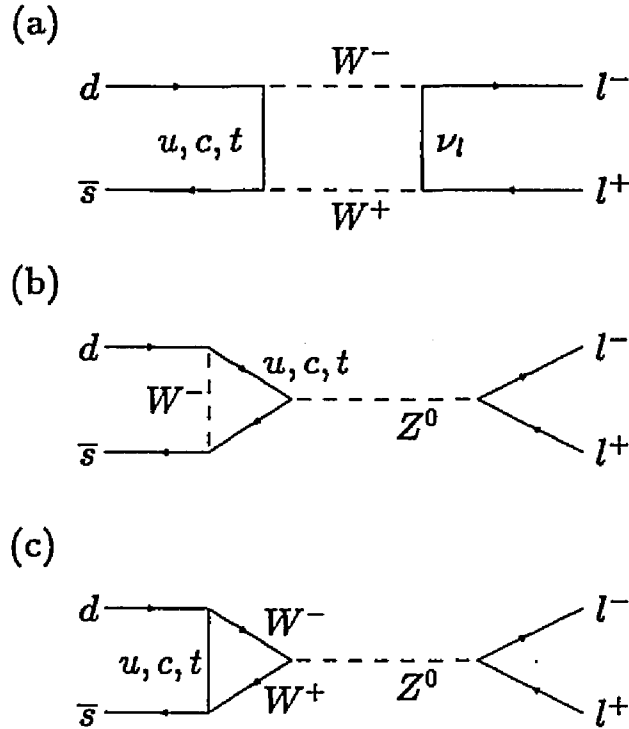
of the imaginary part of the amplitude, other intermediate states are exceedingly small. The contribution of this diagram is difficult to calculate, but it has been estimated by G. Belanger and C. Q. Geng[38]. They found that this diagram could contribute between 0.5 and 3.0 % of the unitarity rate if other contributions in the real part of the amplitude were neglected. This uncertainty has serious adverse effects on the ability to use the $K_L^0 \longrightarrow \ell^+ \ell^-$ measurements to constrain CKM matrix elements and the mass of the top quark.

The short-distance contributions to the real part of the amplitude are illustrated in figure 2.4. The rate from these diagrams will be dominated by the contribution of the top quark since it is so much more massive than the u and c quarks. The u and c contributions are further suppressed since the GIM mechanism will allow them partially to cancel. They do not cancel completely since their masses are not the same. Thus, to a good approximation, the amplitude from the short distance diagrams will be proportional to[39]:

$$\left(\frac{M_t}{M_W}\right)^2 |Re(V_{td}^* V_{ts})|^2 \quad (2.20)$$

2.8 Radiative Corrections

The final topic that needs consideration is the effect of radiative corrections on $K_L^0 \longrightarrow \ell^+ \ell^-$ decays. Radiative corrections have two significant implications[40]. First, they represent a correction to the calculation of the expected rate at which the decays should occur. Secondly, they are experimentally interesting since they could displace real events outside


 Figure 2.4: Short distance contributions to $K_L^0 \rightarrow l^+ l^-$.

of the experimentally defined signal region. The effect on di-electron events is expected to be much greater than the effect on di-muon events simply because of the large difference in masses of the two leptons.

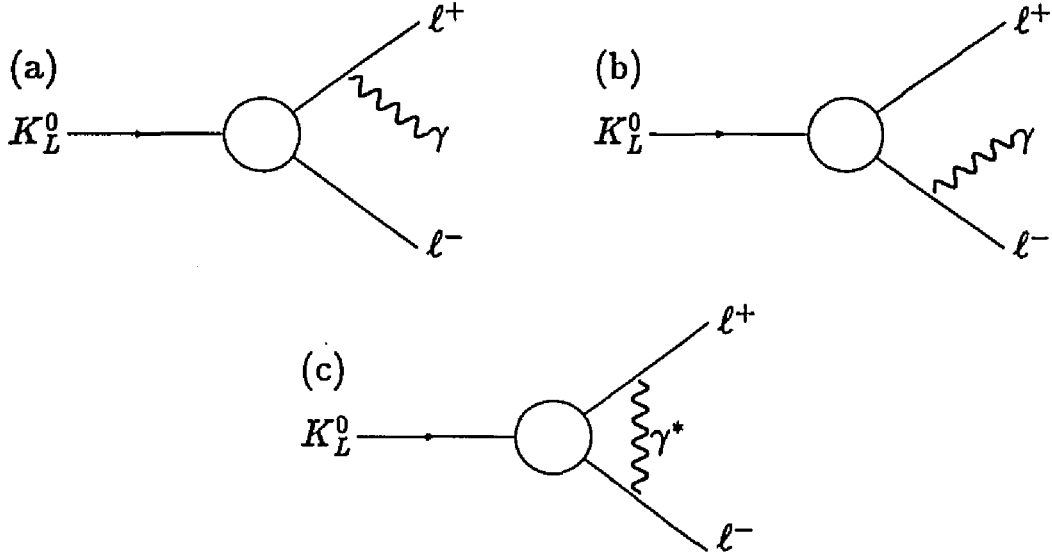
The fractional rate given by the diagrams (a) and (b) in figure 2.5, referred to as inner bremsstrahlung (IB), was calculated by Bergström[41]. The work presented actually pertained to radiative corrections of the decay $\pi^0 \rightarrow e^+ e^-$, but is generally applicable to pseudoscalar meson decays. With slight corrections to his presentation, he found this fractional rate to be:

$$\frac{1}{\Gamma_{l^+ l^-}^0} \frac{d\Gamma^{IB}}{ds} = \frac{\alpha}{\pi} \frac{1}{m_K^4} \left\{ \frac{s^2 + m_K^4}{m_K^2 - s} \ln \left(\frac{1+v}{1-v} \right) - \frac{2m_K^2 s v}{m_K^2 - s} \right\}, \quad (2.21)$$

where

$$v \equiv \sqrt{1 - \frac{4m_l^2}{s}} \quad \text{and} \quad s = (p_+ + p_-)^2 \quad (2.22)$$

Notice that equation 2.21 diverges at the kaon mass. Diagram (c) in figure 2.5, referred to as the virtual vertex correction (VIRT), needs to be included in order to eliminate

Figure 2.5: Radiative corrections to $K_L^0 \rightarrow \ell^+ \ell^-$ decays.

this divergence. This term is important to the overall correction but is expected to have little effect on the overall decay spectrum away from the kaon mass. Including this effect and calculating the change in rate yields:

$$\frac{(\Gamma^{IB} + \Gamma^{VIRT})}{\Gamma_{\ell^+ \ell^-}^0} = \frac{\alpha}{\pi} \left\{ \frac{3}{2} \ln \left(\frac{1-v_0}{1+v_0} \right) + \frac{9}{4} + O \left(\frac{m_\ell^2}{m_K^2} \right) \right\} \quad (2.23)$$

$$\approx -0.0427 \rightarrow e^+ e^- \quad (2.24)$$

$$\approx -0.0052 \rightarrow \mu^+ \mu^- \quad (2.25)$$

where

$$v_0 \equiv \sqrt{1 - \frac{4m_\ell^2}{M_K^2}} \quad (2.26)$$

Clearly at first order there is a very significant effect for $K_L^0 \rightarrow e^+ e^-$ and a small, essentially insignificant, effect for $K_L^0 \rightarrow \mu^+ \mu^-$. In order for the radiative corrections to produce a noticeable change in the rate from unitarity and other contributions, at least 40,000 $\mu^+ \mu^-$ events would need to be observed. This estimate neglects the lack of certainty in the contributions from the real part of the amplitude and other experimental uncertainties. Nonetheless, these corrections can be incorporated into the unitarity bound.

One potentially serious effect of the corrections is experimentally interesting. Notice that equation 2.21 implies that the spectrum of reconstructed masses is now spread from the lowest possible mass to the mass of the kaon assuming perfect mass resolution. If equation 2.21 is integrated over the reconstructed mass from the lowest possible mass, $s = 4m_l^2$ to the experimental cutoff used in the experiment, defined as $s = (1 - \delta)M_K^2$ where δ is the ratio of the square of the value of the lower mass cut value to the square of the mass of the kaon, the fraction of events lost due to the radiative corrections pushing events outside of the mass window can be obtained. This loss is found to be:

$$-\frac{1}{\Gamma_{l^+l^-}^0} \int_{4m_l^2}^{(1-\delta)m_K^2} \frac{d\Gamma^{IB}}{ds} ds = -\frac{\alpha}{\pi} \left\{ 2 \ln(\delta) \left[\ln \left(\frac{1-v_0}{1+v_0} \right) + 1 \right] \right. \\ \left. + \left(\frac{3}{2} - 2\delta \right) \ln \left(\frac{1-v_0}{1+v_0} \right) + \frac{13}{4} - \frac{\pi^2}{3} \right. \\ \left. - 2\delta + O \left(\frac{m_l^2}{m_K^2} \right) \right\} \quad (2.27)$$

$$\approx -0.1746 \longrightarrow e^+e^- \quad (2.28)$$

$$\approx -0.0244 \longrightarrow \mu^+\mu^- \quad (2.29)$$

There is also the possibility that events could be displaced from the expected signal region in colinearity space (see section 4.7). This has been studied in detail by J. Belz for $K_L^0 \longrightarrow e^+e^-$ events[42]. The effect yielded an additional 0.7% loss in events. Since the muon is much more massive, the effect on $K_L^0 \longrightarrow \mu^+\mu^-$ decays should be down by at least an order of magnitude. An additional correction at this level is insignificant for $K_L^0 \longrightarrow \mu^+\mu^-$. Finally, the effect of radiative corrections on $K_L^0 \longrightarrow \pi^+\pi^-$ is not known. One might expect the effect to be similar to $K_L^0 \longrightarrow \mu^+\mu^-$ due to the similarity of the masses. In order to calculate the effect properly, however, the calculation by Bergström would have to be redone replacing the Dirac spinors with Klein-Gordon functions. The effects of radiative corrections to the $K_L^0 \longrightarrow \mu^+\mu^-$ branching ratio are, therefore, not included in this dissertation.

Chapter 3

The E791 Detector

3.1 Overview

Figure 3.1 illustrates the E791 detector from the incident proton beam to the last detector element[43]. The neutral kaon beam used in the experiment was produced by the interaction of 24 GeV/c protons on a thin cylindrical copper target. Immediately downstream of the target, a series of separated lead foils converted photons, two sweeping magnets removed charged particles from the secondary beam and three collimators defined the solid angle of the beam. After the beam was filtered and shaped in this fashion, the remaining particles, primarily kaons and neutrons, entered the decay region. In the absence of decays, these particles would travel through the centerline of the detector. The daughter particles of kaons that did decay entered the main experimental area after passing through a thin window at the end of the evacuated decay region. A series of five sets of drift chambers (DC's) and two spectrometer magnets tracked and measured the momenta of the daughters. Farther downstream, a set of two trigger scintillation counters (TSC's) provided information on the presence of charged tracks to the acquisition hardware and were used in the offline tracking algorithms. Two electron identification detectors were also used. The first of these was a Čerenkov counter (CER) which was placed between the two sets of TSC's. The second electron detector was a lead glass array (PbG) which was immediately downstream of the second TSC. A thick iron wall following the PbG served to filter out nearly all remaining particles except muons. The muons that traversed the iron filter entered two detector systems that provided for muon detection. The first of these was a muon hodoscope (MHO)

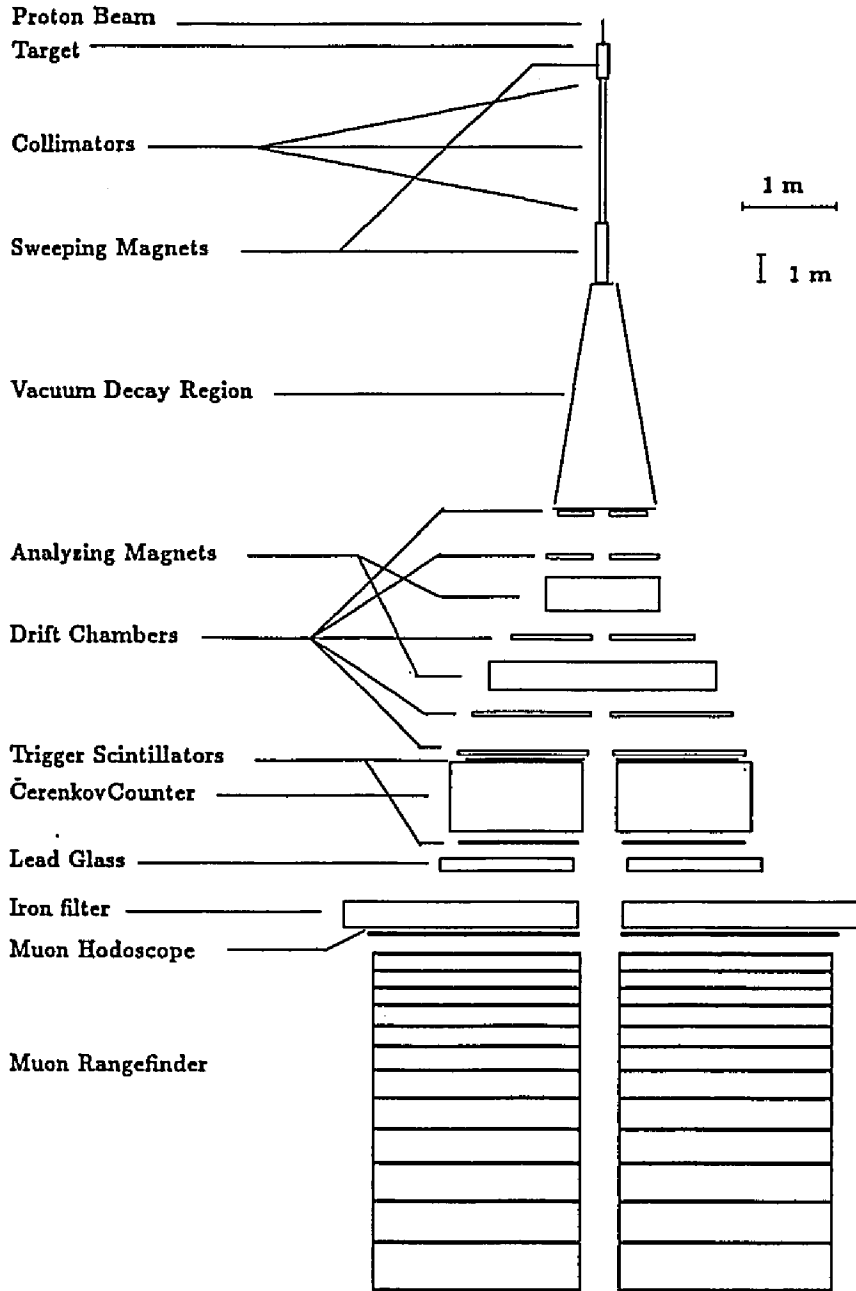


Figure 3.1: Schematic view of the BNL E791 detector and beamline.

immediately followed by a sizeable muon rangefinder (MRG). In areas of the detector with significant air gaps, such as the spectrometer magnets, helium filled bags were installed in order to minimize interactions of the charged tracks and the neutral beam with molecules of air.

3.2 B5 Beamline

3.2.1 The Proton Beam

The Brookhaven National Laboratory Alternating Gradient Synchrotron (AGS) provided E791 with 24 GeV/c protons while operating in slow extracted beam (SEB) mode. This mode provided for a reasonably uniform spill length of 1.2 to 1.4 seconds by accelerating the protons, then debunching them and finally extracting them into the B5 beamline. Since the spill was not perfectly uniform, the effective spill length typically varied between 1.0 and 1.3 seconds. The spill cycle time also varied between 2.8 and 3.4 seconds. The maximum intensity maintained in the AGS was about 15×10^{12} protons per spill (15 Tp/spill), of which approximately 4-6 Tp/spill was available to E791. The average intensity was approximately 4 Tp/spill in 1989 and 5 Tp/spill in 1990. The optimal intensity that the E791 detector could use was approximately 4.6 Tp/ (effective spill second), or on the order of 5.5 Tp/spill. This value represents a compromise between maximizing kaon production at the target and minimizing the amount of background noise generated. Since E791 was competing with other experiments for available protons, the intensity was usually slightly below the optimal value.

3.2.2 The Target

The protons provided by the AGS were incident on a copper target. The steering of the proton beam onto the target was monitored by a series of segmented wire ionization chambers (SWIC's). The copper target was a thin rod with a square cross section and 203 mm in length (1.33 nuclear interaction lengths). The cross section of the target was a 5 mm square in 1989 and a 3 mm square in 1990. This choice of target dimensions was made as a result of target studies[44]. Identical targets were used in the 1988 and 1990 running periods. The change to a larger diameter target in 1989 was made in an attempt to catch a larger fraction of the proton beam. Further studies indicated, unfortunately, that the

larger diameter target had the adverse effect of making the data noisier; thus the target was replaced with a thinner one in 1990.

The target was mounted on an aluminum holder that allowed for the dissipation of heat generated by interactions. The holder could also be rotated with respect to the E791 detector centerline. The angle between this centerline and the target axis was referred to as the targeting angle. The proton beam entered the E791 beamline at shallow vertical incidence to the detector centerline. Targeting angle studies showed that the most reasonable targeting angle was 48 mrad. This choice of targeting angle was actually a trade-off between kaon production and noise generated. At smaller targeting angles the kaon yield is greater, but the amount of noise generated also increases. The reverse occurred at larger targeting angles. The target was supported from above in 1989 and from below in 1990. Schematic illustrations of the target holders used in 1989 and 1990 are shown in figures 3.2 and 3.3[44].

3.2.3 The Neutral Beamline

The interactions at the target produced a myriad of particles. Since the only particles of interest were neutral kaons, a series of lead foils, sweeping magnets and collimators served to remove unwanted particles and to define the solid angle of the secondary beam. The apparatus for this was located in the upstream end of the E791 beamline and is shown in figure 3.4[45]. Two sweeping magnets followed the target. These magnets removed charged particles from the beam. A series of eighteen 5-mm thick lead foils was placed in the upstream half of the first sweeping magnet. These foils converted γ 's into e^+e^- pairs. The attenuation factor of each foil is about 0.5, yielding a total attenuation factor on the order of 10^{-6} . These charged pairs were then removed by the sweeping magnets. In the downstream half of the first sweeping magnet, between the two sweeping magnets and in the second sweeping magnet, a set of precision collimators defined the solid angle of the secondary beam. These collimators were flared brass channels surrounded by lead shielding with a vertical opening of 20 mrad and a horizontal opening of 5 mrad. The coordinate system that defined the position of all detector elements had its origin at the projected position where the collimator opening shrank to a point. The centerline of this system was 78" above the experimental floor.

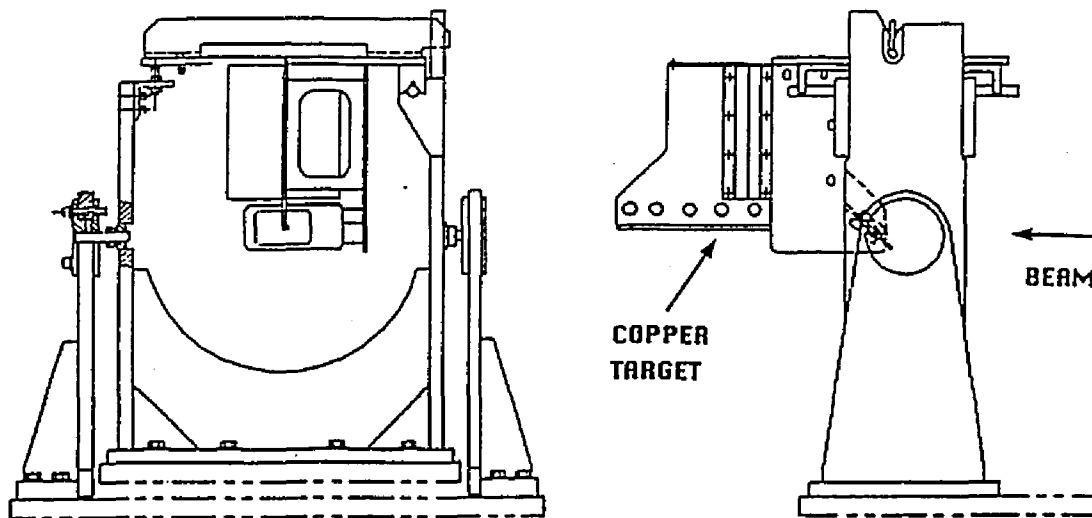


Figure 3.2: The target holder used in 1989.

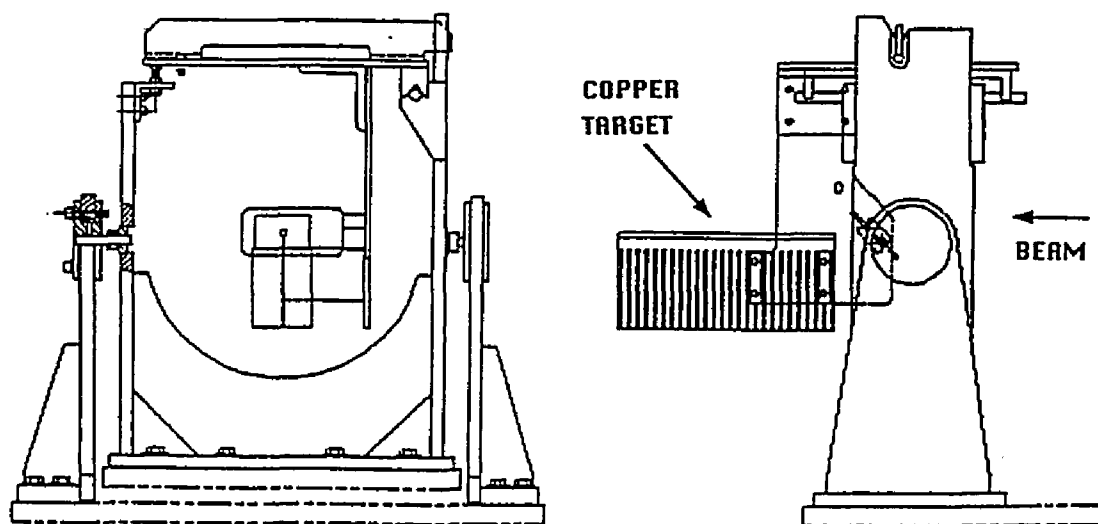


Figure 3.3: The target holder used in 1990.

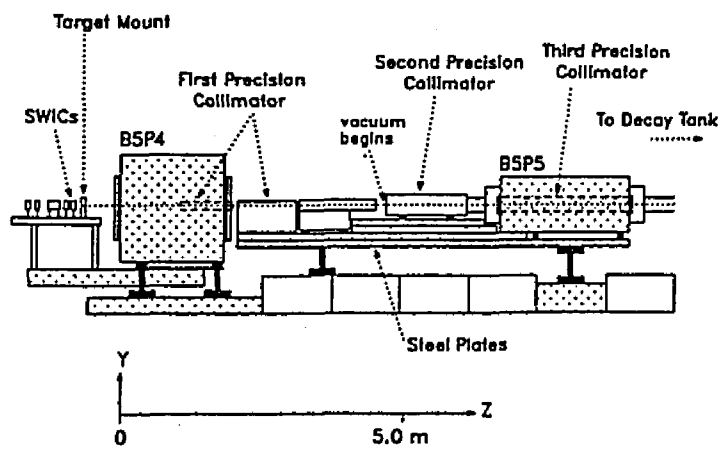


Figure 3.4: The upstream end of the E791 beamline.

3.2.4 The Vacuum Decay Region

After exiting the final collimator and sweeping magnet, kaons entered an evacuated decay region. This decay volume was constructed of a conical steel tank 8.4 m long. The upstream end of the tank was at a z position of 9.4 m. At the downstream end of the tank the diameter was 0.97 m. A portion of the upstream end of the decay volume was packed with a boron water slurry. The entire volume was encased in concrete shielding in order to absorb stray particles. A diagram of the shielding used in the vacuum region as well as the upstream end of the beamline is shown in figure 3.5[46]. The end of the decay volume was sealed by a flange and Mylar window that differed in the 1989 and 1990 running periods. In 1989 the flange contained three rectangular windows. These consisted of two side windows for the decay products to exit and a smaller center window that allowed for the neutral beam to exit with minimal interactions. The side windows consisted of 0.51 mm thick Mylar, while the center window, also Mylar, was 0.25 mm. The dimensions of the side windows were 0.35 m by 0.69 m while the central window had the dimensions 0.14 m by 0.46 m. In 1990, the endcap was replaced with a circular flange and window. The radius of the window was 0.4794 m and consisted of 0.13 mm of Mylar and 0.43 mm of Kevlar. The windows used in 1989 and 1990 are shown in figures 3.6 and 3.7[42].

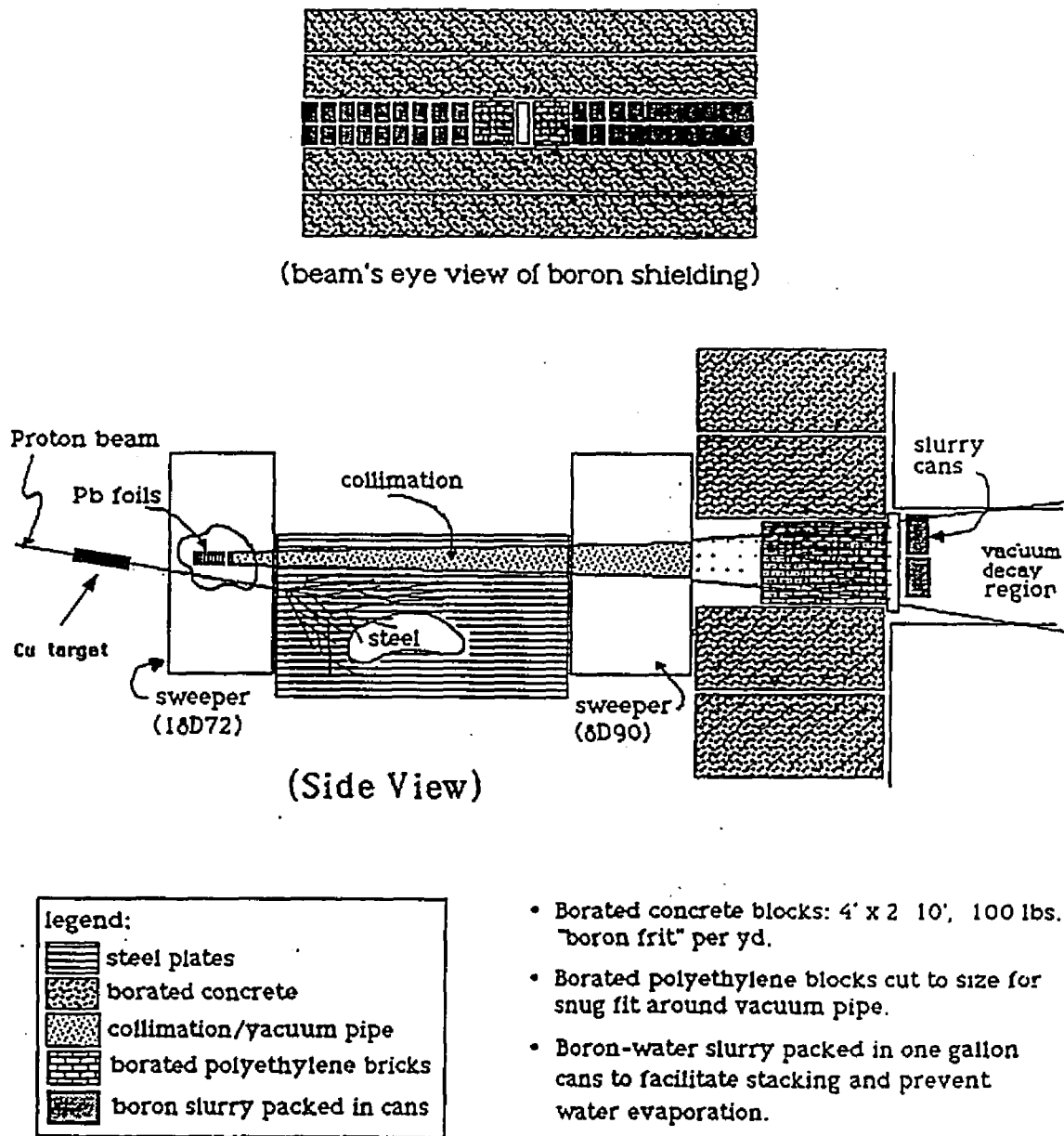


Figure 3.5: Beamline shielding diagram.

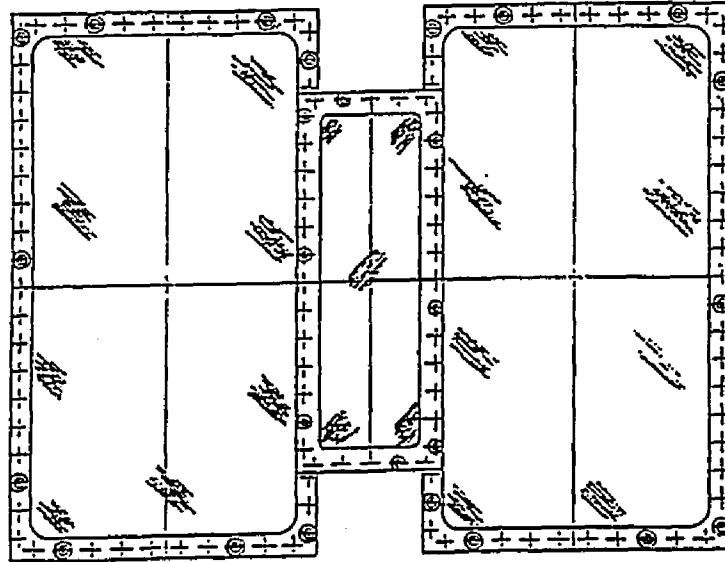


Figure 3.6: Vacuum window used in 1989.

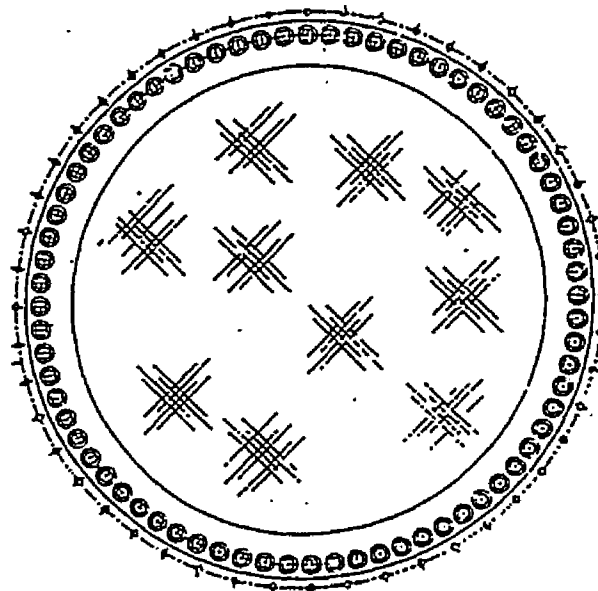


Figure 3.7: Vacuum window used in 1990.

3.3 Spectrometer

3.3.1 Overview

The E791 spectrometer was designed to measure the positions and momentum of the charged tracks from K_L^0 decays. These quantities were measured twice in the spectrometer. The measurements were almost completely independent, making the spectrometer a redundant detector. This redundancy was of great value since it permitted the elimination of much of the background associated with the experiment. The spectrometer consisted of two large dipole magnets, five sets of precision drift chambers and two sets of trigger scintillation counters. It can be thought of as an upstream, or front, spectrometer and a downstream, or back, spectrometer. The trigger scintillation counters were used in triggering and offline tracking and are thus common to both halves. The third drift chamber set is also common to both spectrometer halves. As a result, the two spectrometer halves are not completely independent.

3.3.2 The Spectrometer Magnets

The spectrometer magnets consisted of two dipole magnets with their center z positions at 21.0 and 24.0 meters. The first, or upstream, magnet was designated as the 48D48 (or D2). It was 48" wide (x) by 48" deep (z) with a gap of 37" (y) between the pole faces. The downstream magnet was designated as the 96D40 (or D3). The dimensions here were 96" wide by 40" deep with a gap of 44" between pole faces. The fields in both magnets were primarily in the y -direction. Each magnet had iron mirror plates on the upstream and downstream faces that forced the field strength to diminish rapidly outside the dipoles while not reducing the geometrical acceptance. The central field in each dipole was approximately 6.3 kG. Integrated over both magnets, the fields imparted approximately equal and opposite 300 Mev/c transverse momentum kicks. The fields were oriented such that positive particles were bent in the $+x$, or beam left, direction in the upstream magnet and in the $-x$ direction in the downstream magnet. A top view of the spectrometer magnets and drift chambers is presented in figure 3.8[47].

The 48D48 had one upper and one lower coil. The space between the upper and lower coils, about 18.7", was filled with a wooden support. The 96D40 had two upper and lower coils. The space between the upper and lower coils was exceedingly small so no supports were implemented. Since the 96D40 was about twice as wide as the 48D48, additional coils

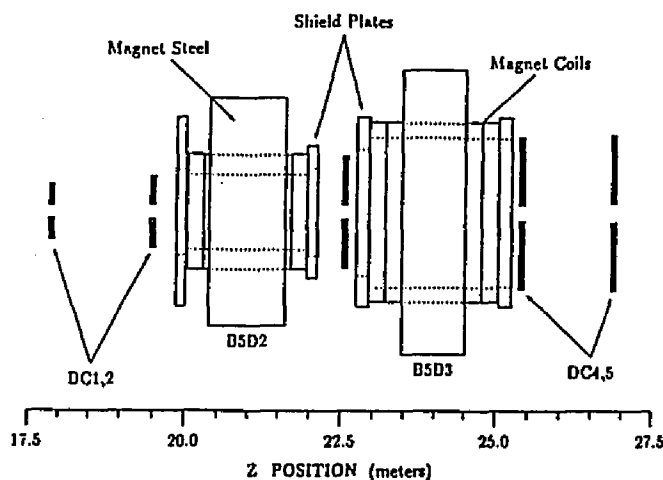


Figure 3.8: Schematic of the E791 spectrometer.

were required in order to keep the field uniformity at about the same level as in the 48D48. In addition, each magnet had a helium bag in the interior in order to minimize scattering of the charged particles and the neutral beam.

The B_y and B_x components of the field were mapped on a 2" cubic grid. The map was made for z positions between 18.6 and 26.7 meters. When combined with the allowed x and y positions, the full map consisted of about 100,000 points. The measured value of the B_x component was small and had a relatively large error. The B_z component was not measured. Consequently, values for B_x and B_z that were calculated by an approximate solution of Poisson's equation were used. Variations in B_y due to errors in positioning the probe were removed by spline fits. In areas in which a measurement was physically impossible, the B_y value was calculated by extrapolation[48].

Since the E791 apparatus was designed to detect two body charged decays, the spectrometer magnets divided the type of events detected into two classes. If a negatively charged particle was beam left (a positively charged particle was beam right), the tracks would initially be bent toward each other in the 48D48. The 96D40 would then bend the tracks away from each other until they were traveling approximately parallel to their initial trajectories. This class of events is referred to as inbends. The location of the charged tracks in the other type of event were reversed and are referred to as outbends.

3.3.3 The Drift Chambers

E-791 used ten drift chamber modules with five of them in each arm of the spectrometer. The chambers, viewed from above in figure 3.8, had successively larger dimensions in increasing z to accommodate for the divergence of the charged tracks. During the 1989 running period, the first chamber was 25% smaller in x and about 12% smaller in y than that used in 1990. In addition, the larger chambers used in the 1990 running period were about 3 cm closer to beam center than those used in 1989. The change in chambers at the first station was made in conjunction with the change in the vacuum window. Helium bags were installed between the first two modules and the last two modules as in the spectrometer magnets.

Each module consisted of two x and two y measuring planes. Each plane consisted of sense, field and guard wires. The two planes of sense wires in each measuring plane were offset from each other by half the distance between consecutive sense wires. These wires were surrounded by field wires that defined an irregular hexagonal cell. The two planes of cells were bordered on the upstream and downstream sides by a plane of guard wires. The general layout of these wires is shown in figure 3.9[49].

The sense wires consisted of 0.001" gold plated tungsten wire. They were strung with a tension provided by a 40 gram weight in order to maintain electrostatic stability. The field and guard wires consisted of 0.0043" gold plated aluminum. Aluminum, rather than tungsten, was used in order to minimize scattering in the chambers. These wires were strung with a tension provided by a 140 gram weight. Under these choices of tensions, the gravitational sag of the horizontal wires (y measuring planes) is identical for all three types of wires. Distortion of the chamber frames was minimal because of the relatively low tensions in the wires. The frames had a gap near beam center incorporated in order to minimize noise due to interactions of the neutral beam with the aluminum frame. The design of the frames is illustrated in figure 3.10[45].

The upstream and downstream faces of each drift chamber module were sealed in a laminate of 0.005" Mylar and 0.00035" aluminum. The chambers were flushed with a mixture of 49% argon, 49% ethane and 2% ethanol at a very slight pressure above atmospheric. The sense wires were grounded and linked to custom preamplifiers mounted directly on the chambers. The field wires were held at a nominal voltage of -2500 volts. The guard wires were also grounded. The guard and field wires provided a uniform field within each measuring plane. Under these high voltage settings and gas mixtures, the drift velocity was $51\mu\text{m}/\text{ns}$ for electrons.

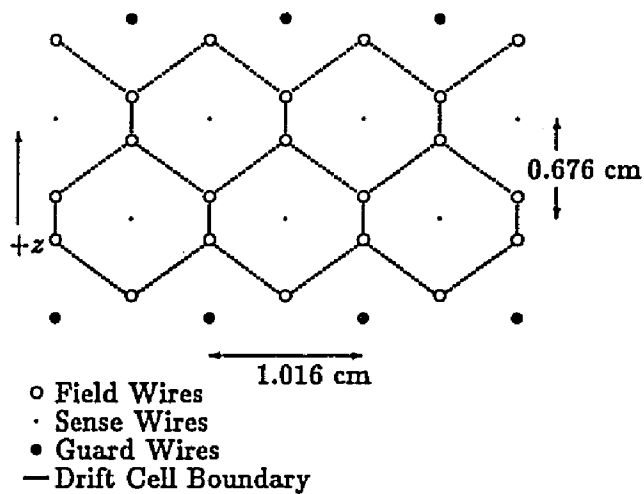


Figure 3.9: Geometry of drift chamber wires.

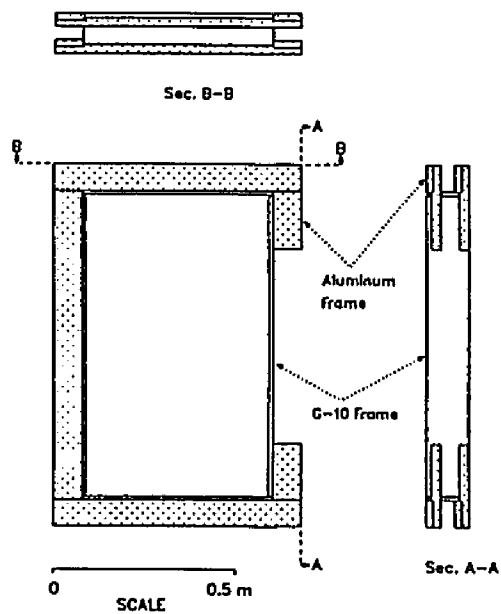


Figure 3.10: The design of the drift chamber frames.

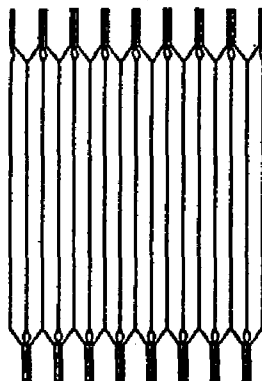


Figure 3.11: The x measuring trigger scintillation counters.

The preamplifiers had an input impedance of 300Ω and a gain of about 20. The outputs of the preamplifiers were input, in groups of 4, to 32 channel boards that contained amplifiers, discriminators and meantimers (ADM's). These boards were located in crates close to the chambers. The signals were carried to them via relatively short ribbon coaxial cables (about 17 feet) with an impedance of 50Ω . The outputs of the meantimers and discriminators, ECL signals, were sent to the level 1 trigger and digitization electronics via Ansley cables.

3.3.4 The Trigger Scintillation Counters

Two sets of trigger scintillation counters were placed at z positions of 26.98 meters and 30.27 meters, respectively. These are shown in figure 3.11[50]. Each set of TSC's consisted of 60 x measuring slats and 63 y measuring slats with the x measuring slats being farthest upstream. The upstream vertical and horizontal slats had the dimensions $2.01 \times 180 \times 0.50$ cm and $2.81 \times 128 \times 0.50$ cm, respectively. The downstream slats differed only in that their thickness was 1.00 cm. The slats were composed of the scintillant Kyowa Glass SCSN-38. Each slat was wrapped in aluminized Mylar to reflect photons incident on the sides of the counters. Each set was enclosed in a light tight box. The enclosure was flushed with compressed air in order to remove excess heat generated by the phototubes.

The horizontal slats had one phototube attached to each slat. The vertical slats had one phototube attached to two adjacent slats both on the top and bottom. The tubes were

staggered between the top and bottom in such a way that each slat had only unique top and bottom pair of phototubes. The phototubes were Hamamatsu R1398's and were glued directly to the slats. Each tube was housed in a magnetic shield to protect against the fringe fields of the D3 spectrometer magnet.

The voltage settings on the phototubes were determined from their plateau region and were typically on the order of -1800 V. Signals from the phototubes were sent to Lecroy 4413 discriminators over 50Ω RG8 coaxial cables. These discriminators were CAMAC based and produced ECL outputs. The output of the discriminators was sent to digitization electronics, meantimers and a latch module.

3.4 Electron Identification Elements

3.4.1 Overview

The electron identification elements of the detector consisted of a set of two Čerenkov counters and a lead glass array. Although they performed slightly different functions, they represented a redundant determination of the presence of electron tracks. As in the spectrometer, this redundancy was critical for background rejection. The electron detection elements were vital parts of background determinations and efficiency calculations of the $\mu^+\mu^-$ analysis.

3.4.2 The Čerenkov Counters

The gas threshold Čerenkov counters consisted of two modules, one on each side of the beam line, located between the two sets of TSC's. Side and top views of one of these modules are illustrated in figures 3.12 and 3.13[51]. Each module was a gastight aluminum box 3.0 meters in length by 1.6 meters in width and contained a volume of 8.50 cubic meters. The upstream and downstream faces were $1/32$ " thick. The CER was filled with a gas mixture of about 40% nitrogen and 60% helium and was at a pressure slightly above atmospheric. The exact mixture of the gas was adjusted periodically in order to produce a precise index of refraction of 1.000140. The index was monitored with an interferometer that used a Helium-Neon laser. This index of refraction gave thresholds for electrons, pions and muons of 0.031, 8.3 and 6.3 GeV/c, respectively. It also yielded a typical electron Čerenkov cone half-angle of 16.7 mrad

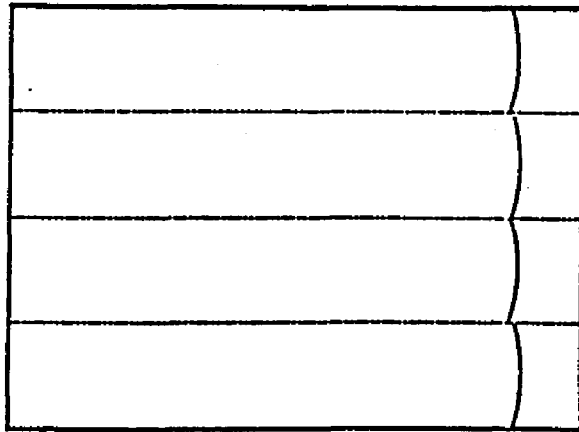


Figure 3.12: Top view of a Čerenkov counter.

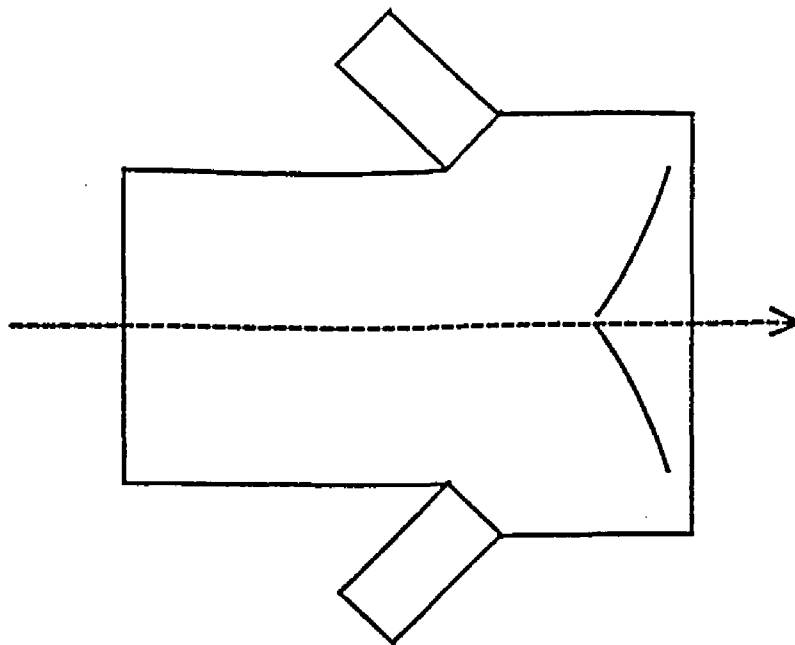


Figure 3.13: Side view of a Čerenkov counter.

Inside each Čerenkov counter there were eight spherical mirrors viewed by eight 5" diameter RCA Quanticon phototubes. The mirrors were 39 x 89 cm² and composed of 1/4" Lucite with 1.0 μm of aluminum evaporated onto their surfaces. A very thin layer of MgF₂ on the mirror surface prevented oxidation. The z position of the center of the mirrors was 29.86 meters. There was a 2.0 mm gap between each of the mirrors with the center of the upper and lower bank of four being located at $y = 0$. The mirrors were focused onto the phototubes with their exact alignment being maximized for electrons from the decay $K_L^0 \rightarrow \mu^\pm e^\mp$. The phototubes were located in two rows of four. One of these rows was on top of the box while the other was on the bottom. Both were located upstream of the spherical mirrors. Each phototube rested behind a quartz window located at the peak of an aluminized cone which acted as a light funnel. The phototubes were coated with a layer of para-terphenyl which acted as a wave shifter. The extensions of the phototubes outside of the counter were housed inside a thick cylindrical iron magnetic shield that also contained two layers of μ -metal. Finally, the tubes were continuously flushed with nitrogen in order to prevent helium diffusion into the tubes.

3.4.3 The Lead Glass Array

The lead glass array, illustrated in figure 3.14, consisted of a layer of active converter lead glass blocks followed by a layer of absorber lead glass blocks[52]. The upstream layer, or converter, consisted of 13 by 2 array of blocks in the $x y$ plane in each arm, for a total of 26 blocks in each arm. The dimensions of these blocks were 10.9 x 90 x 10 cm³. The total span of the converter was 1.42 x 1.87 x 0.1 m³. The absorber consisted of nine blocks in the x direction and 12 blocks in y . The dimensions of the absorber, or back blocks, were 15.3 x 15.3 x 32.2 cm³. The upstream faces of the converter and absorber blocks were located at z positions of 30.9 and 31.1 meters, respectively. All of the blocks were wrapped with an inner layer of 0.002" aluminized Mylar and an outer layer of 0.006" vinyl, or simply a layer of 0.008" aluminized vinyl. The upstream face of the absorber blocks and the downstream face of the converter blocks were not wrapped so that the blocks could be periodically exposed to ultra-violet radiation in order to cure radiation damage. These unwrapped faces were covered with a layer of black felt in order to keep the blocks lighttight. The entire PbG was housed in a lighttight and temperature controlled box to further prevent outside light from entering the detector and to eliminate temperature dependent effects.

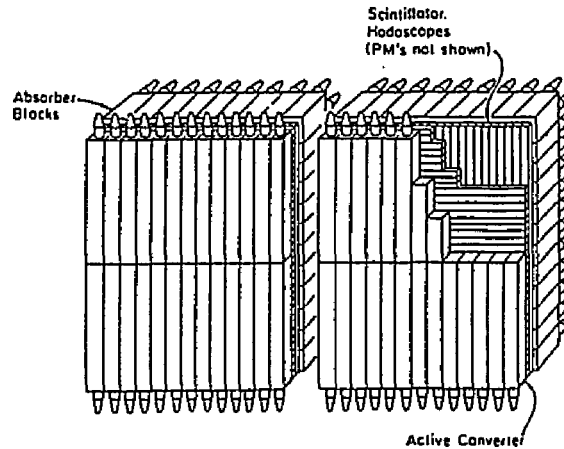


Figure 3.14: The lead glass array.

All of the PbG blocks were Schott F2 glass. The front, or converter, blocks had lightguides and phototubes mounted on the upper or lower edges of the blocks as appropriate. The absorber blocks had their phototubes mounted on the downstream face of the blocks. The interface between the blocks and the phototubes was a lightguide sealed between the block and phototube with a thin layer of the optical grease RTV16. Each tube was housed inside a μ -metal shield. Four different types of tubes were employed in the PbG array. Faster tubes were placed close to beam center to accommodate the higher rates due to the neutral beam. The converter blocks had 3" diameter Amperex 3462 tubes on the outer seven upper and lower blocks on each side. The remaining six upper and lower blocks nearest beam center used 3.5" EMI 9531R phototubes. The absorber used 5" EMI 9618R phototubes in general. The faster 5" Amperex 58AVP(DVP) tubes were used on the two columns closest to the detector centerline as well as the four central blocks in the third column. The response of the system was monitored via the use of a nitrogen laser and an optical dye. When excited by the laser, the optical dye produced light that was similar to that produced by electrons passing through the glass. This light was fanned out to the individual blocks by a bundle of optical fibers.

3.5 Finger Counters

A bank of scintillators was installed between the converter and back blocks of the PbG. This detector was referred to as the finger hodoscope (FNG). Each arm of the FNG consisted of

27 vertical counters and 36 horizontal counters. These slats were 5.1 cm wide, 1.5 cm thick and 143 cm long. They were constructed of the same material as the TSC's. The placement of phototubes was also identical to the TSC's. Each slat was wrapped in a layer of 0.002" aluminized Mylar and a 0.006" layer of black vinyl. Three different types of phototubes were used. The y measuring slats used Amperex XP2230 phototubes, while the x counters used Amperex 56AVP phototubes on top and EMI 9902 tubes on the bottom. The lowest y slat on each arm also used the EMI 9902 tubes due to space constraints. Each slat also had a green LED glued to it in order to provide test pulses to the system.

The FNG was used in 1988 to indicate the presence of γ 's from the four body decays $ee\gamma\gamma$ and $\mu\mu\gamma\gamma$. The presence of the γ 's was indicated by two clusters in each arm of the FNG. One of these clusters, in each arm, was presumed to be from the lepton in the decays $ee\gamma\gamma$ and $\mu\mu\gamma\gamma$. This detector element was not used in the 1989 or 1990 analyses. The finger counters can be seen in figure 3.14 but will not be considered beyond this short description.

3.6 Muon Identification Elements

3.6.1 Overview

The final elements in the E791 detector constituted the muon identification system. These elements were used in identifying the $\mu^+\mu^-$ candidates in the data samples. They were also used in the determination of efficiencies of $\mu^+\mu^-$ detection. The system consisted of one passive and two active elements. The passive element was a large iron wall immediately downstream of the PbG. This element filtered out all particles except muons and punch-throughs. The active elements were a muon hodoscope and a muon rangefinder immediately downstream of the iron filter. The muon rangefinder was originally designed in a way that would allow a measurement of the longitudinal polarization of the muons in the $K_L^0 \rightarrow \mu^+\mu^-$ decay. However, constraints that developed as the experiment was constructed precluded a full implementation of the original design concept.

3.6.2 The Muon Hodoscope

The muon hodoscope had its front face located at a z position of 33.7 meters. It was directly downstream of a 91-cm iron muon filter which had a back face about 5 cm upstream of the MHO. Both were shown in figure 3.15[51]. The MHO consisted of 11 x measuring slats and

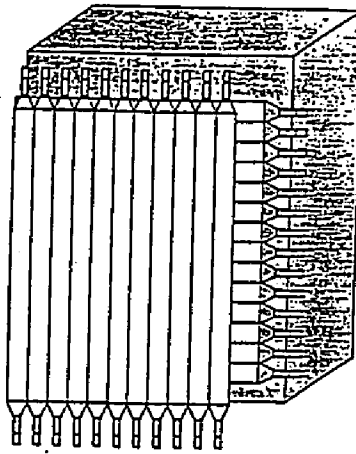


Figure 3.15: Illustration of the MHO and iron filter.

14 y measuring slats in each arm. The x and y measuring slats had lengths of 2.69 and 2.29 meters, respectively. The widths and thicknesses were identical for both and were 18.8 and 2.54 cm, respectively. The slats were made of Bicron BC408 scintillator. Each slat was wrapped in aluminized Mylar and black polyethylene. The horizontal slats had phototubes on one end while the vertical slats have phototubes on both ends. The end of the horizontal slats nearest beam center were blackened to eliminate reflections. The tubes were attached by tapering the last 15 cm of the slat from 18.7 cm to 5.1 cm and gluing the end directly to the phototube a clear epoxy. The tubes used were 2" Amperex XP2230's. They were encased in a cylindrical magnetic shield. Each slat also had a yellow LED embedded in a pre-formed notch, allowing test pulsing of the MHO system.

3.6.3 The Muon Rangefinder

The last detector element of E-791 was the muon rangefinder. The upstream face of the MRG was located at a z position of 34.4 meters. It was a two-arm system with each arm having the dimensions $2.25 \times 3.05 \times 12.7 \text{ m}^3$. The system consisted of 75 slabs of 3" Carrara marble in the upstream portion and 25 slabs of 3" aluminum in the remainder on each side. The marble slabs were constructed from four smaller slabs glued together with 3M 2216 B/A adhesive. After this construction, the entire slab had a steel band attached to the outside edge in order to preserve the structural integrity. Each slab was followed by a 2" air gap. The entire structure rested on a table and I-beam structure made of 6063-T6

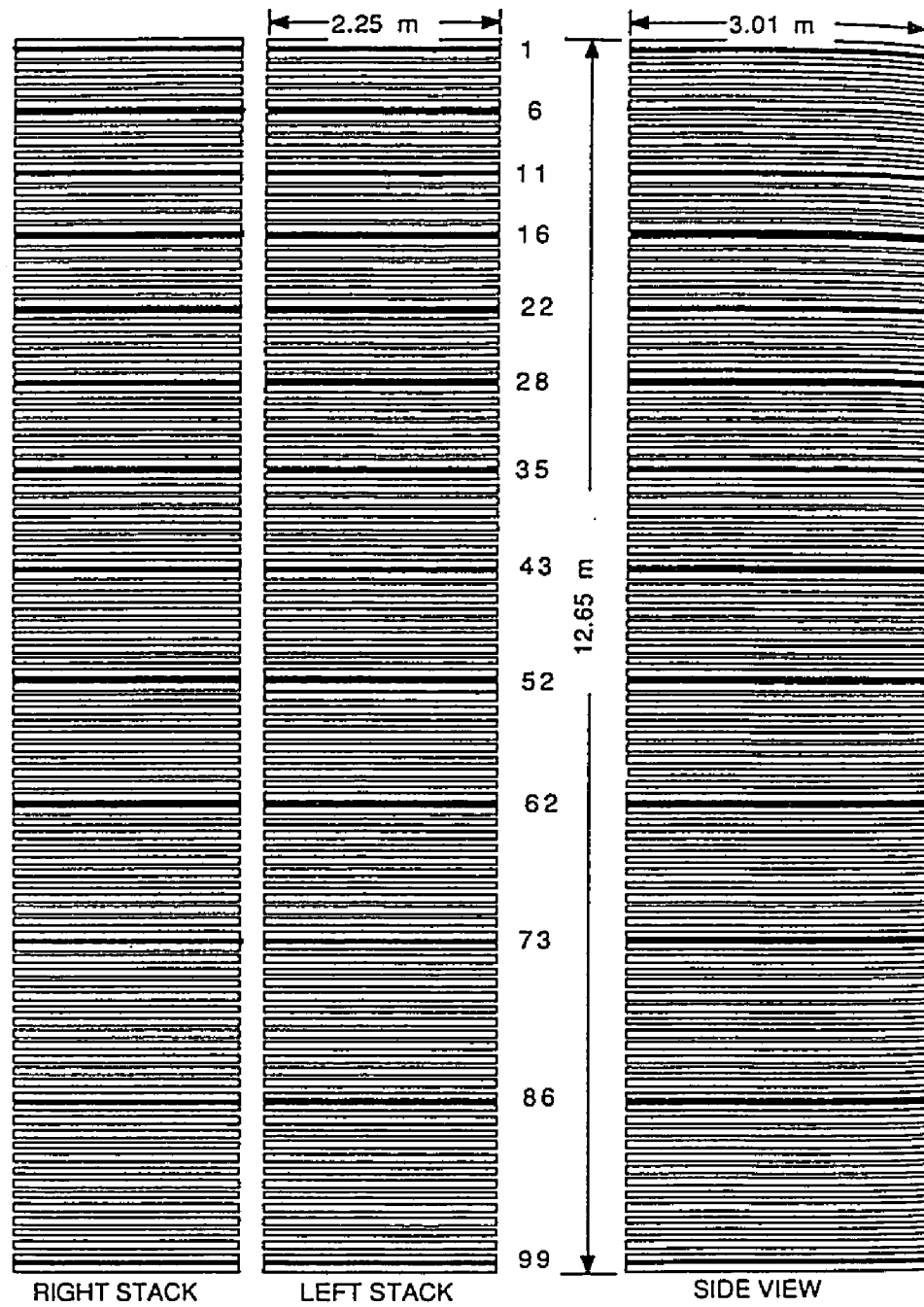


Figure 3.16: Top and side views of the muon rangefinder.

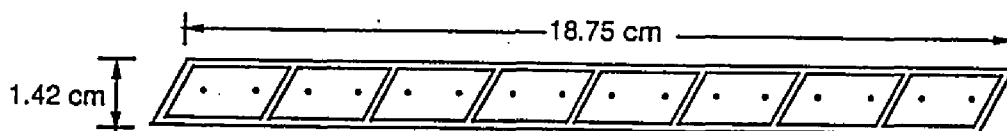


Figure 3.17: Cross sectional view of an extrusion.

aluminum alloy.

Thirteen of the air gaps were instrumented with x and y measuring proportional wire chambers. With the upstream-most air gap being labeled as 1, gaps 1, 6, 11, 22, 28, 35, 43, 52, 62, 73, 86, and 99 were instrumented to provide range measurements in 10% momentum intervals. A top view of the MRG is given in figure 3.16. The planes were constructed from extruded aluminum sections. Figure 3.17[53] is a cross sectional view of an extrusion[53]. Each section contained eight individual cells separated by an aluminum web at 30° to the normal. The cross section had cell dimensions of 1.2×2.1 cm with the aluminum walls being $1/16''$ thick. Two $75 \mu\text{m}$ gold plated tungsten wires separated by 1.06 cm were strung with 500 grams of tension in each cell. The wires, in turn, were held in place by Noryl wire-holders mounted in Lexan end-caps which were epoxyed to both ends of the section. The epoxy used on the endcaps as well as on the Noryl holders was Bondmaster 666 which also provided a gas seal.

The individual sections were then bonded together into planes with Loctite Depend. The x measuring planes contained 12 sections while the y measuring planes contained 16. Thin aluminum sheets were bonded across the epoxyed sections with a silver based conductive epoxy for grounding purposes. The dimensions of the x and y measuring planes were $225 \times 301 \times 1.42$ cm³. A front view of an x measuring plane is illustrated in figure 3.18[53]. A mixture of 49% argon, 49% ethane and 2% propanol was supplied to the planes via the gas distribution system sketched in figure 3.19[53]. Custom-made amplifier and discriminator electronics were attached to each plane. A pulse test signal was provided to all of the electronics for diagnostic purposes.

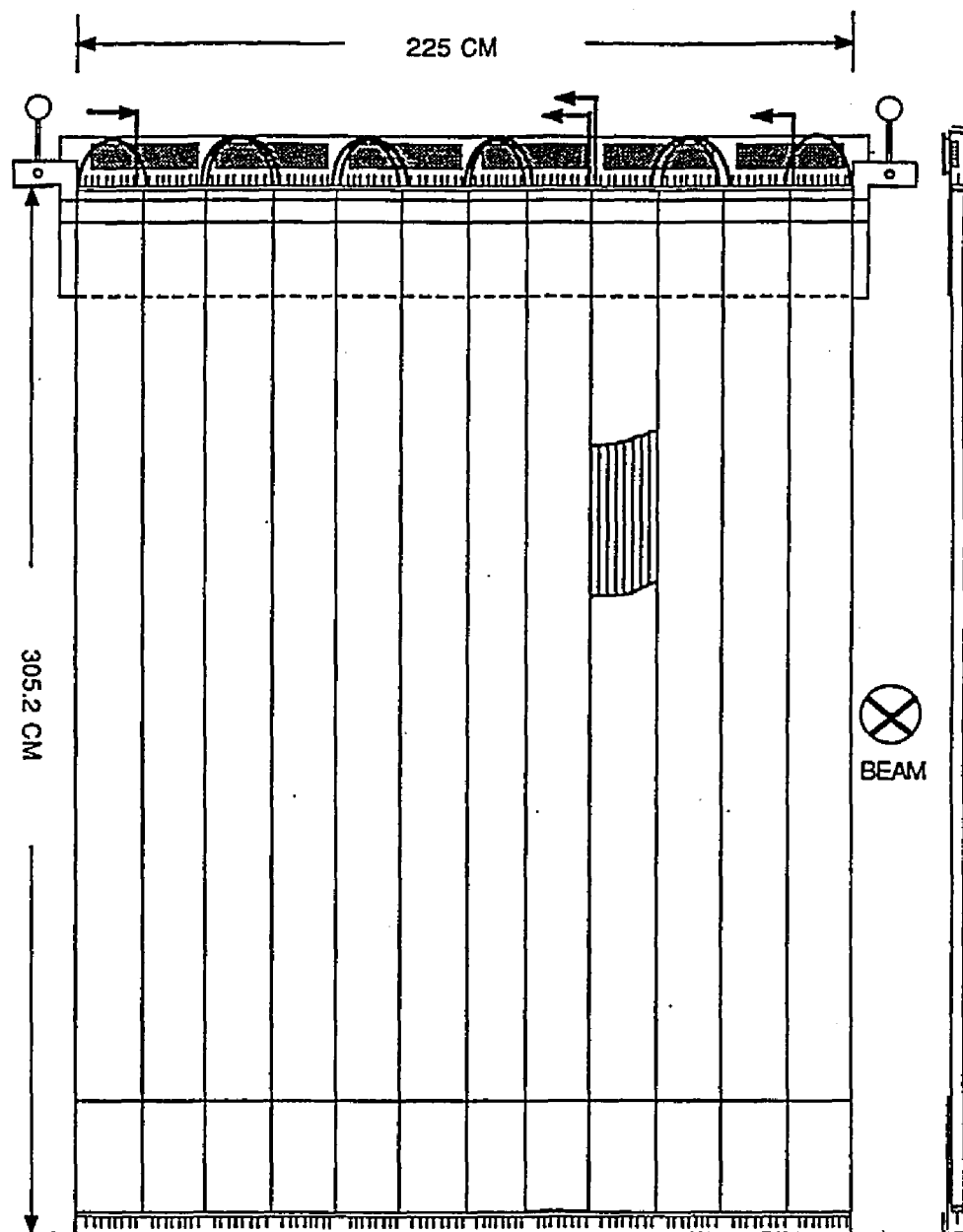


Figure 3.18: Illustration of an x measuring plane.

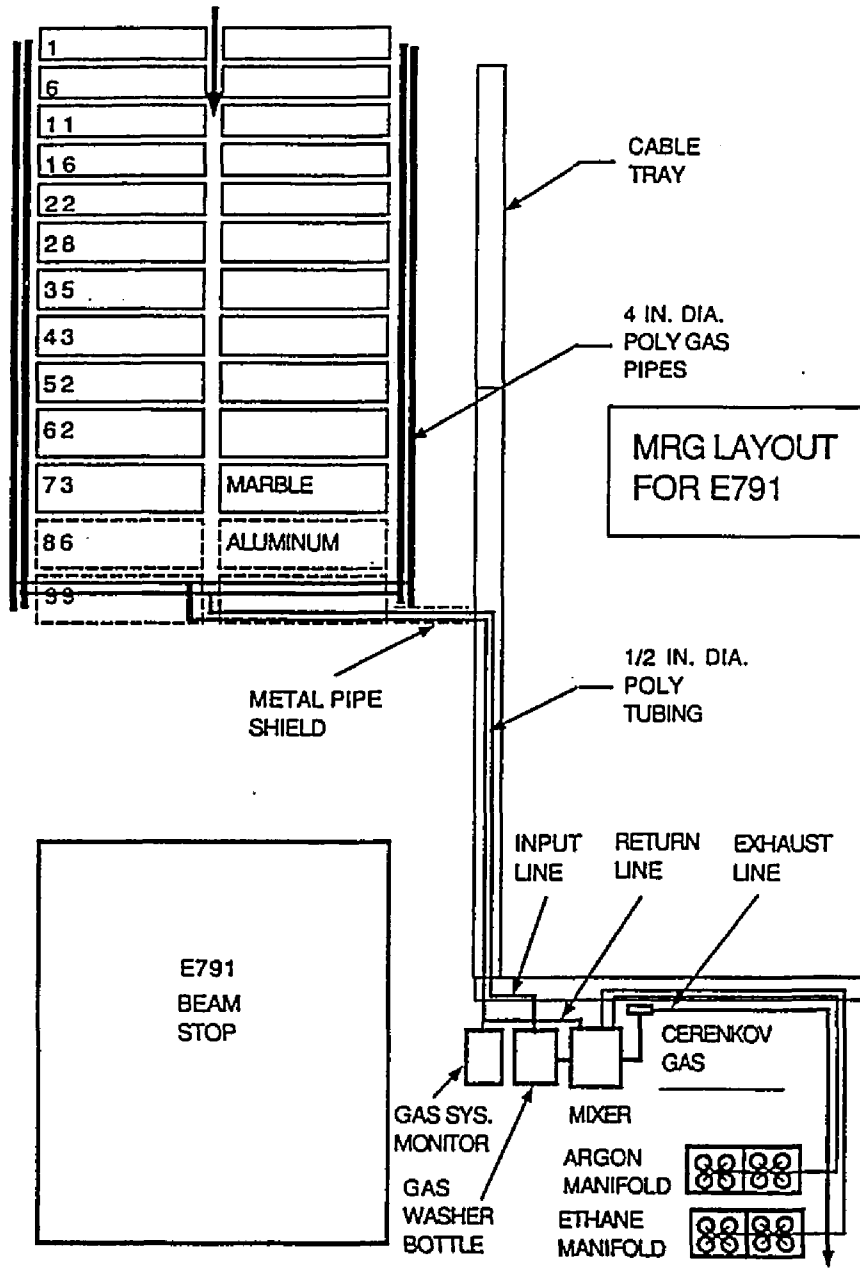


Figure 3.19: Schematic of the gas distribution system.

Chapter 4

The Data Acquisition System

4.1 Overview

Many particle physics experiments have problems associated with high rates, and that is particularly true in rare decay experiments. In order to reduce the initial rates in E791 to a manageable level, a complex data acquisition system was needed. This system required a multi-level triggering system. The information from individual detectors also needed to be digitized quickly. In order to minimize deadtime, several stages of buffers were required to hold the digitized data. Finally, since the data were obtained in spills, an online software trigger was needed so that data could be processed during periods when no data were being acquired.

Information from the detector elements was subjected to three distinct levels of triggering. These are the level 0 (L0), level 1 (L1) and level 3 (L3) triggers. A level 2 (L2) trigger was originally envisioned and implemented but eventually not used. Since the experiment was searching for several different decay modes, any given event could initially satisfy the criteria for more than one of the modes, which required the triggers to be highly parallel. The information from the detector elements was also highly parallel. Each detector required different and occasionally multiple sets of electronics to process signals. These electronics were of four different types and comprised the digitization system. The output associated with each detector element was eventually put together in a data set referred to as an event. The creation of this large data set from the smaller sets was controlled by a set of custom CAMAC modules, called the readout supervisor, and crate scanners associated with the digitization electronics for each detector. The final level of triggering

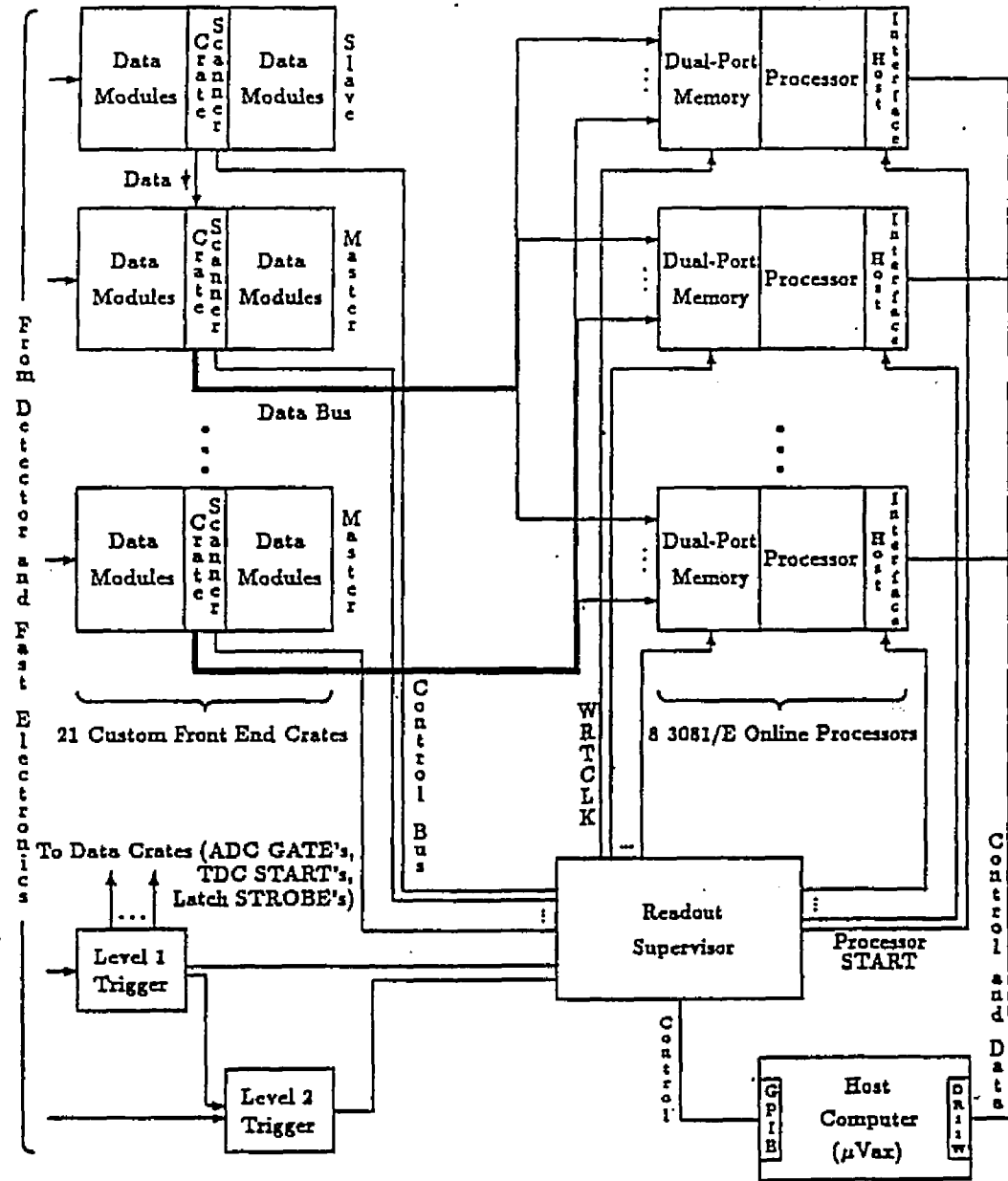


Figure 4.1: Schematic of the E791 acquisition system.

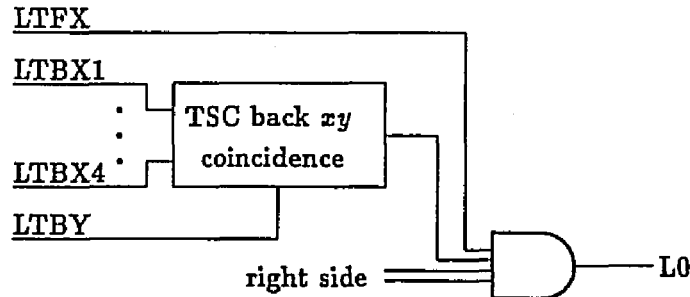


Figure 4.2: Logic to the L0 trigger.

was performed in a set of 3081E processors. After the final level of triggering, events were uploaded via a micro-VAX computer to tape. A schematic of the acquisition system is shown in figure 4.1[47].

The naming convention for the signals in the figures in this chapter corresponds to a short series of characters that uniquely identify the detector elements. The leftmost element is L or R, denoting the left or right arm of the detector. If there is no L or R, the implication is that the signals were AND'ed over the left and right sides of the detector. The next character(s) identify the individual detector elements. They can be a drift chamber (D1, D2, D3), a coincidence between drift chambers (D12), a front or back TSC (TF or TB), the CER (C) or the MHO (M). The next character, X or Y, refers to x or y measuring elements where applicable. The lack of an X or Y indicates an AND over the x and y elements. The final character identifies the logical segmentation within the detector element. For example, the signal referred to as RMX3 refers to the third set of OR 'ed x measuring slats in the right arm of the MHO.

4.2 Level 0 Trigger

The most rudimentary trigger in the experiment was referred to as the level 0 trigger. This trigger indicated the presence of at least one charged particle in each arm of the detector. An illustration of the L0 logic is given in figure 4.2[54]. It required hits in both the upstream and downstream TSC's. In the upstream TSC, the meantimed signals from the x counters

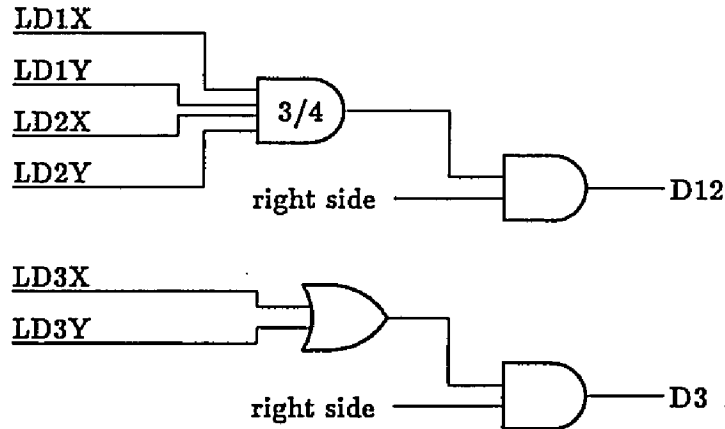


Figure 4.3: Drift chamber inputs to the level 1 trigger.

were OR 'ed together in groups of 16. In the downstream TSC, the meantimed signals from the x counters were also OR 'ed together in groups of 16 but then AND'ed with the OR of all the y channels in the appropriate arm of the detector. L0 was then defined as the logical AND of these four outputs obtained from a Lecroy 4508 programmable logic unit (PLU).

4.3 Level 1 Trigger

The next level of triggering was level 1. The purpose of the L1 trigger was to determine the presence of tracks that traversed the entire detector. Detailed information on the L0 and L1 triggers can be found in references [55], [56] and [57]. This trigger took on several levels of detail. The simplest of these was the L1 trigger for minimum bias (MB) events. The next higher level incorporated signals from the CER and MHO with the MB requirements to indicate so called physics events. This crude form of particle identification (PID) flagged the kaon decay products based upon the type of decay. In addition to these, a set of calibration events were defined as L1 triggers for diagnostic and calibration purposes. The final levels of the trigger applied prescales and various inhibit signals.

To form the L1 trigger, the L0 signal first enabled a second PLU. A re-timed (RT) signal from the AND of the front and back TSC x counters was then AND'ed with signals in the first three drift chambers. This signal was replaced with the L0 signal about halfway through the 1990 run to eliminate deadtime caused by the re-timer[58]. This combination

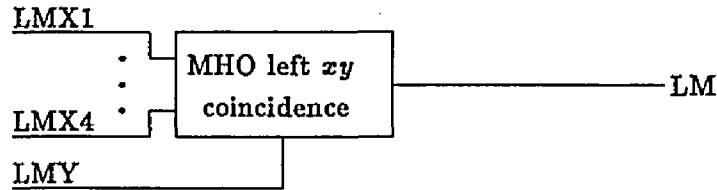


Figure 4.4: Muon Hodoscope inputs to the Level 1 trigger.

of DC and TSC hits defined a MB event and is referred to as a Level 1 minimum bias trigger. The logic for the DC related parts of this trigger is illustrated in figure 4.3. The pattern of DC hits required was 3 out of 4 x - and y -measuring planes in each arm of the first two sets of DC's, and 1 out of 2 x/y planes in both arms of the third set of DC's. The L1 logic, at this point, prescribed an 8-fold coincidence of DC hits in coincidence with a L0 trigger. MB events or L1 MB triggers then followed two parallel paths. One of these prescaled (PS) the MB events in hardware by a factor of 2000 with a flip-flop (F/F). The second of these proceeded to incorporate crude PID from the CER and MHO detectors. The logic for the MHO PID is shown in figure 4.4. The electron PID requirements were a simple in-time hit in the CER counter.

Physics events were either dilepton events of the form $\mu_L\mu_R$, $\mu_L e_R$, $e_L\mu_R$, and $e_L e_R$ or 2π events. A lepton is identified by a positive signal in the appropriate detector. The MHO y -measuring slats were OR 'ed together to form one signal while the x -measuring slats were divided into four logical groups with the slats in each group being OR 'ed. Pions, on the other hand, were defined by a veto in both the CER and MHO. Events with $\pi^+\pi^-$ PID were prescaled in hardware by a factor of 100. An event with $\pi^+\pi^-$ PID would only be a L1 trigger if either the MB or $\pi^+\pi^-$ prescales were satisfied. Dilepton events were not subjected to any prescales. Before a physics event was defined, the two inputs were pulse shaped (PS). A schematic of the logic leading to this point of the L1 trigger is given in figure 4.5[59].

The final stage of the L1 trigger incorporated various signals to insure the event was valid. Physics events would enable the L1 trigger unless various inhibit signals were present. These requirements were: 1) the event occurred within the beam gate, 2) a calibration event

Bit	Requirements	Trigger
0	D·L0·RC·LM	μe
1	D·L0·LC·RM	$e\mu$
2	D·L0·RM·LM	$\mu\mu$
3	D·L0·RC·LC	ee
4	D·L0/pr	minimum bias prescaled
5	D·L0· \bar{C} · \bar{M}	$\pi\pi$
6	D·L0· \bar{C} · \bar{M} /pr	$\pi\pi$ prescaled

Table 4.1: Summary of Level 1 physics trigger requirements.

was not present, 3) the readout supervisor was not busy with a previous event and 4) a physics veto was not set. The L1 trigger was also enabled by calibration events unless the calibration veto was set, the RS is busy or the dead-timer indicates a physics event is still in the stream. The final stage of the logic leading to the L1 trigger is illustrated in figure 4.6[59]. A summary of the allowable physics triggers is given in table 4.1. Calibration events could be of the form of analog-to-digital converter pedestal triggers, time-to-digital converter monitoring triggers, or a random trigger occurring at the rate of 50 Hz. These calibrations could occur both inside and outside of the beam gate. Finally, the L1 trigger could be changed to correspond to a high rate (~ 10 kHz) of random triggers, L0 triggers and other detector-specific calibration triggers.

4.4 Digitization

4.4.1 Overview

The L1 trigger sent signals to the digitization electronics which included two types of time-to-digital converters, amplitude-to-digital converters and latch modules. Several detectors, in particular the CER and PbG, used two different types of digitization electronics because of the need for several different types of information from them. The PbG, for example, was used to determine hit times and the amount of energy deposited requiring the use of analog to digital converters and time-to-digital converters. All of the digitization electronics

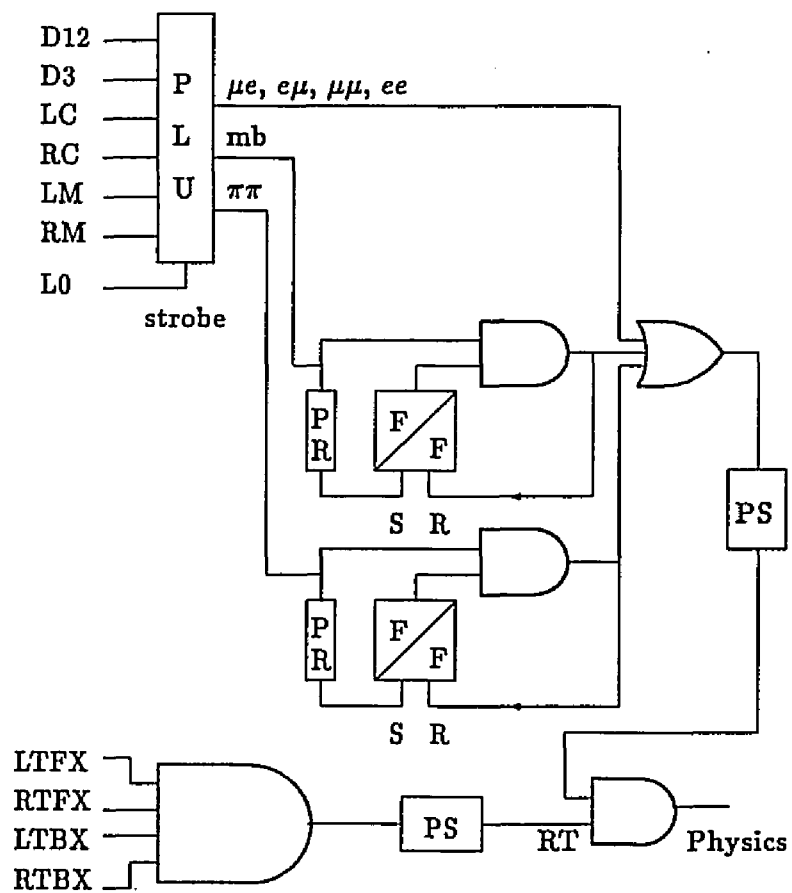


Figure 4.5: Level 1 physics trigger.

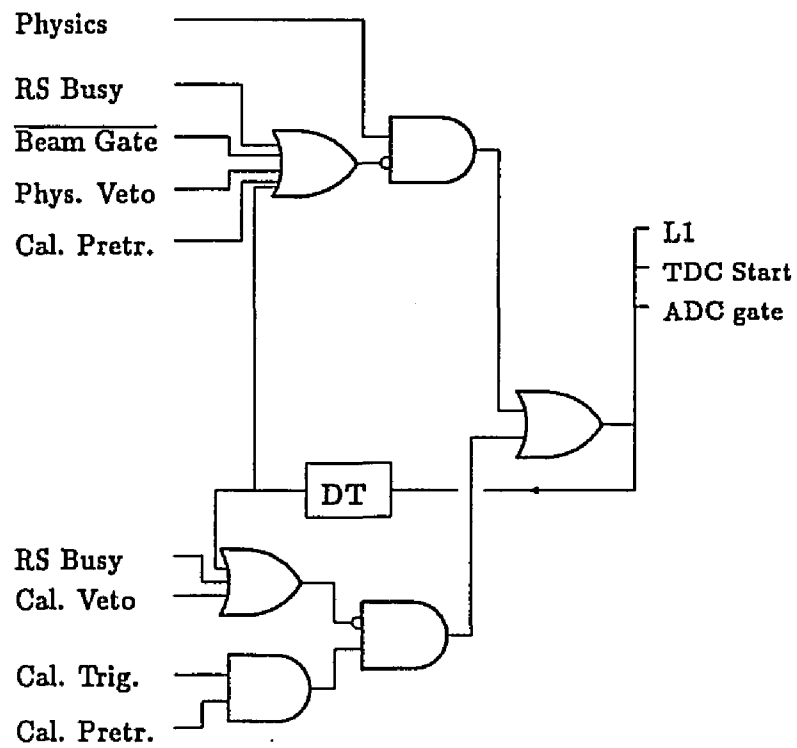


Figure 4.6: Final stage of Level 1 logic.

followed the custom FASTERBUS protocol followed by E791[60]. This protocol required that the digitized contents be transferred to buffers so that the electronics could be re-enabled for the next event.

4.4.2 The 6-Bit Time-To-Digital Converters

The 6-bit fine-binned time-to-digital converters (TDC 's) were used to record hit times in the DC's, y -measuring slats of the TSC's and the PbG. They were custom built 32 channel, 2.5 ns least-count TDC 's. Approximately 5000 channels were read out corresponding to nearly 150 modules. The 2.5 ns least-count signal was generated via the overlap of two square waves which had their phases offset by a quarter wavelength. The digitization to time was performed via a 6-bit gray code counter[61][62]. This yielded a 160 ns total dynamic range. The converters were started by emitter-coupled logic (ECL) signals from the L1 trigger and are stopped by the discriminated signals from the individual detectors. Early hits which were present when the L1 ECL signal arrived were recorded as zero time hits. Late hits were recorded as an overflow of the counter (> 160 ns).

4.4.3 The 8-Bit Fine-Binned Time-To-Digital Converters

Detector elements requiring more precise timing information used custom built 8-bit fine-binned time-to-digital converters (FTDC's). These included the x measuring slats of the TSC's, the CER, the FNG, and the MHO. The FTDC's were started and stopped in a manner similar to the TDC 's. The time was digitized by charging a capacitor via a constant current source. The FTDC's were 210 ps least count and had a dynamic range of 55 ns. Each of the 35 modules used in the experiment contained 32 channels. An early hit, in these level triggered devices, unlike the TDC 's which were edge triggered, would result in no hit being recorded. A late hit, on the other hand, would result in the largest possible time being recorded[63][64].

4.4.4 The Amplitude-To-Digital Converters

Custom built 8-bit bilinear amplitude-to-digital converters (ADC 's) were also used to digitize signals from the CER, MHO and FNG. The sensitivity of the ADC 's for small signals (0-63 channels) was 150 fC/count while for large signals (64-255 channels) it was 470 fC/count. This yielded a 100 pC dynamic range and fine resolution for small signals. Nearly 500

channels of data were digitized by the ADC's. The charge integration gate widths were set in L1 and varied between 55 and 130 ns. Digitization occurred within 200 ns of the end of the gate[65].

4.4.5 The Latch Modules

The latch modules were used for signals from the MRG and trigger information for the readout supervisor. They were custom built and primarily concentrated on digitization of the MRG signals. A L1 ECL signal instructed the latches to record the state of the signals. If a signal was present, a hit was present; otherwise no hit was present. The modules consisted of 96 channels per module. A total of 26 modules were used in the MRG digitization. All channels, nearly 2500, were read out on each event. This is in contrast to the other digitization electronics which only had hit channels read out[66].

4.5 Level 2 Trigger

The Level 2 trigger (L2) was a hardware trigger that used a memory lookup to cut events. The purpose of the trigger was to accept only those events that exhibited correlations between the upstream and downstream x and y TSC counters. Good tracks would exhibit correlations between the counters, where downstream counters were within a narrow band of those in the upstream counters. The correlations were checked for x and y counters separately. Uncorrelated hits were distributed randomly with respect to each other. The L2 trigger could also make a rough calculation of the invariant mass and colinearity of an event. These quantities are described in a later section. The lookup table was created from a sample of Monte Carlo events. Although the trigger had been thoroughly tested and verified, it was not used because the detector rates could not justify its incorporation. The trigger would have rejected approximately 67% of the raw events but only 15 % of the good two-body events[67][68].

This trigger was used in pass-through mode in all running periods. In this mode all events were considered to pass the L2 trigger, but no L2 calculations were performed. The trigger also contained a buffer for the digitized data from L1. This stage 1 buffer was transferred to the stage 2 buffer during this phase of triggering. These buffers allowed two events to exist in the readout pipeline at once. The stage one buffer resided in the data modules associated with the digitization electronics. The stage two buffer resided in the

crate scanner used to read out the digitized event.

4.6 Readout

The transfer of data from the stage 1 and 2 buffers as well as to the turbo memory of the 3081E's was controlled by the readout supervisor (RS). The RS was a set of 12 custom built CAMAC modules. Each module monitored the state of a particular set of crates of electronics. Each crate contained up to 16 modules (TDC 's, FTDC's, ADC 's or latches). While 21 crates existed, only 12 crate scanners were required. This reduction was achieved by slaving nine crates to the others in groups of two. This allowed for readout of two crates via a single crate scanner and significantly reduced the number of memory ports required by the turbo memory of the 3081E's. Each crate scanner was fanned out to the eight possible turbo memory boards of the eight 3081E's[69].

When a L1 trigger occurred, the RS would allow digitization if the stage 1 buffer was clear. If it was not, the trigger was inhibited. As soon as the stage 2 buffer was clear, the RS would allow transfer of the digitized event to the stage two buffer. Had the L2 trigger been used and an event had failed, the stage two buffer would have been cleared and the stage 1 buffer, if filled, would have been transferred. The next transfer stage was from the stage 2 buffer to the turbo memory of an available 3081E. The priority of data transfer, however, was in the reverse order of the description given here.

The 3081E's were processor boards designed to emulate the instruction set of the IBM 3081. Turbo or dual port memory (DPM) was added to each processor board. The size of the DPM was two Mbyte. It acted as a large buffer to hold events for later processing. Each of the eight boards had inputs from the 12 crate scanners. In addition to controlling the transfer from the stage 2 buffer to the DPM , the RS also broadcast a 4 bit number, called a fine event number, to all of the crate scanners. This number, which was also transferred to the DPM , was an identification tag for the event. It was used to insure that the data from the individual crate scanners came together properly. Finally, the number of words transferred from the crate scanners to the DPM was also sent. When the maximum number of words allowed from one of the scanners was transferred, it signaled the RS . The RS then took the filled 3081E out of the data pipeline and placed a free one in. When the processor board was finished with the Level 3 algorithm, it signaled the RS again. The RS then allowed the board to return to the data pipeline in the next spill. Approximately

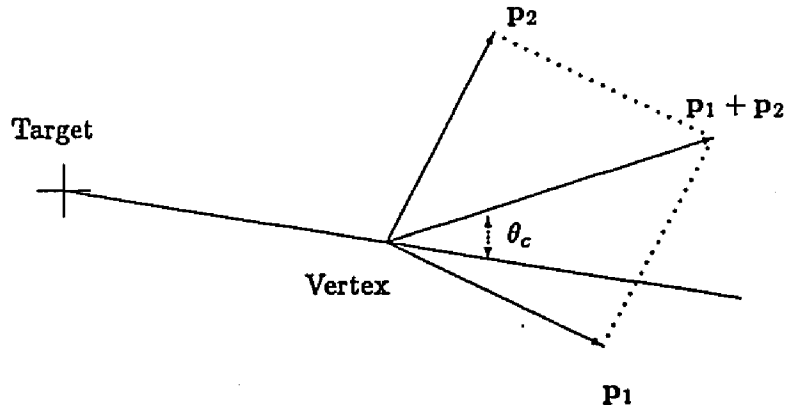
2000 events filled a 3081E. The maximum transfer rate was about 0.64 Gbyte/sec and the average readout time was 10 μ sec per event[70].

4.7 Level 3 Trigger

Once the DPM of a 3081E was filled, the RS took it out of the data pipeline and instructed the processor to begin the Level 3 (L3) calculation. The L3 trigger was a software trigger and the algorithms used in it changed between 1989 and 1990 (as well as 1988). The result of the change in the L3 code was a significantly higher efficiency for the L3 trigger in 1990. The heart of the L3 trigger was a fast tracking algorithm that allowed for a rough calculation of and loose cuts on the invariant mass and colinearity of an event[71]. MB events were processed by the L3 code, but no cuts were applied. This was done in order to obtain a sample of semileptonic events, which typically had large colinearity angles, and to obtain a sample of two body events that could be used to calculate the efficiency of the trigger.

The first stage of the L3 trigger was to unpack the TDC words from the drift chambers. This stage required that good hits be present in all drift chamber planes. A good hit could be a single, an in-time pair, an adjacent pair or a triple. A maximum of four in-time pairs were allowed in each measuring plane. The L3 code then constructed all possible pairs in the first two drift chamber sets, creating a set of possible tracks. These tracks were required to be divergent from the beam centerline. The next stage of the trigger determined whether two of the formed tracks could correspond to an actual decay. This was accomplished by creating all possible pairs of tracks in both arms and comparing them to real data via a lookup table. The x and y views of each track were considered separately. The actual comparison was not always done for all possible pairs. Possible tracks in each arm were formed and then compared to a lookup table in order of descending time sum, or best quality hits to worst quality hits. When two possible sets of tracks were found, the one with the best vertex quality was chosen. The tracks in each arm were then projected to the center of D2 where a 300 MeV/c transverse momentum kick was applied. The track was then projected to DC3 where hits in a loose region around the expected position were required.

The third stage of L3 was a rough calculation of the kinematics of the event. This calculation was performed for all decays indicated from the L1 trigger. The track momentum was calculated by integrating a reduced map of the magnetic field over the path of the

Figure 4.7: Definition of colinearity θ_c .

Trigger		Approximate rates per spill (Hz)
L0	TSC Coincidences	1.4×10^6
MB	$L0 * D_{12} * D_3$	80000
L1	MB_{pre} and $MB * PID$	9000
L3	Online Analysis of L1	150

Table 4.2: Summary of trigger rates.

particle in D2, a second estimate of the momentum kick, and comparing it to the track deflection. The colinearity angle and invariant mass of the event were then calculated.

The colinearity angle of an event was defined to be the angle between two vectors related to the event. An illustration of the colinearity angle for an event is given in figure 4.7. The first of these vectors was determined from the positions of the target and the vertex of the decay. The second was formed by adding the momenta of the two tracks. Events with large colinearity tended to be three-body decays in which the third, undetected, body carried away a significant amount of momentum. The colinearity angle was required to be less than 10 mrad. The invariant mass of the event was also calculated. The mass was required to be greater than $460 \text{ MeV}/c^2$. In the 1989 running period there was an upper limit of $550 \text{ MeV}/c^2$ imposed on the invariant mass from L3 while in 1990 there was no upper limit[72]. An event would pass the L3 trigger if any of the modes indicated by L1 passed. As mentioned previously, MB events automatically passed L3.

The final stage of L3 was the transfer of events to a DEC μ -VAX and output to tape. The transfer to the μ -VAX was supervised by the RS. The interface between the 3081E and the μ -VAX was a DR11W interface. Events were stored in a buffer and periodically written to 6250 bpi tape. The μ -VAX would also occasionally copy the buffer contents to a file for diagnostic online analysis. The purpose of this analysis was to monitor the various detectors in order to find problems in real time. The online analysis was done only during periods of no data transfer so that deadtime would not be introduced.

4.8 Running Conditions

The average intensity of protons was 4 Tp in 1989 and 5 Tp in 1990, leading to rates on the order of 25 MHz in the drift chambers. The implementation of a multi-level triggering system permitted a significant reduction in the rates present in subsequent stages of the electronics. A summary of the rates is given in table 4.2. The L0 trigger reduced the data rate to about 1.5 MHz. The raw MB rate (before prescaling) was approximately 100 kHz corresponding to a MB prescaled rate of approximately 20 Hz. The total L1 rate was reduced from the L0 rate by a factor of nearly 150, to 8-9 kHz. The L3 trigger rate was reduced from the L1 rate by a factor of 50, to approximately 150 Hz. A 6250 bpi tape could be filled in 20-30 minutes with approximately 500 spills.

A typical event comprised on the order of 1.0 Kbytes in size. A 6250 bpi tape contained an average of 75,000 physics events in addition to a large number of calibration events. The calibration events were significantly larger in size than the physics events since all channels in the detector were read out. Each year of running yielded close to 3000 tapes of data. A summary of the acquired data is given in table 4.3. Since the triggers were not mutually exclusive, the relative percentages of each event type add up to well over 100%.

Event Type	Total 1989	Total 1990	Fraction 1989	Fraction 1990
μe events	37,087,700	49,111,200	20.7%	18.8%
$e\mu$ events	40,312,100	52,510,900	22.2%	20.4%
$\mu\mu$ events	58,242,000	99,198,800	41.9%	29.5%
ee events	31,645,900	32,481,100	13.7%	16.0%
minimum bias events	47,608,300	55,010,200	23.2%	24.1%
L3 $\pi\pi$ events	25,317,300	23,397,800	9.9%	12.8%
L1 $\pi\pi$ prescaled	10,710,600	6,700,900	2.8%	5.4%

Table 4.3: Breakdown of 1989 and 1990 events by trigger type. Totals are rounded to the nearest hundred and percentages to the nearest tenth.

Chapter 5

The Offline Code

5.1 Overview

The use of computers to analyze data acquired from a detector is common to all modern particle physics experiments, and E791 was no exception. The code needed by E791 was rather complex, although the general computational needs of the experiment could be described in very general terms. The set of code that was common to all analysis needs was referred to as the standard offline. This set of code, written in a FORTRAN dialect, consisted of over 600 subroutines and over 200 commons. In addition, a large number of routines from standard libraries such as CERNLIB were utilized[73].

In this chapter, the primary structure and function of the various areas of the standard offline is presented. The description of the offline code is usually part of that dedicated to data analysis. Given the large amount of code used in the general analysis and its complexity, it appears reasonable to discuss the code in a separate chapter. This chapter consists of six sections. The first of these is an overview of the code. The remaining sections encompass Monte Carlo event generation, processing of raw data, pattern recognition, track fitting and track counter association.

The offline code was divided into eleven distinct stages. Functionally, however, the offline code can be thought of as consisting of the five parts mentioned above. In addition to these parts, several other useful features were incorporated into the standard code. A mechanism existed for automatic updating of commons. The updated commons were typically related to the geometrical positions of the detectors and the constants used to interpret the digitized output of the detectors. The other features were incorporated as part of a user written

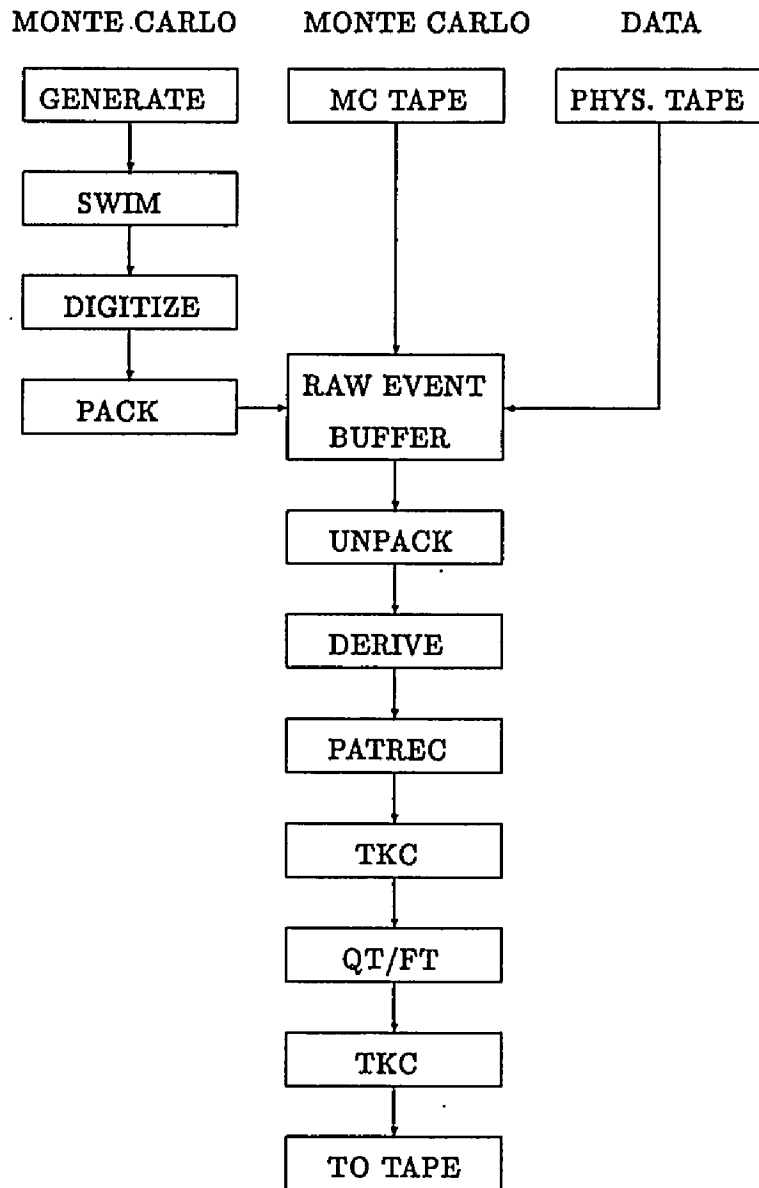


Figure 5.1: Offline analysis flowchart.

interface to the offline code. The offline used this routine in several ways. It was called after each of the 11 distinct stages of the code. This allowed the user to analyze and potentially cut events after each successive stage. The user could also control the flow of the program in this area. Stages could be skipped or re-executed and the entire program could be halted if desired. In addition, a number of entry points were defined. These pseudo-subroutines were used for controlling program flow, checked the status of special operations such as input and output, checked unusual events and non-fatal errors, and finally processed special events such as calibrations and scaler records. A simple flowchart of the offline code, excluding the user interfaces, is given in figure 5.1. It should be understood that the user interface is invoked after each stage depicted in this flowchart.

5.2 Generation of Monte Carlo Events

The first logical area of the offline code pertained to the generation of Monte Carlo events. It consisted of the first three stages of the offline code. The first stage generated a kaon and its daughter particles. The second stage swam the daughter particles through the detector and generated decays of the daughters when applicable. The third stage digitized the response of the detector to the daughters and their decay products. The generation of the kaons used many parameters that were obtained from data. Other parameters, the exponential lifetime distribution and the relative branching fractions for example, were also used in the Monte Carlo generation[74][75].

Several parameters were obtained from data for use in the Monte Carlo generation. These included the relative number of events to generate at each time period of the experiment, the momentum distribution of kaons and the distributions of data in vertex x/z and y/z . During the pass 4 analysis, it was observed that the distributions in time and in kaon momentum were not optimal. Consequently, corrections to these parameters were made. A description of the corrections is given in appendix A.

In the Monte Carlo generation, a K_L^0 was created with a momentum chosen from the corrected Skubic distribution and a decay time chosen from its exponential decay distribution[76]. At the z position of the decay, calculated from the lifetime, the x and y positions were chosen from the vertex x/z and y/z distributions. The daughter particles were then generated. If several types of decays were allowed, they were generated according to their relative probabilities. For two-body decays, the spherical angles of one of

the daughters were chosen from a flat distribution in phase space. For three-body decays, one additional angle, obtained by sampling the Dalitz plot, for a second daughter was also chosen. The remaining parameters were then fixed by conservation of 4-momentum. The daughters were then projected to the first drift chamber set. If either of the daughters did not pass through the apertures, the event was cut.

The daughters were swum through the detector elements using a fourth-order Runge-Kutta algorithm in regions of magnetic fields. At each detector aperture, the effects of multiple scattering and energy loss due to bremsstrahlung were taken into account. Multiple scattering could occur at or before the aperture. If the scattering occurred before the aperture, it corresponded to a change in position as well as a change in direction at the aperture. Scattering at the aperture, on the other hand, corresponded only to a change in direction at the aperture. The final stage of generation digitized the track and filled data commons in such a way that Monte Carlo events could be analyzed in an identical fashion to data events in later stages. Schematically, the generation of Monte Carlo events is illustrated in figures 5.2 and 5.3[77].

5.3 Processing of Raw Data

Four stages of the standard offline code were relevant to the processing of events. The purpose here was to input and output data as well as process them into a form that could be used by the remaining stages of the offline code. Stages 4 and 11 read in, and wrote out, events, respectively. The events were input in a packed form. They were originally written in the packed form in order to conserve space. The output stage insured that all output data were packed before writing the event. Stages 5 and 6 unpacked and derived data into a user friendly form. The offline code also contained a feature that allowed the user to inhibit stages 5 and 6 for selected detector elements, thereby allowing the user to decrease, significantly, computer time for jobs that did not use all detector elements.

5.4 Pattern Recognition

In stage 7 of the offline code, raw events were processed through a pattern recognition routine (PT). PT used hits in the TSC's and the DC's to reconstruct tracks in each spectrometer arm[78]. Logically, PT consisted of five distinct parts: hit finding, 2-D track finding, 3-D

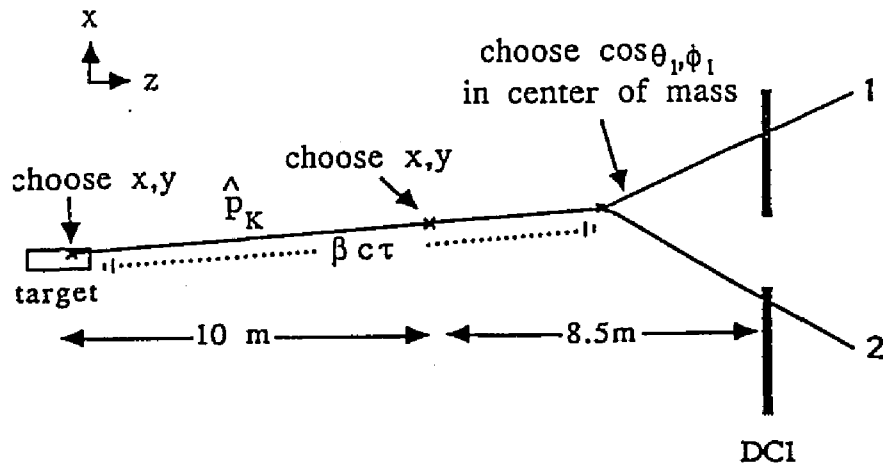


Figure 5.2: Schematic of the Monte Carlo generation stage.

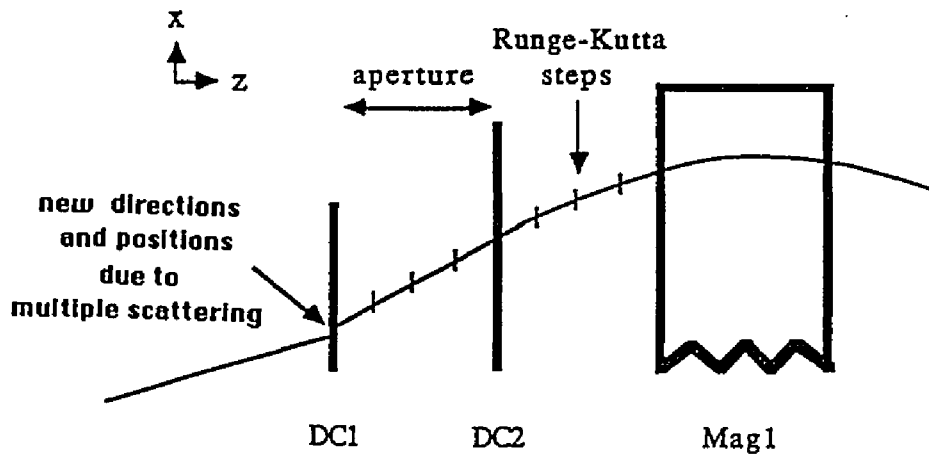


Figure 5.3: Schematic of the Monte Carlo swimming stage.

track finding, vertex reconstruction, and ambiguity resolution. This version of PT was used for the 1989 and 1990 analyses. The version used in 1988 was significantly different and will not be discussed in this dissertation. A thorough discussion of the PT routine is given in reference [79].

Hit finding began with the TSC's. The x slats of the TSC's were required to have a hit on both the top and bottom tubes. Furthermore, the hit time was required to be within -5 to 21 ns of the event time and the meantime to within -3 to 18 ns. The y slats were required to have hit times in the same ranges as the x slats or a zero time hit and a latch hit. The latch hit was allowed since a good hit could be masked by an early accidental hit. Hits in the DC's were then identified and classified into several types. First, all pairs and triples with good time sums were identified. At least three of five planes in each view were required to have hits of this type. If the remaining two planes did not have good time pairs or triples, PT allowed pairs or triples without good time sums or single hits to be considered. Pairs or triples without good time sums were broken up into single hits. Figures 5.4 and 5.5 illustrate triples and pairs with good time sums.

The algorithm proceeded by identifying all possible (maximum of 60) tracks in each view of each arm. This 2-D track identification stage is illustrated schematically in figure 5.6. Beginning with the TSC's, a potential track was projected upstream through successive DC's. Hits were searched for within relatively broad windows that became progressively larger around the position to which a potential track was projected. When hits in DC3 were located, a momentum measurement could be made. This measurement, made in the downstream magnet, was required to be consistent with the momentum in the upstream magnet. This condition allowed the windows for hits in DC2 and DC1 to be smaller. Ambiguities for pairs were resolved by minimizing the PT track χ^2 . An illustration of the type of ambiguity present for pairs with good time sums is given in figure 5.7. The hit wire position was used for single hits in DC planes. PT was unable to resolve this type of ambiguity until the final stage.

In the third stage, the two dimensional track candidates in x and y were combined to obtain 3-D track candidates. In order to eliminate redundant tracks, tracks were removed if they shared more than 13 hits with another identified 3-D track. The positions of the hits were then corrected for the small rotations of the DC's. Finally, x and y track χ^2 's from the previous stage were recalculated.

The fourth stage of PT looped over all 3-D track candidates to find the pair with the

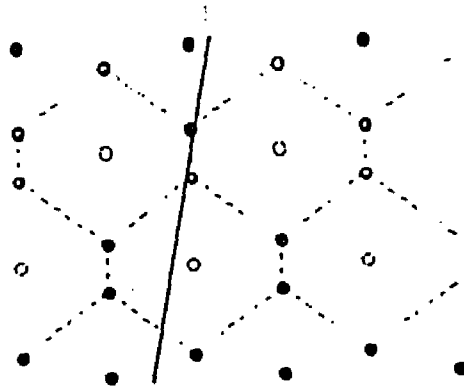


Figure 5.4: Illustration of a good time sum triple.

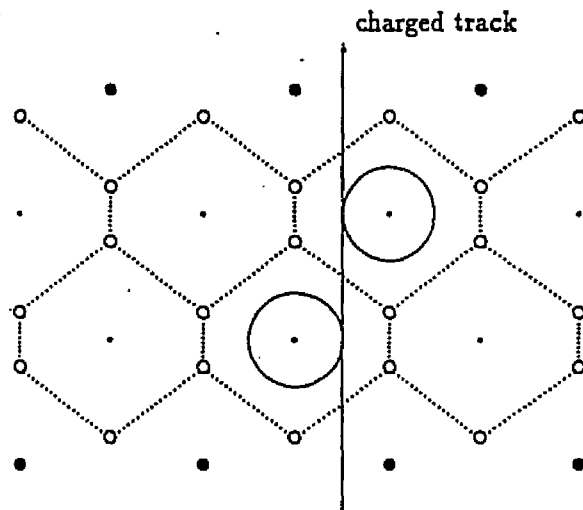


Figure 5.5: Illustration of a good time sum pair.

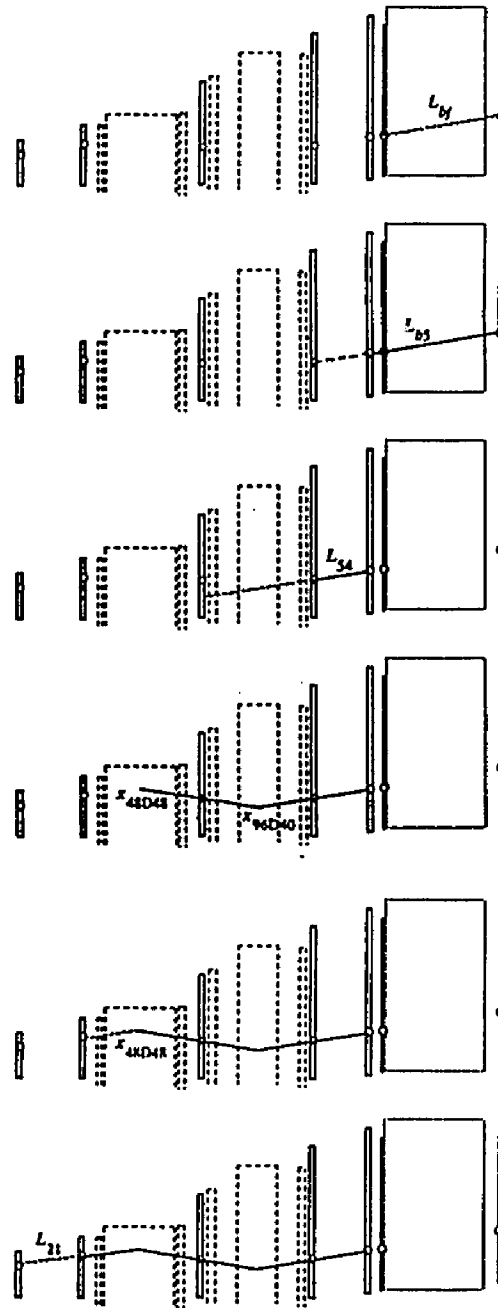


Figure 5.6: Schematic of 2-D track finding.

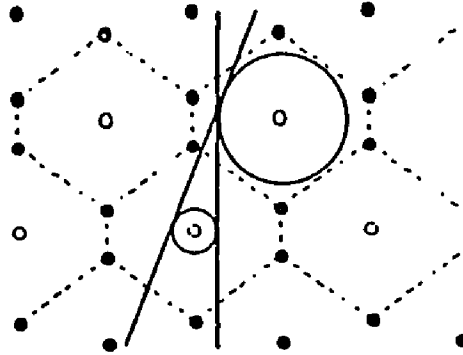


Figure 5.7: Illustration of the ambiguity in a good time sum pair.

best vertex position. If the distance of closest approach (DOCA) was larger than 12 cm, the pair was not considered. The pair that had the smallest DOCA was chosen for the remainder of the processing. The vertex was taken to be the midpoint between the DOCA of these two tracks. Other tracks with DOCA's within 6 cm of the calculated vertex were saved for further processing by the fitters. The purpose of the final portion of this stage was to correct the hit positions for electrostatic deflection of the wires and propagation delays.

In the final stage, the single hit ambiguities could be resolved. Resolution of ambiguities involved varying the side on which the track was assumed to occur and choosing the solution which minimized the track χ^2 . Doubles and triples broken into singles had all possible hit locations checked. The track momenta, vertex position, colinearity and masses (as indicated by the L3 trigger word) were then calculated (or recalculated).

5.5 Track Fitting Algorithms

Events that successfully passed PT were subsequently processed through more refined fitters, specifically through two independent fitting programs. These algorithms were commonly known as QT and FT. Each of these fitters used the full magnetic field map. QT and FT determined the best left-right ambiguity solution, where applicable, based on the choice that minimized their respective track χ^2 . After processing all tracks in an event, the fitter then calculated the quality of the vertex. In cases where more than two tracks were present, the pair that minimized the vertex χ^2 was chosen. At this stage the colinearity angle was

calculated. Finally, the two-body invariant mass was calculated. Complete descriptions of the fitting algorithms can be found in references [80], [81], [82] and [83].

While QT was commonly known as a fitter, it was not an actual algorithmic fit but rather an iterative calculation of track parameters. QT also treated the the two magnets as distinct spectrometers. The x and y views of the track were treated distinctly for each of the two spectrometer halves. The calculation proceeded by taking the values of the track momentum, hit wire positions, track directions and scattering angles from those calculated in PT. The particle was then stepped along intervals of 20 cm using a fourth order Runge-Kutta algorithm and the three components of the magnetic field to solve the equations of motion. The particle was stepped along the route DC 1 to DC 2 to DC 3 for the upstream spectrometer half and along the route DC 5 to DC 4 to DC 3 for the downstream spectrometer half. The difference between the actual wire hit position at DC 2 (or DC 4) and the position as calculated by the QT trajectory was used to correct the direction of the particle at DC 1 (or DC 5) for both the x and y views. The differences between the wire hit positions at DC 3 and those calculated by QT were used to correct the particle momentum (from x view) and the y view scattering angle at DC 2 (or DC 4). This iterative calculation continued until the deviations, between successive iterations, were within $10 \mu m$. If this condition could not be met, the event failed the QT fitter.

QT calculated x and y view χ^2 's for each track. These are given by equations 5.1 and 5.2 where δq is the second degree of freedom for the x view given in table 5.1:

$$\chi_x^2 = \frac{1}{2} \begin{pmatrix} \delta p & \delta q \end{pmatrix} \begin{pmatrix} \sigma_{pp} & \sigma_{pq} \\ \sigma_{pq} & \sigma_{qq} \end{pmatrix}^{-1} \begin{pmatrix} \delta p \\ \delta q \end{pmatrix} \quad (5.1)$$

$$\chi_y^2 = \frac{1}{3} \begin{pmatrix} \delta\theta_{y2} & \delta\theta_{y3} & \delta\theta_{y4} \end{pmatrix} \begin{pmatrix} \sigma_{22} & \sigma_{23} & \sigma_{24} \\ \sigma_{23} & \sigma_{33} & \sigma_{34} \\ \sigma_{24} & \sigma_{34} & \sigma_{44} \end{pmatrix}^{-1} \begin{pmatrix} \delta\theta_{y2} \\ \delta\theta_{y3} \\ \delta\theta_{y4} \end{pmatrix}, \quad (5.2)$$

where the σ_{ii} are Monte Carlo widths of the degree of freedom distributions, and the σ_{ij} ($i \neq j$) are the means of the Monte Carlo distributions of the correlation terms. The degrees of freedom are listed and defined in table 5.1. QT also calculated a vertex χ^2 in much the same way as PT, except that the vertex was given by the weighted uncertainties of the two tracks rather than by the midpoint. The vertex χ^2 was then defined as the DOCA divided

View	Degree of Freedom	Definition
X	δp $\frac{\delta p}{\sigma_p} + q \frac{\delta \theta_{x3}}{\sigma_{\theta_{x3}}}$	Back minus Front Momentum Normalized Sum of δp and $\delta \theta_{x3}$
Y	$\delta \theta_{y2}$ $\delta \theta_{y3}$ $\delta \theta_{y4}$	<i>y</i> -view Scattering Angle at DC2 <i>y</i> -view Scattering Angle at DC3 <i>y</i> -view Scattering Angle at DC4

Table 5.1: QT degrees of freedom. q is the sign of the charge.

by the rms of the DOCA distribution in a Monte Carlo calculation:

$$\chi_v^2 = \frac{d_{min}^2}{(z_1 - z_v)^2 (\sigma_{\theta L}^2 + \sigma_{\theta R}^2)}. \quad (5.3)$$

In equation 5.3, d_{min} is the vertex DOCA, z_1 and z_v are the z positions of the first DC and the vertex and $\sigma_{\theta L}$ and $\sigma_{\theta R}$ are the respective uncertainties in the track directions at the first DC plane.

In contrast to QT, FT was a mathematically rigorous fit to all the hits in a track in the entire spectrometer. The process was iterative as in QT and used the PT parameters as initial values. Track and vertex χ^2 's based on the differences between the observed and fit hit positions were calculated.

FT began by using the values of the x and y positions, their derivatives with respect to z and the ratio of charge polarity to momentum as calculated by PT. These are referred to as the 5-vector $\vec{\alpha} \equiv (x, y, \frac{dx}{dz}, \frac{dy}{dz}, \frac{q}{p})$ where q is the sign of the charge. The particle was then stepped along the entire spectrometer arm. There was the subtlety that the actual track was slightly different than the fitted track due to neglecting scattering and chamber resolution. This discrepancy represented a potential problem in regions of magnetic fields. To account for this, the field strength for the ideal track was adjusted so that it more closely approximated that experienced by the actual track.

The FT χ^2 was then calculated as:

$$\chi^2(\vec{\alpha}) = \sum_i^{m=20} \sum_j^{n=20} (x_i^{data} - x_i^{theory}) W_{ij}^x (x_j^{data} - x_j^{theory}). \quad (5.4)$$

The indices i and j run over the twenty drift chamber measurements in each arm. The weight matrix $W_{ij}^{\vec{r}}$ is the inverse of the covariance or error matrix $E_{ij}^{\vec{r}}$ given by:

$$E_{ij}^{\vec{r}}(p) = E_{ij}^{\text{DC}} + \frac{E_{ij}^{\text{MS}}}{p^2} \quad (5.5)$$

In equation 5.5 E_{ij}^{DC} is the uncorrelated error matrix corresponding to the drift chamber resolution of $\sim 150 \mu\text{m}$ and E_{ij}^{MS} is the correlated error matrix resulting from multiple scattering. For E_{ij}^{DC} , FT used a diagonal matrix whose elements were simply the individual drift chamber resolutions. The matrix E_{ij}^{MS} was calculated from Monte Carlo events. The iteration involved varying $\vec{\alpha}$ until the minimum track χ^2 was found.

As in PT and QT, FT looped over all fitted tracks in each arm in order to find the pair that formed the vertex. Unlike QT and PT, FT took the pair that minimized the vertex χ^2 . This involved a 9-vector $\vec{\beta}$ given by:

$$\vec{\beta} \equiv \left(x, y, z, \frac{dx_1}{dz}, \frac{dy_1}{dz}, \frac{q_1}{p_1}, \frac{dx_2}{dz}, \frac{dy_2}{dz}, \frac{q_2}{p_2} \right). \quad (5.6)$$

The subscripted variables were obtained from $\vec{\alpha}$ for each track and x, y, z located the position of the vertex. This vector was then used to calculate the vertex χ^2 :

$$\chi^2(\vec{\beta}) = \sum_i^{n=10} \sum_j^{n=10} \left(\alpha_i^{\text{data}} - \alpha_i^{\text{theory}} \right) W_{ij}^{\alpha} \left(\alpha_j^{\text{data}} - \alpha_j^{\text{theory}} \right). \quad (5.7)$$

Here, the weight matrix W_{ij}^{α} is the inverse of the covariance matrix found by the combination of the individual track matrices, modified to account for multiple scattering within the vacuum window. These choices for the parameters in $\vec{\alpha}$ and $\vec{\beta}$ allowed for the minimization of the χ^2 in a single matrix inversion provided reasonable estimates were used.

5.6 Track Counter Association

The final stages of the offline code related the projection of the pattern-recognized or fitted track to hits in the PID detectors and the TSC's. This association was done in either stage 8, 10 or both. The tracks from the fitters were first linearly projected from the fifth DC set through the remaining detector elements. The offline then looked for a hit in the PID detectors that corresponded to the projected track. If one was found, commons were filled with the track identification number and information relevant to the detector. This information included positions, hit times, confidence levels, etc. Track counter association (TKC) could be done from the results of PT, QT or FT.

5.6.1 The Čerenkov Counter

TKC for the Čerenkov counter involved correcting raw times from the FTDC's and locating hits. The FTDC times were corrected using constants obtained from a separate study of well-identified K_{e3} electrons. Although the corrections were channel dependent, the CER contained only a total of 16 channels. First, the track associated hits were located by projecting a simulated cone of Čerenkov light with an opening of 16.7 mrad to the mirrors. Next, based on the mirrors hit, TKC produced simulated hits in the phototubes. Finally, TKC looped over all hits that corresponded to simulated hits, selecting the one with the best corrected time, which is the one closest to zero.

5.6.2 The Lead Glass

The code for the PbG first calculated a correction to the raw ADC signal with a calibration constant. This constant was tracked over the entire run in 1990 and as periodic updates in 1989. Next, the energies deposited in the blocks hit by the simulated track and immediately adjacent blocks were summed. For the converter blocks, this involved the hit block and the two adjacent blocks in x . For the back blocks, the energies deposited in the hit block and the surrounding eight blocks were summed. These sums yielded the quantities of interest, namely E_{conv} , E_{back} and $E_{tot} = E_{conv} + E_{back}$.

5.6.3 The Muon Hodoscope

TKC for the MHO was slightly more complicated. The MHO contained five pieces of information used by TKC. These were the x and y position of the hit and the three times from the two x and the one y phototubes. The track-associated hit was taken to be the one closest to the simulated hit. As in the CER and PbG, the raw times from the TDC 's were corrected from a separate study. In this case, however, well-identified muons from $K_{\mu 3}$ decays were used. The differences between the actual and simulated hit positions were then calculated. These differences were then used to calculate the probability that the actual hit was track-associated, based on space match alone. This probability corresponded to a convolution of a uniform distribution representing a MHO counter and a normal distribution. The convoluted probability is:

$$P(x) = \frac{1}{2w} \left(ERFC \left(\frac{-w/2 + \mu - x}{\sigma\sqrt{2}} \right) - ERFC \left(\frac{-w/2 + \mu - x}{\sigma\sqrt{2}} \right) \right) \quad (5.8)$$

where w is the width of a MHO counter, x is either $x_{dif} = x - x_{sim}$ or $y_{dif} = y - y_{sim}$ and μ and σ are the Gaussian fit parameters.

Similarly, a probability based on the time information alone could also be calculated. The following quantities were chosen as variables for the probability distribution:

$$T_1 = t_y - \hat{t}_x \quad (5.9)$$

$$T_2 = \frac{t_y + \hat{t}_x}{2} - t_{isc} \quad (5.10)$$

where

$$\hat{t}_x = \begin{cases} t_{xbot} & \text{if } |t_{xbot} - t_y| \leq |t_{xtop} - t_y| \\ t_{xtop} & \text{otherwise.} \end{cases} \quad (5.11)$$

The probabilities were then calculated from:

$$P(T_1) = \frac{1}{\sqrt{2\pi\sigma^2}} e^{-(T_1 - \mu)^2 / 2\sigma^2} \quad (5.12)$$

and

$$P(T_2) = \frac{1}{(2\pi)^{3/2} \sigma^3 \alpha_1 \alpha_2} e^{-\alpha_2^2 T_2^2 + \beta_2^2 / 4\alpha_2^2} \\ \times \left(2 - \text{ERFC} \left(-x\alpha_2 + \frac{\beta_2}{2\alpha_2} \right) + \text{ERFC} \left(x\alpha_2 + \frac{\beta_2}{2\alpha_2} \right) \right) \quad (5.13)$$

where

$$\alpha_1^2 = \frac{3}{2\sigma^2} \\ \alpha_2^2 = \frac{1}{2\sigma^2} - \frac{1}{4\alpha_1^2 \sigma^4} \\ \beta_2 = \frac{z}{2\alpha_1^2 \sigma^4}.$$

The μ and σ parameters were obtained from separate studies for each time variable. From these probabilities a confidence level for each variable and an overall confidence level were constructed. The overall confidence level was used in the final analysis cuts. A discussion and derivation of these quantities can be found in references [84] and [85].

5.6.4 The Muon Rangefinder

The MRG used a simple space match table to find track-associated hits. This table was generated in a separate study using $K_{\mu 3}$ events. Each track-associated hit in the MRG was

determined by comparison to this table. When two consecutive x and y planes had no track associated hits, the stop gap was determined. This gap was defined to be the one in which the last TKC hit occurred. The expected stop gap was determined from the momentum of the particle. A cut on the difference between actual and expected stop gaps was used in the final analysis cuts.

Chapter 6

The Production Analysis

6.1 Overview

All offline analysis was done on an IBM 3090 mainframe. The bulk of the analysis was done on a machine at BNL. However, a machine at Cornell was also used for a portion of the production analysis. This processing was referred to as the production analysis and consisted of 5 main passes. The first pass, pass 0, was used only in 1990. In this stage, raw 6250 bpi tapes were copied to IBM 3480 cartridges. Pass 1 was a data reduction pass. Here the raw events were pattern recognized and loose cuts were applied. The next stage, pass 2, was a refinement of the pattern recognition results and involved the two main fitters of the offline code. Pass 3 separated the events according to event type in a process called stripping. Finally, pass 4 was the main analysis pass of the data. Here, final kinematic and particle identification cuts were applied to the stripped events. An additional pass, although separate from the previous ones, generated sets of Monte Carlo events and wrote them to cartridges for use in the pass 4 analysis.

The pass 4 analysis was the most complex stage. Six different sets of events were used in the analysis. These were the data samples from pass 3 for $\mu^+\mu^-$, $\pi^+\pi^-$, and MB as well as Monte Carlo $\mu^+\mu^-$, $\pi^+\pi^-$, and semileptonic decays. The main purpose of this pass was to divide the pass 3 subsets into additional subsets as a function of the kinematic and particle identification cuts. This process permitted a detailed study of the systematic effects of the cut values used.

Nearly 1000 branching ratios, each from the same data set but corresponding to different sets of cuts, for the $K_L^0 \rightarrow \mu^+\mu^-$ decay were calculated for each year. Given that there

existed 1989, 1990 and combined samples, approximately 3000 different branching ratio groups were used to study systematic effects.

6.2 Pass 0

In 1990 data tapes were initially written to 6250 bpi tape. The tapes had proved to be unreliable under extended use in the previous year so a decision to copy the tapes to IBM 3480 cartridges was made. This action had several advantages. First, the cartridges were more reliable under extended use. Secondly, the cartridges had a significantly ($\sim 1/2$) lower cost while providing nearly 30% more storage space. They were also physically smaller and easier to handle. Once the tapes were copied to cartridges, they were recycled into the raw data acquisition stream. If there were any errors associated with the copy, the tapes were not recycled. This recycling significantly lowered the total cost of storing raw data. This procedure was not used in 1989, although later passes used the 3480 cartridges exclusively. There were 2935 physics tapes written in 1989 and 2219 in 1990. These numbers exclude tapes written for calibration and special studies.

6.3 Pass 1

Pass 1 performed several tasks to reduce the size of the data set. First, all calibration events except for those related to the PbG were discarded. Calibration events related to the PbG were prescaled by a factor of two for 1989 data and three for 1990. Next, the events were categorized as dilepton events, $\pi^+\pi^-$ events, MB $\pi^+\pi^-$ events or MB events based on the value of the invariant mass for each mode. A sample of the raw input events, prescaled by 5000, was written out. While these events were processed by the rest of the program, they were written out regardless of passage or failure of subsequent processing. At this stage the MB events were prescaled by a factor of 60 for 1989 and 30 for 1990. MB $\pi^+\pi^-$ events were prescaled by a factor of 3 for 1989 and 2 for 1990. Finally, all events had the PT program applied to them. If the event failed PT, it was discarded. If the event was a MB event, it was not subjected to any further cuts. A loose colinearity cut of $\theta_c^2 < 10 \text{ mrad}^2$ or P_T^2 (transverse momentum squared) $< 800 \text{ MeV}^2/c^2$ was then applied. Events were then subjected to a loose mass cut of $m > 470 \text{ MeV}/c^2$. In 1989, an additional upper mass cut of $m < 530 \text{ MeV}/c^2$ was imposed. After passing these criteria, the appropriate bit in

Pass 1 Event Type	Number (89)	Fraction (89)	Number (90)	Fraction (90)
raw prescale events	45,856	0.9%	38,300	0.6%
min. bias prescale	458,743	8.6%	891,800	13.6%
μe pass 1 bits	560,800	10.5%	843,400	12.8%
$e\mu$ pass 1 bits	620,600	11.7%	893,500	13.6%
$\mu\mu$ pass 1 bits	1,981,700	37.2%	2,822,800	42.9%
ee pass 1 bits	97,900	1.8%	129,600	2.0%
minimum bias $\pi\pi$	269,800	5.1%	409,400	6.2%
$\pi\pi$ pass 1 bits	1,438,000	27.0%	793,800	12.1%

Table 6.1: Physics events out of pass 1 in 1989 and 1990. Totals are rounded to nearest hundred and percentages to nearest tenth.

the pass 1 word was set so that the event could be easily identified later. The appropriate bits in the pass 1 word were also set for events that bypassed any of the processing or cuts. An event could be part of several processing modes. The flow of the pass 1 production for 1989 is illustrated in figure 6.1. Both of the 1989 and 1990 running periods contained 100 output cartridges from pass 1. The 1990 cartridges were later reorganized onto 150 carts because of increased space requirements of the pass 2 production. Nonetheless, the pass 1 production reduced the data approximately by a factor of 25. Table 6.1 lists the output of the pass 1 production as a function of event type. The percentages in this table add to more than 100% since the modes were not mutually exclusive.

6.4 Pass 2

Pass 2 performed the refined fitting of the events that were output from the pass 1 program. PT was re-applied since there were several large common blocks needed by the fitters that were not written to cartridges. No further cuts on PT quantities were made. Events that were in the raw prescale or $\pi^+\pi^-$ prescale were not processed in pass 2 unless they were members of the remaining modes. The QT and FT fitting programs were then applied to the events. If the event was part of the MB sample, it was written out regardless of the results of the fitting. The remaining samples were required to pass at least one of the fitters. If the

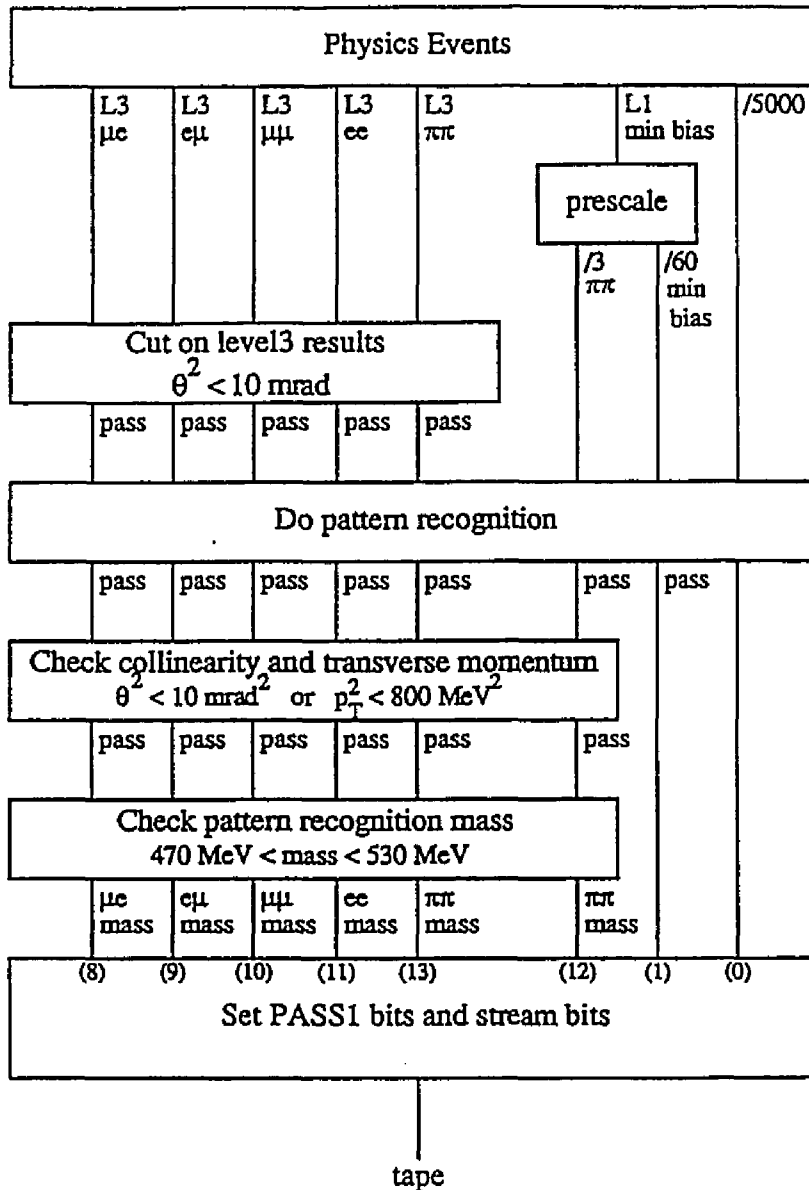


Figure 6.1: Flow of the pass 1 analysis. The upper mass cut was changed to 30 GeV in 1990.

Event Type	—— CUTS ——	1989 # of Carts	1990 # of Carts
MB	None	9	17
MB $\pi\pi$	None	5	8
$\mu\mu$	TKC hits in MHO: $M \geq 480 \text{ MeV}/c^2$	6	9
ee	TKC hits in CER	2	2
μe	TKC hits in CER, MHO: $M \geq 480 \text{ MeV}/c^2$	4	4

Table 6.2: Summary of the pass 3 output for 1989 and 1990.

two body invariant mass, as calculated by the fitters, was greater than $470 \text{ MeV}/c^2$, the appropriate bit in the pass 2 word was set and the event was written out. As in the pass 1 program, an event could be a member of several modes. No reduction of data was done in this pass. Accordingly, every input pass 1 cartridge corresponded to a pass 2 output cartridge. The flow of the pass 2 analysis is illustrated in figure 6.2.

6.5 Pass 3

The next stage of event processing was the stripping of events. In this stage, the output of the pass 2 program was separated into five distinct streams and written to separate cartridges. MB and MB $\pi^+\pi^-$ events were selected by their pass 2 word bits. No cuts were applied to these two samples. The $\mu^+\mu^-$ sample was also selected by the pass 2 word bit but had the additional requirement of a track-associated hit in both the left and right arms of the MHO counter. A low mass cut of $480 \text{ MeV}/c^2$ was also applied to these events. The e^+e^- sample was selected on the pass 2 word bit with the condition of a track associated hit existing in both arms of the CER counter. Finally, the $\mu^\pm e^\mp$ sample was chosen by imposing a $480 \text{ MeV}/c^2$ lower mass cut and requiring track-associated hits in the CER and MHO counters as appropriate. Events could be part of the FT and QT stream but were required to be a member of at least one stream. Table 6.2 is a summary of the number of cartridges written for each of the different modes. Each output cart contained approximately 55,000 events. Each mode was required to have the appropriate pass 2 word bits set.

6.6 Generation of Monte Carlo Samples

The final stage of the production analysis required the use of Monte Carlo generated events. These events were generated in a stage of the production analysis that was somewhat

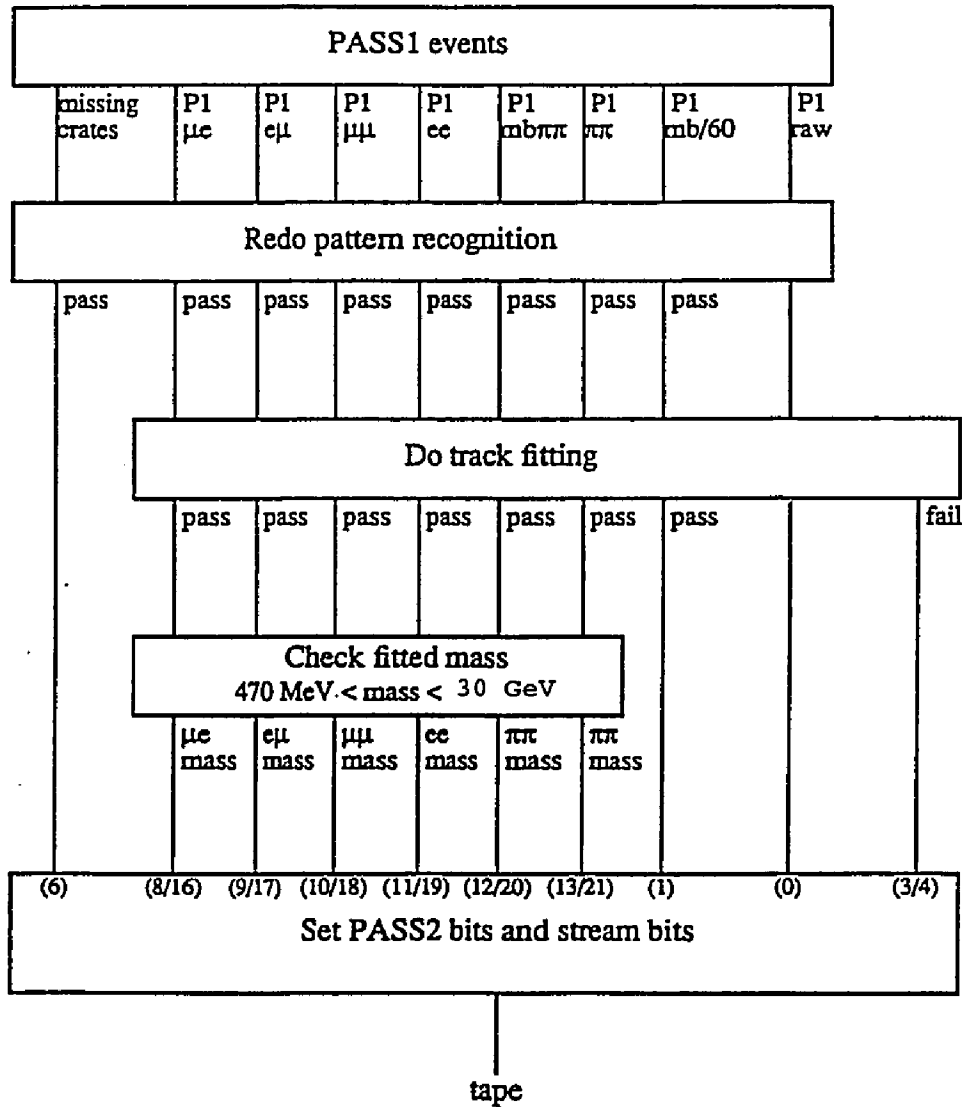


Figure 6.2: Flow of the pass 2 production.

MC Event Type	\sim Generated	1989 # of Carts	1990 # of Carts
$\mu\mu$	2.5×10^6	2	2
ee	2.5×10^6	2	2
μe	2.5×10^6	2	2
$\pi\pi$	2.5×10^6	2	2
Semileptonic	5.0×10^6	4	10

Table 6.3: Summary of Monte Carlo generation output.

disjointed from the main passes. Events of five different types were generated. These modes were $\mu^+\mu^-$, $\pi^+\pi^-$, $\mu^\pm e^\mp$, e^+e^- , and semileptonic decays. The $\mu^\pm e^\mp$ and e^+e^- Monte Carlo samples are not relevant to this dissertation and will not be discussed further. Over 3×10^6 events were generated for the $\pi^+\pi^-$ and $\mu^+\mu^-$ modes. The number generated in the semileptonic sample was not recorded. The size of the Monte Carlo semileptonic set was required to be about twice as large as the data semileptonic set. Since the generated sample was used just for background subtraction in the data $\pi^+\pi^-$ sample, only a set with reasonable statistics was required. There was no need to know the total number of generated events. The number of generated events written to cartridges after applying loose cuts was about 140,000 for $\pi^+\pi^-$ and $\mu^+\mu^-$. There were 2-3 times this number written in the semileptonic sample for each year. More events were required in the semileptonic sample since a larger fraction of them did not satisfy the pass 4 analysis.

As mentioned in chapter 5, the Monte Carlo events had some corrections applied due to non-optimal generation parameters. These corrections are discussed in appendix A. The $\pi^+\pi^-$ and semileptonic Monte Carlo events were also corrected for K_S^0 contamination. This correction is discussed in appendix B. Although K_S^0 's do not decay semileptonically, a correction was required due to the way in which the data $\pi^+\pi^-$ sample was corrected. A summary of the number of carts generated for each decay mode is given in table 6.3. These cartridges contained roughly identical densities, roughly 70,000 events per cartridge, except for the semileptonic sample in which the 1990 cartridges were about half as dense as the 1989 cartridges. The difference had no effect on the final analysis and was only incorporated to take batch scheduling difficulties into account.

6.7 Pass 4

Pass 4 was the most detailed stage of the production analysis. The six different sets of events obtained from pass 3 and the Monte Carlo generation stage were used in the analysis. This production stage divided the previous sets of data into additional subsets as a function of the kinematic and particle identification cuts. This process permitted a detailed study of the systematic effects of the cut values used. Nearly 1000 branching ratios for the $K_L^0 \rightarrow \mu^+ \mu^-$ decay were calculated for each year. The 1989, 1990 and combined samples produced approximately 3000 branching ratio values which were used to study systematic effects. Finally, each of the data sets contributed one or more parameters used in the actual calculation of the branching ratios.

As much as possible, identical cuts were used for each sample from the previous pass. Two notable exceptions were the cuts applied to the Monte Carlo and to the MB samples. The Monte Carlo events, unlike the data, did not have PID cuts from the detectors applied because the Monte Carlo was never designed to simulate the response of the PID detectors. The semileptonic sample was used to calculate L1 bit and PID bin efficiencies. The bin efficiencies were efficiency grids as a function of momentum and position. The efficiencies were binned in these variables in order to account for their dependence on these quantities. In order to calculate these efficiencies with reasonable statistics, some slightly different cuts were used. Complete descriptions of all cuts, which involve parameters such as vertex position, χ^2 's, PID quantities and similar quantities, are given in appendix C.

The flow of the pass 4 production is shown in figure 6.3. From this illustration it is clear that the pass 4 analysis is a highly parallel production pass. It is parallel not only because all modes could be processed through the code, but also because it calculated many different quantities simultaneously. The pass 4 nomenclature for this production is really more of an afterthought than a well-thought out scheme. It has only been after the analysis that this stage has been realized as an actual production pass. There are implications in this observation to a future improved experiment. These will be discussed further in the concluding chapter.

Pass 4 began by flagging events based on the values of the cut variables. For every cut there was a nominal value. If an event failed the nominal value for more than one cut, excepting mass and colinearity, it was removed from the production stream. In addition, an event was removed if it was outside the range of the cut under question. Naturally,

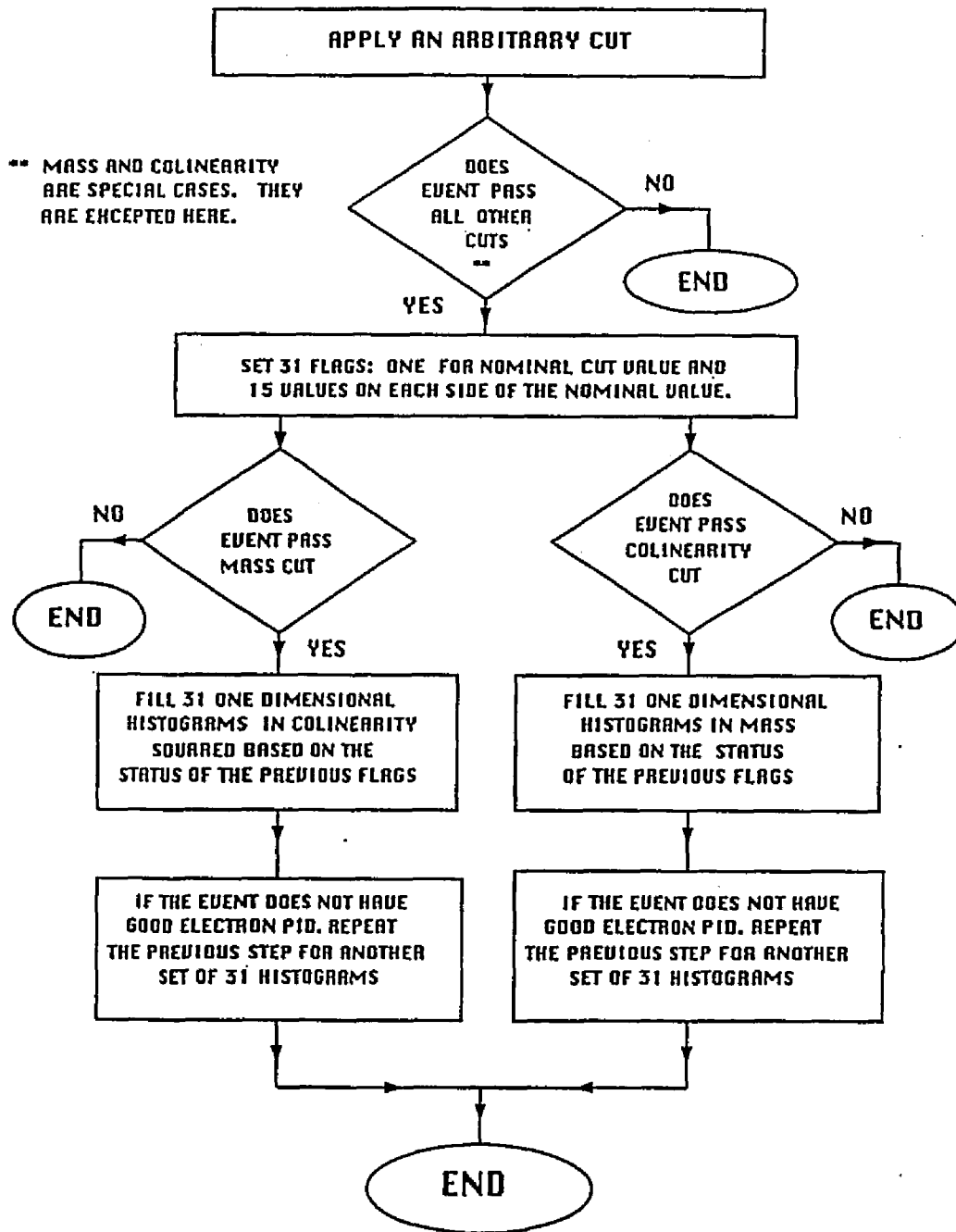


Figure 6.3: Flow of the pass 4 production

the production was parallel in the QT and FT fitters. Consequently, all systematic studies conducted assumed that the effects of the cuts were uncorrelated.

This stage was followed by grouping the events, according to the flags, in mass and colinearity histograms. These events were weighted according to the corrections described in appendices A and B. This phase of pass 4 represented the bulk of the analysis for calculating the number of events and the acceptances. The analysis was essentially finished after this stage. The remaining processing of the pass 4 code involved calculating efficiency grids and integrating them in order to obtain efficiencies.

The efficiency grids for the L3 and PID efficiencies were generated from MB $\pi^+\pi^-$ and MB data. The results from this part of the production pass were read when the pass was applied to Monte Carlo events. The Monte Carlo events provided weights used in the integration of the efficiency grids. The grid for the $\pi^+\pi^-$ interaction correction was generated in a separate study but was integrated in pass 4. In the case of the L1 efficiency, a slight redefinition of the cut values allowed a straight forward calculation to be performed. The cuts used in this phase are described in detail in appendix C.

The final features of the pass 4 code were relatively minor. Numerous tabulations and diagnostic plots were created in order to insure that the pass was working properly. Pass 4 had the capability of running on small data sets with the outputs summed at a later stage. This feature allowed the user to maximize the use of the batch workers. The summing of output results was done in such a way that the total obtained from small sets could not be distinguished from a run on the complete data set. The data from both years could also be summed. This procedure was more complicated and is discussed in appendix D.

Chapter 7

Event Selection and Efficiency Calculations

7.1 Overview

After the production analysis passes were completed, events were divided into many subsets. Each of these subsets resulted from a set of cuts as described in the previous chapter. The final selection of events and calculation of efficiencies was similar for all subsets. To avoid confusion, all references to sample sets in this chapter are assumed to be the subset under nominal cut values unless otherwise indicated. For all practical purposes, the analysis was completed at the end of production pass 4. The remaining work pertained only to extracting the information obtained from the final pass. If the systematic study had not been conducted, much of the work in the extraction of results could have been done by hand. A description of the extraction process is the focus of this chapter. The results obtained from applying the methods described in this chapter are presented in chapter 8. Chapters 7 and 8 are, consequently, formatted in a similar fashion.

7.2 $K_L^0 \rightarrow \mu^+ \mu^-$ Sample

Figure 7.1 is a colinearity squared versus mass plot of the combined 1989 and 1990 sample of $K_L^0 \rightarrow \mu^+ \mu^-$ events. The signal region here was defined to be a box below 2.0 mrad^2 and within $\pm 6.0 \text{ MeV}/c^2$ of the kaon mass ($497.67 \text{ MeV}/c^2$). Two types of anticipated backgrounds are exhibited in this figure, namely K_{c3} and $K_{\mu 3}$ decays. Events above 489

MeV/c^2 were generally K_{e3} decays in which the pion and electron were both misidentified as muons. The value $489 \text{ MeV}/c^2$ is the kinematic endpoint for this decay under perfect mass resolution. This background was commonly referred to as double mis-id. Events on the left side of the figure were generally $K_{\mu 3}$ decays. Here the pion was misidentified as a muon and the background was commonly referred to as single mis-id. The background to the $\mu^+\mu^-$ signal region was dominated by double mis-id events. The background to the sample was calculated in a box identical in mass center and mass width to the signal region but extending from 2.5 to 6.5 mrad^2 in colinearity squared. Figures 7.2 and 7.3 are histograms in mass and colinearity squared of the 1989 and 1990 combined samples.

The calculation of the background from K_{e3} decays encompassed a three-step process. First the number of events containing an electron signal was determined. Since the electron identification detectors were not perfectly efficient, a correction for the inefficiency had to be made to the number of identified K_{e3} background events. Finally, an extrapolation factor was needed to determine the number of events in the signal region given the number in the background region. The premise here was that any event in the background box passing as a $\mu^+\mu^-$ candidate but exhibiting electron ID was actually a K_{e3} decay. Figure 7.4 is identical to 7.3 but contains only events that also exhibit electron ID. Figure 7.5 is similar but only contains events that do not exhibit electron ID.

The electron identification efficiency was determined from a sample of K_{e3} events obtained from the pass 3 $\mu^+\mu^-$ sample. The calculation was done in the background region of colinearity space. Events were counted, with and without electron PID, in this background region, but without $\mu^+\mu^-$ PID. This set of events, to a good approximation, consisted entirely of K_{e3} decays. The ratio of the number of these events exhibiting electron PID to the total in the background region yielded the electron identification efficiency. Figure 7.6 is a histogram of K_{e3} events without electron identification.

Extrapolation into the signal region was performed in much the same way. In this case, the set of K_{e3} events with electron PID were used. The ratio of the number of events in the signal region in colinearity space to the number in the corresponding background region was calculated. This factor gave the number of expected K_{e3} background events in the $\mu^+\mu^-$ signal region given the number in the background box and the electron inefficiency correction.

The determination of the $K_{\mu 3}$ contribution to the background was similar to the calculation of the K_{e3} background. First, the number of events in the background region in

colinearity space, between 2.5 and 6.5 $mrad^2$, was determined. Figure 7.7 is the histogram of this plot. The background due to this decay appears small and flat in colinearity. The number of events in the background region was then corrected for the electron identification inefficiency and extrapolated flat into the signal region. The electron identification inefficiency was used in the $K_{\mu 3}$ background subtraction in order to account for $K_{e 3}$ events that were not removed with the electron identification requirements. The ratio of $K_{e 3}$ to $K_{\mu 3}$ backgrounds was approximately 4 to 1.

7.3 $K_L^0 \rightarrow \pi^+\pi^-$ Sample

Figure 7.8 is a colinearity squared versus mass plot of the final sample of $K_L^0 \rightarrow \pi^+\pi^-$ events used for normalization. The signal region here was defined to be identical to that used in the $K_L^0 \rightarrow \mu^+\mu^-$ sample. The $\pi^+\pi^-$ sample was subjected to the identical cuts used in the $K_L^0 \rightarrow \mu^+\mu^-$ sample except that no PID was required. A reasonably uniform background over the figure is apparent. This background arises from the semileptonic decays $K_{e 3}$ and $K_{\mu 3}$ in which the invariant mass is calculated assuming that both tracks are pions. In addition, there is a background to the $\pi^+\pi^-$ signal from K_S^0 decays. The correction for K_S^0 contamination, described in detail in appendix B, was performed on an event by event basis while the semileptonic background subtraction is performed with Monte Carlo semileptonic events. The semileptonic background subtraction was performed on both the mass and colinearity projections of the signal windows of figure 7.8. Figures 7.9 and 7.10 are these mass and colinearity projections for the $\pi^+\pi^-$ sample. The dashed lines are the superposition of the background obtained from Monte Carlo. The contributions from $K_{e 3}$ and $K_{\mu 3}$ events, determined from Monte Carlo, are shown in Figures 7.11 and 7.12.

The number of events in the tail of the colinearity projection above 3.0 $mrad^2$ and in the wings of the mass projection between 482-490 and 505-520 MeV/c^2 were tabulated for data and semileptonic Monte Carlo. The ratio of these values for data and Monte Carlo gave the factor by which to adjust the Monte Carlo histograms. The number of $\pi^+\pi^-$ events in the signal region was then calculated by subtracting the adjusted number of Monte Carlo events in the signal region from the number of data events in the same region. The calculation of the background in mass and colinearity squared spaces yielded slightly different values for the final $\pi^+\pi^-$ count. The average was used as the final value and the difference was used as a systematic error. The values of these numbers are presented in chapter 8.

7.4 Calculation of Acceptances

The geometrical acceptances of the detector for $K_L^0 \rightarrow \mu^+\mu^-$ and $K_L^0 \rightarrow \pi^+\pi^-$ decays were calculated using Monte Carlo events. The absolute acceptance differed slightly for the two decays. This difference was primarily due to the fact that the daughter particles had different masses and, thus, exhibited slightly different distributions of their kinematic quantities. The calculation of the acceptances was straightforward. The value of the systematic error due to the correction of the Skubic distribution, described previously, was obtained in the process of modifying the generated momentum distribution[76].

The number of Monte Carlo events in the signal region of colinearity space was tabulated. This number divided by the total number of generated events yielded the fractional acceptance for each mode. The error on the acceptances was calculated binomially but was extremely small. The quantity of interest was the ratio of $A_{\pi\pi}/A_{\mu\mu}$. This value was a measure of the relative difference in geometrical acceptances for the two decays. Changing the vacuum window and first drift chamber set used in the 1989 running period significantly increased the fractional acceptances in the 1990 running period.

7.5 Level 1 Efficiency Calculation

A correction for the efficiency of the L1 trigger was also determined. It was possible to lose a potential $\mu^+\mu^-$ candidate if the L1 trigger word lacked a bit that indicated a $\mu^+\mu^-$ event. This efficiency was calculated using $K_{\mu 3}$ decays in which the pion decayed from MB data. Cuts nearly identical to those used in the other samples were used except in the case of the mass and colinearity cuts. The mass window used was 370-480 MeV/ c^2 and the colinearity cut was 100 mrad². Events were then subjected to $\mu^+\mu^-$ PID. If an event passed these $\mu^+\mu^-$ criteria and also had the proper bit in the L1 trigger word set, L1 was considered efficient.

7.6 Level 3 Efficiencies

All dilepton events were required to pass the L3 trigger in order to be written to tape. The L3 algorithm was a fast and coarse check of the mass and colinearity of an event. Naturally, the code was not expected to have a perfect efficiency. MB $\pi^+\pi^-$ events were subjected to the L3 code, but no cuts were made. Since the L3 efficiency was dependent

only on basic kinematic quantities, opening angle, vertex z position, and momentum, the MB $\pi^+\pi^-$ sample was used to generate efficiency grids, or bin efficiencies, as a function of, or bins in, these variables. The efficiency for each decay mode was then generated by integrating the grid, weighted by the relative number of events in each bin from each mode. The weights were obtained from Monte Carlo data.

Due to the finite number of data events used to create the bin efficiencies and the large number of Monte Carlo events, bins existed in which there were Monte Carlo events but no bin efficiency. This situation could have led to a possible systematic effect in the L3 efficiency calculation. To estimate the effect, the L3 efficiency was first calculated only for bins with a nonzero efficiency. The three-dimensional bin efficiencies were then projected into three one-dimensional sets corresponding to each of the three bin parameters. Efficiencies for events with zero three-dimensional bin efficiencies were then calculated. These were combined with the previous set of efficiencies to produce a total of three final efficiencies. The four efficiencies of this group were then averaged to obtain the L3 efficiency. The difference between this efficiency and the minimum and maximum of the set yielded an estimate of the systematic error. This process was applied to $\mu^+\mu^-$ and $\pi^+\pi^-$ Monte Carlo events. An additional estimate of the L3 efficiency for $\pi^+\pi^-$ was calculated simply by integrating the L3 bin efficiency grid. As expected, the efficiency obtained with this method was in close agreement to the efficiency obtained from Monte Carlo events.

Due to the memory-intensive nature of the L3 efficiency calculation, the systematic effects due to the analysis cuts were not considered. The grid of bin efficiencies was $20 \times 20 \times 20$. To consider all of the systematic effects due to the cuts, as in the counting and other efficiencies, would have required more than 50 Mbyte of additional memory in the pass 4 code. By comparison, all of the pass 4 analysis, including systematic studies, could be run in less than 16 Mbyte of total memory. The systematic effect due to the fitting program, however, was calculated.

The real quantity of interest was the ratio of L3 efficiencies for $\pi^+\pi^-$ and $\mu^+\mu^-$ rather than the absolute efficiencies themselves. While the ratio is easily formed, the error associated with the result needs careful consideration. Since the same set of bin efficiencies was applied to both $\pi^+\pi^-$ and $\mu^+\mu^-$ Monte Carlo events, the statistical error associated with the L3 efficiency for each was correlated. The same was true of the systematic error. The extreme cases would have been perfect correlation or anti-correlation. The former would have caused the statistical and systematic errors to vanish while the latter would have required

the errors to be summed in quadrature. Clearly, neither of these held for the samples used. A study indicated that over 85% of the bins were correlated for Monte Carlo data. It also showed that the rms value of the difference in the number of events in each bin for the two modes was on the order of 5%. This result indicated that there was significant correlation between the errors. The error on the ratio of the L3 efficiencies was taken to be that on only one of the absolute samples (the statistical errors are identical). The systematic error on the ratio was taken to be the the largest systematic error of the two modes. This is still believed to be an overestimate of the error. However, without additional information it is the most conservative choice to make.

7.7 $\mu^+\mu^-$ Particle Identification Efficiency

The next factor that needed consideration was the efficiency of detecting $\mu^+\mu^-$ events with the PID detectors. The determination of this efficiency was a two-stage process. The first stage used well-identified muons from $K_{\mu 3}$ decays to obtain bin efficiencies for the MHO and MRG. The second stage used Monte Carlo events as weights to integrate the bin efficiency grids. Efficiencies for each muon detector separately and the correlated efficiency of the two muon detectors were obtained.

7.8 $\pi^+\pi^-$ Interaction Correction

Pions, unlike electrons and muons, could interact hadronically with the material of the detectors. This led to a slight loss of the $K_L^0 \rightarrow \pi^+\pi^-$ decays that were within the acceptance of the experiment. A separate study was made to obtain the interaction probabilities as a function of momentum of the pion. This grid was subsequently integrated using Monte Carlo events as weights. The systematic effect of the analysis cuts was not considered in this correction factor.

The correction grid was calculated using a set of special trigger tapes. This trigger required three of the four TSC planes, as required in both arms for a L0 trigger, but in only one of the two arms. The arm which had both front and back TSC hits was required to be a lepton. The other side was assumed to be a pion. Naturally, the lepton track had to pass all analysis cuts. If the pion track did not pass the analysis cuts it was assumed to have interacted in the dense material downstream of the first TSC set. An old version of PT that

did not incorporate the TSC information was used. The correction grid was then integrated with weights obtained from the Monte Carlo $\pi^+\pi^-$ sample. Finally, the calculation of the correction was only done for the QT fitter.

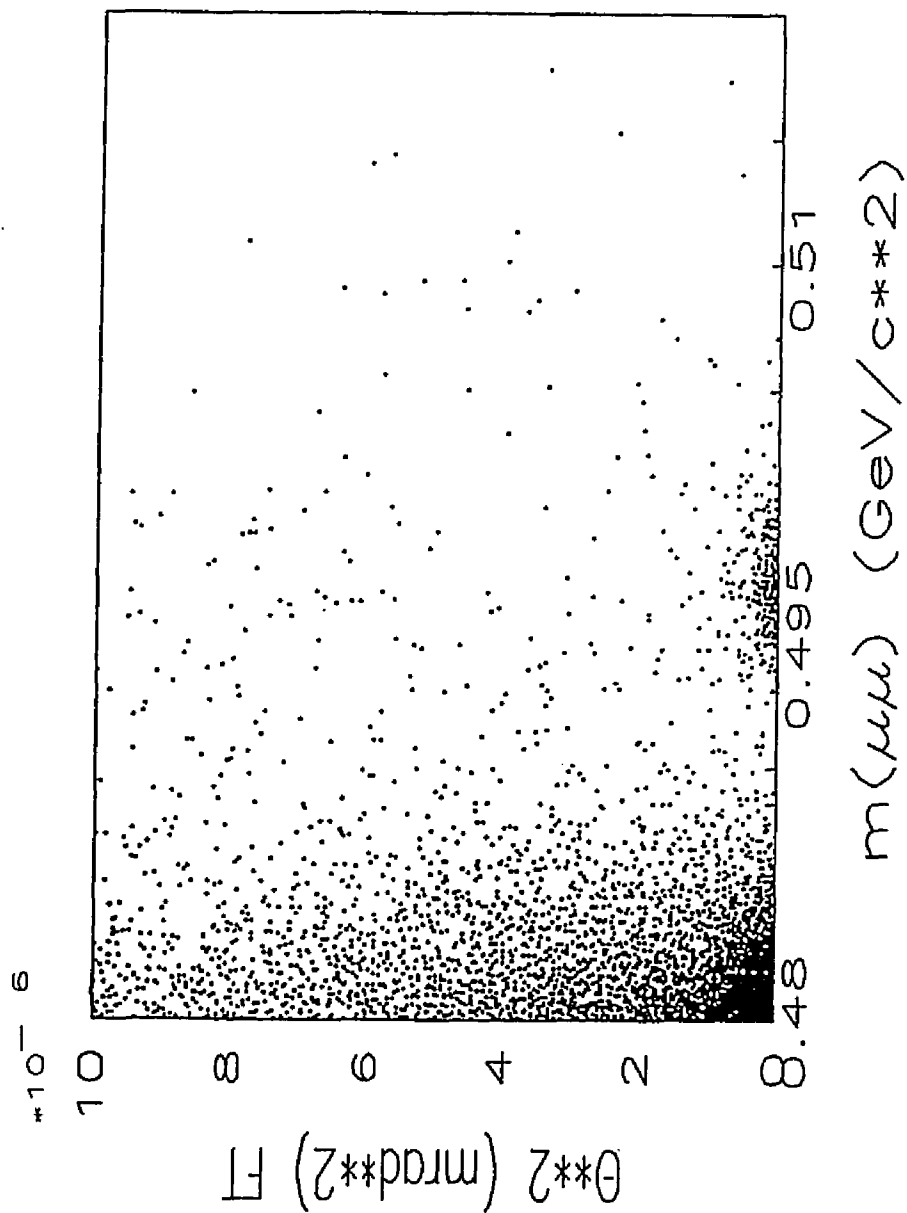


Figure 7.1: θ_c^2 vs. mass plot for the combined 1989 and 1990 $\mu^+\mu^-$ sample.

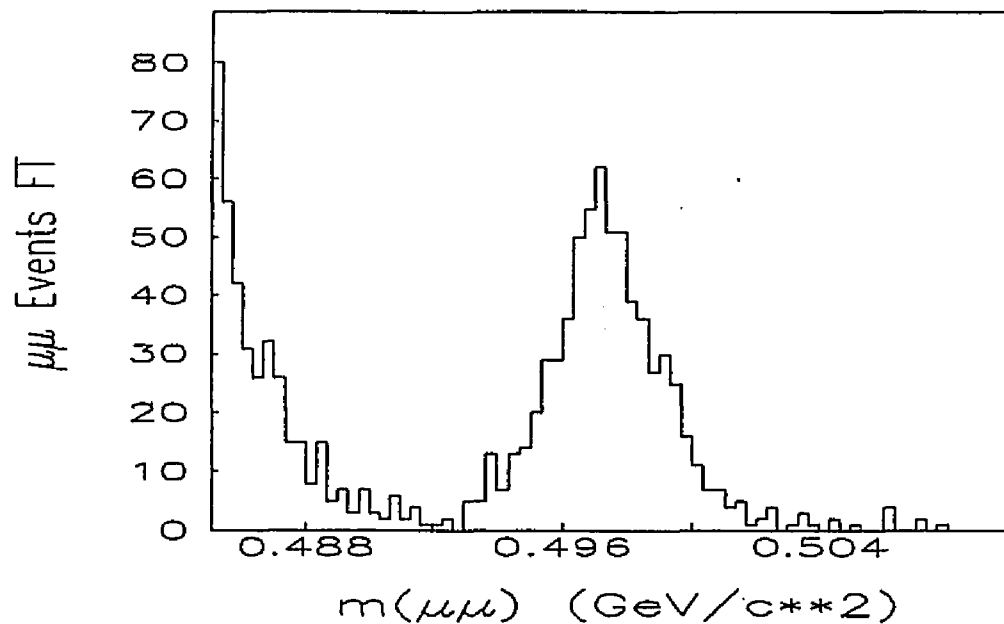


Figure 7.2: Mass histogram for the combined 1989 and 1990 $\mu^+\mu^-$ sample.

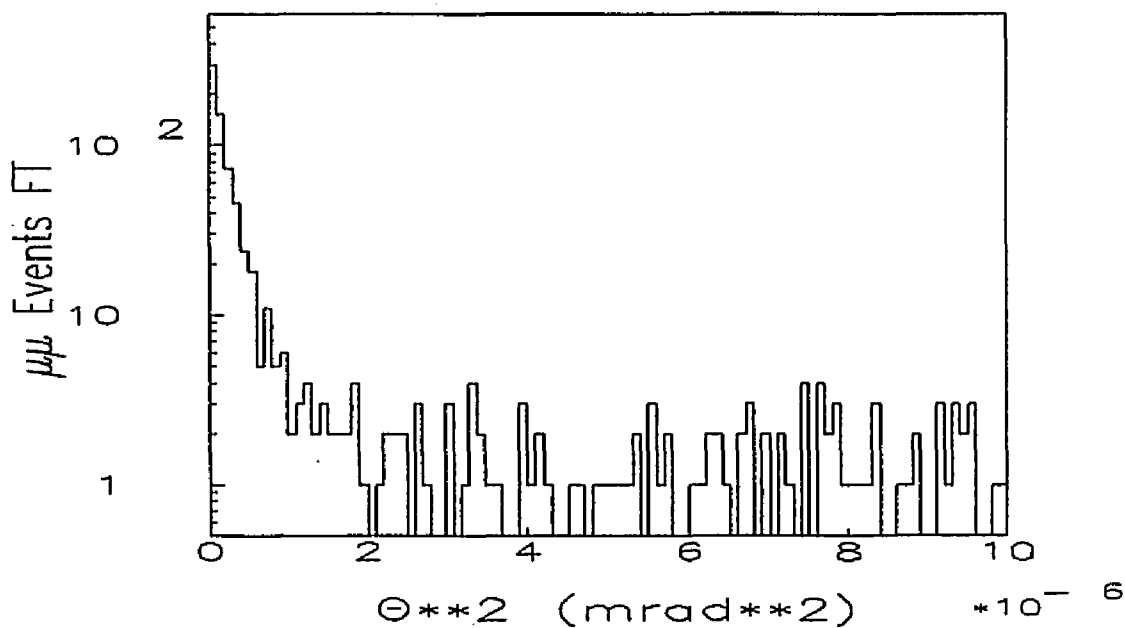


Figure 7.3: θ_c^2 histogram for the combined 1989 and 1990 $\mu^+\mu^-$ sample.

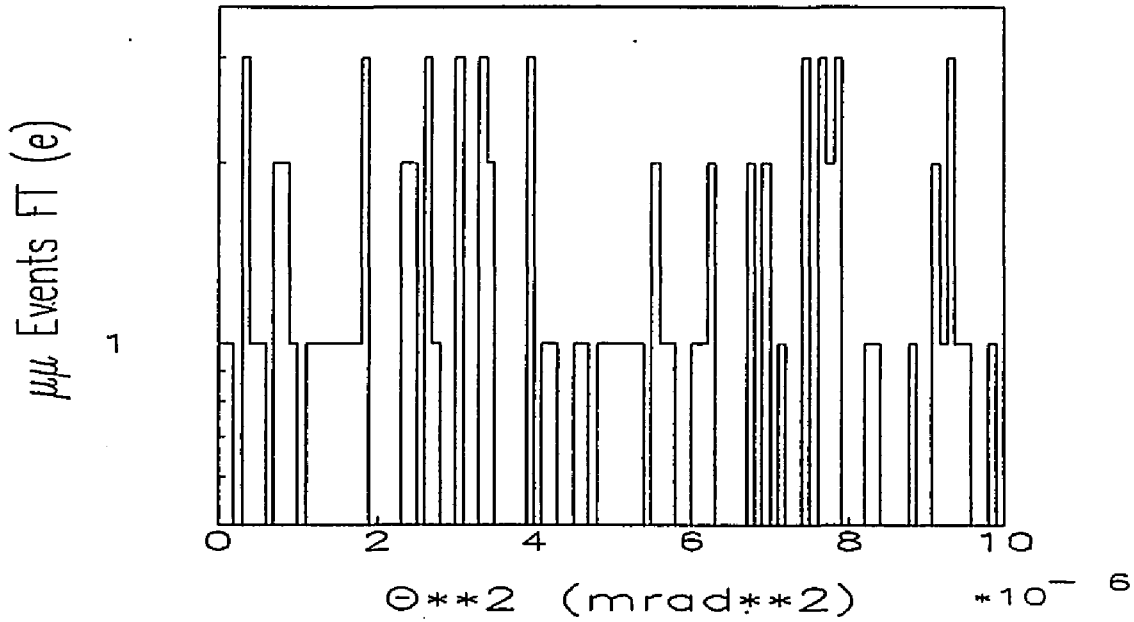


Figure 7.4: θ_c^2 histogram for the combined 1989 and 1990 $\mu^+\mu^-$ sample. Events were required to have electron PID.

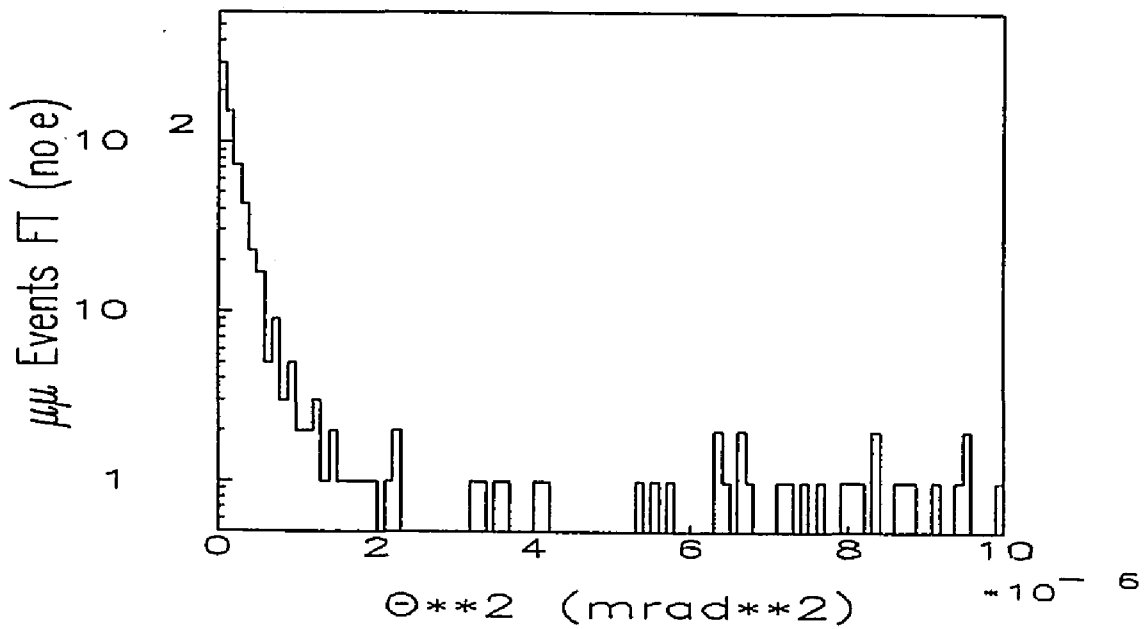


Figure 7.5: θ_c^2 histogram for the combined 1989 and 1990 $\mu^+\mu^-$ sample. Events were required to have no electron PID.

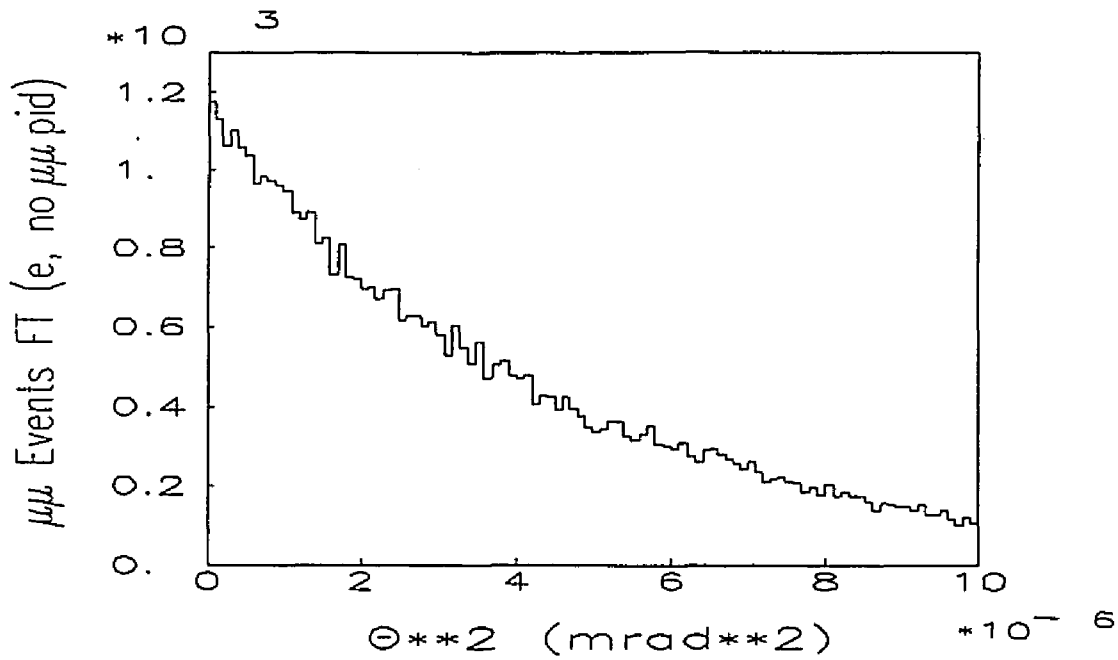


Figure 7.6: θ_c^2 for a sample of K_{e3} events without $\mu^+\mu^-$ PID.

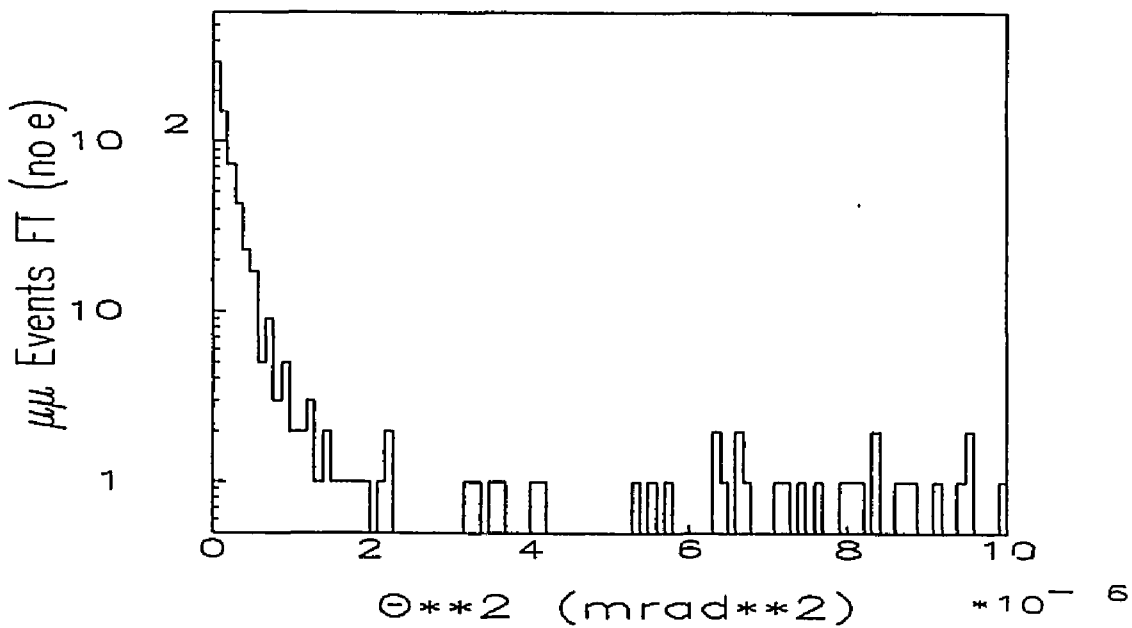


Figure 7.7: θ_c^2 histogram for the combined 1989 and 1990 $\mu^+\mu^-$ sample. Events were required not to have electron PID.

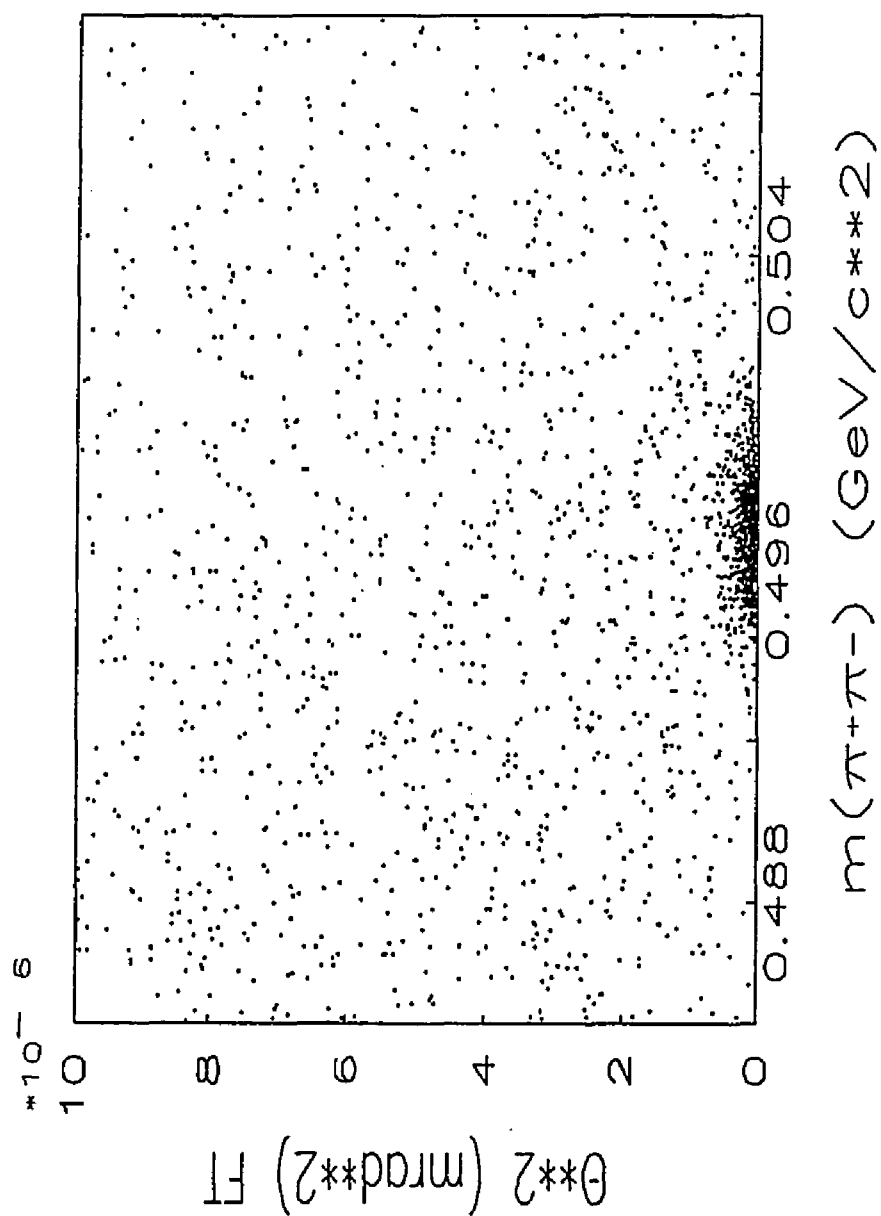


Figure 7.8: θ_c^2 vs. mass plot for a prescale of the combined 1989 and 1990 $\pi^+\pi^-$ sample.

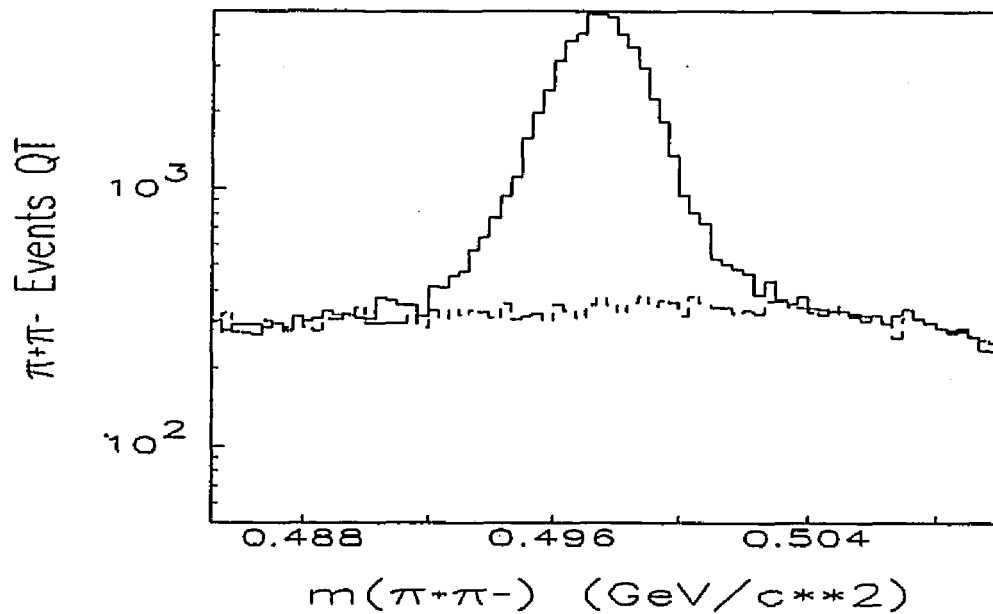


Figure 7.9: Mass histogram for the combined 1989 and 1990 $\pi^+\pi^-$ sample.

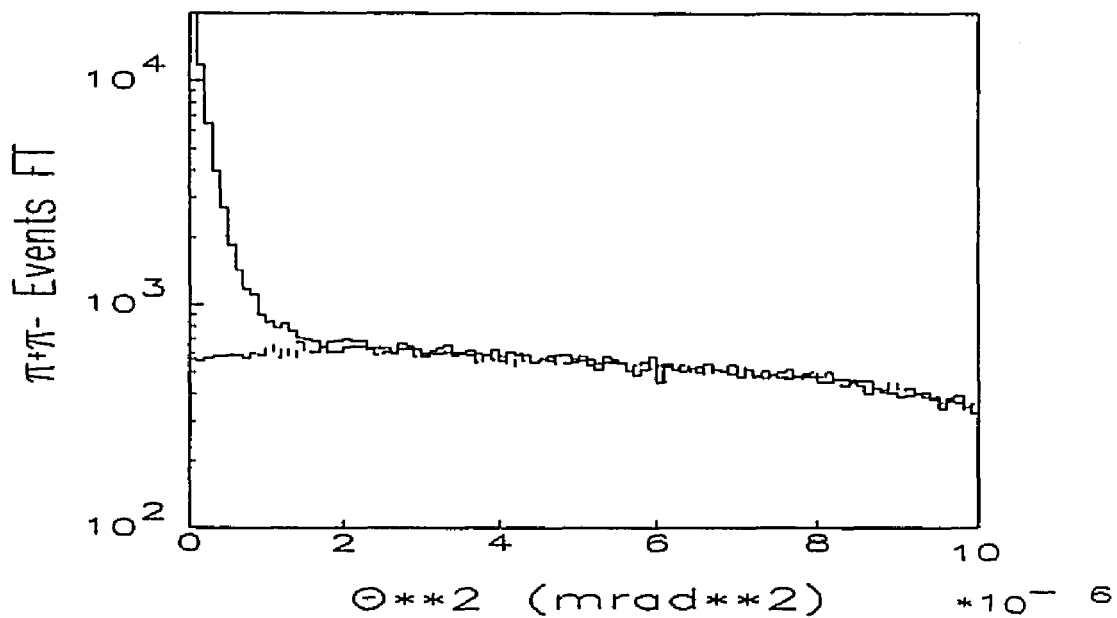
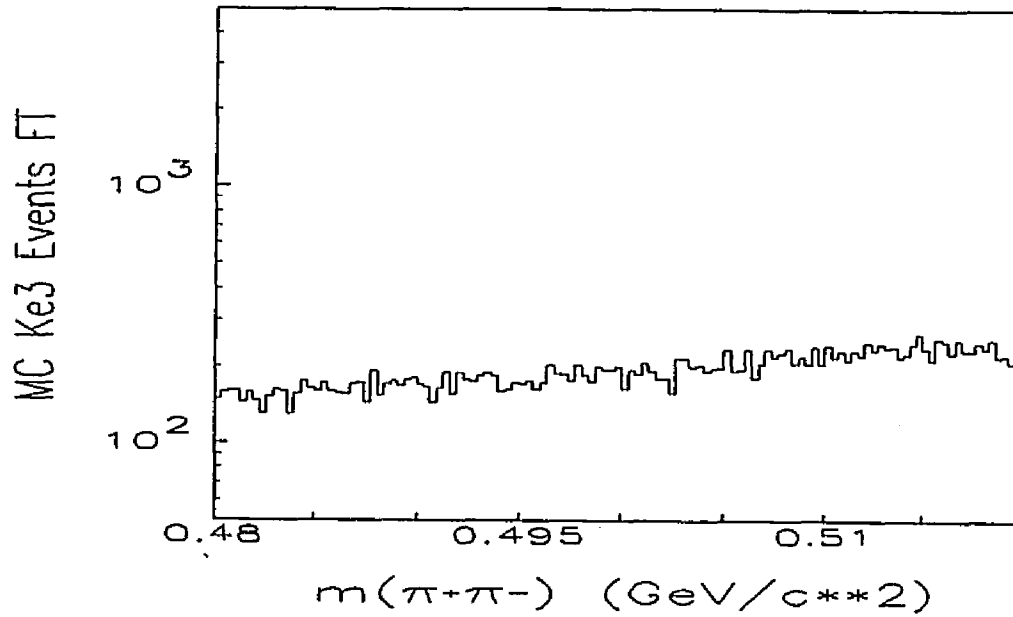
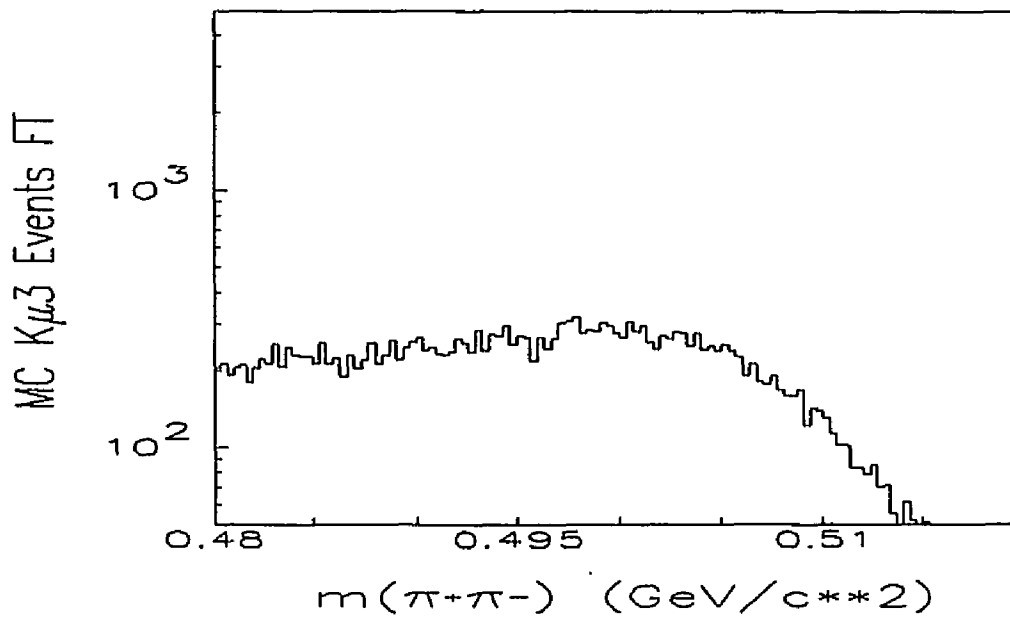


Figure 7.10: θ_c^2 histogram for the combined 1989 and 1990 $\pi^+\pi^-$ sample.

Figure 7.11: θ_c^2 for a sample of Monte Carlo K_{e3} events.Figure 7.12: θ_c^2 for a sample of Monte Carlo $K_{\mu 3}$ events.

Chapter 8

Results

8.1 Overview

This chapter summarizes the results of the experiment and the analyses described in the appendices and previous chapters. Most of the results presented in this chapter have had the systematic effects due to the analysis cuts studied, which are presented in appendices E through H and in each section. The results for both the FT and QT fitters are presented in this chapter with the results for QT being enclosed in parentheses unless otherwise noted. The combined sample was used in a fashion identical to the individual samples from each running period. As a reminder, the combined result refers only to the combination of the 1989 and 1990 samples unless otherwise noted. The 1988 results were incorporated via the method of maximum likelihood. The 1988 data were not reanalyzed with the 1989 and 1990 samples and thus could not be combined the same way. The results from 1988 are presented in each section but not incorporated into the tables. A description of the method used to combine the samples, as well as the maximum likelihood method, is given in appendix D. The methods used in obtaining the results presented in this chapter are described, in detail, in chapter 7. This chapter is, essentially, formatted in an identical manner to the previous chapter. There is a one to one correspondence of the content of sections in both chapters.

8.2 $\mu^+\mu^-$ Counting Results.

The electron identification efficiencies and extrapolation constants used in the $\mu^+\mu^-$ background subtraction are listed in table 8.1. There is good agreement between the values

Data Set	Electron efficiency	Error	Extrapolation constant	Error
1989	89.65% (89.58%)	0.34% (0.35%)	1.158 (1.152)	0.019 (0.019)
1990	88.89% (88.72%)	0.29% (0.30%)	1.027 (1.027)	0.014 (0.014)
1989+1990	89.20% (89.07%)	0.22% (0.23%)	1.081 (1.078)	0.011 (0.012)

Table 8.1: Electron efficiency and extrapolation constants for the $\mu^+\mu^-$ sample. QT values are enclosed in parentheses.

Data Set	Signal	K_{e3} background	$K_{\mu 3}$ background	Candidates $N_{\mu^+\mu^-}$	Error
1989	294.0 (292.0)	19.4 (16.7)	1.6 (1.7)	273.0 (273.5)	17.8 (17.7)
1990	368.0 (370.0)	20.8 (18.5)	2.4 (5.5)	344.8 (346.0)	19.8 (19.7)
1989+1990	662.0 (662.0)	40.0 (35.1)	4.0 (7.2)	618.0 (619.7)	26.6 (26.6)

Table 8.2: $\mu^+\mu^-$ counting results. QT values are enclosed in parentheses.

calculated for FT and QT. The electron identification efficiency was conspicuously lower in 1990 than 1989, which may be an indication that the electron identification detectors had aged. The decrease in efficiency could be due to changes in the detector, described in chapter 3, or beam intensity differences between the two running periods. The general trend of efficiencies, as will be presented, appears to imply that there was a slight deterioration in the response of the detectors rather than other factors. The extrapolation constant also changed significantly between the two running periods. This difference was probably due to changes in the vacuum window, target and L3 code. The systematic studies did not consider changes in these values.

Table 8.2 lists the results of the $\mu^+\mu^-$ counting. In general, the number of signal, candidate and background events obtained from the QT fitter is larger than that from the FT fitter for the $\mu^+\mu^-$ data set. The exceptions are in the K_{e3} background and the number of signal events for 1989. It is interesting to note that the FT-QT difference in the number of events in the signal region before background subtraction is equal and opposite for 1989 and 1990. This had the combined effect of making the counts appear identical for the combined sample. Nevertheless, the counts appear to be in good agreement for the given statistics. In 1988, 87 $\mu^+\mu^-$ events were observed after background subtraction. Plots of the number of $\mu^+\mu^-$ candidates as a function of the cuts used in the systematic studies are presented in appendix E.

8.3 $\pi^+\pi^-$ Counting Results.

Tables 8.3 and 8.4 summarize the results of the $\pi^+\pi^-$ counting. In general QT counted fewer $\pi^+\pi^-$ events than did FT, in contrast to the $\mu^+\mu^-$ data sample. The difference in this sample is quite large compared to that in the $\mu^+\mu^-$ data set. Additionally, the systematic effects in $\mu^+\mu^-$ and $\pi^+\pi^-$ effectively add, increasing the systematic error between the fitters in the final branching ratios. Two other systematic effects are also present that introduce errors, with one being more significant.

The first effect arises in the counting of events counted in the signal region before background subtraction. One would naively expect these values to be identical in the two methods. After all, they are simply tabulated in different spaces. If the tabulations were performed with integers the assumption would be correct. However, recall that every data $\pi^+\pi^-$ event was weighted by the probability that it originated from a K_L^0 in order to account

Data Set	Mass Space			Colinearity Space		
	Data Wings	MC Wings	Ratio	Data Wings	MC Wings	Ratio
1989	5732 (5674)	10878 (10898)	0.527 (0.521)	11358 (11147)	22304 (22348)	0.509 (0.499)
1990	12093 (12015)	16199 (16165)	0.747 (0.743)	24042 (23604)	32386 (32543)	0.742 (0.725)
1989+1990	17827 (17690)	23911 (23793)	0.746 (0.743)	35401 (34753)	48192 (48185)	0.734 (0.721)

Table 8.3: $\pi^+\pi^-$ counting results used for background subtraction. QT values are enclosed in parentheses.

Data Set	Signal	Background	Candidates $N_{\pi^+\pi^-}$	Error	Systematic
1989	19483 (19061)	3846 (3813)	15637 (15248)	153 (151)	66 (81)
1990	41280 (40496)	8300 (8170)	32980 (32326)	229 (226)	23 (100)
1989+1990	60764 (59557)	12145 (11983)	48619 (47574)	277 (274)	90 (182)

Table 8.4: $\pi^+\pi^-$ counting results. QT values are enclosed in parentheses.

for K_S^0 contamination as described in appendix B. This weight required the tabulation to be done with real numbers. In addition, weights were applied to Monte Carlo events to correct the kaon momentum, time distribution and K_L^0 probability (only for Monte Carlo semileptonic decays). The floating point representation of a real number on the computer used to perform the analysis had an average fractional rounding error of a few parts out of 10^8 . This error, propagated over the observed events, is entirely consistent with the observation that the 1989 and 1990 signal counts each disagree by one event out of a few 10^4 events for tabulations in mass and colinearity spaces for each fitter. This disagreement is two events for the combined samples, again entirely consistent with this observation. This begs the question of the need for higher precision in the offline code. An error of a few hundredths of a percent is essentially insignificant for these data. More will be said on this topic in the concluding chapter.

The second difference pertained to the method of background subtraction. The calculations of the background in mass and colinearity spaces yielded slightly different results. The systematic effect of this background subtraction is on the order of 0.2% for FT and approximately 0.4% for QT. The values for the final $\pi^+\pi^-$ counts were taken to be the average between the values obtained in mass and colinearity spaces. The difference was then used as a systematic error. The statistical error on the final $\pi^+\pi^-$ count, after background subtraction, was taken to be the smaller of the errors in mass and colinearity space.

The prescale parameter, P, for $\pi^+\pi^-$ events was 6000 in 1988 and 1989, and 4000 in 1990. The combined 1989 and 1990 sample had an effective prescale of 4642. This value was calculated in the combination of the two data sets and its determination is described further in appendix D. Plots of the number of $\pi^+\pi^-$ candidates as a function of the cuts in the systematic studies are presented in appendix E. Finally, the number of $\pi^+\pi^-$ events in 1988 after background subtraction was 8226 ± 148 .

8.4 Acceptance Calculation Results.

In 1988 the ratio of $\pi^+\pi^-$ to $\mu^+\mu^-$ acceptances was 1.180 ± 0.012 . Table 8.5 summarizes the results of the acceptance calculations for 1989 and 1990. The differences between the results for FT and QT are exceedingly small. Although it is not apparent from the table, QT counted fewer Monte Carlo events than FT. The difference was small for both $\mu^+\mu^-$ and $\pi^+\pi^-$ Monte Carlo and on the order of a few hundredths of a percent. Plots of the

absolute acceptances as a function of the cuts considered in the systematic studies are given in appendix F.

The absolute acceptances for $\pi^+\pi^-$ and $\mu^+\mu^-$ events increased dramatically from 1989 to 1990. This increase was due to the replacement of the vacuum window and first set of drift chambers. In 1988 the absolute acceptance for each mode was significantly lower than those in 1989 due to the use of much more restrictive cuts. As is illustrated in the systematic plots, presented in appendix F, the tighter the cut, the lower the absolute acceptance. In spite of the differences between the three running periods, the ratio of $\pi^+\pi^-$ to $\mu^+\mu^-$ acceptances is essentially constant within error.

The systematic effect of the choice of kaon momentum distribution was also studied. The effect was calculated by determining the acceptances with kaon momentum distributions obtained from a pure Skubic distribution, 1989 data, 1990 data, and a combined sample of 1989 and 1990 data. The value of the acceptance under a pure Skubic distribution was important since the 1988 value was based on this distribution, without corrections in the Monte Carlo generation. Corrections to the Skubic distribution from 1989 or 1990 data alone would cause respective decreases or increases in the acceptance ratios listed in table 8.5. These changes are tabulated in table 8.6.

The acceptances for 1988 contained different systematic effects. The first value, 2.784%, represents the error introduced by using only a Skubic distribution. In addition, a 3.738% effect was introduced by tighter track χ^2 cuts than those used in 1989 and 1990. Both corrections have the effect of increasing the quoted 1988 $\mu^+\mu^-$ branching ratio. The net effect of these two corrections would be to change the quoted 1988 $\mu^+\mu^-$ branching ratio by a factor of 1.067.

8.5 Level 1 Efficiency Results.

The L1 efficiency calculation was the only efficiency in which the systematic effects due to the cuts were studied in detail. This decision was the result of computer memory and time constraints in the pass 4 production. A summary of the results of the L1 efficiency calculation for 1989 and 1990 is given in table 8.7. FT and QT produce nearly identical efficiencies in this calculation. As in most other cases, QT again counted fewer events than did FT. Plots of the L1 efficiency as a function of the cuts considered in the systematic studies are given in appendix G.

Data Set	$A_{\mu^+\mu^-}$	Error	$A_{\pi^+\pi^-}$	Error	$A_{\pi^+\pi^-}/A_{\mu^+\mu^-}$	Error
1989	3.161 (3.160)	0.010 (0.010)	3.707 (3.706)	0.011 (0.011)	1.173 (1.173)	0.005 (0.005)
1990	4.363 (4.363)	0.013 (0.013)	5.079 (5.074)	0.015 (0.015)	1.164 (1.163)	0.005 (0.005)
1989+1990	3.682 (3.674)	0.008 (0.008)	4.303 (4.290)	0.009 (0.009)	1.169 (1.168)	0.004 (0.004)

Table 8.5: Acceptance calculation results. Absolute acceptances are in percentages. QT values are in parentheses.

Data Set	Upper Systematic	Lower Systematic
1989	0.0043 (0.0043)	0.0158 (0.0157)
1990	0.0037 (0.0036)	0.0140 (0.0139)

Table 8.6: Systematic errors on acceptance ratio results. QT values are in parentheses.

The significance of the L1 efficiency systematic plots lies in their relationship to other efficiency calculations. The plots show that the L1 efficiency was reasonably stable as a function of the cut values. Any systematic effect introduced by the cuts seems to cancel out in the ratio. This result implies that other efficiencies will also exhibit the same stability and thus it appears reasonable to assume that any systematic effect introduced in the other efficiencies (L3, PID, $\pi^+\pi^-$ absorption) is small. The L1 efficiency for 1988 was $(98.5 \pm 1.5)\%$, consistent with that for 1989. The 1990 value is lower by about two standard deviations, consistent with changes in the electron identification efficiencies and is a second indication that the response of the detectors was diminishing in time.

8.6 Level 3 Efficiency Results.

The results of the L3 efficiency calculation are presented in table 8.8. FT and QT numbers exhibit some disagreement, although the differences are consistent within error. As noted in the previous chapter, the statistical error on the ratio of the efficiency for $\pi^+\pi^-$ to $\mu^+\mu^-$ was taken to be the larger of the statistical errors on the absolute efficiencies. Additionally, the systematic error was taken to be the largest of the differences between the three values calculated for each mode and the value obtained from data (see section 7.6). As a result, the systematic error represents the difference between the absolute efficiency calculated from data $\pi^+\pi^-$ and that calculated from Monte Carlo. In 1988 the L3 efficiency was 0.79 ± 0.02 . During that running period $\pi^+\pi^-$ events were not subjected to L3 cuts so that this number represents both the ratio and the L3 efficiency for $\mu^+\mu^-$ events.

The combined result for the L3 efficiency ratio exhibits an unusual property. In all of the other calculations the combined result fell between the 1989 and 1990 values. This was also the case, as expected, for the absolute L3 efficiencies for each mode. The ratio for the combined sample, however, was lower than the ratio for either running period. Rather than an indication of an error, this observation implies that the ratio, which is very close to unity, is very sensitive to small statistical fluctuations and small systematic errors. Nevertheless, the results are consistent when the statistical and systematic errors are considered.

Data Set	Candidates	Pass L1	Efficiency ($\epsilon_{\mu+\mu^-}$) _{L1}	Error
1989	659 (629)	649 (619)	98.48 (98.41)	0.48 (0.50)
1990	1314 (1268)	1283 (1239)	97.64 (97.71)	0.42 (0.42)
1989+1990	1316 (1263)	1291 (1239)	98.06 (98.06)	0.38 (0.39)

Table 8.7: L1 efficiency calculation results. Efficiencies are in percentages. QT values are in parentheses.

Data Set	($\epsilon_{\mu+\mu^-}$) _{L3}	Error	($\epsilon_{\pi+\pi^-}$) _{L3}	Error	($\epsilon_{\pi+\pi^-}/\epsilon_{\mu+\mu^-}$) _{L3}	Error	Systematic
1989	64.72 (64.04)	0.39 (0.45)	64.64 (64.39)	0.28 (0.28)	0.9992 (1.0055)	0.0057 (0.0071)	0.0031 (0.0008)
1990	88.78 (88.75)	0.20 (0.26)	89.45 (89.75)	0.15 (0.14)	1.0076 (1.0113)	0.0023 (0.0030)	0.0053 (0.0014)
1989+1990	75.77 (75.56)	0.19 (0.36)	75.97 (75.57)	0.26 (0.19)	0.9973 (1.0002)	0.0034 (0.0048)	0.0043 (0.0032)

Table 8.8: L3 efficiency calculation results. Efficiencies are in percentages. QT values are in parentheses.

Data Set	ϵ_{MHO}	Error	ϵ_{MRG}	Error	$(\epsilon_{\mu^+\mu^-})_{PID}$	Error
1989	93.17 (93.09)	0.22 (0.23)	98.66 (98.65)	0.13 (0.14)	91.93 (91.83)	0.26 (0.27)
1990	92.41 (92.43)	0.16 (0.17)	98.40 (98.44)	0.13 (0.12)	90.94 (90.99)	0.20 (0.21)
1989+1990	92.88 (92.83)	0.16 (0.17)	98.54 (98.55)	0.12 (0.12)	91.51 (91.47)	0.20 (0.20)

Table 8.9: $\mu^+\mu^-$ particle identification efficiency results. Efficiencies are in percentages. QT values are in parentheses.

8.7 $\mu^+\mu^-$ Particle Identification Efficiency Results.

The particle identification efficiencies for the MHO and MRG detectors as well as the correlated results are listed in table 8.9. The results from QT and FT are essentially identical. In 1988 the correlated efficiency for $\mu^+\mu^-$ identification was $(92.9 \pm 1.1)\%$. As in the L1 efficiency calculation, a general downward trend over the running periods has been observed.

The PID efficiency calculation was not subjected to the systematic studies undertaken in other counting areas. The cuts on the MHO and MRG were, however, part of the systematic studies in the other calculations. Plots of the number of $\mu^+\mu^-$ candidates and L1 efficiency as a function of these cuts are given in appendices E and G. The effect of requiring tighter muon identification cuts is to lower the $\mu^+\mu^-$ PID efficiency. Additionally, the efficiency for 1990 is consistently lower than that in 1989. This observation seems to confirm the assumption that the detectors have become less efficient due to aging.

8.8 $\pi^+\pi^-$ Interaction Correction Results.

The final value needed for the branching ratio is the correction for pion interactions. In 1989 this value was calculated to be $\delta_{int} = (98.5 \pm 0.2)\%$. Upon recalculation in 1989, it was found to be $(97.0 \pm 1.0)\%$. This calculation represented a significant change from the value calculated in 1988. Under the 1990 analysis and reanalysis of 1989 data, the correction was again recalculated. This time the correction was calculated to be $(95.67 \pm 0.60)\%$. This represented a slight change from the value calculated in 1989 but is consistent within error. The changes represent more sophisticated calculations as well as higher statistics obtained from the $\pi^+\pi^-$ data samples.

8.9 Branching Ratio Calculation Results.

The results from the preceding sections can now be combined to obtain a measurement of the branching ratio for $K_L^0 \rightarrow \mu^+\mu^-$. The branching ratio is given by:

$$B(K_L^0 \rightarrow \pi^+\pi^-) \left(\frac{N_{\mu^+\mu^-}}{P * N_{\pi^+\pi^-}} \right) \left(\frac{A_{\pi^+\pi^-}}{A_{\mu^+\mu^-}} \right) \left(\frac{\epsilon_{\pi^+\pi^-}}{\epsilon_{\mu^+\mu^-}} \right)_{L3} \left(\frac{1}{\epsilon_{\mu^+\mu^-}} \right)_{L1} \left(\frac{1}{\epsilon_{\mu^+\mu^-}} \right)_{PID} (\delta_{int}). \quad (8.1)$$

The results for the 1989, 1990 and combined data sets are given in table 8.10. The results for combining these results and that of 1988 via the method of maximum likelihood are shown in table 8.11. There were two types of systematic errors present. The first was the sum, in quadrature, of all the errors on the contributions to the branching ratio previously presented, except for the $\mu^+\mu^-$ value. These were considered systematic errors since they were dependent on parameters introduced into the hardware and software by the users. The errors on the $\pi^+\pi^-$ counting, for example, could have been reduced by nearly a factor of 100 simply by removing the prescale. The errors on the efficiency could also have been reduced significantly simply by eliminating the prescale. The errors associated with the use of Monte Carlo events, as another example, could also have been reduced simply by generating more events.

The second type of systematic error originated from the systematic errors quoted in the previous sections and a systematic error associated with the dependence of the branching ratio on the cut values. Plots of the branching ratio as a function of the cut values used in the systematic studies are given in appendix H. The errors listed in table 8.11 contain all of the statistical and systematic errors. The statistical and systematic errors were not separated after using the method of maximum likelihood (see appendix D).

Data Set	Branching Ratio ($\times 10^{-9}$)	Error	Systematic
1989	7.32 (7.58)	0.48 (0.49)	0.17 (0.18)
1990	6.71 (6.87)	0.38 (0.39)	0.15 (0.15)
1989+1990	6.93 (7.08)	0.30 (0.30)	0.15 (0.15)

Table 8.10: Branching ratio calculation results from data. QT values are in parentheses.

Data Set	Branching Ratio ($\times 10^{-9}$)	Error
1989+1990	6.94 (7.15)	0.36 (0.37)
1988+ 1989+1990	6.77 (6.95)	0.34 (0.35)

Table 8.11: Branching ratio calculation results from maximum likelihood. QT values are in parentheses.

The systematic errors obtained from the study of the dependence of the branching ratio on the cut values were on the order of 1.5%. Table 8.10 shows that there is a noticeable difference between the results from the QT and FT fitters. Consequently, this difference represents a sizeable systematic effect. The most likely value for the branching ratio is believed to lie between the values calculated from the two fitting packages. In obtaining the systematic errors given in appendix H, this observation was taken into account. If a systematic trend was observed such as to shift the branching ratio in the direction of the other fitter, it was not included as an error. This error is taken into account by the systematic difference between the two fitters.

The vast majority of the plots in appendix H show no definite systematic trends. The few plots that do are in colinearity for 1989 data for both fitters and in the mass window size for FT in 1990 data. These systematics are taken to be 1.3% and 1.4% for QT and FT, respectively, in 1989 and 1.1% for FT in 1990. In addition, a systematic error that depended on how the corrections and errors to the 1988 result were incorporated was introduced. This error was asymmetric with values of +0.05 and -0.02. The final systematic error is the difference between the fitters. Here, the largest error in table 8.11 was used and added in quadrature to the systematic errors from the 1988 result and to the difference between the mean and the individual fitter results. Incorporating these errors and applying the maximum likelihood method yields a combined 1988, 1989 and 1990 value for the branching ratio of:

$$B(K_L^0 \rightarrow \mu^+ \mu^-) = (6.86 \pm 0.37) \times 10^{-9}. \quad (8.2)$$

Chapter 9

Conclusion

The branching ratio $B(K_L^0 \rightarrow \mu^+ \mu^-)$ has been measured using data obtained in BNL experiment 791 during running periods in 1988, 1989 and 1990. During the three running periods, 87, 274 and 346 respective candidate events were observed, forming an overall sample of 707 $\mu^+ \mu^-$ events. The result for the branching fraction using the total data set is $B(K_L^0 \rightarrow \mu^+ \mu^-) = (6.86 \pm 0.37) \times 10^{-9}$. This result is very near the unitarity bound of 6.81×10^{-9} and is consistent with earlier measurements.

An improved experiment to succeed E791 is under construction and is expected to begin acquiring data in 1994. This experiment, E871, is designed to increase the sensitivity to $K_L^0 \rightarrow \mu^\pm e^\mp$ by a factor of 20 to 30 over E791[86]. This implies that E871 may observe 10,000 to 20,000 $K_L^0 \rightarrow \mu^+ \mu^-$ events and well over 10^6 $K_L^0 \rightarrow \pi^+ \pi^-$ events, with prescales similar to those in E791. This experiment could produce a 1% measurement of the $K_L^0 \rightarrow \mu^+ \mu^-$ branching ratio. Since much has been learned in the process of analyzing the 1989 and 1990 data samples, it appears reasonable to mention potential problems and solutions in this chapter. The remainder of this conclusion focuses on these items for an improved experiment.

For an experiment collecting such a large amount of data, rounding error due to the binary representation of real numbers could become a significant source of error. In the analysis of 1989 and 1990 data from E791, a rounding error of a few thousandths of a percent was observed. The character of such an error depends on the implementation of the analysis code. For example, analyzing small portions of the data set and summing the results would yield a smaller error than analyzing the entire data set in one job. An error on the order of several tenths of a percent to a full percent should be expected in the

counting of $10^6 \pi^+\pi^-$ events. This error would be on the same order of magnitude or greater than the statistical error on the $\pi^+\pi^-$ counting. This error could be reduced by increasing the prescales at the cost of increasing the statistical error on the $\pi^+\pi^-$ sample. The only other alternative is to perform the $\pi^+\pi^-$ counting with double precision real numbers. This second procedure has the disadvantage of increasing memory and CPU time requirements, but does essentially eliminate digital error.

The statistical errors associated with the contributions to the $K_L^0 \rightarrow \mu^+\mu^-$ branching ratio could also become significant. In E791 these individual errors were typically on the order of 0.5% with a total error, from all contributions except $\mu^+\mu^-$ counting, close to 2.0%. For E871, the total error, excluding the contribution from the $\mu^+\mu^-$ counting, will still be on the order of 0.5% unless the prescales are significantly lowered and the number of Monte Carlo events generated are significantly increased. While this type of change is usually incorporated into higher precision experiments, the changes could introduce other problems. Lowering the prescales and increasing the number of generated events, for example, increases the amount of storage space needed and CPU time required to analyze the events and, potentially, could require the use of double precision numbers in the offline analysis.

Other systematic errors may also become important contributions to the total uncertainty in E871. Already, there is a systematic difference of 0.4% between the two methods of subtracting the background in the $\pi^+\pi^-$ sample. Other systematic effects, such as those associated with the correction to the Skubic distribution, could also give large contributions. The systematic errors due to the choices of cut values were typically small. The largest systematic effect was the 1.3% difference between the QT and FT fitters, which is larger than the statistical error expected in E871. The difference appears to originate predominately from the $\pi^+\pi^-$ counting. Since the sample from QT was a subset of the FT sample, future studies may indicate which, if either, of the fitters is more correct, or how to rectify the discrepancy.

The pass 4 analysis was a very time intensive analysis stage, primarily because of the need to perform TKC each time the code was run. If an additional stage of production analysis were added, the CPU time requirements could be significantly reduced. This stage would output TKC-related quantities to tape, as PT, QT, and FT related quantities were in the pass 1 and pass 2 analyses. Such a stage would allow all remaining analysis to be completed with a minimum of computational needs; nearly all required information would be available upon reading an event. The disadvantage of this process is that CPU time

would be minimized at the expense of increased storage space requirements.

Finally, the previous observations represent correctable problems or even potential increases in analysis efficiency. None of them appears to imply limitations on the improved experiment. Consequently, E871 can be expected to yield results of much higher precision than those of E791.

Appendix A

Corrections to the Monte Carlo Data Set

The pass 4 production analysis showed that some of the parameters used in the generation of Monte Carlo events were not optimal. These were parameters obtained from the MB $\pi\pi$ sample. The parameters used in the Monte Carlo generation included the relative number of events to generate at each time period of the experiment, a correction to the Skubic distribution, and the distributions of data in vertex x/z and y/z . The distribution in time and the distribution of the kaon momentum were not optimal. Consequently, corrections to these parameters were made. These corrections were applied to the generated set of events rather than directly to the generation.

The simplest correction required was to the distribution in time. The time period was expressed in terms of run or tape number. Two problems were observed in this parameter. After the initial generation of events, several runs were cut from the analysis stream due to detector problems. The Monte Carlo events were generated prior to the cuts and thus contained generated events over runs that were not used in the analysis. This could cause a systematic effect in the calculation of the acceptance of the detector since a knowledge of the absolute number of events generated was required. A separate study indicated that the effect led to approximately a 1% correction in the absolute acceptances for $\mu^+\mu^-$ and for $\pi^+\pi^-$. Note that this systematic effect cancels completely in the ratio of acceptances.

The second problem was a bit more severe and came about from the observation that the ratio of data events to Monte Carlo events as a function of run number was not reasonably flat. Again, the problem was believed to have arisen because the Monte Carlo events were

generated before the final analysis cuts were chosen. This problem could lead to systematic effects in the acceptances and efficiency calculations. Unlike the previous problem, this systematic would not necessarily cancel out in the calculation of the branching ratio.

Inconsistencies therefore were corrected in the pass 4 analysis. The correction was incorporated as a weight to the events from each run. The weights were obtained by calculating the ratio of Monte Carlo $\pi^+\pi^-$ events to data $\pi^+\pi^-$ events as a function of run number after the final analysis cuts had been applied. The correction distribution was then normalized such that the integral of the weights divided by the number of non-zero weights was 1. This normalization preserved the original number of generated events.

An alternative way of applying the corrections was considered. This method involved normalizing the correction distribution so that the maximum weight was one. In essence, this method works by throwing away, or rescaling with weights less than one, a large number of Monte Carlo events until there is agreement between data and Monte Carlo. This method would have required that the number of generated events be corrected. Since very large numbers of Monte Carlo events were generated, implying an exceedingly low statistical error, the former method was used. The effect of the latter could have been to significantly and needlessly increase the statistical error associated with the Monte Carlo depending on the actual number of events generated.

The next correction involved the distribution of the kaon momentum. Kaons were initially generated with the Skubic distribution. A correction was applied to match the distribution to that which was experimentally observed. The corrections were required since the Skubic distribution was obtained with different materials from those used in E791. It was also obtained at different energies but was adjusted to the energy used in E791 with Feynman scaling. The problem was detected by comparing data and Monte Carlo kaon momentum distributions from $\pi^+\pi^-$ data. A correction was required since a potentially serious systematic effect on the acceptances and efficiencies could occur. The final corrections showed that there was approximately a 1.5% correction to the ratio of acceptances. The bulk of the effect occurred in the $\mu^+\mu^-$ absolute acceptance, while the absolute acceptance for $\pi^+\pi^-$ remained essentially unchanged.

The corrections were applied in the same manner as those from the time distribution. The calculation of the corrections was a bit more complicated. First, a weight was applied to Monte Carlo data that effectively removed the problematic correction to the Skubic. The ratio of Monte Carlo to data events as a function of kaon momentum was obtained. The

distribution was then fit with a 5th order polynomial. The polynomial was normalized such that the integral over accepted momenta was one. Finally, the polynomial was convoluted with the original corrections to the Skubic distribution. This final distribution represented the corrections to be applied to Monte Carlo events on an event-by-event basis. As with the corrections in time, these corrections were calculated after the final analysis cuts had been applied.

This process was complicated by the fact that $\pi^+\pi^-$ data also contained semileptonic events. This required that the Monte Carlo $\pi^+\pi^-$ and semileptonic events be added appropriately before calculating the corrections. As a result, the corrections could only be calculated by completing the entire analysis described in this dissertation without the corrections. The final results were obtained by performing the entire analysis a second time. In addition, the corrections to the kaon momentum distribution were calculated with 1989, 1990 and a combined data set. This allowed a calculation of the systematic effect due to the kaon momentum distribution used in Monte Carlo generation. Finally, although these corrections were not applied at the generation stage, they were completely consistent with the distributions required by the generator.

The parameters in vertex x/z and y/z were determined to be in reasonably good agreement. Consequently, no corrections were made to these parameters. However, they could have been corrected to obtain better agreement between data and Monte Carlo events. Plots of data and Monte Carlo events for several of the generated parameters are shown in figures A.1 through A.6. Except for the distributions in time, which are presented for the 1989 and 1990 runs separately, all plots are for the combined 1989 and 1990 samples. The solid lines represent data $\pi\pi$ and the circles represent Monte Carlo. All of the plotted data have been corrected for K_S^0 contamination. In addition, the Monte Carlo $\pi\pi$ has had the semileptonic background appropriately added. The analysis chapters of this dissertation give a full description of sample identification requirements.

Lastly, although this method was developed as a result of the observation of a problem in the Monte Carlo generation, it could prove useful in an upgrade to E791 (currently underway). A Monte Carlo data set could be created prior to the definition of final analysis cuts. This would require that a significantly larger number of events be generated than needed. When the final cuts are determined, a portion of the Monte Carlo events could be rescaled by discarding events or applying weights until there is agreement between data and Monte Carlo. While this requires a second stage to the Monte Carlo generation, and possibly

significantly more CPU time, there could be a significant reduction in the time required to complete the analysis. Monte Carlo events could be generated during the period prior to a stage of precise analysis. The final stage of generation, or more appropriately de-generation, then represents only a minimal use of CPU time. Implemented properly, this method is entirely equivalent to the current generation scheme.

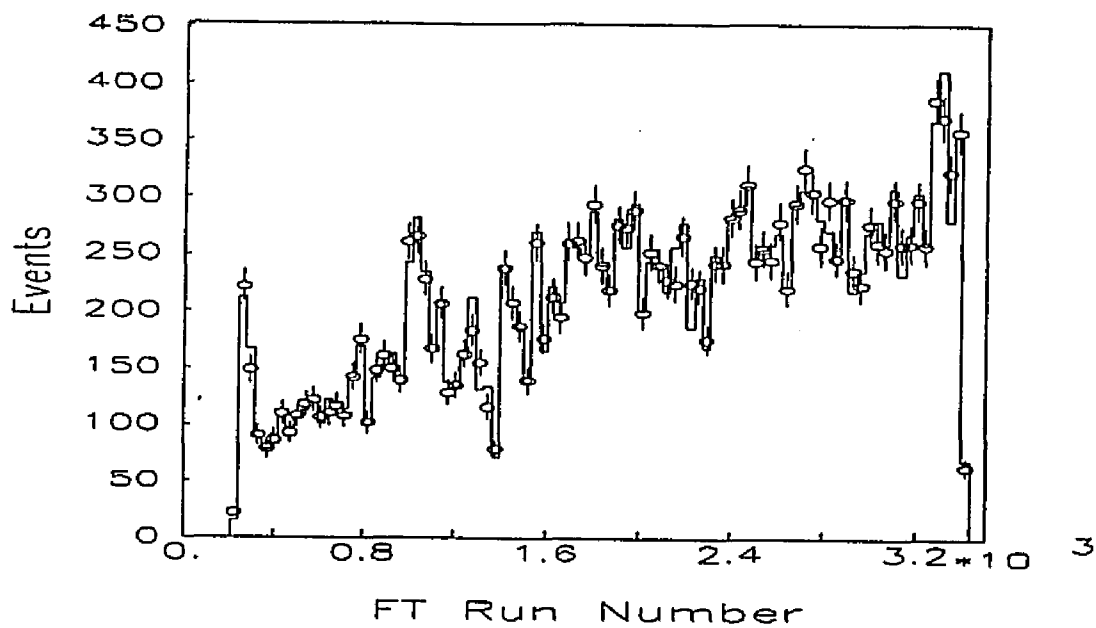


Figure A.1: Data and Monte Carlo $\pi^+\pi^-$ sample as a function of run number in 1989.

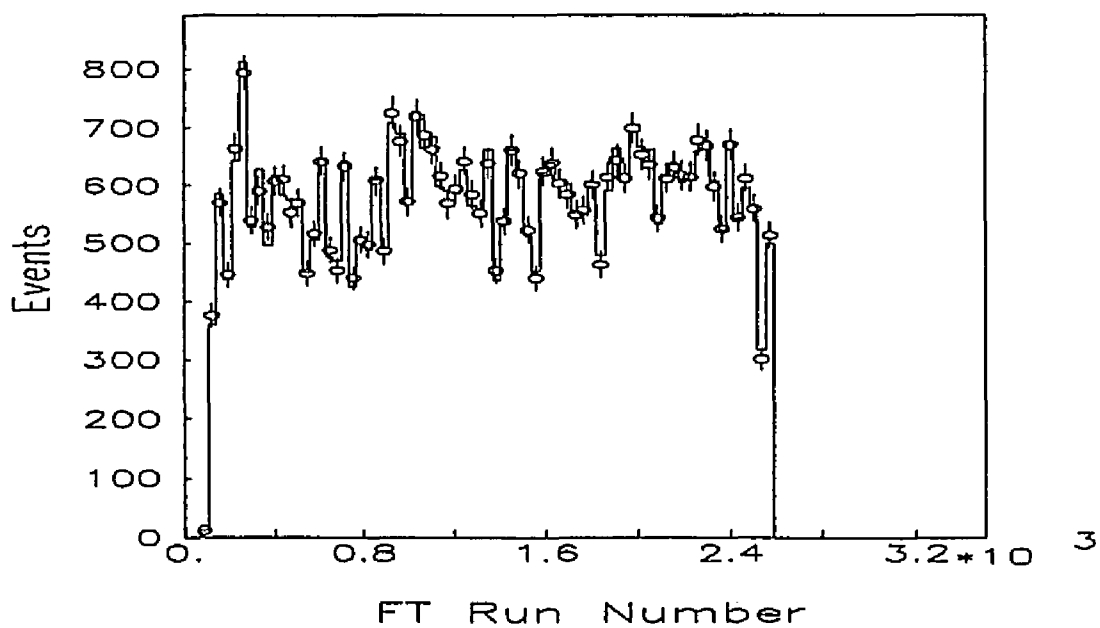


Figure A.2: Data and Monte Carlo $\pi^+\pi^-$ sample as a function of run number in 1990.

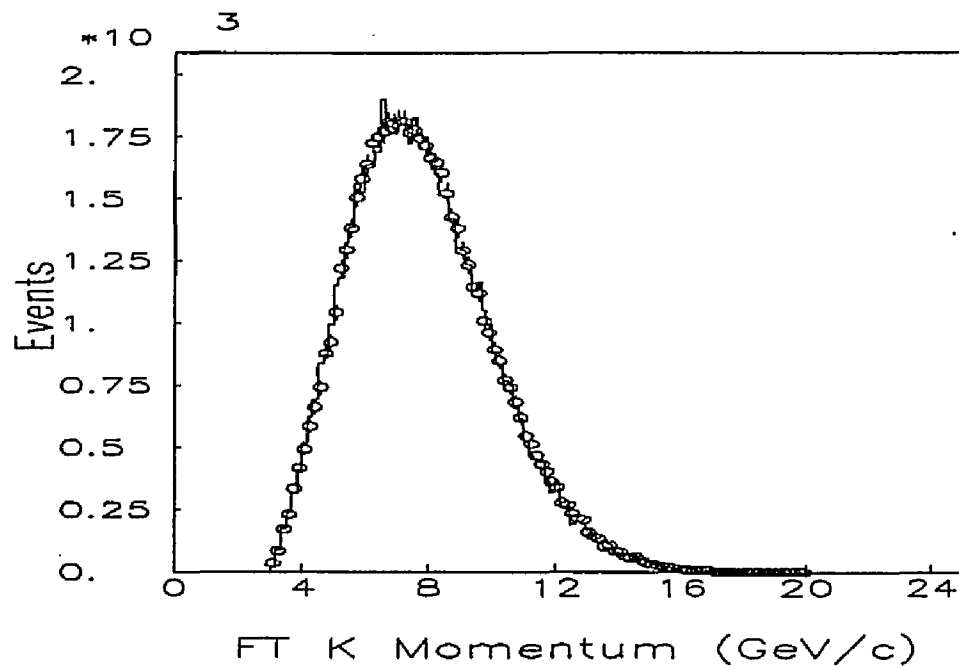


Figure A.3: Data and Monte Carlo $\pi^+\pi^-$ sample as a function of kaon momentum for combined samples.

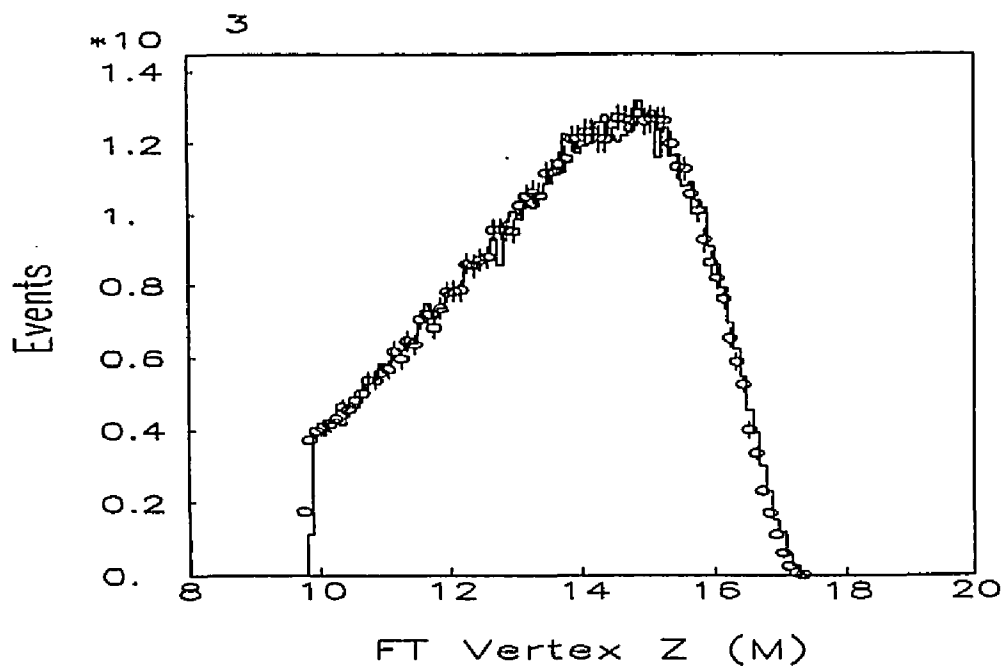


Figure A.4: Data and Monte Carlo $\pi^+\pi^-$ sample as a function of vertex z position for combined samples.

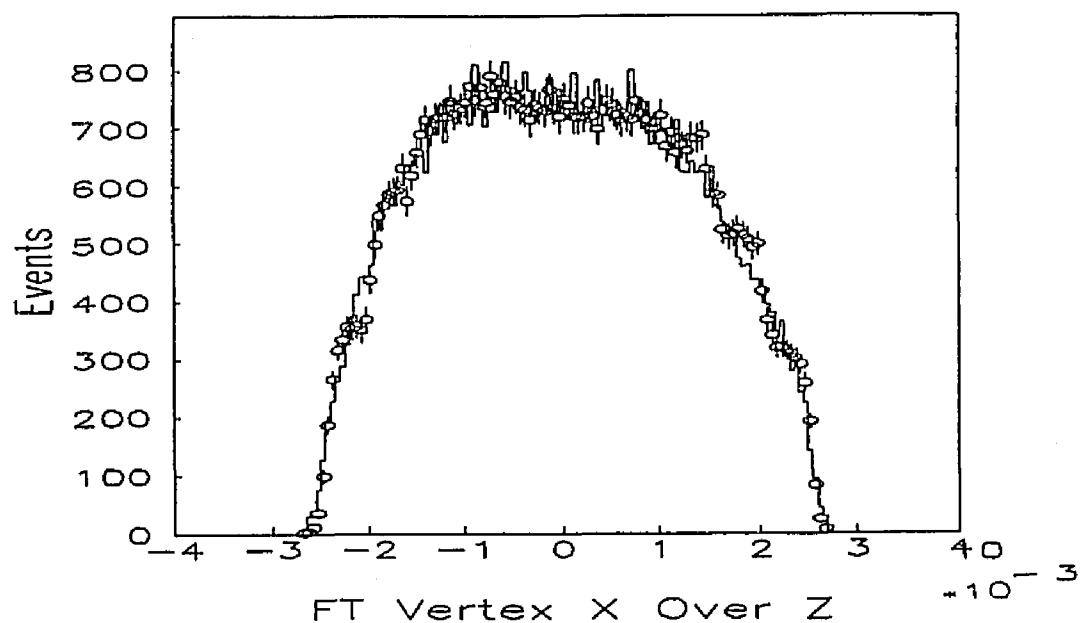


Figure A.5: Data and Monte Carlo $\pi^+\pi^-$ sample as a function of vertex x/z for combined samples.

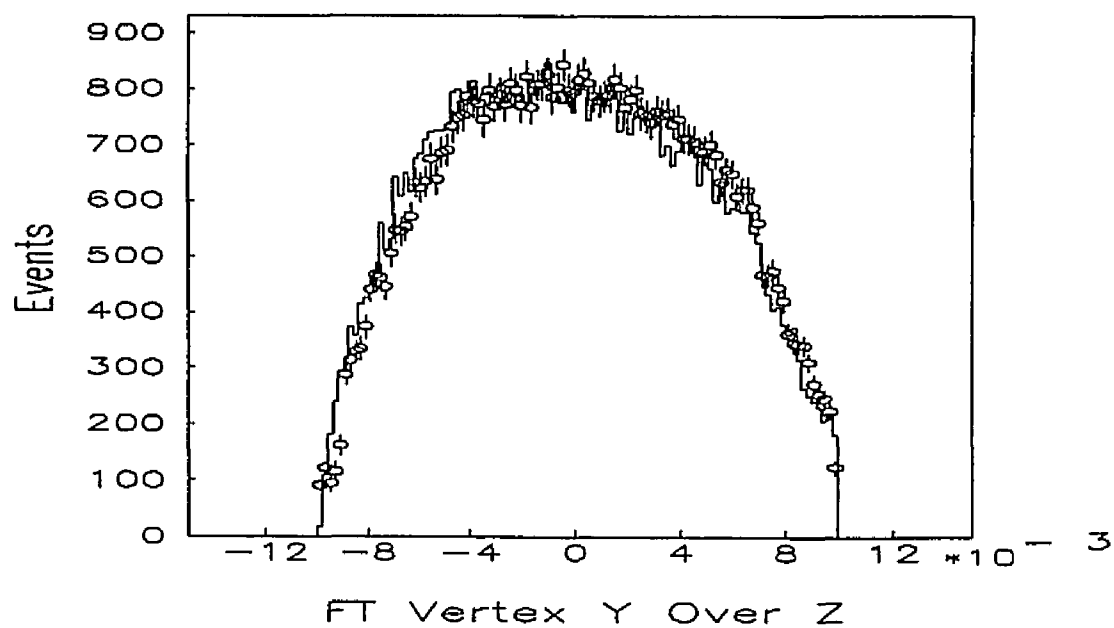


Figure A.6: Data and Monte Carlo $\pi^+\pi^-$ sample as a function of vertex y/z for combined samples.

Appendix B

Correction for K_S^0 Contamination

The vast majority of observed $\pi^+\pi^-$ events was from K_L^0 decays. The distance from the target to the decay volume corresponded to many K_S^0 lifetimes. Nevertheless, a small number of K_S^0 decays could enter the final $\pi^+\pi^-$ sample. The method employed to correct for K_S^0 contamination was actually employed in the pass 4 analysis. Given an event and its lifetime, or, correspondingly, momentum and vertex z position, the probability that the decay originated from a K_L^0 can be calculated. This entire probability of a kaon decaying into two pions as a function of time (neglecting an overall normalization factor) is given by [87]

$$\begin{aligned} \left| \langle \pi^+\pi^- | H | K^0(t) \rangle \right|^2 &\sim e^{-t/\tau_S} + |\eta_{+-}|^2 e^{-t/\tau_L} \\ &+ 2|\eta_{+-}| e^{-(t/2\tau_S + t/2\tau_L)} \cos(\Delta m_K t/\hbar - \phi_{+-}). \end{aligned} \quad (\text{B.1})$$

The three terms, respectively, correspond to the contributions of K_S^0 , K_L^0 , and quantum mechanical interference between the two. τ_S and τ_L are the lifetimes of the short- and long-lived neutral kaon states and Δm_K is their mass difference. The CP violation parameters $|\eta_{+-}|$ and ϕ_{+-} are related to the ratio of decay amplitudes as follows:

$$\eta_{+-} = \frac{\langle \pi^+\pi^- | H | K_L^0 \rangle}{\langle \pi^+\pi^- | H | K_S^0 \rangle} = |\eta_{+-}| e^{i\phi_{+-}} \quad (\text{B.2})$$

The most recent values of the above parameters are listed in Table B.1 [32]. A correction to the interference term was necessary to account for the fact that the strong interactions which produce the beam in E791 produce a small number of \bar{K}^0 's in addition to K^0 's. This "dilution" factor has been measured at AGS energies [88], and can be expressed in terms

Factor	Value
τ_S	$(0.8922 \pm 0.0020) \times 10^{-10} s$
τ_L	$(5.17 \pm 0.04) \times 10^{-8} s$
$BR(K_S^0 \rightarrow \pi^+\pi^-)$	$(68.61 \pm 0.28)\%$
$BR(K_L^0 \rightarrow \pi^+\pi^-)$	$(0.203 \pm 0.004)\%$
$\Delta m_K/\hbar$	$(0.5351 \pm 0.0024) \times 10^{10} s^{-1}$
$ \eta_{+-} $	$(2.268 \pm 0.023) \times 10^{-3}$
ϕ_{+-}	$46.0^\circ \pm 1.2^\circ$

Table B.1: Factors used in calculation of K_S^0 contamination correction.

of the kaon momentum p (in GeV/c):

$$D(p) = 1 - 1.5e^{-0.17p} \quad (\text{B.3})$$

In the corrected form, the interference term in Equation B.1 is multiplied by $D(p)$.

The correction for K_S^0 contamination was applied on an event-by-event basis in the pass 4 analysis. Each data $\pi^+\pi^-$ event was given a weight based on the properly normalized K_L^0 term in equation B.1. All histograms, efficiency grids, and tabulations then used this weight instead of a weight of 1.0. An alternative way of making the correction was considered but was discarded since it has some effect on the semileptonic background events. Nonetheless, it did allow another estimate of the total effect of the correction. In this method the events were not corrected directly but rather corrections were applied to the sum of the number of events. The ratio of this sums to the sum of the weights yielded the expected correction. The overall effect on the $\pi^+\pi^-$ counting reduced the number of events by about 1.1%.

This correction, unfortunately, also applied to the semileptonic background for which it was inappropriate since K_{e3} and $K_{\mu 3}$ decays have no contamination from K_S^0 . This undesired correction was taken into account by applying it to the set of Monte Carlo semileptonic events. Consequently, the semileptonic decays from data and Monte Carlo have been adjusted in an identical manner. This application of an incorrect weight to the semileptonic samples was not expected to cause any bias since the Monte Carlo semileptonic events should have matched the background in the $\pi^+\pi^-$ data sample. The match between data

and Monte Carlo was studied with and without the K_S^0 correction. In both cases data and Monte Carlo events tended to agree, however comparisons without the K_S^0 correction exhibited noticeable differences. This additional necessity to account for undesired corrections in the alternative method formed the decision to make the corrections on an event-by-event basis.

Appendix C

Analysis Cuts

This appendix summarizes the cuts used in the pass 4 production analysis. Since the analysis was performed on six different data sets, the cuts cannot be listed in one simple table. Most of the cuts were identical for each mode, but the exceptions are listed in this appendix. Many of the cuts did not remove the events from the production stream but rather flagged them for later processing. Every event, however, was required to pass the pass 3 production and earlier production stages, or the Monte Carlo generation stage.

The first set of cuts applied to the identification of the data and Monte Carlo modes. Some of the cuts were somewhat redundant since they should have been satisfied by the previous production passes. Nonetheless, they were incorporated to insure a well defined sample and to diagnose any problems with the previous production passes. All events were required to pass PT and one of the QT or FT fitters. Events could not originate from runs deleted from the analysis stream. Data events were required to have the appropriate L1, L3, pass 1, and pass 2 word bits set. The L3 word required that the event passed L3. MB $\pi^+\pi^-$ events were eventually cut from the final sample if they failed L3 but were processed through other cuts so that the efficiency of the L3 trigger could be calculated. Monte Carlo events were required only to have been generated with the appropriate decay products since they were not a direct part of the earlier streams. These initial cuts are summarized in table C.1 and the cuts on run number are listed in table C.2.

The next set of cuts were aperture cuts. These cuts were identical for data and Monte Carlo events. The tracks from kaon decays were required to be within the detector apertures. These cuts were applied to the vacuum region, the vacuum window, the apertures of the spectrometer magnets and the beam center edge of the PbG. The cuts in the regions of

Cut	Data Events	Monte Carlo Events
Pass L1	YES	N/A
Pass L3	YES	N/A
Pass MC mode	N/A	YES
Pass PT	YES	YES
Pass QT or FT	YES	YES
Pass run cuts	YES	YES

Table C.1: Event identification cuts.

Year	Bad Run Number(s)	Problem
1989	5377 7457 → 7509	Severe MRG inefficiency Beam tests, DC's moved without survey
1990	10872 → 10886	DC inefficiency due to bad gas mix.

Table C.2: Runs removed from event stream.

the spectrometer magnets were complex. They were implemented as part of the standard offline code and were referred to as the SWMDCT cuts. They insured that the tracks did not traverse material in the magnets or regions of uncertain magnetic field. In the vacuum region, the vertex x/z and y/z insured that the decay occurred within the solid angle defined by the collimators. The vertex z cut was chosen to eliminate the bulk of K_S^0 contamination. The vacuum window cuts differed for 1989 and 1990. In 1989 they were imposed to reject tracks that traversed the center flange. In 1990, however, the cut insured that the tracks were within the radius of the window. The final aperture cut was at the beam center edges of the PbG. It was discovered that the PbG was a limiting aperture in 1989. A very small number of events could be detected in the other detectors but miss the lead glass blocks. The PbG was moved closer to beam center in 1990 in order to eliminate this problem. A summary of these aperture cuts is given in table C.3. Histograms of Monte Carlo and data events as a function of these cut variables are presented in appendix A and in figures C.1 through C.4. The figures presented in this appendix are for the vacuum window and the PbG inner edge. Other figures, related to these cuts and the Monte Carlo generation quantities, are presented and discussed in chapter 5 and appendix A.

The kinematic quantities, and other quantities calculated with them, were the focus of the next set of cuts. First, events were required to have oppositely charged tracks. Next, the momentum of the tracks was required to be above 1.5 GeV/c. In order to eliminate Λ^0 's, a momentum asymmetry cut on the tracks was introduced. Next a cut on the difference between the front and back momenta of the tracks was implemented for FT only. This cut was an implicit part of the QT track χ^2 cut. Finally, cuts on the track, vertex χ^2 's, mass and colinearity values for FT and QT were also applied. Data and Monte Carlo histograms for these cut variables, after all cuts were applied, are given in figures C.5 through C.18. Unless otherwise indicated, all of the figures in this appendix are of the $\pi^+\pi^-$ data and Monte Carlo samples. Table C.4 summarizes all of these kinematic cuts.

The last set of cuts pertained to particle identification. These cuts were applied to the $\mu^+\mu^-$ and MB samples. The electron requirements were used to identify background to the $\mu^+\mu^-$ sample. In the calculation of the bin MHO and MRG efficiencies, slightly different cuts were used. These are described later in this appendix. There were two cuts common to all of the data samples and one common to data and Monte Carlo. First, all data events were required to have an event time from the DC's within ± 4.0 ns of the time defined by the TSC's. Second, all events were required to have at least two tracks, one in each arm,

Cut	Nominal Value	Data Events	Monte Carlo Events
Vertex z	> 9.75 m	YES	YES
Vertex x/z	< 0.0027	YES	YES
Vertex y/z	< 0.0100	YES	YES
Vacuum window (89)	$z > 0.0019$ m	YES	YES
Vacuum window (90)	$r < 0.4794$ m	YES	YES
SWMDCT	0.5 cm inside	YES	YES
PbG inner x (89)	$z > 0.3032$ m	YES	YES
PbG inner x (90)	$z > 0.2732$ m	YES	YES

Table C.3: Aperture cuts.

Cut	Nominal Value	Data Events	Monte Carlo Events
Track charges	opposite	YES	YES
Track Momentum	$> 1.5 \text{ GeV}/c$	YES	YES
Momentum Asymmetry $(P_+ - P_-)/P_{avg}$	< 0.66	YES	YES
Momentum Match (FT) $(P_F - P_-)/P_{avg}$	< 0.05	YES	YES
Reconstructed mass	± 6.0 of M_K	YES	YES
Colinearity squared	$< 2.0 \text{ mrad}^2$	YES	YES
Track χ^2	< 200 (FT) < 50 (QT)	YES YES	YES YES
Vertex χ^2	< 18 (FT) < 25 (QT)	YES YES	YES YES

Table C.4: Kinematic cuts.

Cut	Nominal Value	Data Events	Monte Carlo Events
PbG Cut	Contour cut	YES	N/A
CER Time	$ t_{cer} < 4.0$ ns	YES	N/A
MHO Confidence Level	> 0.0005	YES	N/A
MRG Gap Difference (actual - expected)	> -3.5	YES	N/A

Table C.5: Particle identification cuts.

from TKC. Except for the later two cut values, these cuts are listed in table C.5. Finally, the PbG cut is a complex cut implemented in the offline code. The cut is made on the values of E/P and E_c/E_t obtained from the PbG. E_c was the energy deposited in the front, or converter blocks and E_t was the total energy deposited in the PbG. The contour of the cut is illustrated in figures C.19 through C.21.

The cuts described thus far allowed for the pass 4 production of $\mu^+\mu^-$ and $\pi^+\pi^-$ events both for data and Monte Carlo as well as for the Monte Carlo semileptonic decay sample. The MB sample is a special set that required slightly different cuts. The MB sample was used to calculate L1 and bin efficiencies for the MHO and MRG. For the L1 efficiency calculation, all of the cuts were identical to the other modes except for the mass and colinearity cuts. The mass cut was made over the region of 380 to 480 MeV/c^2 . The colinearity cut was loosened to 100 mrad^2 . These changes were made in order to obtain a statistically significant sample. Notice that the only way in which the L1 efficiency for $\mu^+\mu^-$ events can be studied is by considering $K_{\mu 3}$ events in which the pion decayed into a muon.

The bin efficiency calculations for the MHO and MRG involved the lower mass and colinearity cuts associated with the L1 efficiency, in addition to slightly different PID cuts. In order to calculate the efficiencies of the muon PID detectors, they must, necessarily,

not be part of the identification of particles. In both the calculation of the MHO and MRG efficiencies, the muon candidate was required to have no hit in the CER $E/P < 0.5$, and a total energy deposited in the PbG less than 1.0 MeV. For the efficiency calculation in the MRG, the additional condition of passing the MHO requirements was imposed.

The final topic of this appendix is the values of the cuts used in the systematic studies. The first set of these are listed in table C.6. Rather than checking systematic effects of the cuts, these divisions were used to diagnose systematic effects as a function of the variable. As can be seen in appendix H, there were no significant dependencies observed. The second set of these, shown in table C.7, are the particle identification cuts for muons. The final set of cuts considered are listed in table C.8. In general, these cuts varied over the range given with identical differences between adjacent cut values. Some of the cuts had a lower value that did not fit into the standard variation scheme. These are also listed in table C.8. An inconsistency in the scheme for the QT track χ^2 divisions was discovered after the analysis was completed. This did not effect the data or results, but did change the final four cut values to 85.0, 88.0, 91.0, and 94.0. These final 4 values are not included in the table since they do not fit in the standard scheme. Finally, the front-back track momentum match cut was made explicitly only for FT implicitly for QT since it was incorporated into the QT track χ^2 , but was studied as an explicit cut for both FT and QT.

Cut Number	Run Number Ranges	Kaon Momentum Ranges (GeV/c)	Vertex z Ranges (m)	Charge Location
1	4243 \rightarrow 5204	2.0 \rightarrow 6.0	9.75 \rightarrow 12.0	All
2	5205 \rightarrow 5842	6.0 \rightarrow 8.0	12.0 \rightarrow 14.0	Inbends
3	5843 \rightarrow 6393	8.0 \rightarrow 10.0	14.0 \rightarrow 15.0	Outbends
4	6394 \rightarrow 6902	10.0 \rightarrow 20.0	15.0 \rightarrow 18.0	N/A
5	6903 \rightarrow 7403	N/A	N/A	N/A
6	10000 \rightarrow 10432	N/A	N/A	N/A
7	10433 \rightarrow 10865	N/A	N/A	N/A
8	10866 \rightarrow 11298	N/A	N/A	N/A
9	11299 \rightarrow 11731	N/A	N/A	N/A
10	11732 \rightarrow 12164	N/A	N/A	N/A
11	12165 \rightarrow 12599	N/A	N/A	N/A

Table C.6: Divisions used in the systematic studies.

Cut Number	MHO Confidence Level Cut	MRG Gap Cut
1	NO CUT	NO CUT
2	0.0001	-0.5
3	0.0050	-1.5
4	0.0010	-2.5
5	0.0050	-3.5
6	0.0100	-4.5
7	0.0500	-5.5
8	0.1000	-6.5

Table C.7: Muon PID cuts used in the systematic studies.

Cut	Lower Value	Upper Value	Delta Value	Number	Additional Lower Cut
Window x (m)	0.0979	0.1169	0.0010	20	NONE
Window r (m)	0.4704	0.4894	0.0010	20	NONE
Mass Center (Mev/c^2)	496.67	498.67	0.10	21	NONE
Mass Window $\pm(Mev/c^2)$	0.50	8.00	0.25	31	NONE
Vertex z (m)	9.00	10.50	0.05	31	NONE
Vertex x/z	0.0017	0.0037	0.0001	21	NONE
Vertex y/z	0.0010	0.0200	0.001	21	0.0001
Low Track Momentum (Gev/c)	0.00	3.00	0.10	31	NONE
Momentum Imbalance	0.01	1.46	0.05	31	-0.06
Front-Back Momentum Match	0.005	0.15	0.005	31	0.0001
Event Time (ns)	0.25	7.50	0.25	31	0.001
PbG Inner x (m)	0.1932	0.3432	0.0050	31	NONE
θ_c^2 ($10^{-6}mrad^2$)	0.10	3.00	0.10	31	0.01
QT Vertex χ^2	1.0	59.0	2.0	31	0.1
FT Vertex χ^2	4.0	33.0	1.0	31	0.1
QT Track χ^2	5.0	83.0	3.0	31	NONE
FT Track χ^2	50.0	350.0	10.0	31	NONE

Table C.8: Cut values used in the systematic studies.

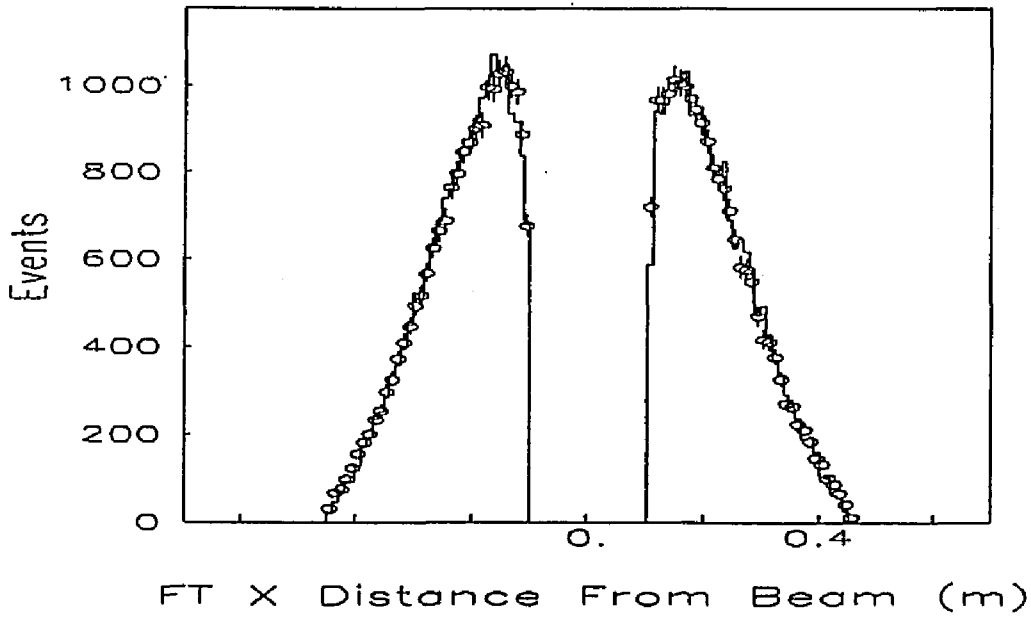


Figure C.1: Data and Monte Carlo histogram as a function of vacuum window cut for 1989.

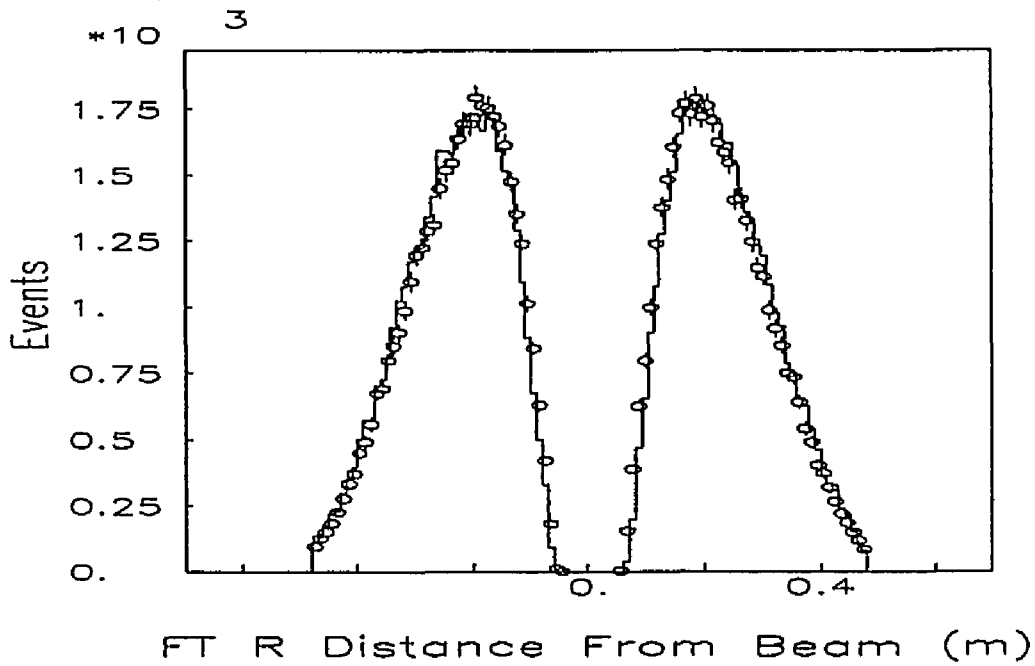


Figure C.2: Data and Monte Carlo histogram as a function of vacuum window cut for 1990.

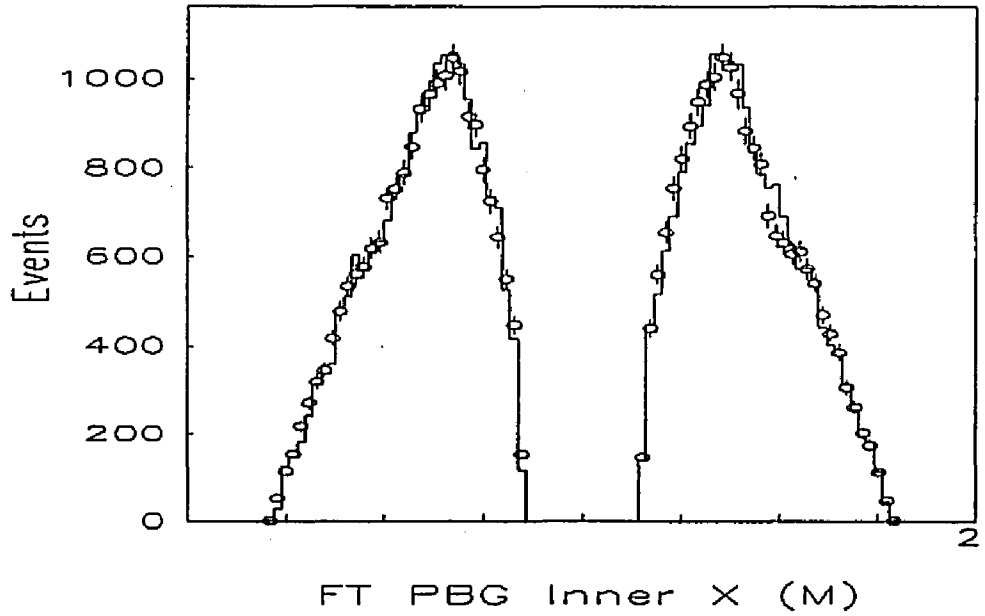


Figure C.3: Data and Monte Carlo histogram as a function of PbG inner x edge cut for 1989.

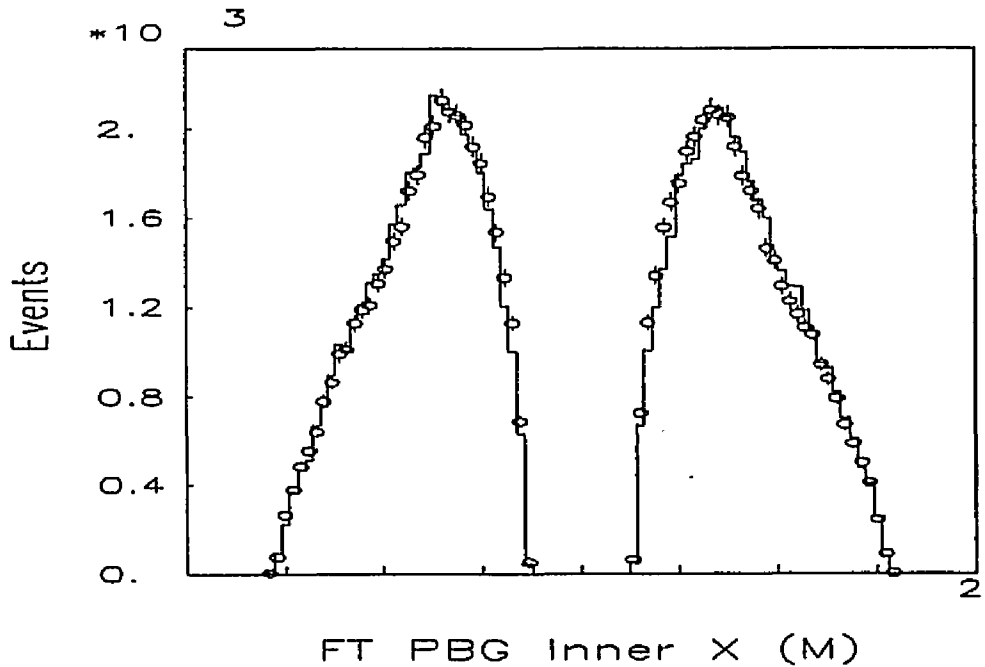


Figure C.4: Data and Monte Carlo histogram as a function of PbG inner x edge cut for 1990.

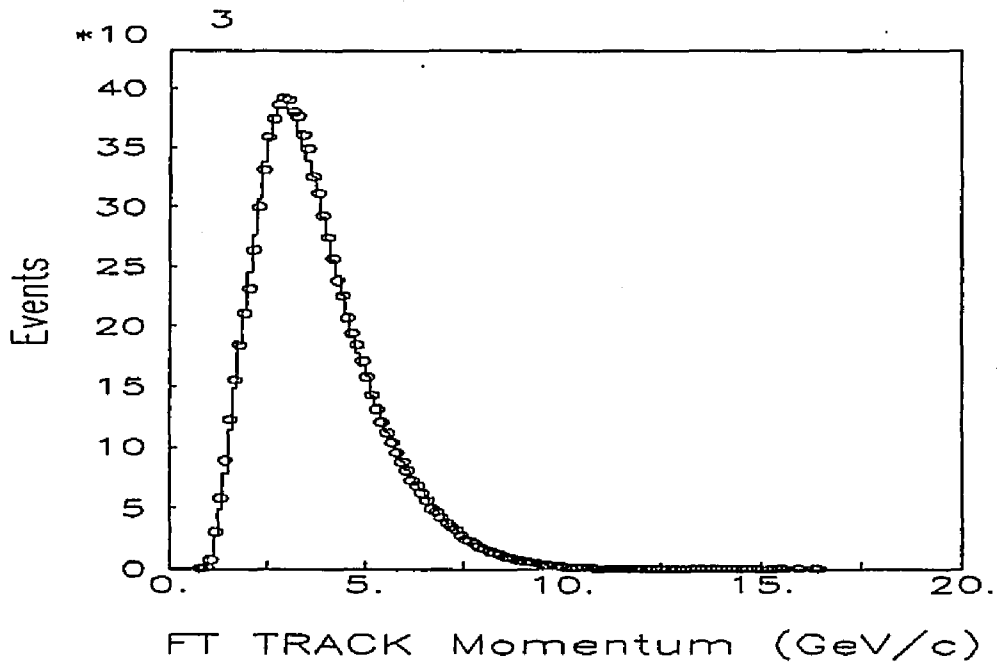


Figure C.5: Data and Monte Carlo histogram as a function of track momentum.

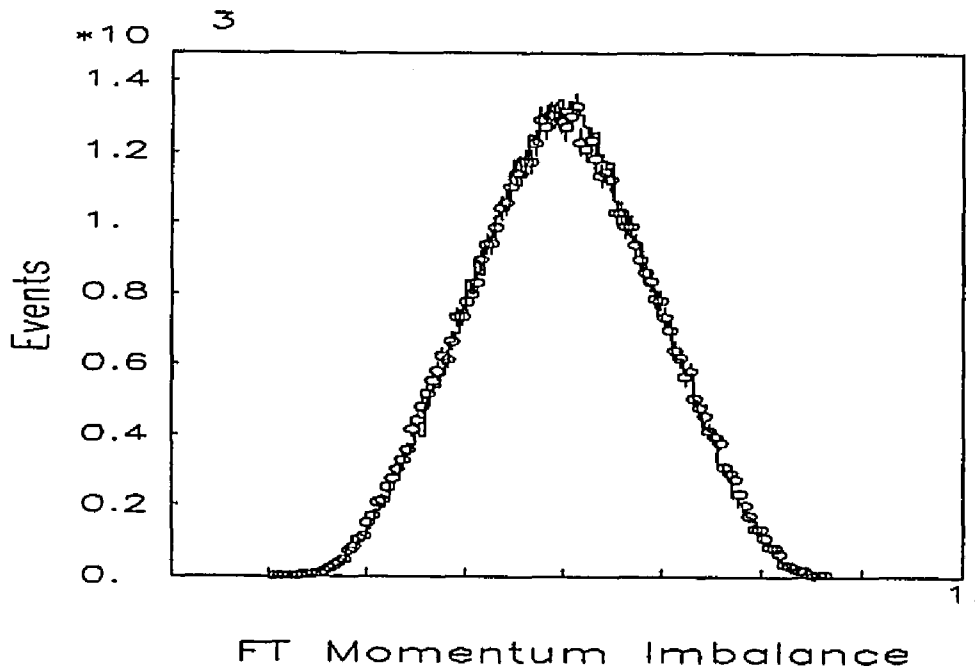


Figure C.6: Data and Monte Carlo histogram as a function of momentum asymmetry.

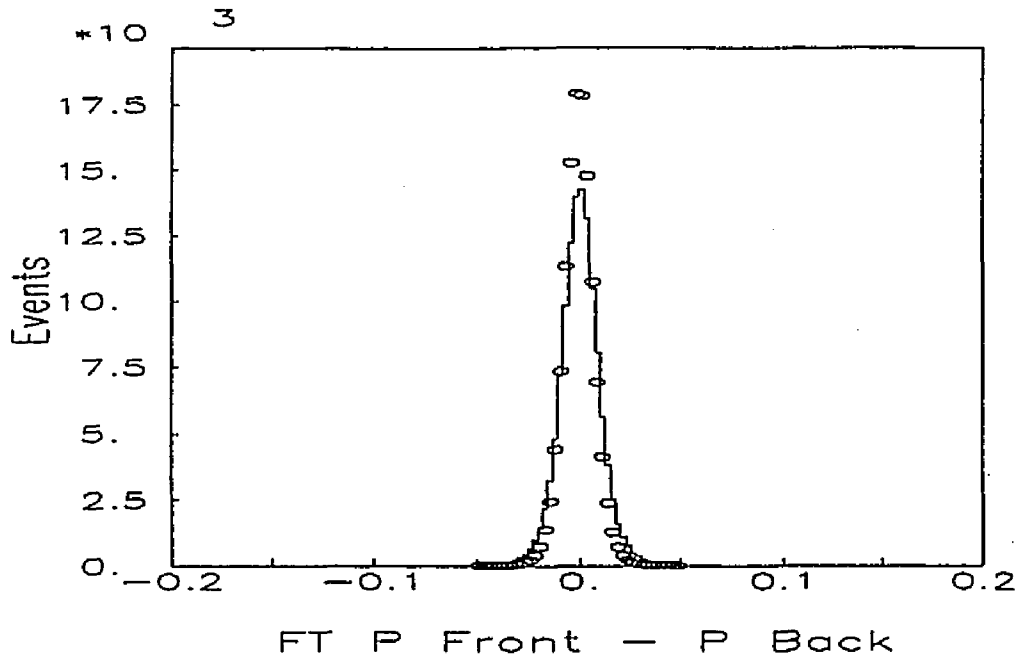


Figure C.7: Data and Monte Carlo histogram as a function of FT $P_F - P_B$ match.

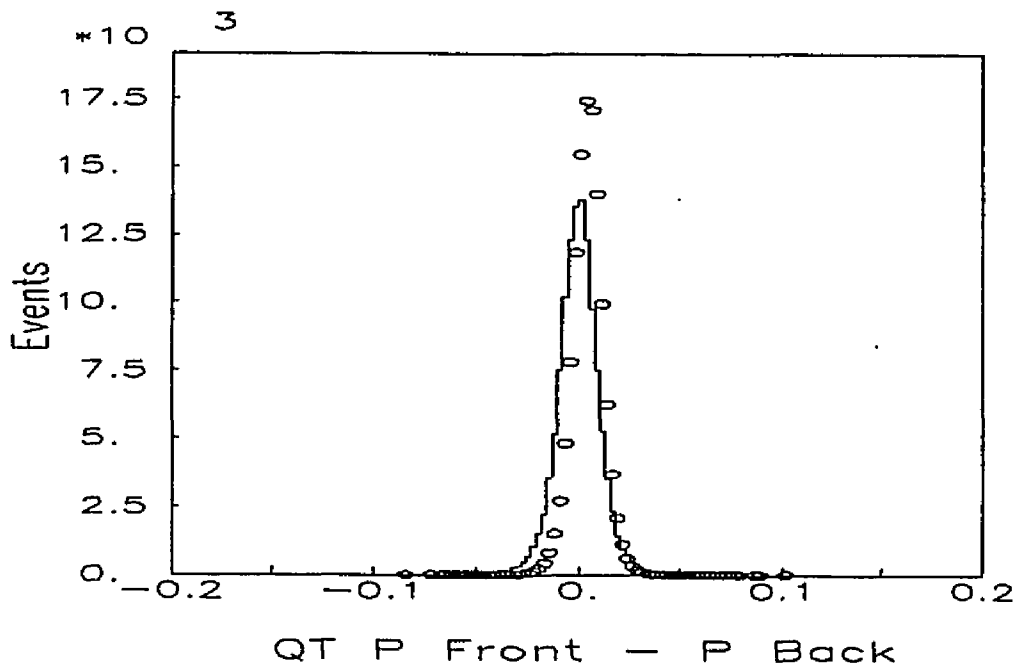


Figure C.8: Data and Monte Carlo histogram as a function of QT $P_F - P_B$ match.

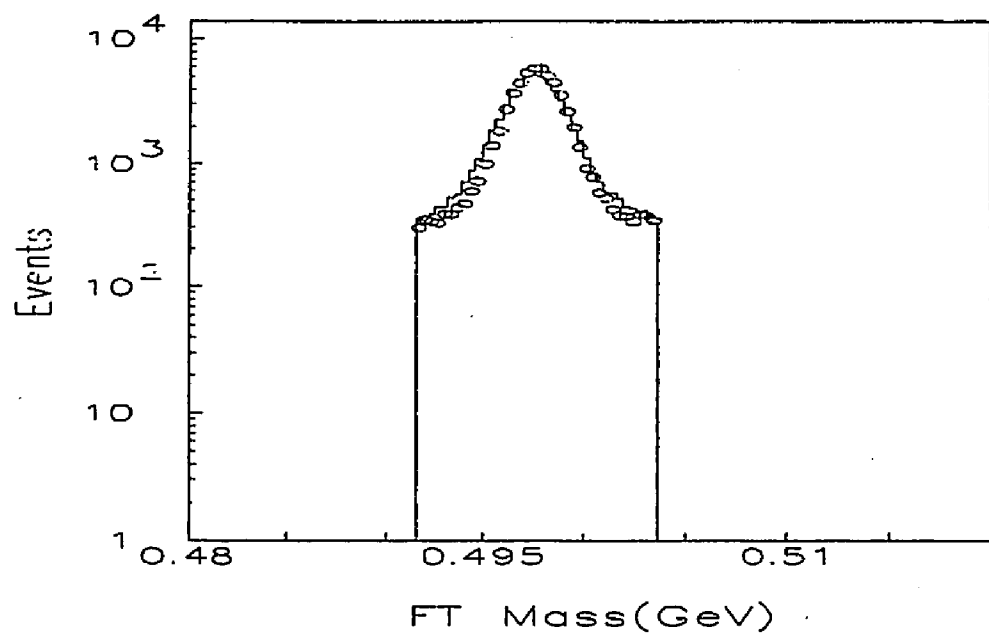


Figure C.9: Data and Monte Carlo histogram as a function of reconstructed mass (with cuts).

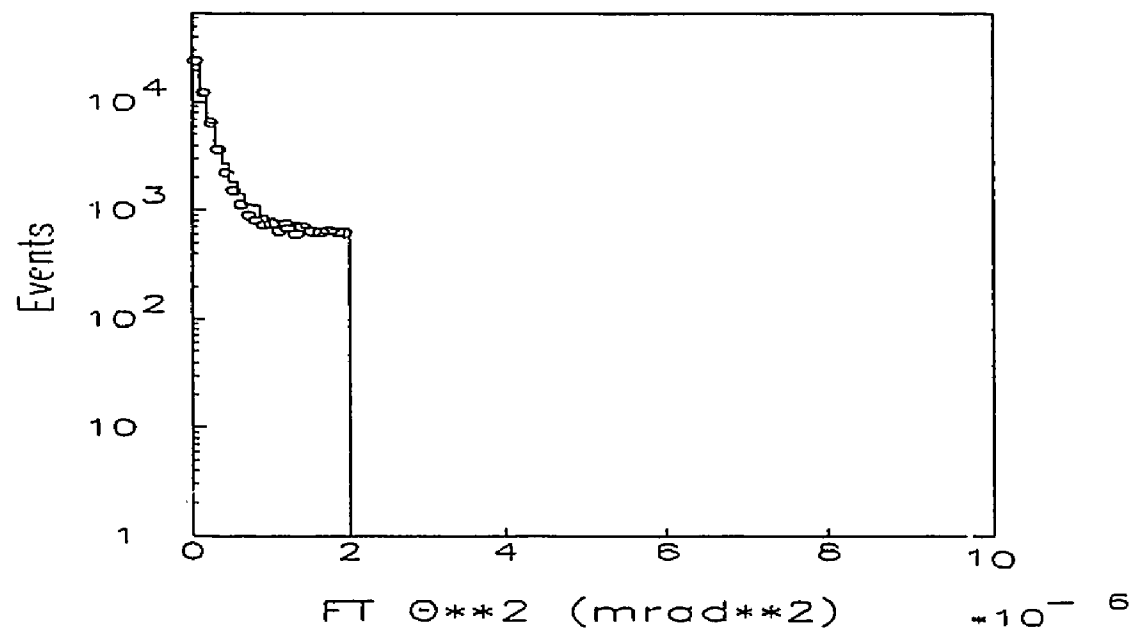


Figure C.10: Data and Monte Carlo histogram as a function of colinearity (with cuts).

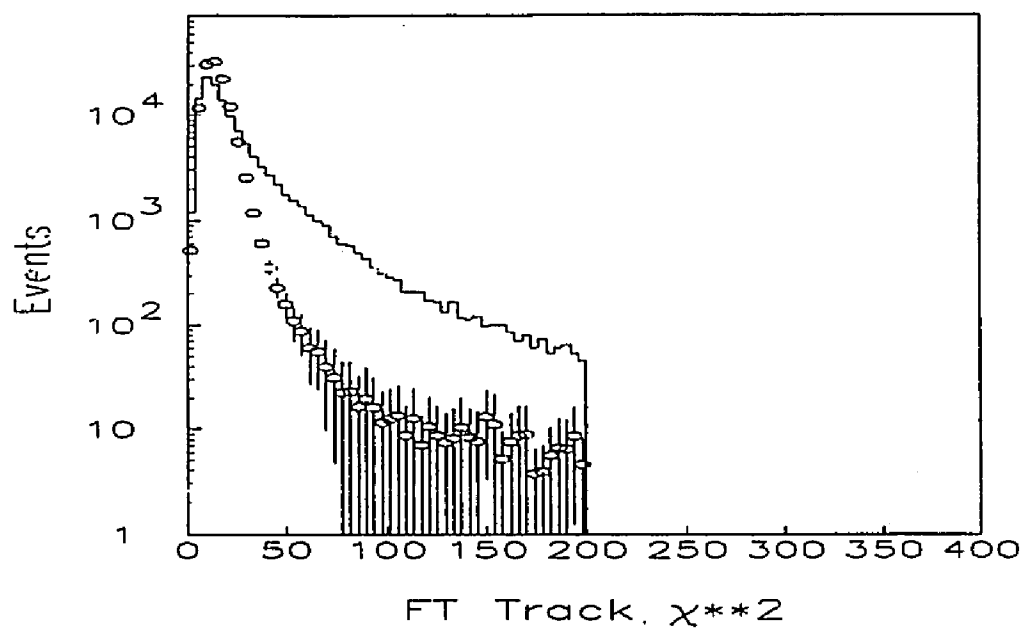


Figure C.11: Data and Monte Carlo histogram as a function of track χ^2 cut (FT).

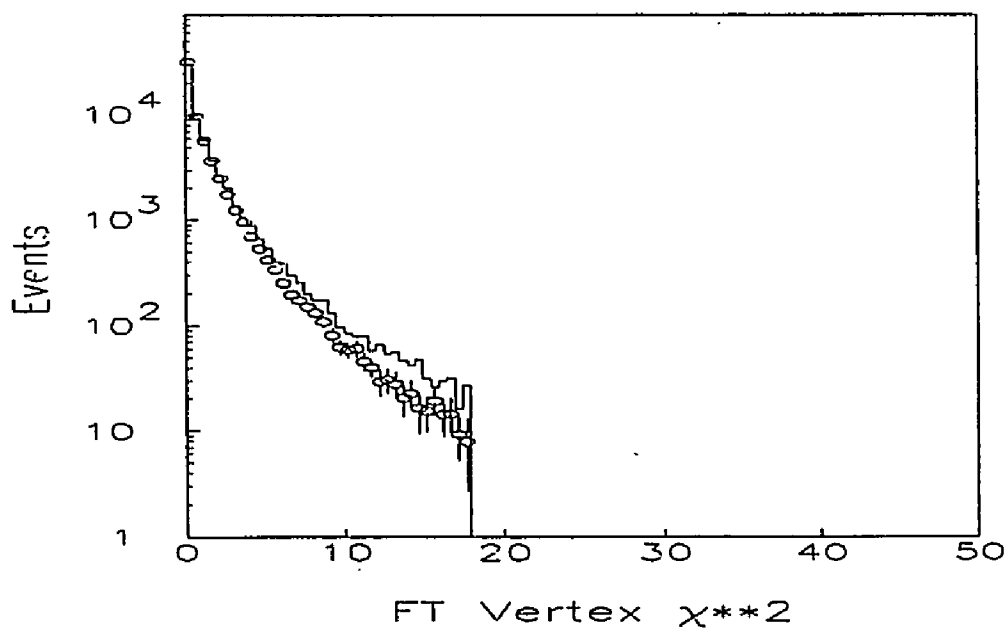


Figure C.12: Data and Monte Carlo histogram as a function of vertex χ^2 cut (FT).

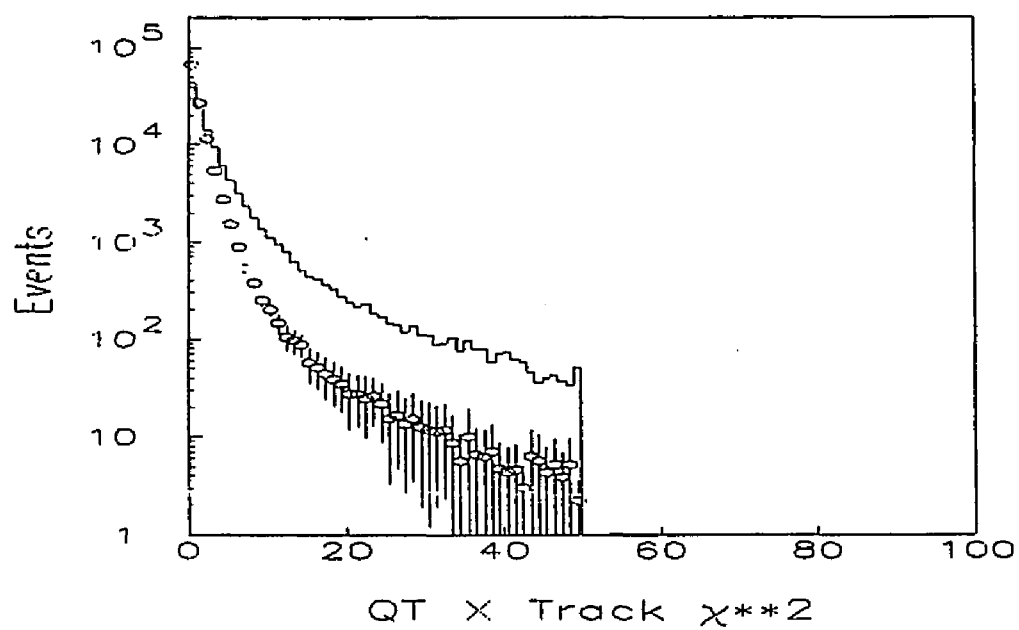


Figure C.13: Data and Monte Carlo histogram as a function of z track χ^2 cut (QT).

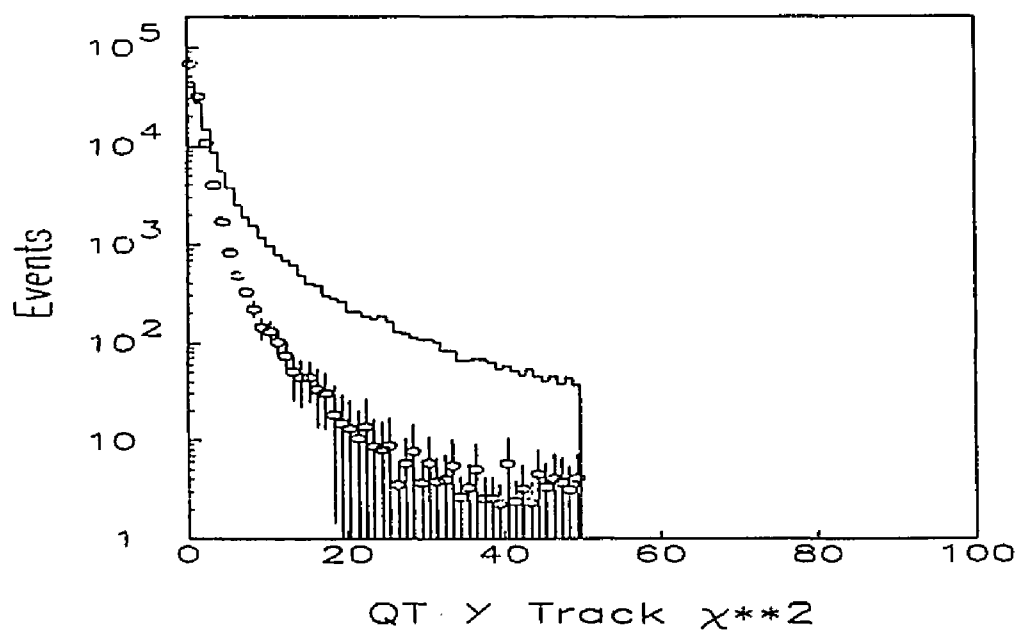


Figure C.14: Data and Monte Carlo histogram as a function of y track χ^2 cut (QT).

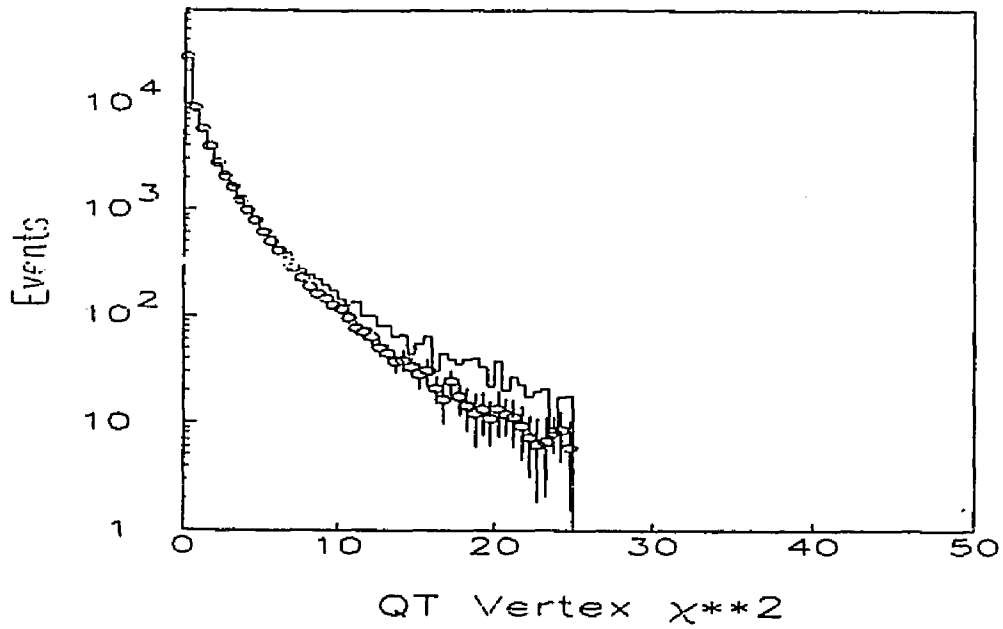


Figure C.15: Data and Monte Carlo histogram as a function of vertex χ^2 cut (QT).

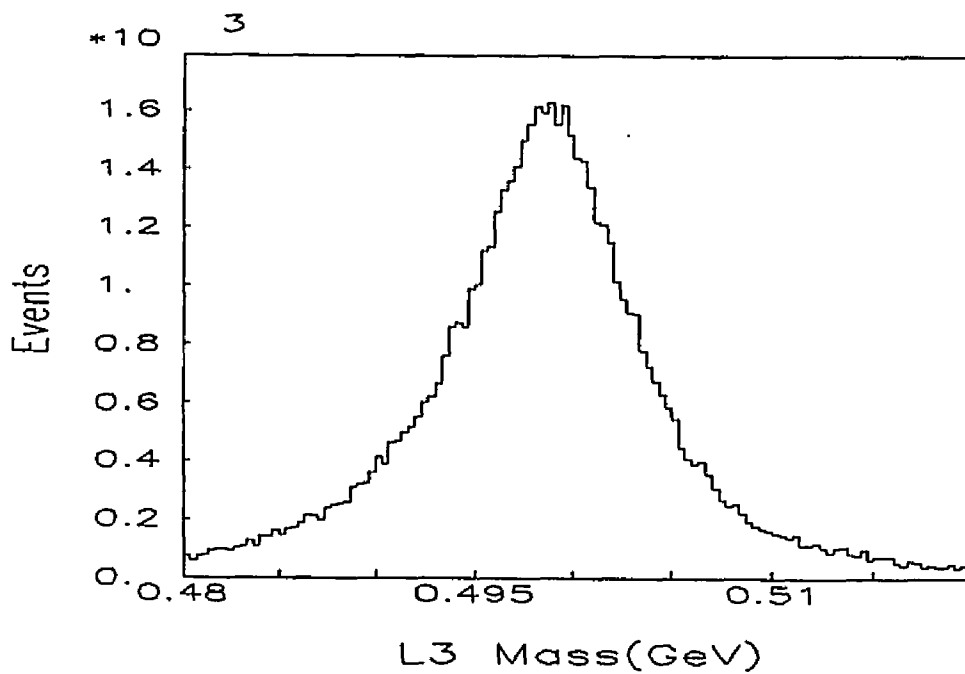


Figure C.16: Histogram of L3 reconstructed mass.

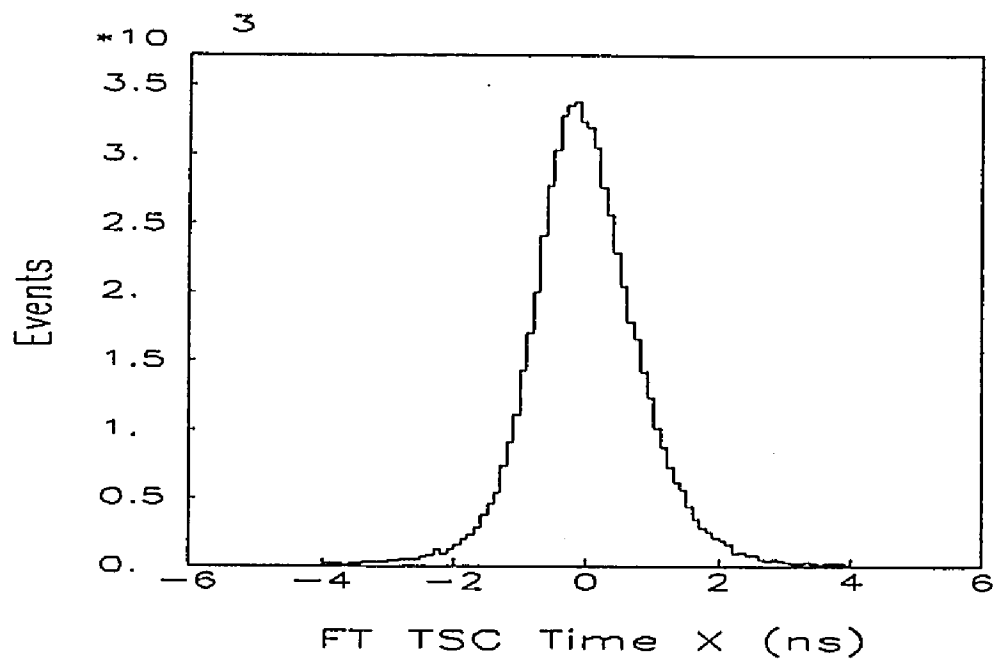


Figure C.17: Histogram of TSC time.

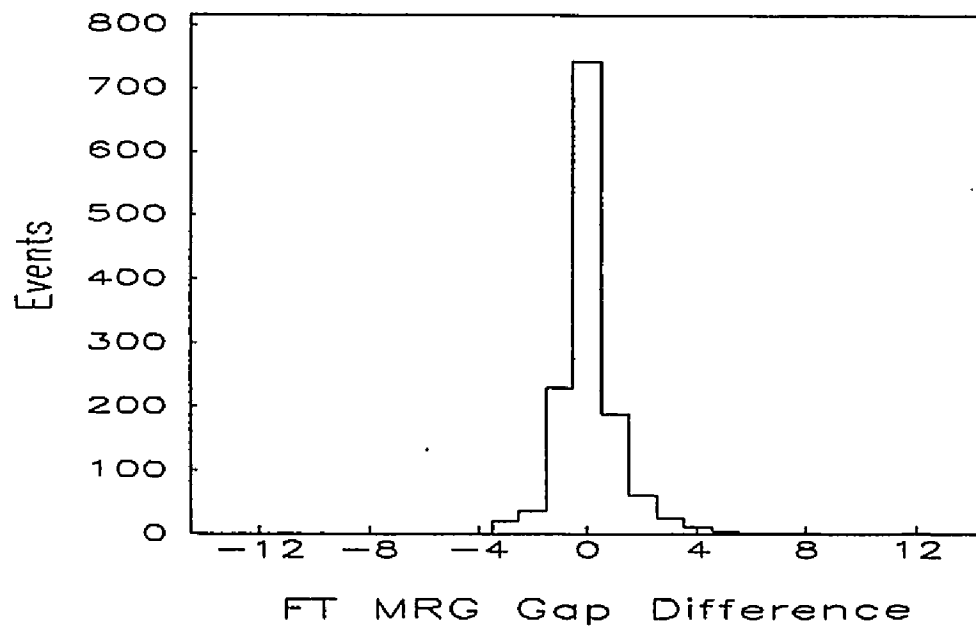


Figure C.18: Histogram of MRG actual-expected cut for the $\mu^+\mu^-$ sample.

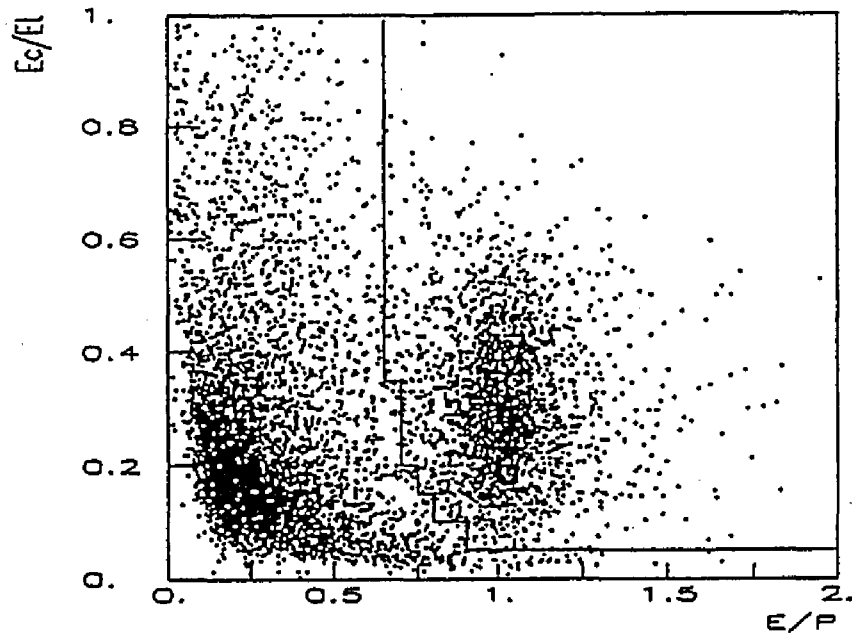


Figure C.19: Illustration of the PbG contour cut. Pions and muons are to the left and below the contour. Electrons are to the right and above the contour.

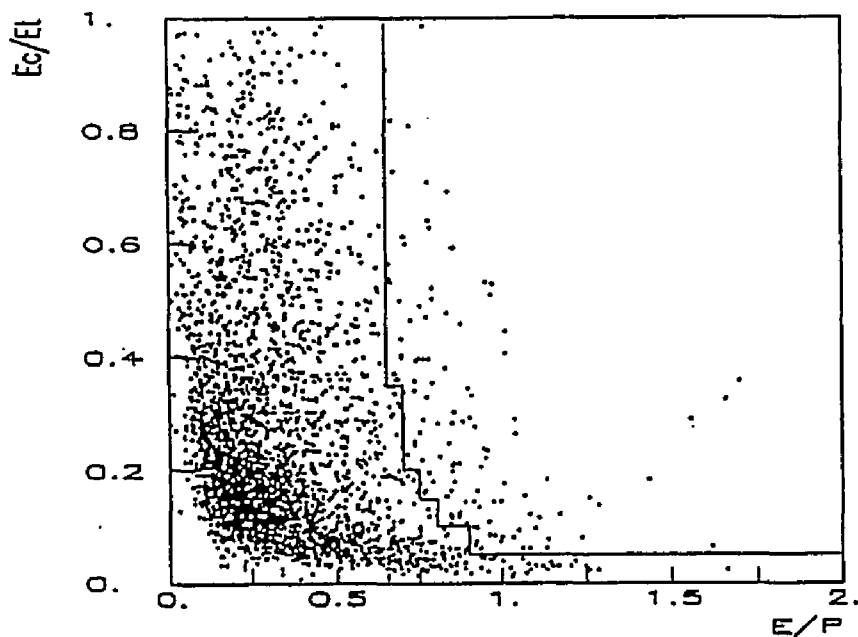


Figure C.20: Illustration of the PbG contour cut for a sample of pions and muons.

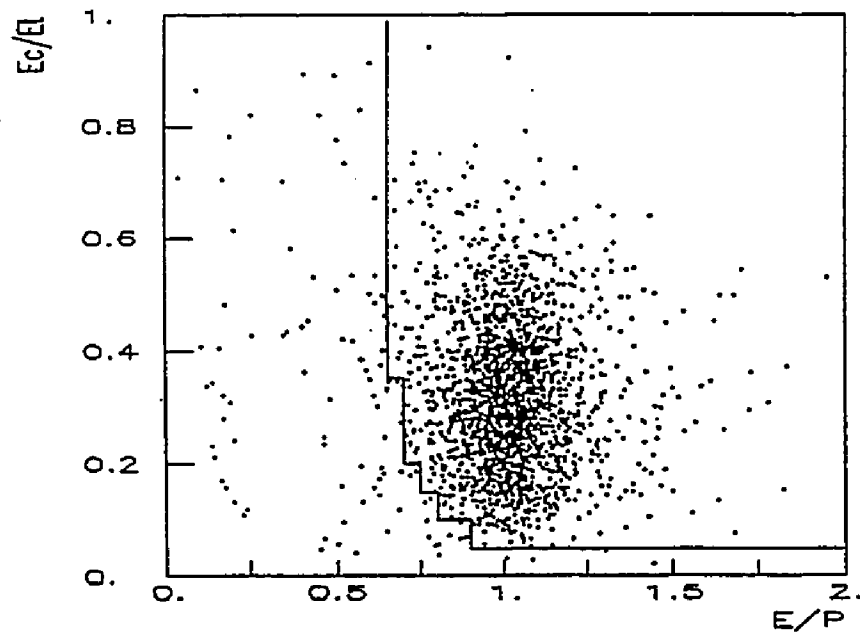


Figure C.21: Illustration of the PbG contour cut for a sample of electrons.

Appendix D

Combination of Data Sets

The 1989 and 1990 data sets could be combined before determining the branching ratio, due to the similarity of the two running periods. The results of the analyses for each year could also be combined by using the method of maximum likelihood. Obtaining combined branching ratios by both of these methods provided a means of cross-checking the results. The branching ratio from 1988 data could be combined with the other two years of data only via the maximum likelihood method, since only the 1989 and 1990 data sets were subjected to a common analysis.

First, consider the problem of combining the 1989 and 1990 data in a fashion consistent with a single running period. The combination of the data and Monte Carlo sets required separate consideration. The combination of the data would appear to be a simple summation of the pass 4 results of the 1989 and of the 1990 running periods. This assumes, however, that prescales, acceptances, efficiencies, etc. were identical, or nearly so, in both running periods. This was not the case, and thus extreme care was needed. The combination of the Monte Carlo sets would also seem to involve similar sums. However, the same problems present in the data sets, as well as different sizes of generated samples for each year forced careful consideration of the Monte Carlo sets.

The $\mu^+\mu^-$ data sample was the easiest set to combine. No prescales were made to this sample and it was used only for counting $\mu^+\mu^-$ candidates and calculating background. Consequently, a simple summation of the data for 1989 and 1990 was sufficient. The $\pi^+\pi^-$ sample was similarly simple for counting purposes. The background subtraction in this sample required combination of the Monte Carlo sample and will be discussed later. From section 8.3 one notes that the signal to background ratio in both running periods was nearly

identical, an initial indication that combination of the data via this method would produce valid results.

The $\pi^+\pi^-$ and MB samples, unfortunately, had different prescales in each year. This difference produced two complications for the combination of data sets. First, after the $\pi^+\pi^-$ sample was combined and background subtracted, the factor needed to determine the number of $\pi^+\pi^-$ events traversing the detector was unknown. This factor, the effective prescale, was calculated by taking the weighted mean of the prescales for each year. Since the signal to background ratio was essentially identical for both years, it did not matter whether the weights were obtained with $\pi^+\pi^-$ counts before or after background subtraction.

The second complication was related to the use of the $\pi^+\pi^-$ and MB sample in the determination of the L1 efficiency and the bin efficiencies for L3, the MHO, and the MRG. Since the prescales were different, an artificial bias toward the year with the lower prescales could be introduced by simply summing the data. For this reason, the set with the lower prescale was rescaled in such a way that both running periods had a common prescale. This rescaling had the effect of increasing the statistical error associated with the data with the lower prescale, but eliminated any potential bias that could have been introduced. After this rescaling, the data samples could simply be summed. Note that the $\pi^+\pi^-$ set was added in different ways for the two different calculations: counting and calculation of the L3 bin efficiencies.

The combination of the Monte Carlo data set presented additional complications. Events were generated according to a distribution that represented the number of kaons produced during each time period (see appendix A). Since different numbers of Monte Carlo events were generated in 1989 and 1990, the solution amounted to determining the relative generation density as a function of time for the combined running periods. Once this density was determined, the samples from each year could be added with an appropriate weight on each. As in the data sample, the weight needed to be less than one since weights greater than one would artificially reduce the error associated with the calculations performed with the Monte Carlo sets.

Efficiencies and acceptances were essentially constant over each period of data acquisition. Consequently, the number of kaons produced at each time interval was directly proportional to the number of $\pi^+\pi^-$ events counted in the same period. There were significant changes in the L3 efficiency, prescales and detector acceptances between 1989 and 1990. In order to determine the correct density for generating Monte Carlo events, a closer

examination is needed of how the density for an arbitrary period was determined.

The number of kaons $(N_{kaons})_i$ produced at an arbitrary time period i is proportional to:

$$(N_{kaons})_i \propto \frac{(N_{\pi^+\pi^-})_i (Prescale)_i}{(A_{\pi^+\pi^-})_i (\epsilon_{\pi^+\pi^-})_{L3,i} (\epsilon_{\pi^+\pi^-})_{int,i} B(K_L^0 \rightarrow \pi^+\pi^-)_i}. \quad (D.1)$$

Since the efficiencies, acceptances and prescales vary for each mode as well as each time period, the numbers of $\pi^+\pi^-$ and $\mu^+\mu^-$ events to generate at each time period are proportional to:

$$(N_{\mu^+\mu^-})_i \propto (N_{kaons})_i (A_{\mu^+\mu^-})_i (\epsilon_{\mu^+\mu^-})_{L1,i} (\epsilon_{\mu^+\mu^-})_{L3,i} (\epsilon_{\mu^+\mu^-})_{PID,i} \quad (D.2)$$

$$(N_{\pi^+\pi^-})_i \propto (N_{kaons})_i (A_{\pi^+\pi^-})_i (\epsilon_{\pi^+\pi^-})_{L3,i} (\epsilon_{\pi^+\pi^-})_{int,i} \left(\frac{1}{Prescale} \right)_i \quad (D.3)$$

Notice that if all the factors, except the number of observed $\pi^+\pi^-$ events, were identical, as they were for the individual running periods, both densities are simply proportional to the number of observed $\pi^+\pi^-$ events.

The number of $\pi^+\pi^-$ and $\mu^+\mu^-$ events generated during any time interval for each running period was known. Changing the proportionality to an equality by the introduction of a constant β and substituting the known values into equations D.1, D.2, and D.3, yielded two equations and two unknowns for each mode. The solution of these equations gave values of β which represented the factors by which the Monte Carlo data sets needed to be multiplied in order to sum them. Since it was desirable to weigh only one data set and to use a weight less than one, the β 's were multiplied by overall factors to meet these criteria.

Finally, the Monte Carlo semileptonic decay sample was also combined. The acceptances and absolute number generated were not known for this mode. Since this set was used only for background subtraction in the $\pi^+\pi^-$ sample, and the events were similar to $\pi^+\pi^-$ events, this set was combined in an identical manner to the Monte Carlo $\pi^+\pi^-$ set. This procedure assumed that the acceptances for semileptonic events were directly proportional to the acceptances for $\pi^+\pi^-$ events, with the constant of proportionality being identical for both running periods. It also assumed that the number generated at each time period was also directly proportional to the number of events satisfying the $\pi^+\pi^-$ criteria divided by the generation density for each time period.

The second method to combine the results was the method of maximum likelihood. This procedure is described in detail in many books on statistics and will not be presented in detail[89]. The challenge in this combination was to construct a likelihood function with all

of the smearing from the various errors incorporated. The simplest way to do this was to run a Monte Carlo program.

The program involved two main loops. First, it looped over a number of possible branching ratios. The upper and lower limits on these were determined empirically. These limits needed to encompass a large enough range so that the error on the combined results could be calculated from the constructed likelihood functions. Secondly, at each branching ratio the program looped over a number of possible experiments. This number was large, on the order of 10,000, in order to eliminate statistical error associated with the Monte Carlo.

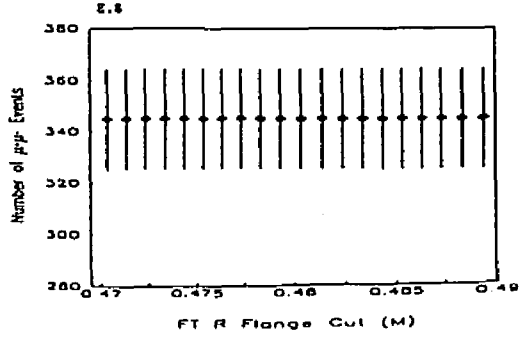
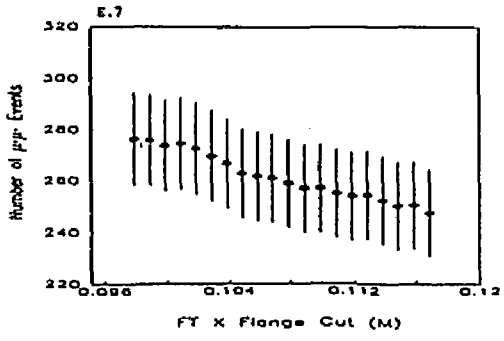
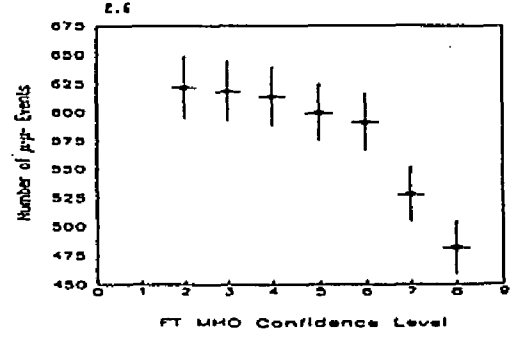
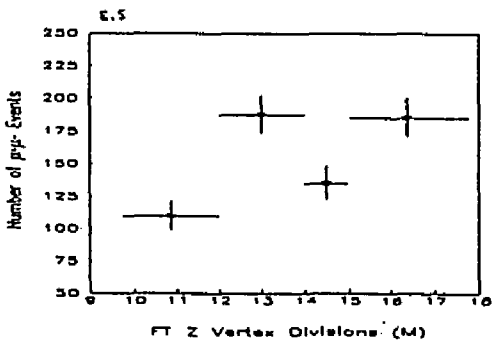
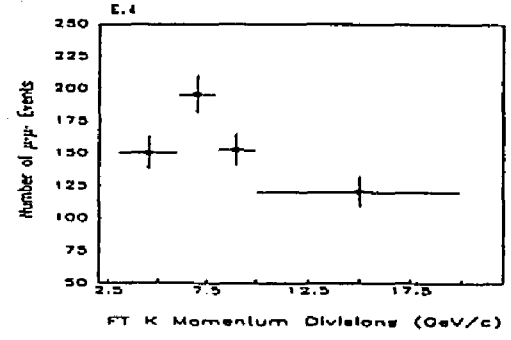
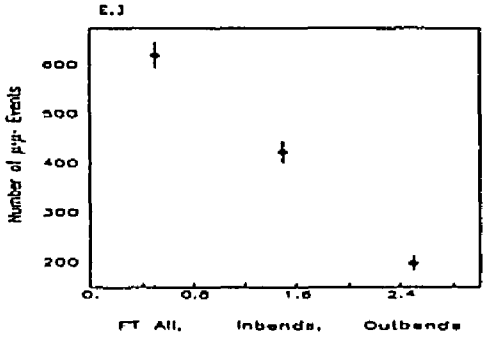
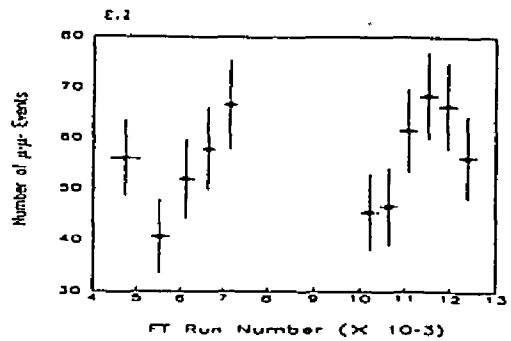
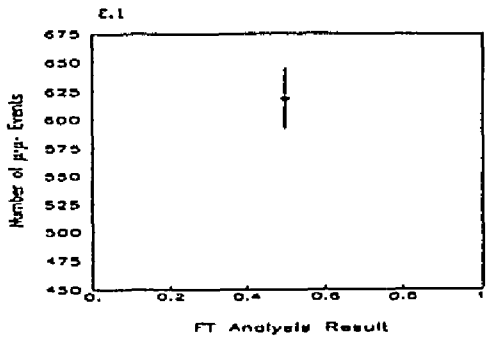
The second loop calculated the number of $\mu^+\mu^-$ events to which the branching ratio in the initial loop corresponded. This calculation was done by using the values of the contributions to the branching ratio, described in chapter 8, modified by adding in the associated error multiplied by a factor obtained randomly from a standard normal distribution. This number of $\mu^+\mu^-$ events was then assumed to be the mean of a Poisson distribution. The probability that the number of physically observed $\mu^+\mu^-$ events corresponded to a Poisson distribution with this mean was then calculated. This probability also corresponded to the probability that the actual branching ratio was the one in the initial loop but that the observed one was the measured value. A large number of cycles in the second loop was required in order to reduce the error on the mean of this probability.

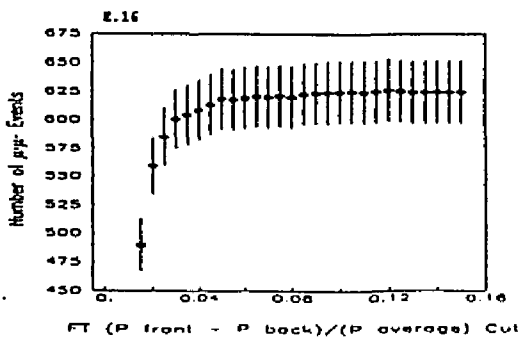
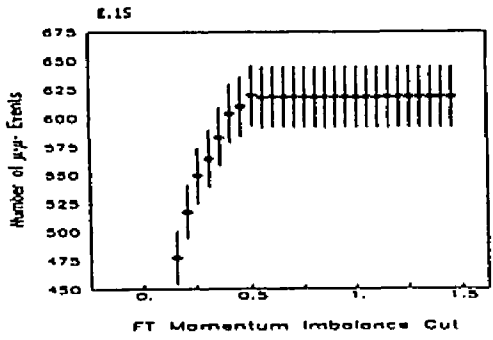
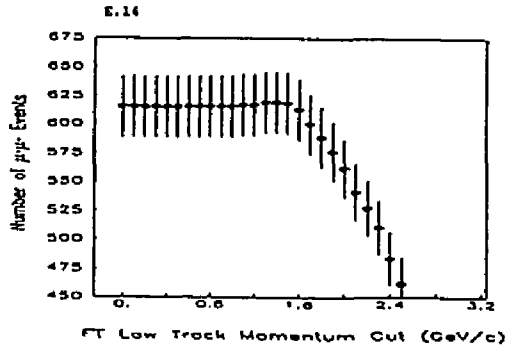
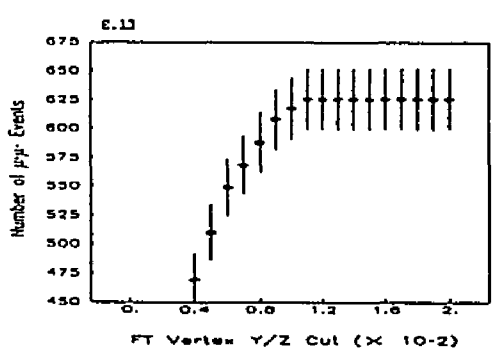
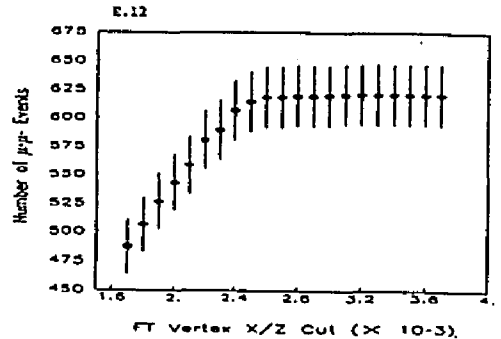
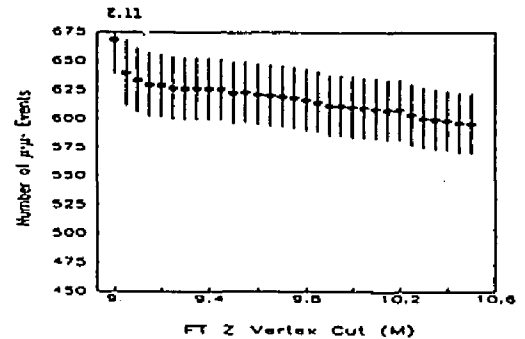
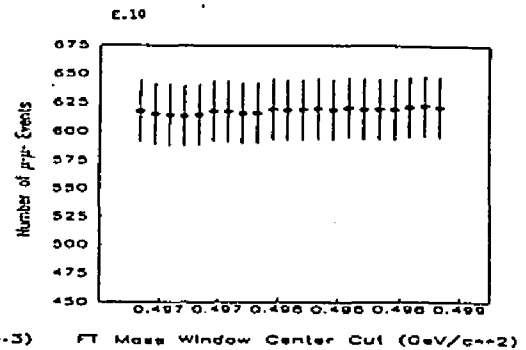
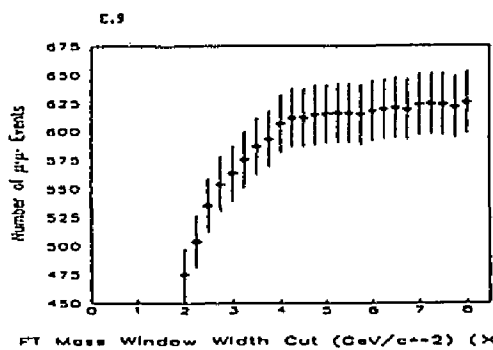
After the range of considered branching ratios was looped over, likelihood functions for the 1988, 1989 and 1990 branching ratios were generated. From these, the likelihood functions for combinations of 1989 and 1990, or all three running periods were constructed. This maximum of logarithm of this function, gave the most likely value for the combined branching ratios. The integral of the likelihood function was used to determine the error associated with the most likely value. This error was defined such that the region within one σ of the most likely value contained the same amount of likelihood, or probability, as that contained within one σ in a Gaussian.

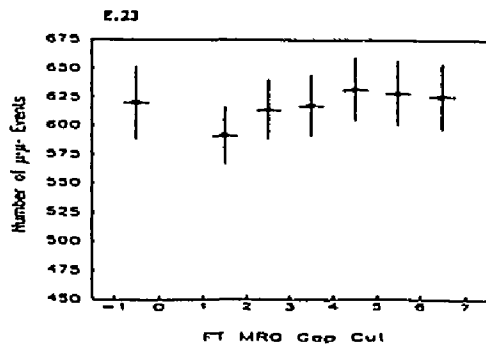
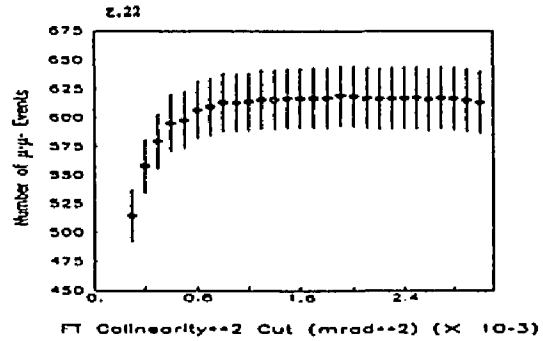
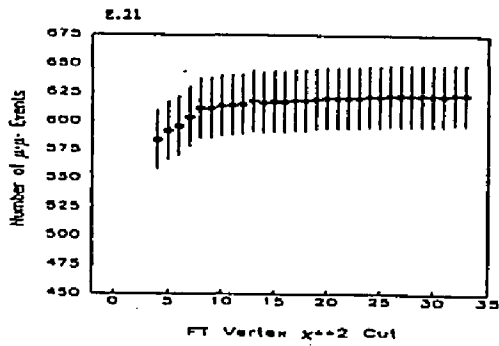
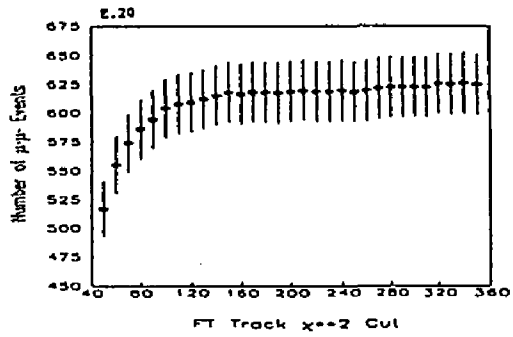
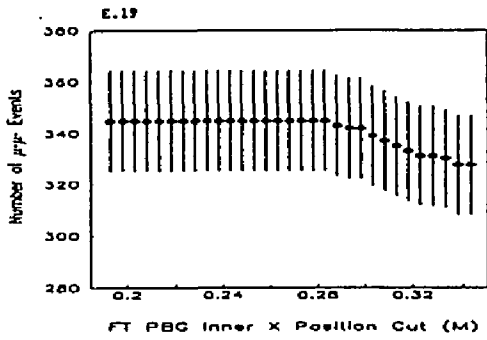
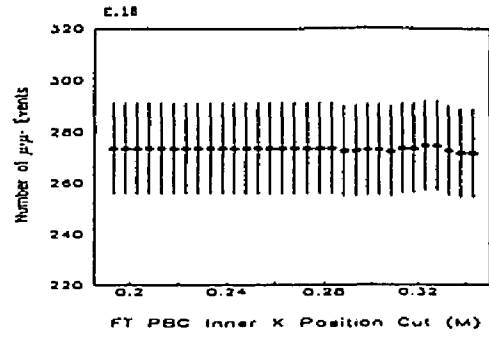
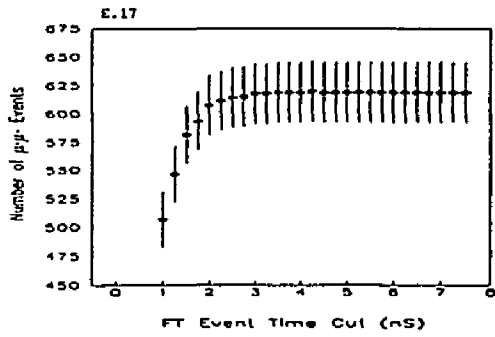
Appendix E

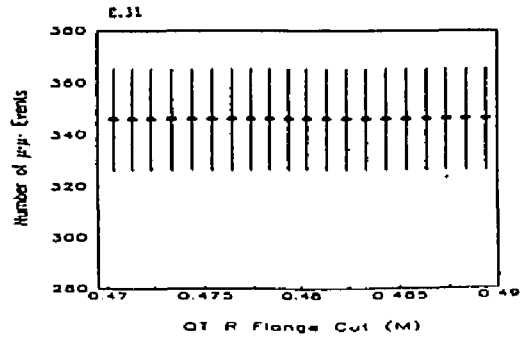
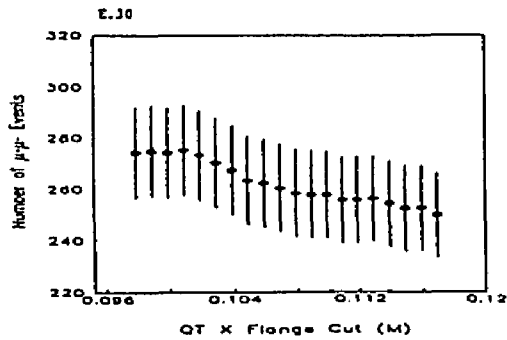
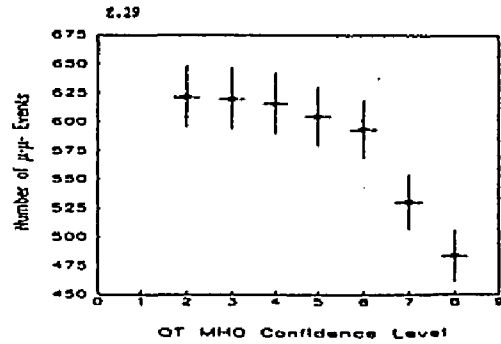
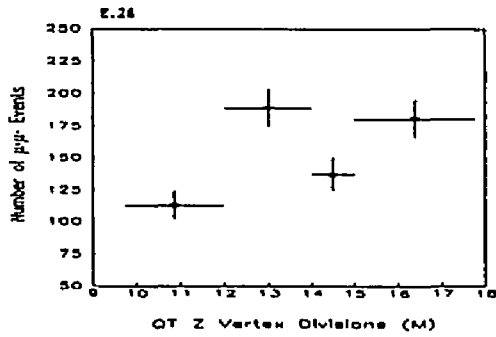
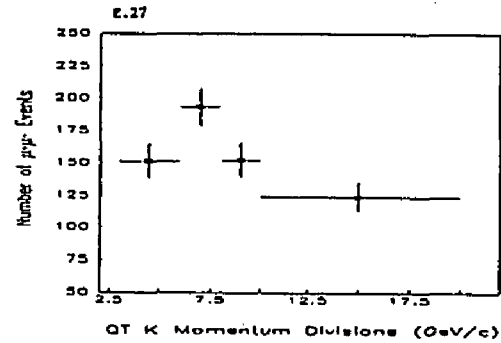
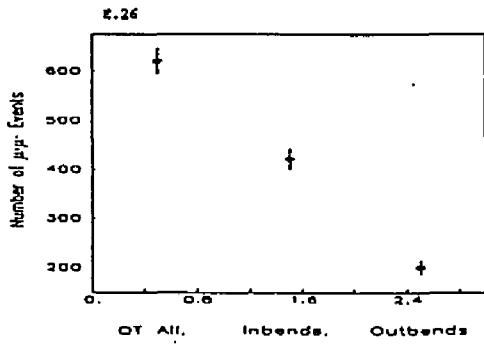
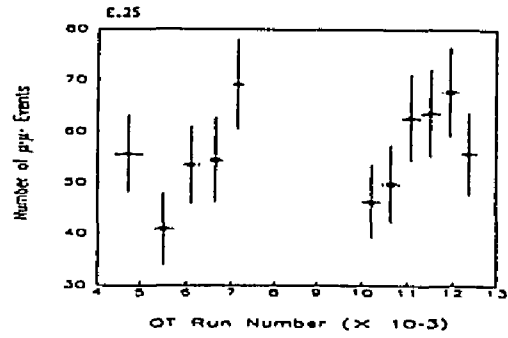
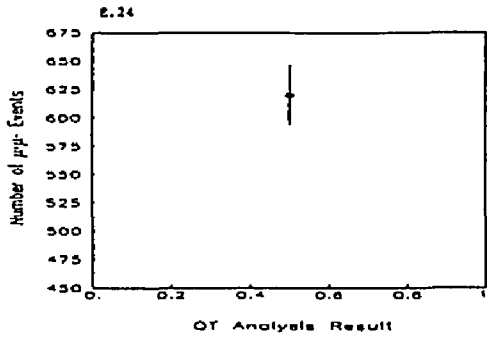
$\mu^+\mu^-$ and $\pi^+\pi^-$ Systematic Studies

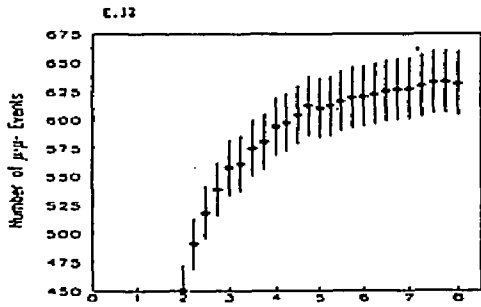
The $\mu^+\mu^-$ and $\pi^+\pi^-$ counting was done as a function of the cut values listed in appendix C. The results of the counting for the nominal values of the cuts were presented in chapter 8. This appendix presents results, as graphs, for all of the other cut values for the combined 1989 and 1990 samples. Although very similar, results from both QT and FT are presented for completeness. The set for the $\pi^+\pi^-$ sample contains plots for the MRG and MHO cuts. These cuts were not applied to the $\pi^+\pi^-$ sample and are included only for completeness and ease of location of similar plots in other appendices. Each plot contains sufficient information for identification of its contents. The figure number appears on the upper left hand corner of each plot and the accompanying caption for each of the figures can be found in the list of figures section at the beginning of this dissertation. Finally, the individual values and errors on each plot are correlated. Each uses identical samples but slightly different cuts as indicated.



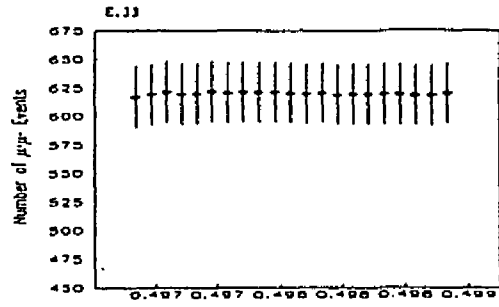




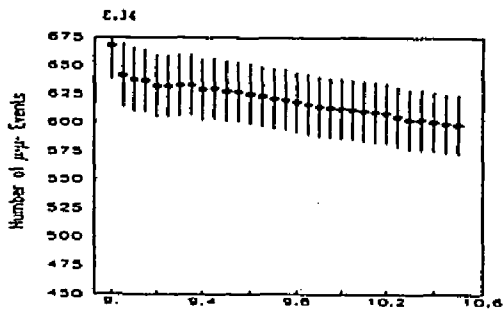




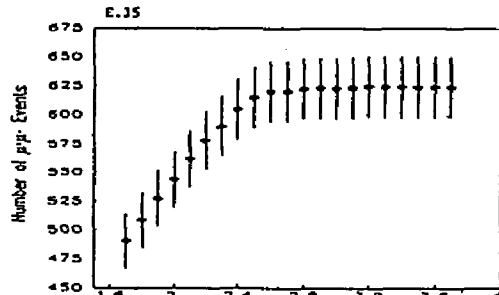
E.32 QT Mass Window Width Cut (GeV/c⁺⁺²) ($\times 10^{-3}$)



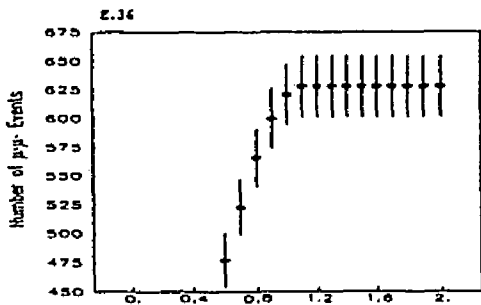
E.33 QT Mass Window Center Cut (GeV/c⁺⁺²)



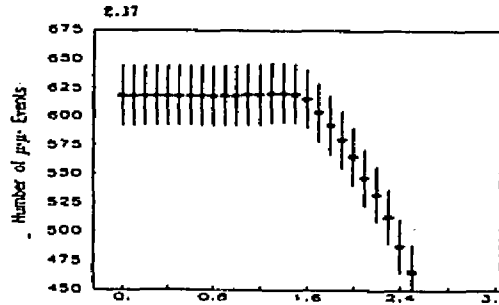
E.34 QT Z Vertex Cut (M)



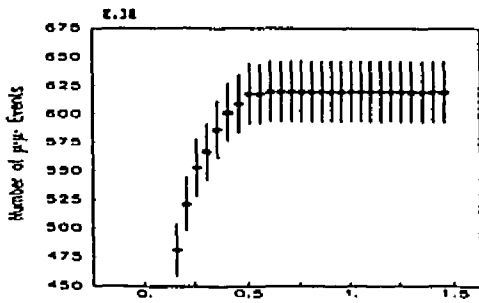
E.35 QT Vertex X/Z Cut ($\times 10^{-3}$)



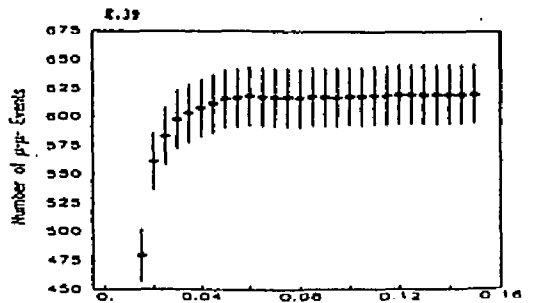
E.36 QT Vertex Y/Z Cut ($\times 10^{-2}$)



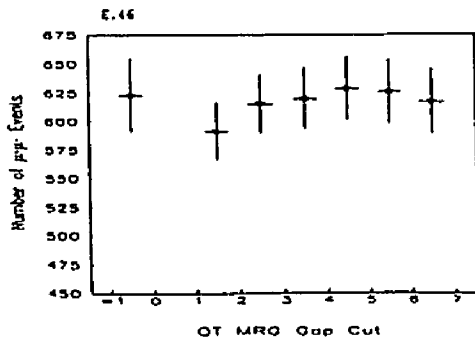
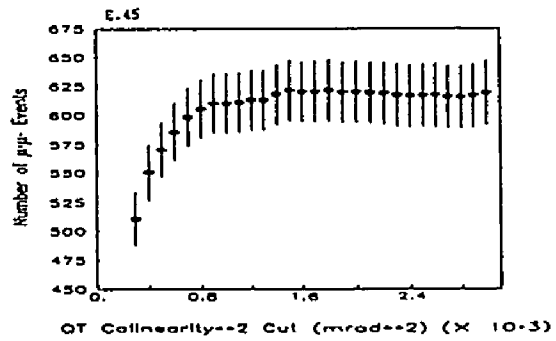
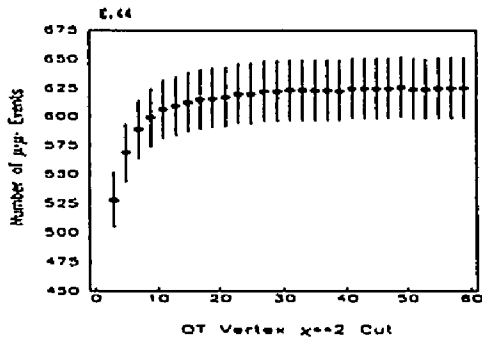
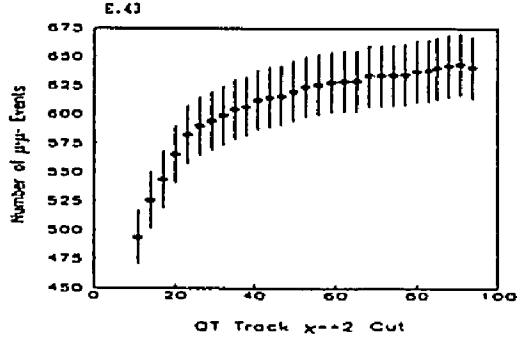
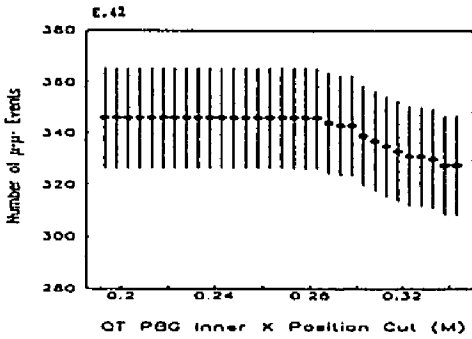
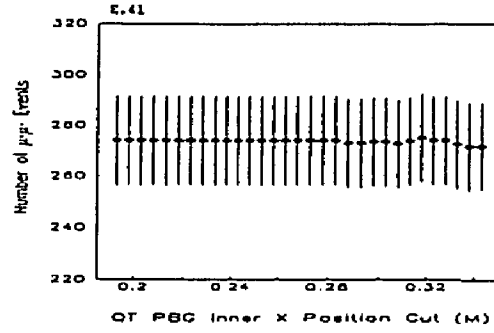
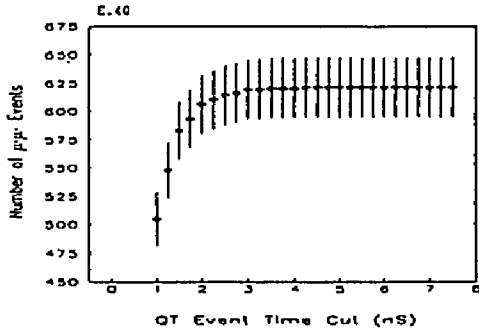
E.37 QT Low Track Momentum Cut (GeV/c)

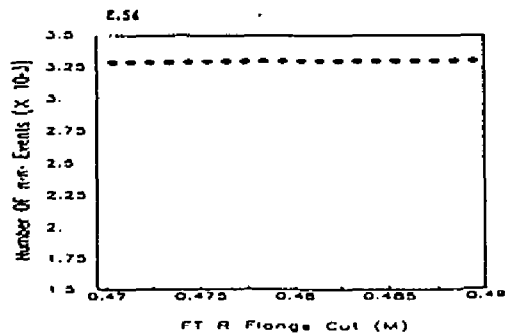
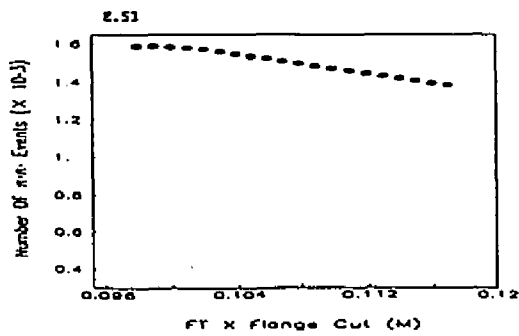
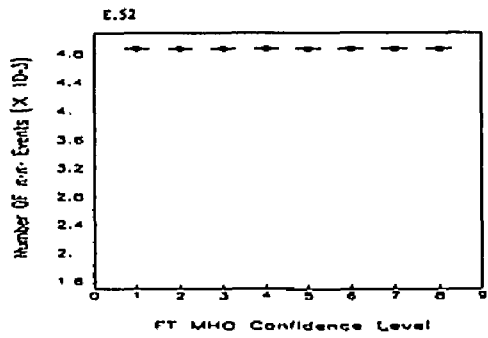
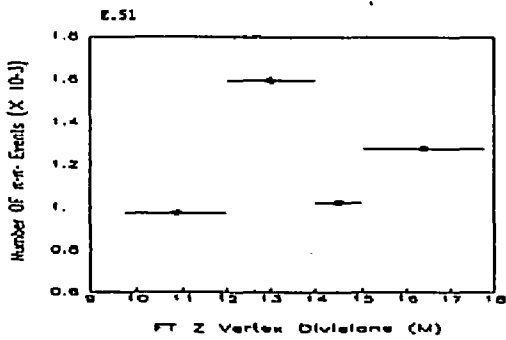
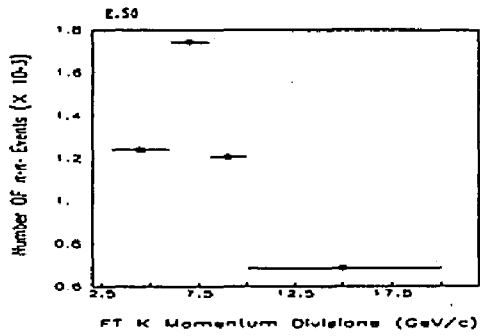
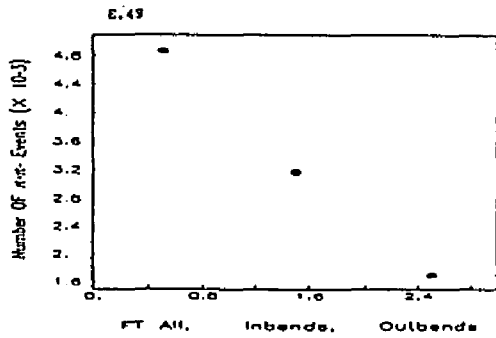
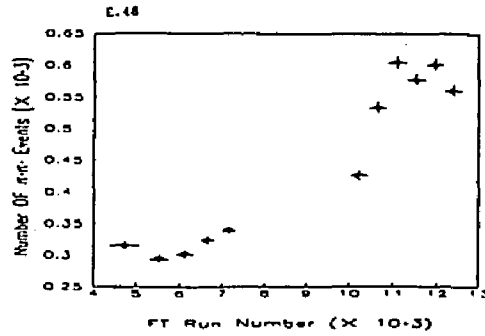
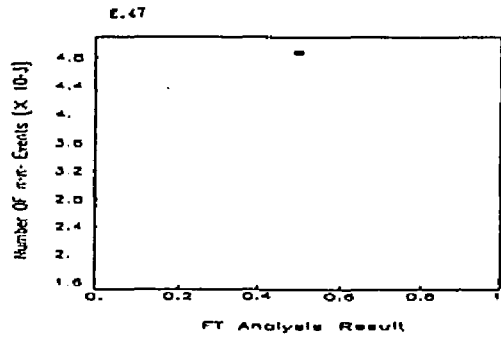


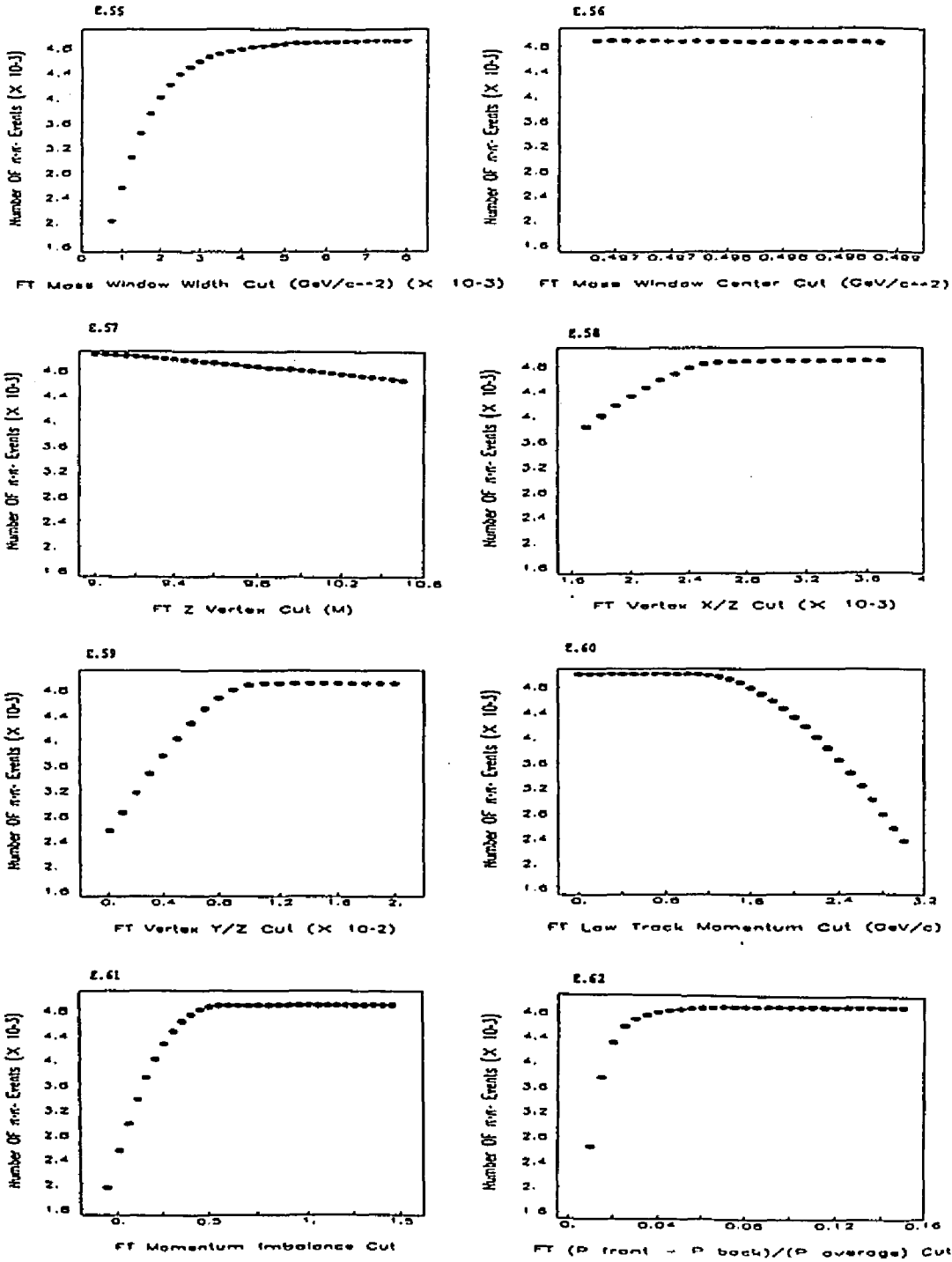
E.38 QT Momentum Imbalance Cut

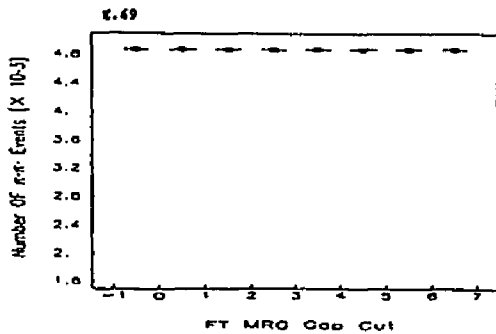
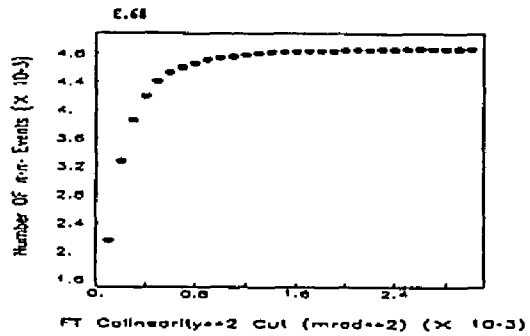
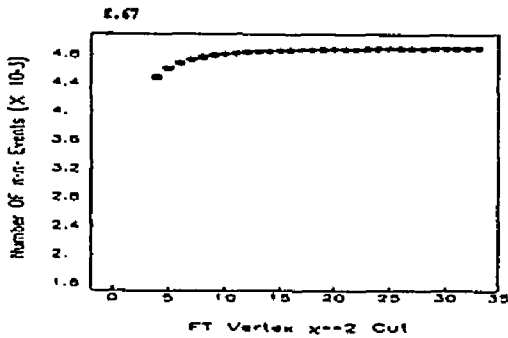
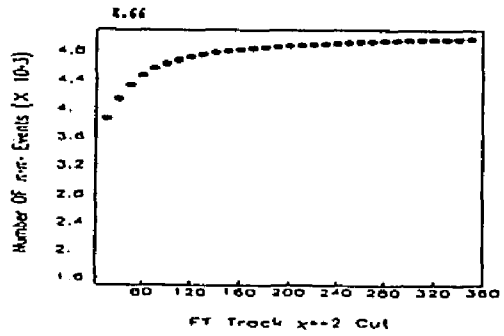
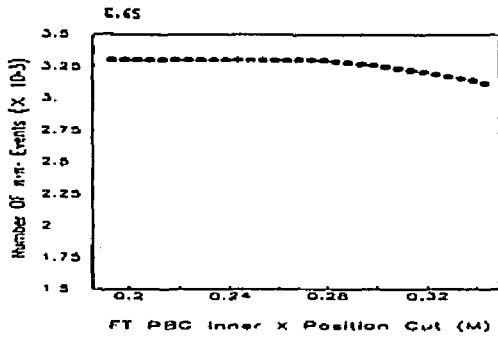
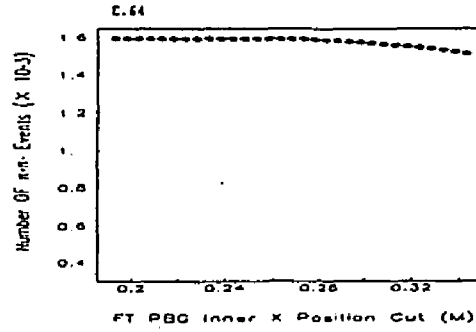
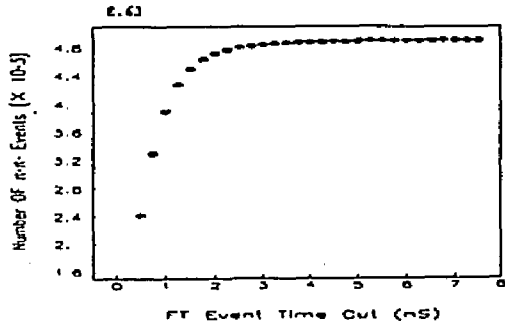


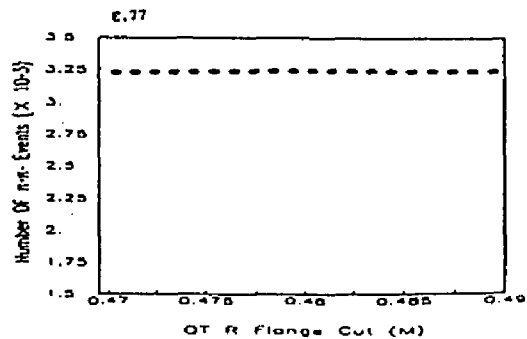
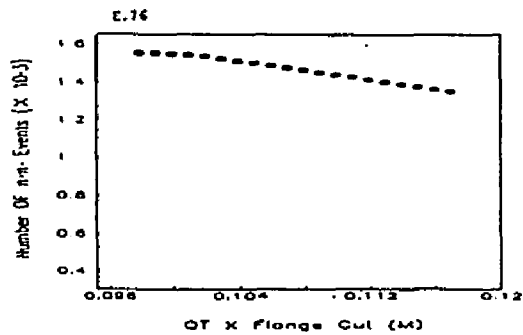
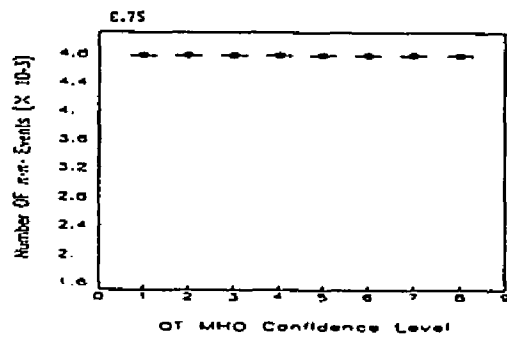
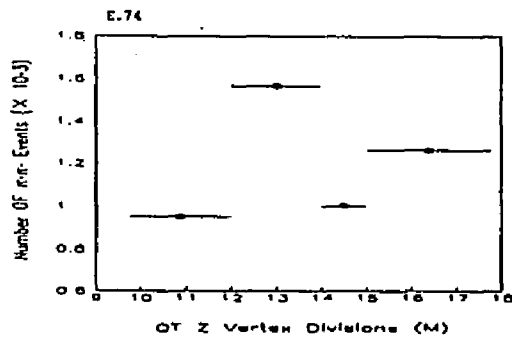
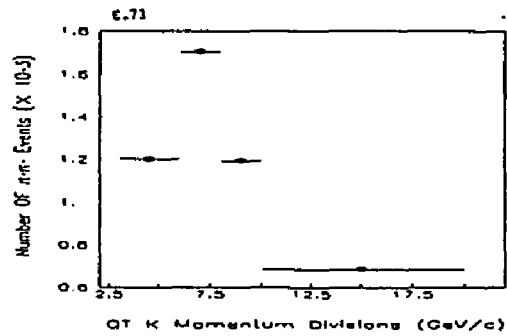
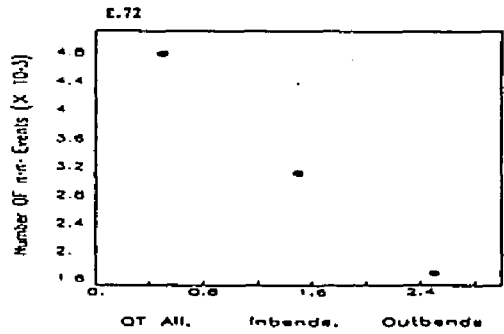
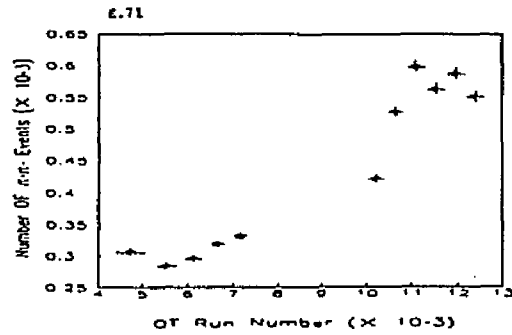
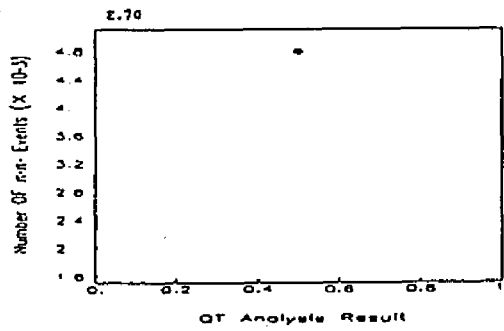
E.39 QT (P front - P back)/(P average) Cut

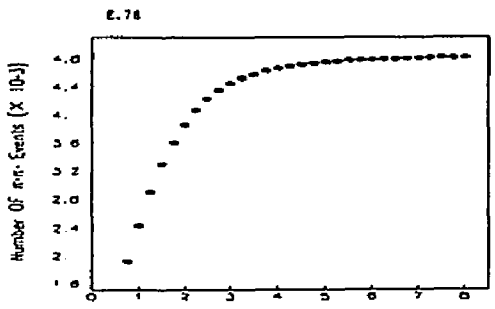




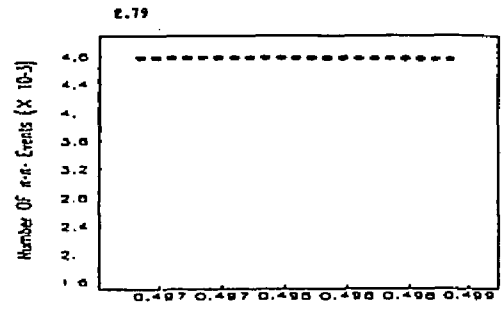




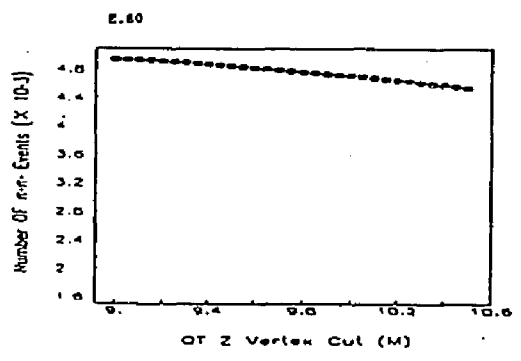




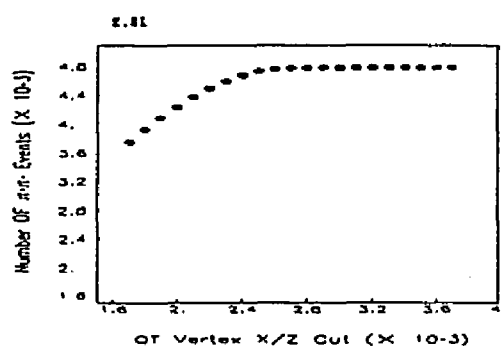
OT Mass Window Width Cut (GeV/c⁻⁻²) (X 10⁻³)



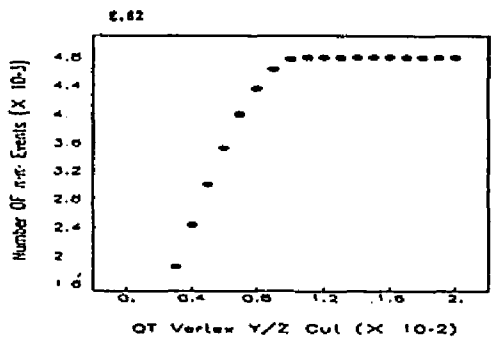
OT Mass Window Center Cut (GeV/c⁻⁻²)



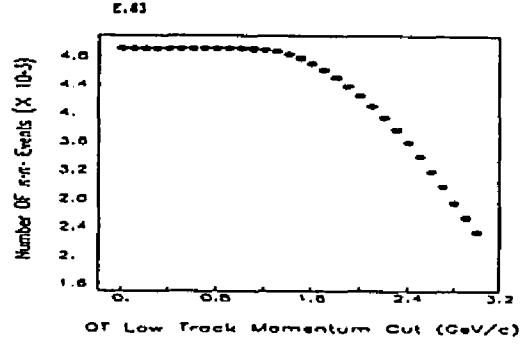
OT Z Vertex Cut (M)



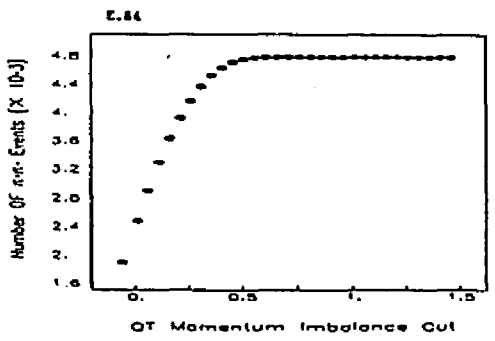
OT Vertex X/Z Cut (X 10⁻³)



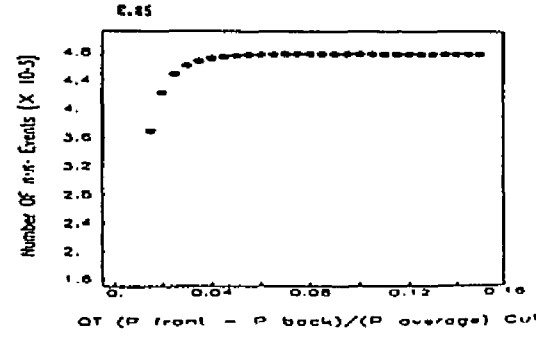
OT Vertex Y/Z Cut (X 10⁻²)



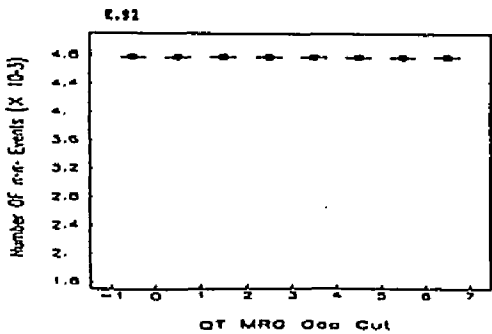
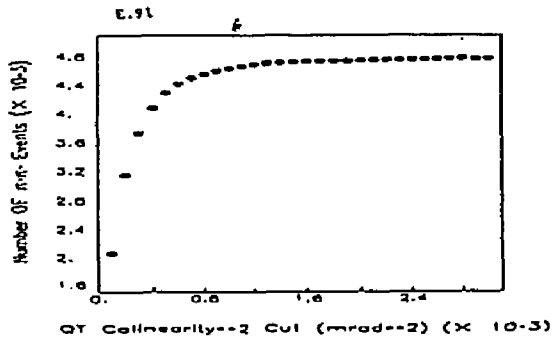
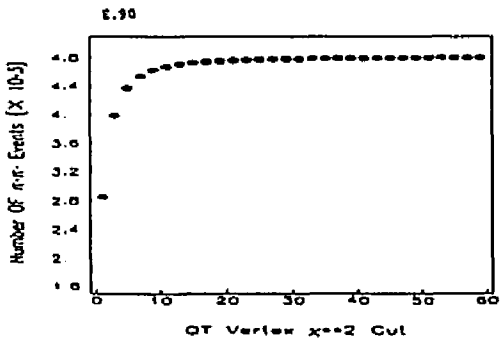
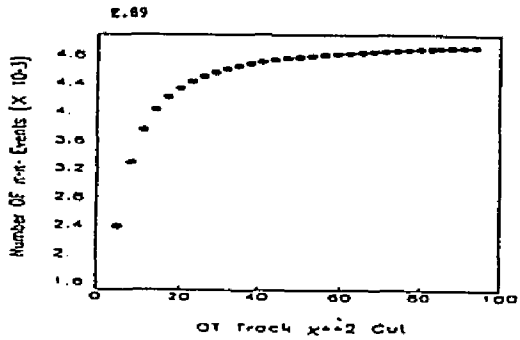
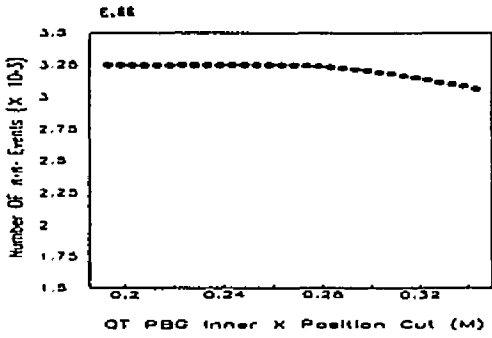
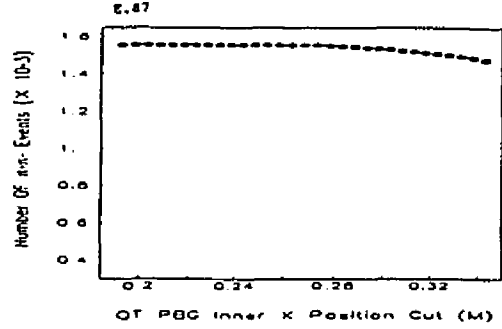
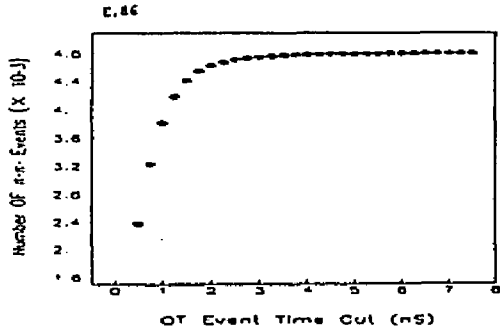
OT Low Track Momentum Cut (GeV/c)



OT Momentum Imbalance Cut



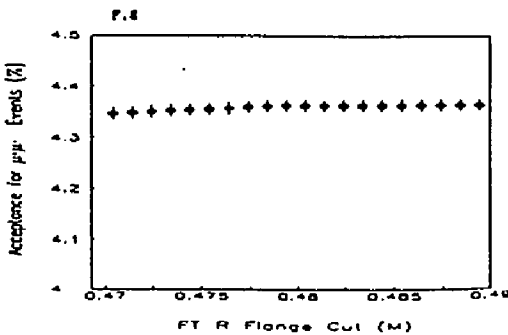
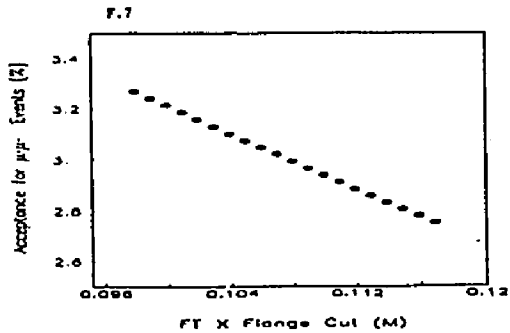
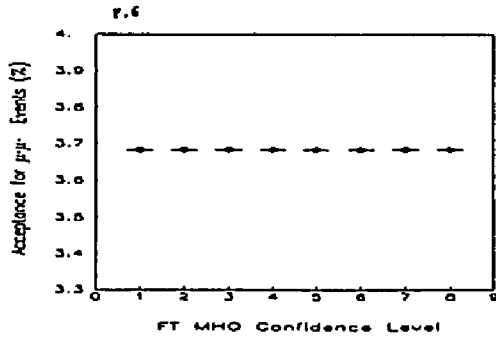
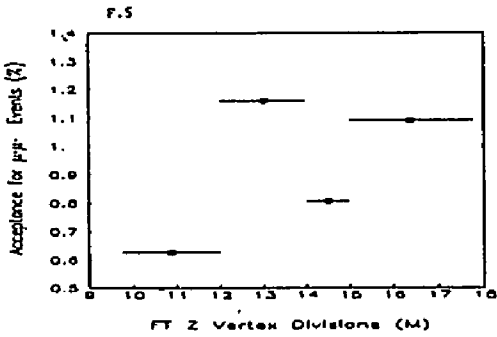
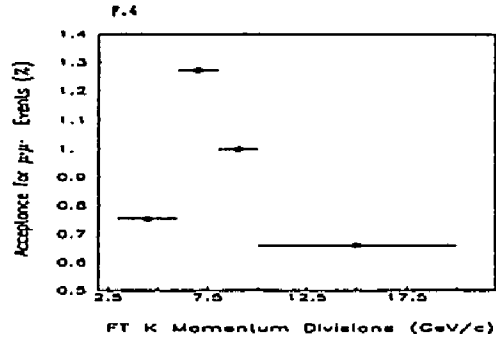
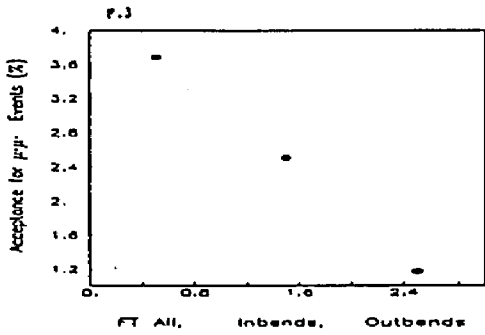
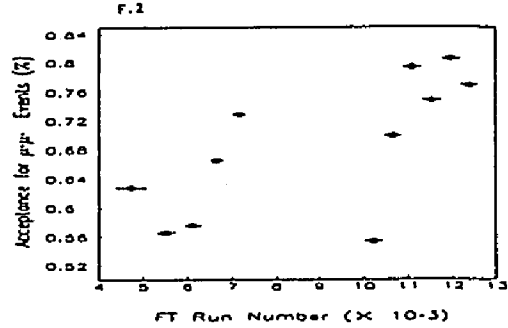
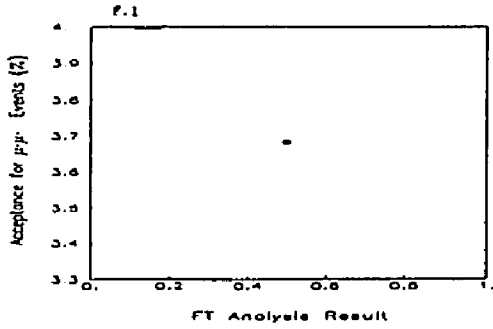
OT (P front - P back)/(P average) Cut

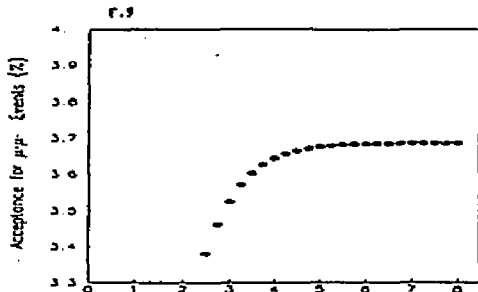


Appendix F

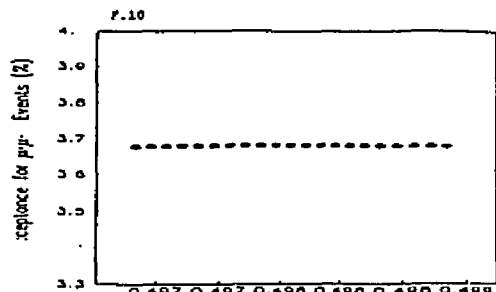
Acceptance Systematic Studies

The $\mu^+\mu^-$ and $\pi^+\pi^-$ acceptance calculations were done as a function of the cut values listed in appendix C. The results of the calculation for the nominal values of the cuts were presented in chapter 8. This appendix presents results, as graphs, for all of the other cut values for the combined 1989 and 1990 samples. Although very similar, results from both QT and FT are presented for completeness and for ease of location of similar plots in other appendices. Since the Monte Carlo sample was used in this calculation, cuts on the event time, MRG and MHO were not made. Nonetheless, plots related to these cuts are included for completeness. The figure number appears on the upper left hand corner of each plot and the accompanying caption for each of the figures can be found in the list of figures section at the beginning of this dissertation. Finally, the values and errors presented on each plot are correlated. They correspond to identical samples but with slightly different cut values as indicated.

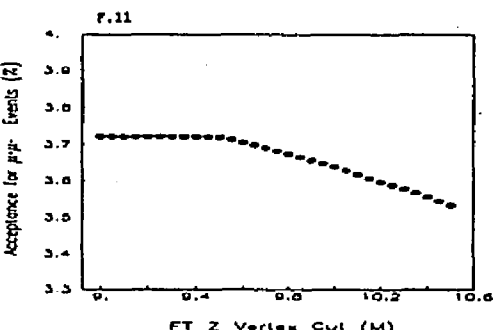




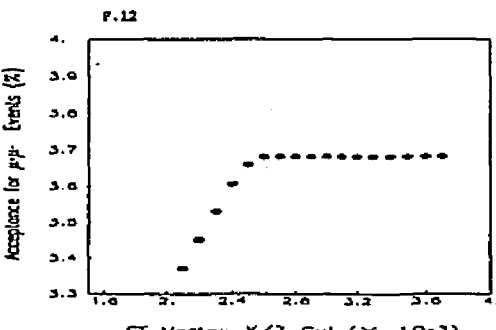
F.9 FT Mass Window Width Cut (GeV/c--2) (X 10-3)



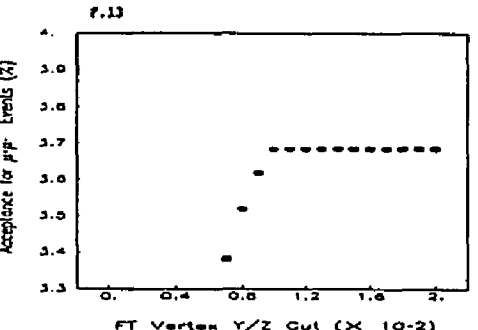
F.10 FT Mass Window Center Cut (GeV/c--2)



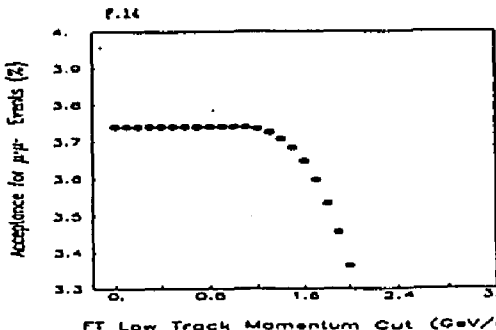
F.11 FT Z Vertex Cut (M)



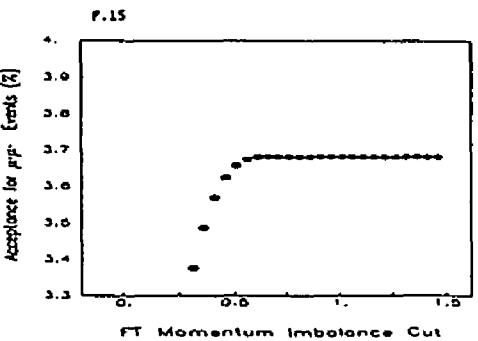
F.12 FT Vertex X/2 Cut (X 10-3)



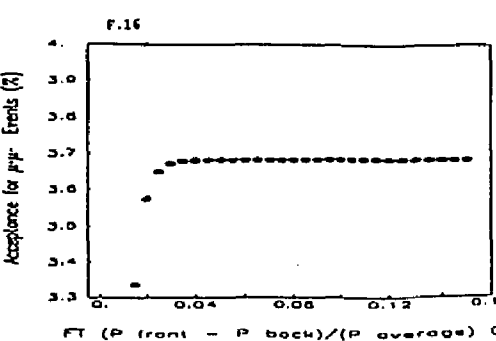
F.13 FT Vertex Y/Z Cut (X 10-2)



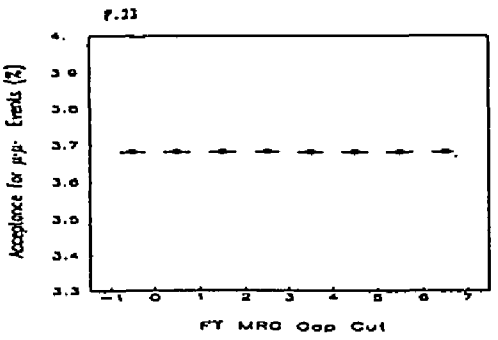
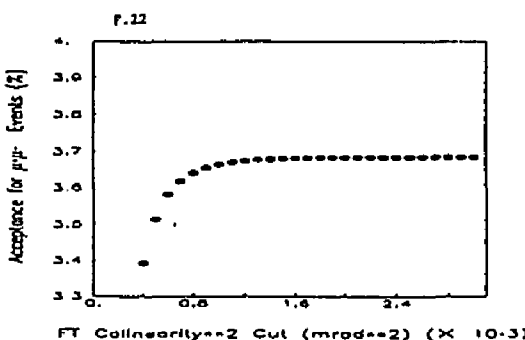
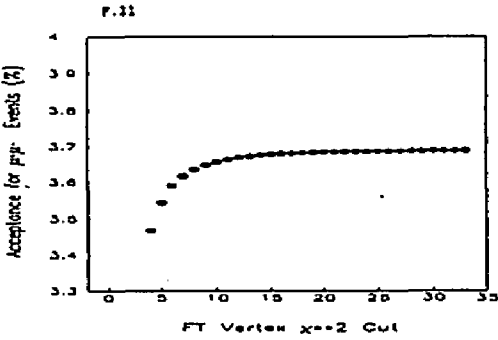
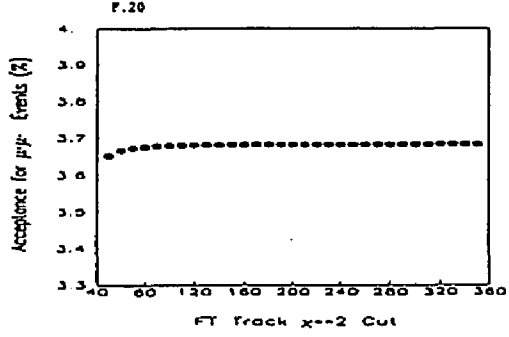
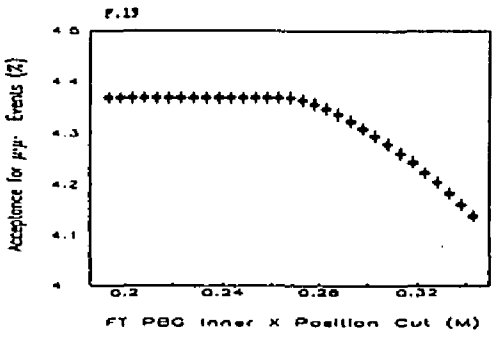
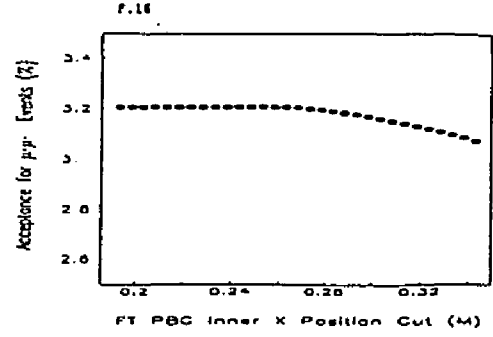
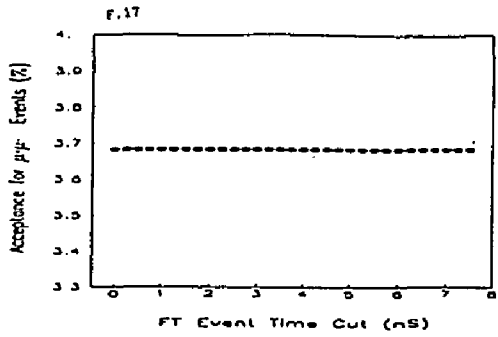
F.14 FT Low Track Momentum Cut (GeV/c)

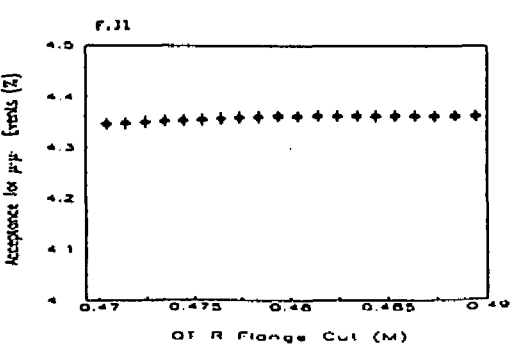
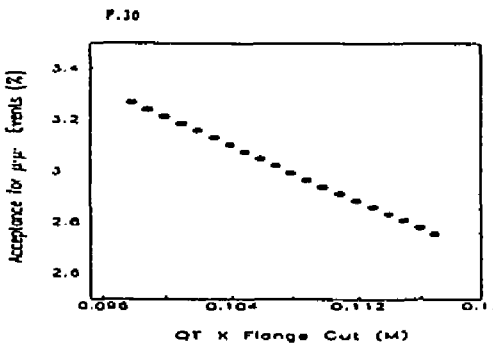
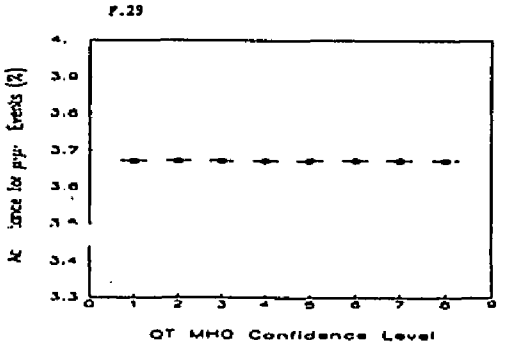
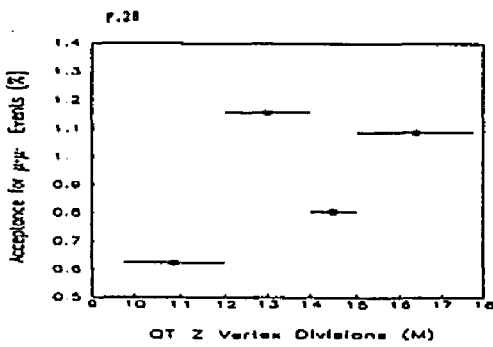
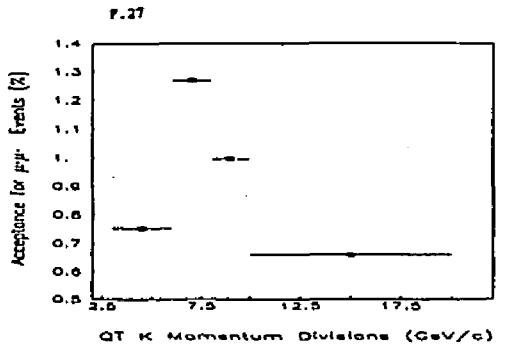
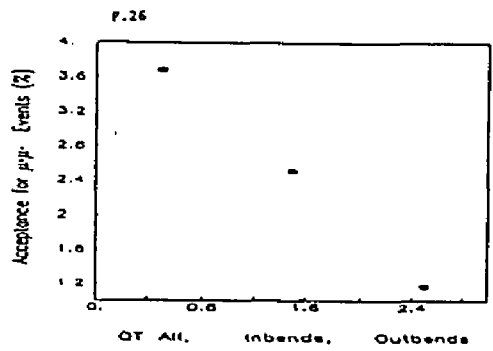
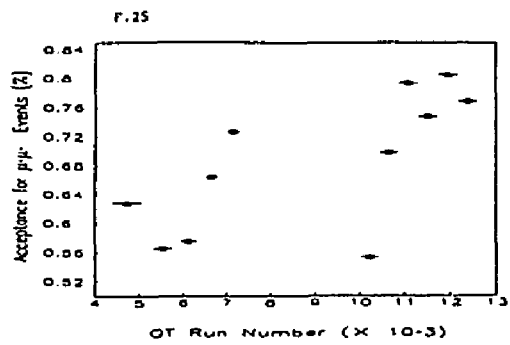
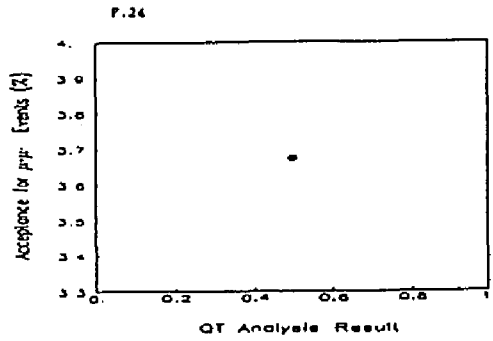


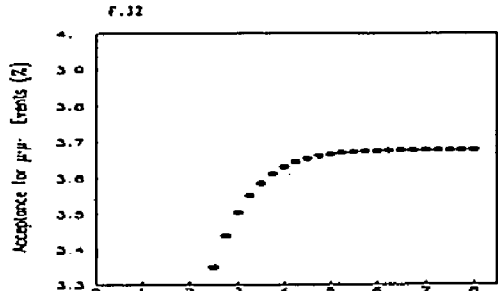
F.15 FT Momentum Imbalance Cut



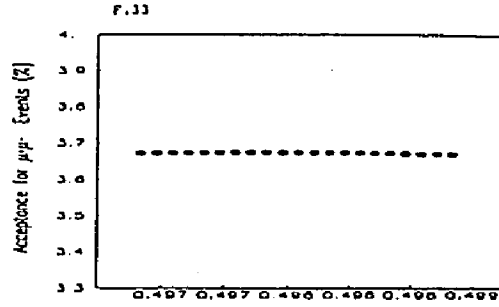
F.16 FT (P front - P back)/(P average) Cut



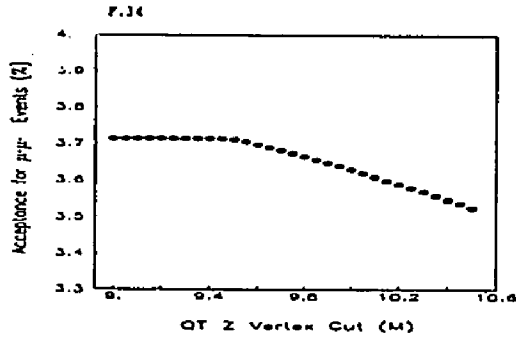




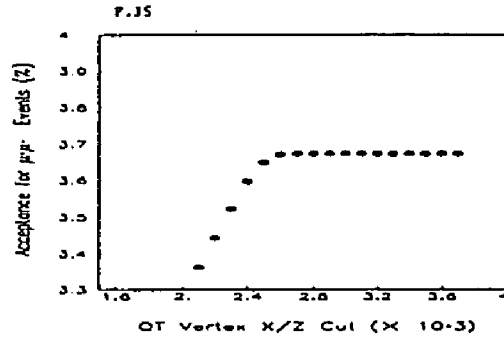
QT Mass Window Width Cut (GeV/c²) (x 10⁻³)



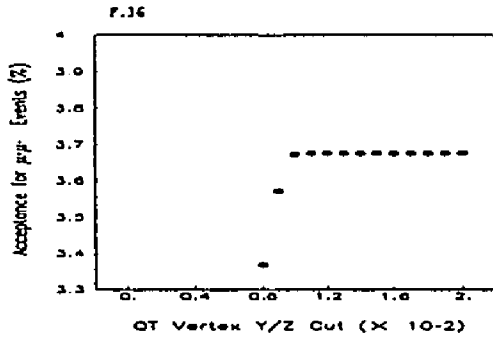
QT Mass Window Center Cut (GeV/c²)



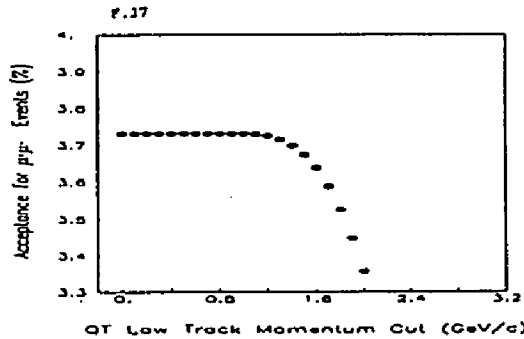
QT Z Vertex Cut (M)



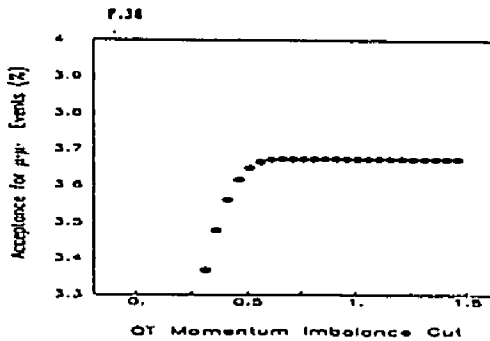
QT Vertex X/Z Cut (x 10⁻³)



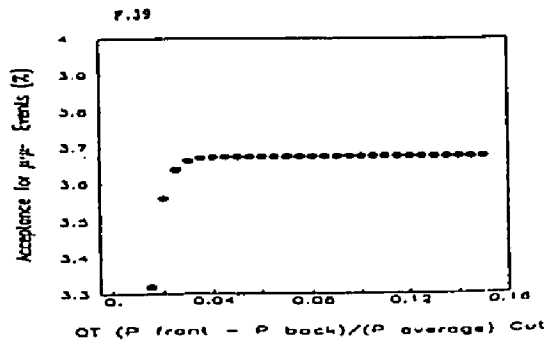
QT Vertex Y/Z Cut (x 10⁻²)



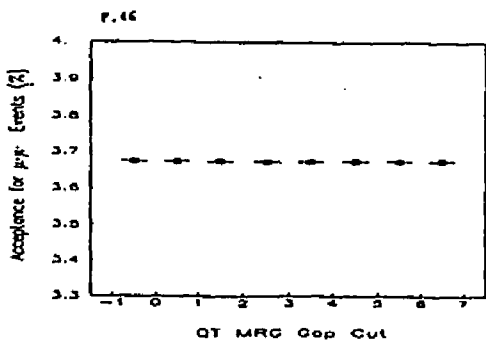
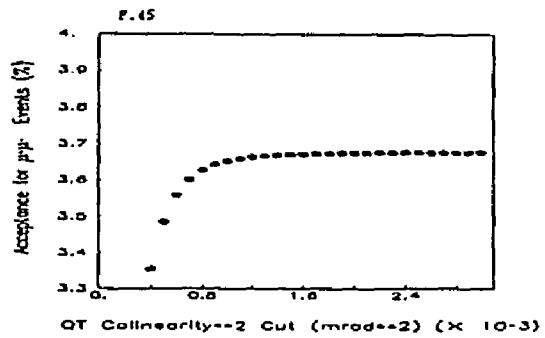
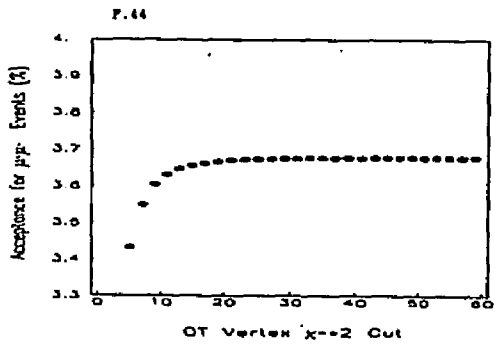
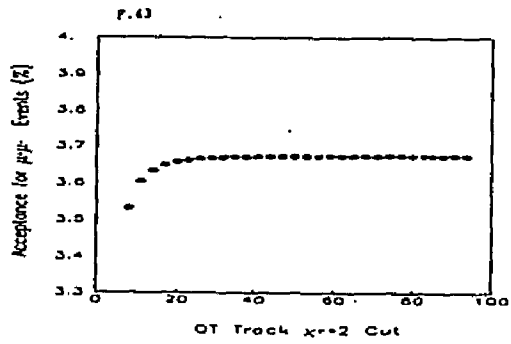
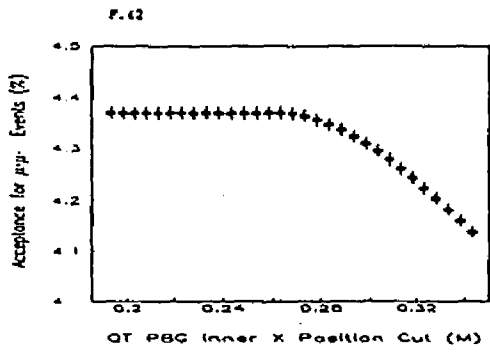
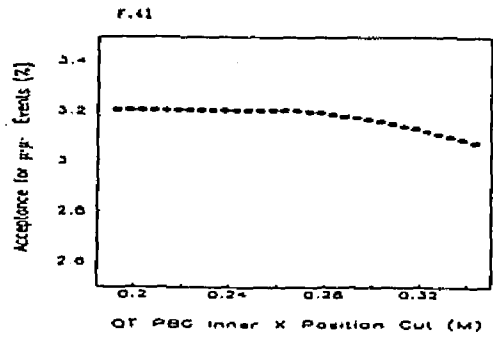
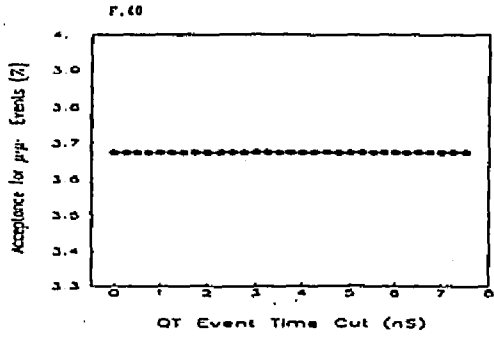
QT Low Track Momentum Cut (GeV/c)

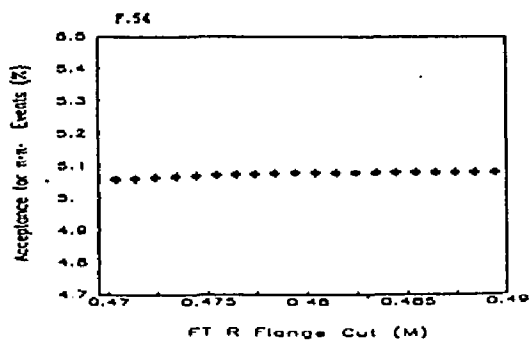
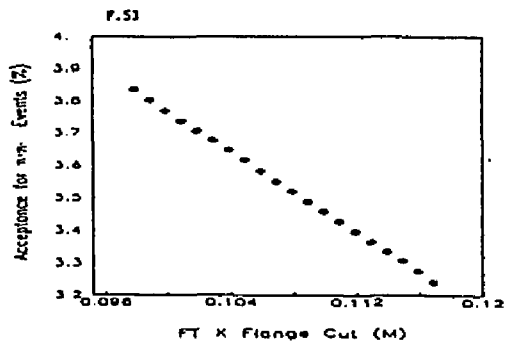
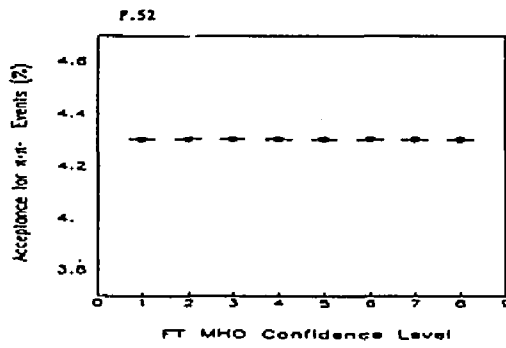
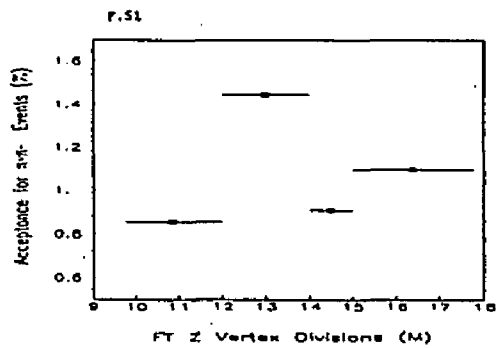
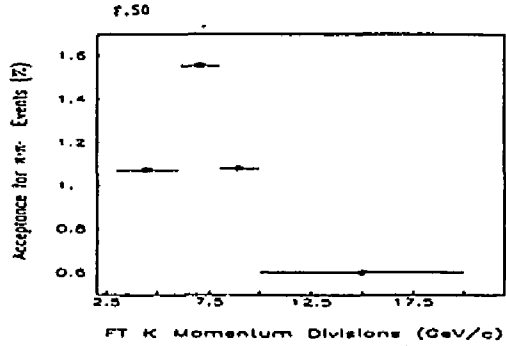
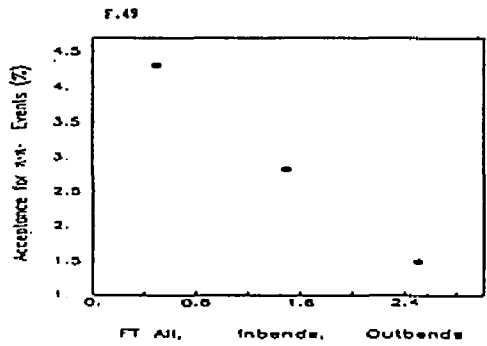
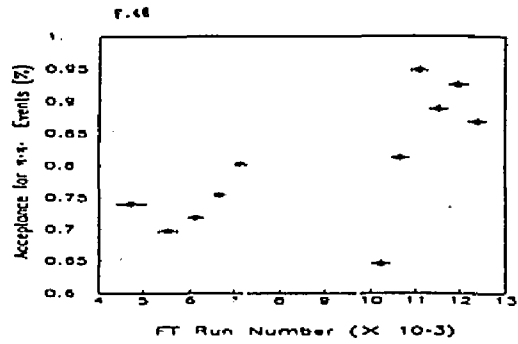
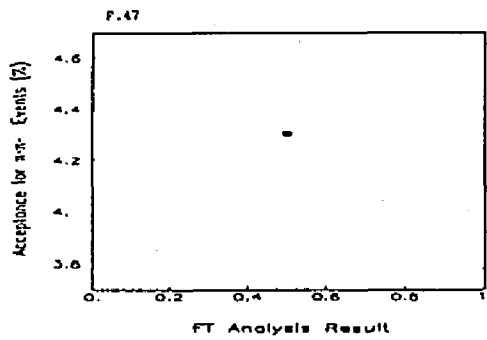


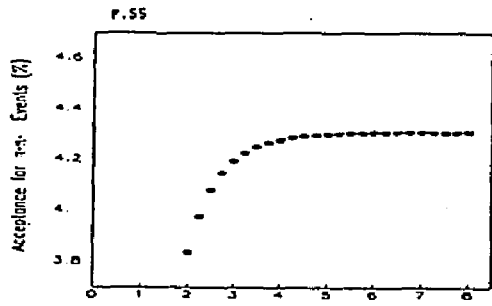
QT Momentum Imbalance Cut



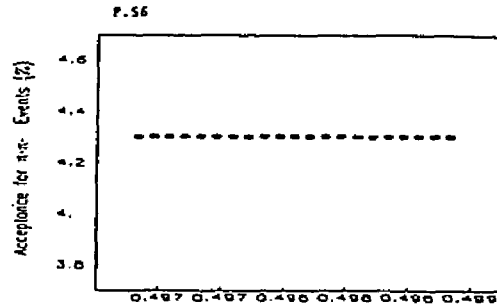
QT (P front - P back)/(P average) Cut



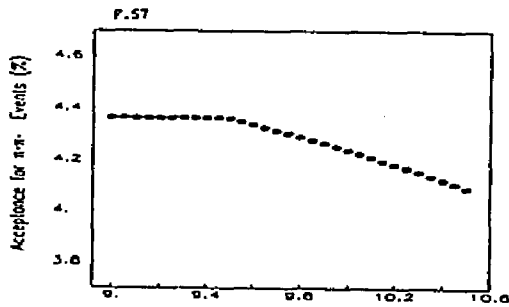




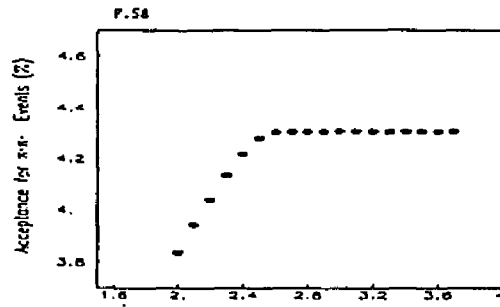
FT Mass Window Width Cut (GeV/c²) (x 10⁻³)



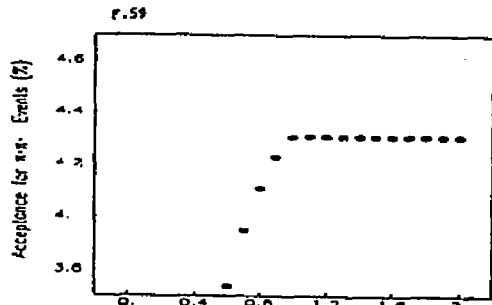
FT Mass Window Center Cut (GeV/c²)



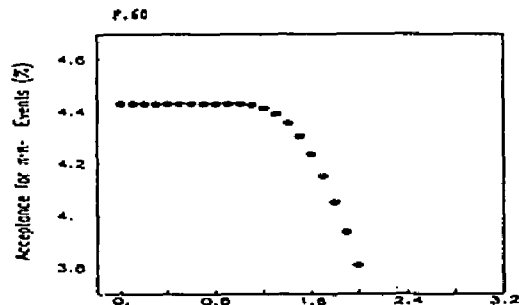
FT Z Vertex Cut (M)



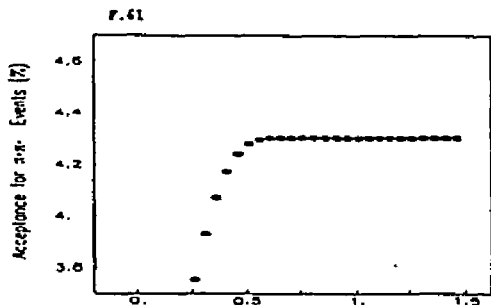
FT Vertex X/Z Cut (x 10⁻³)



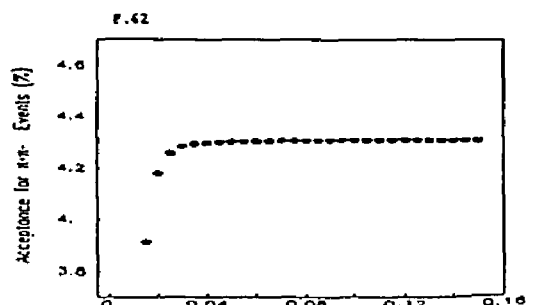
FT Vertex Y/Z Cut (x 10⁻²)



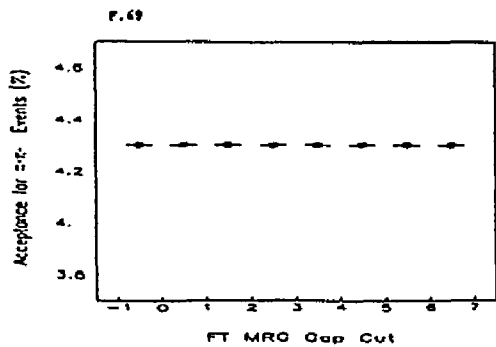
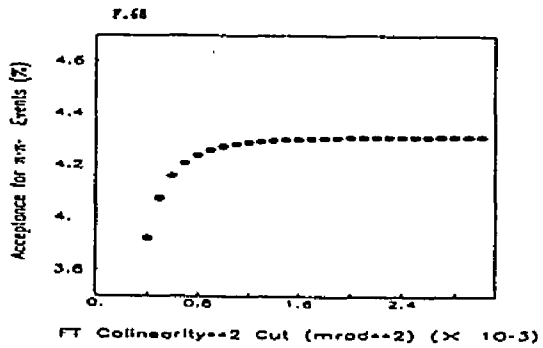
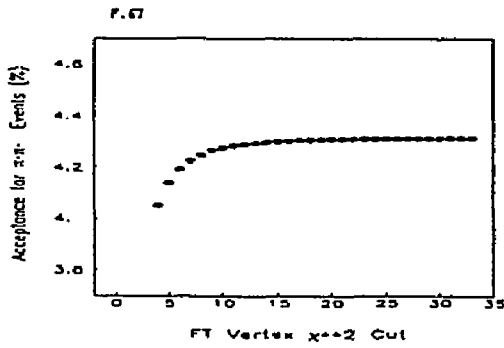
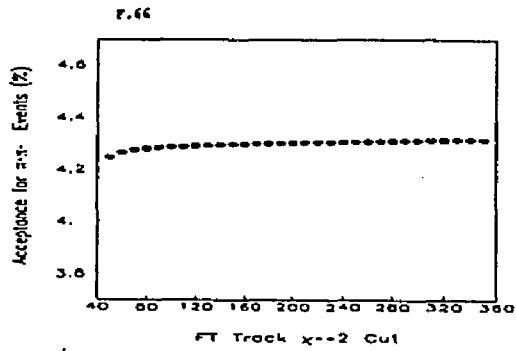
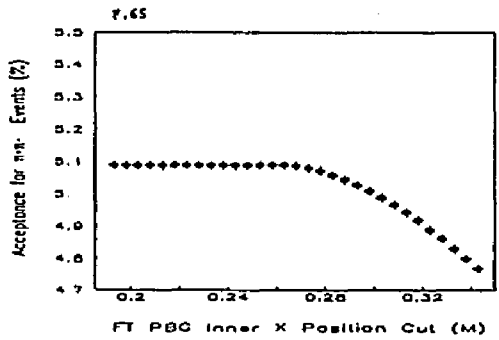
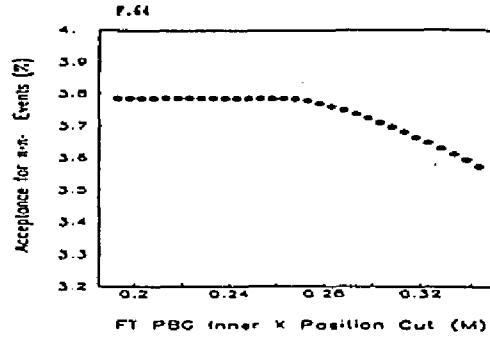
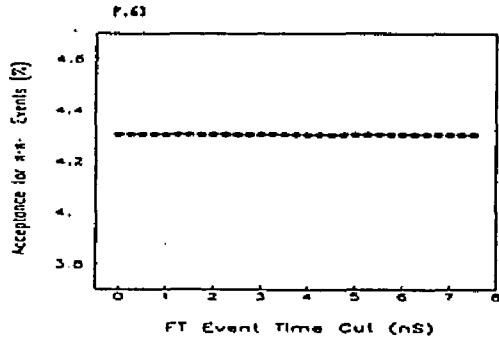
FT Low Track Momentum Cut (GeV/c)

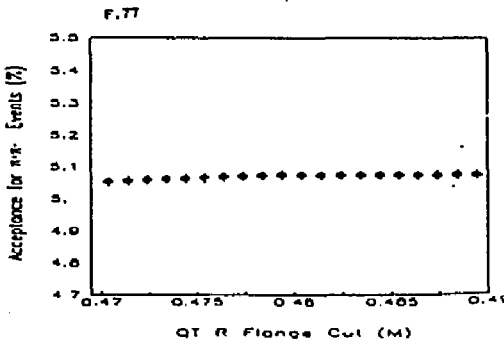
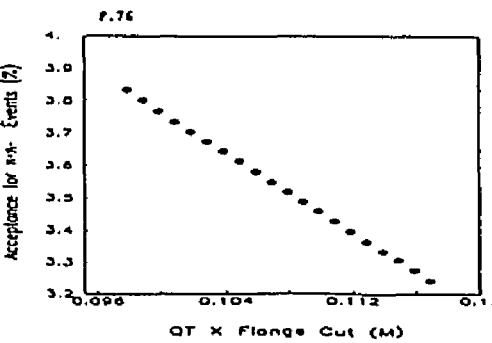
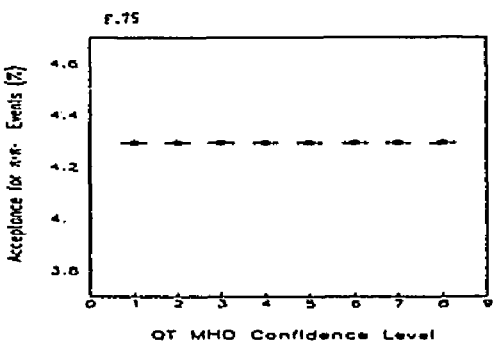
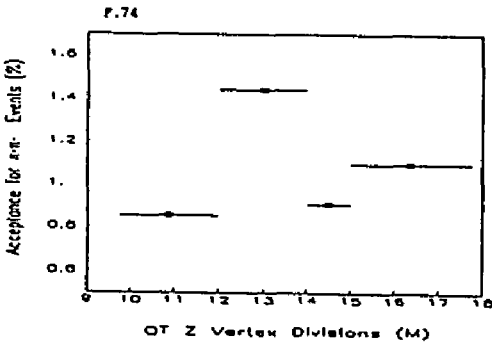
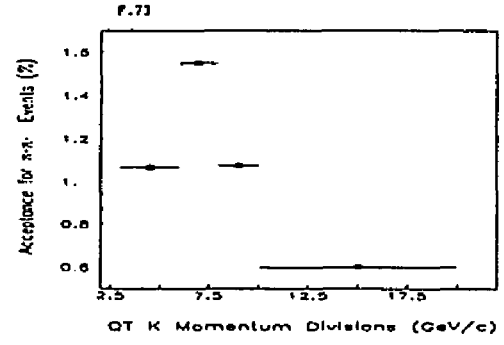
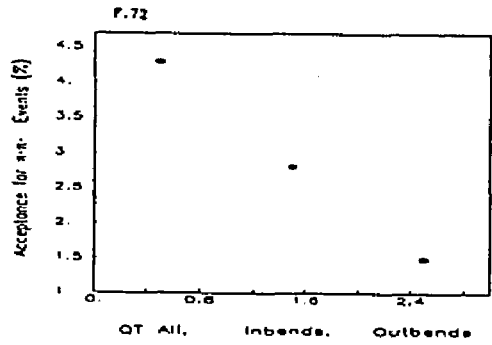
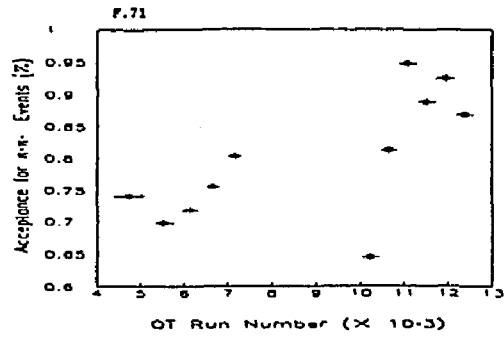
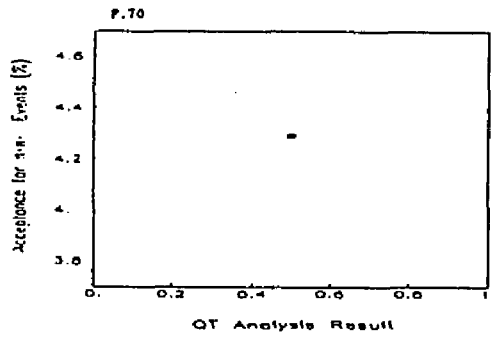


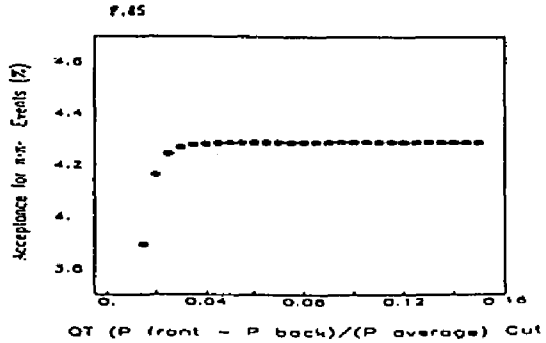
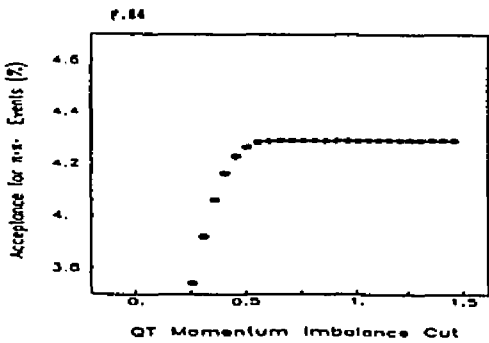
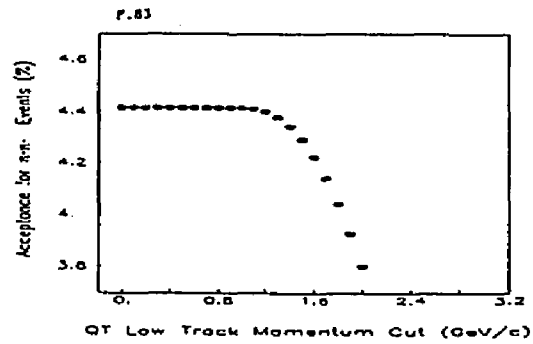
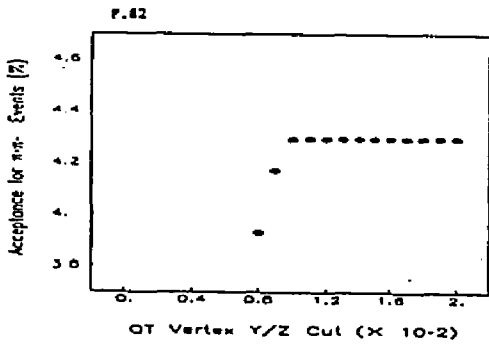
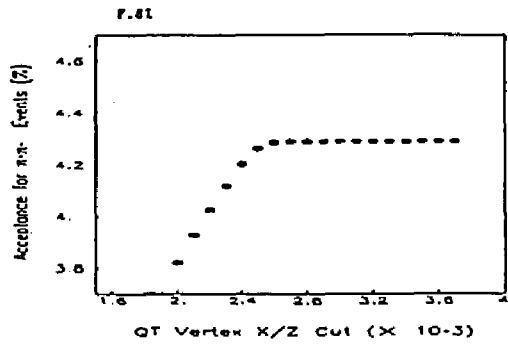
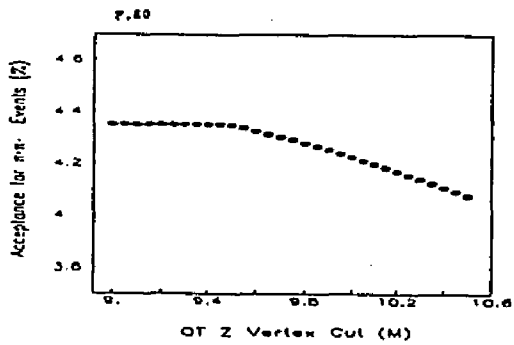
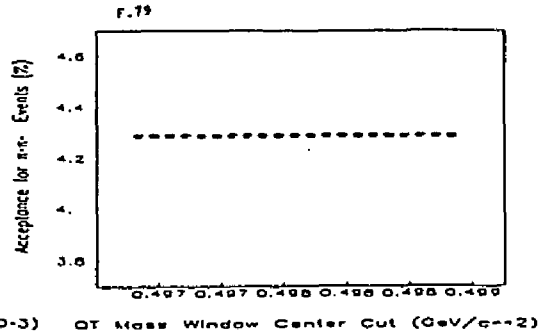
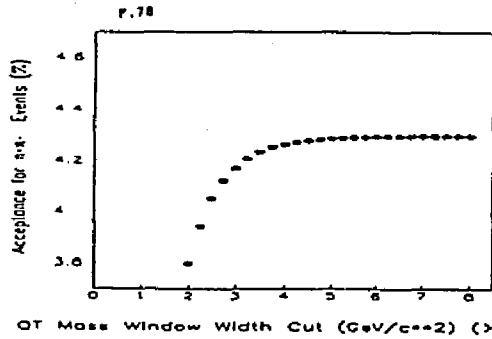
FT Momentum Imbalance Cut

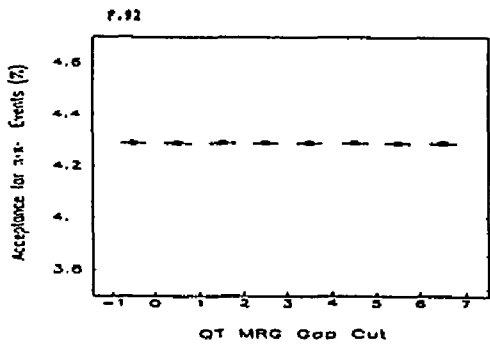
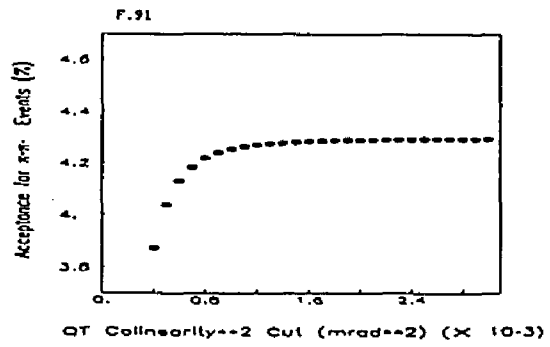
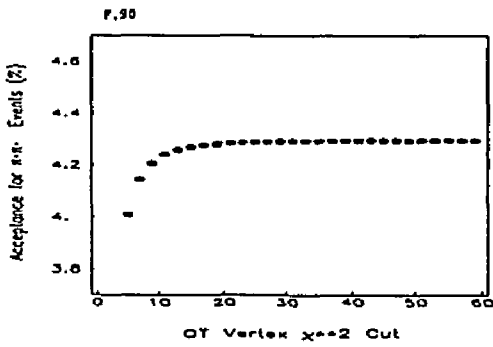
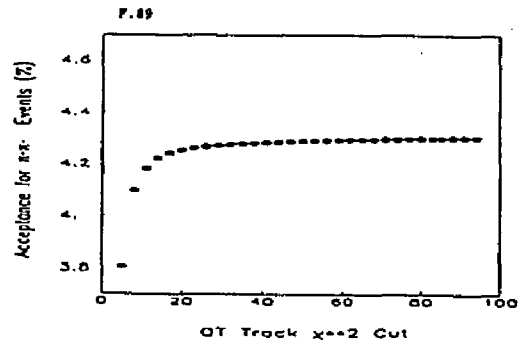
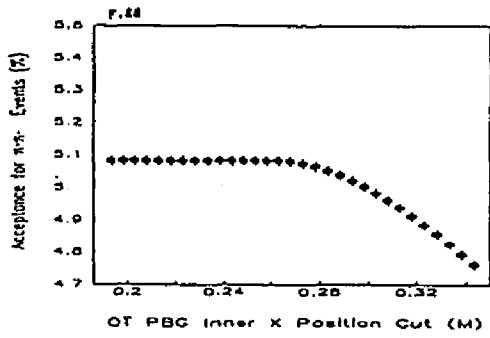
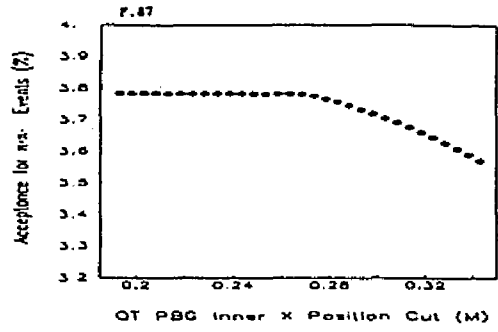
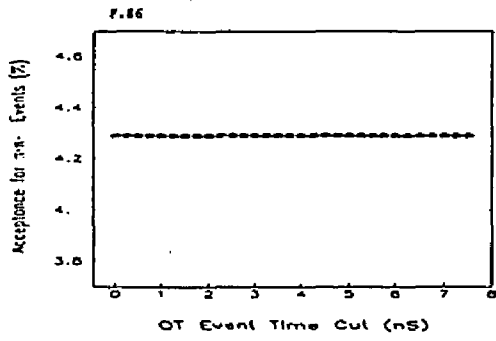


FT (P front - P back)/(P average) Cut





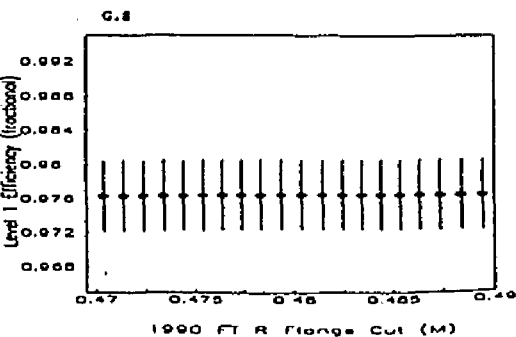
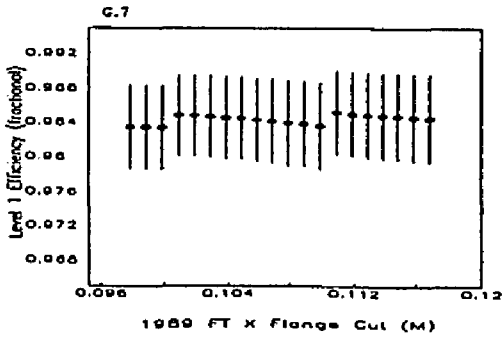
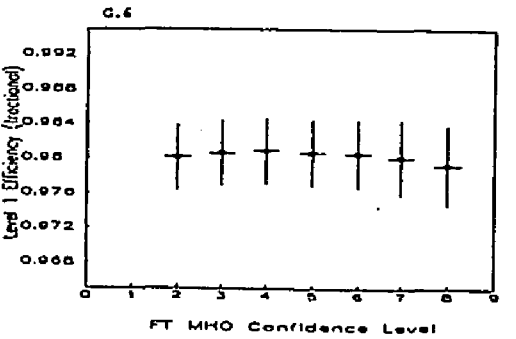
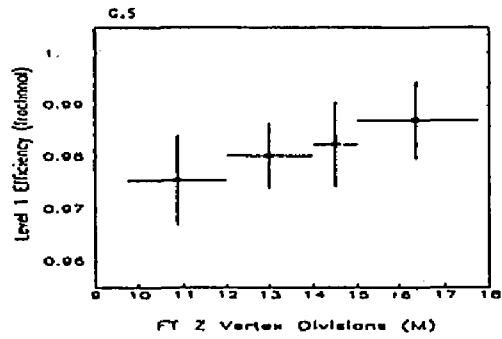
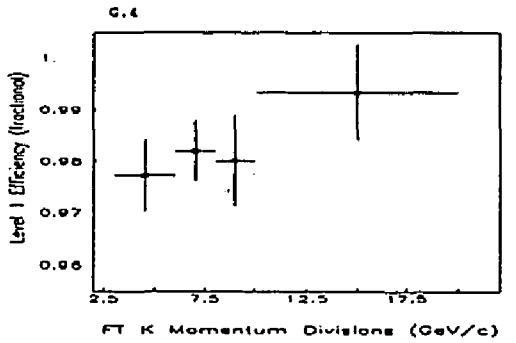
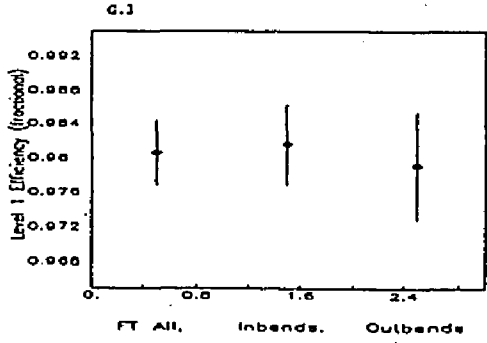
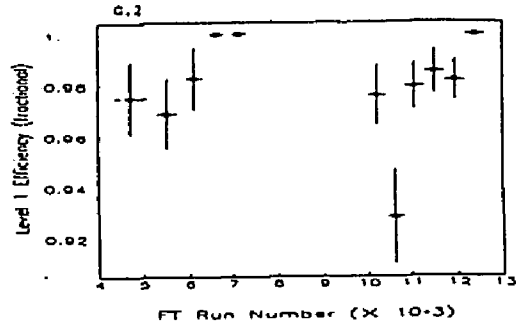
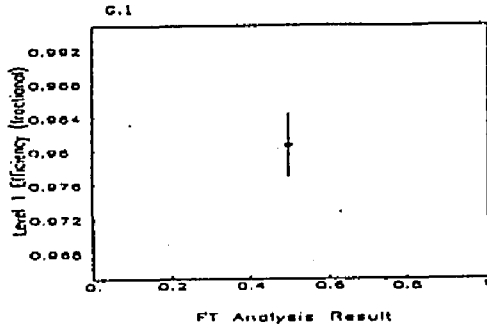


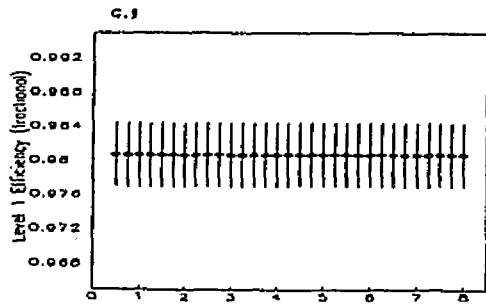


Appendix G

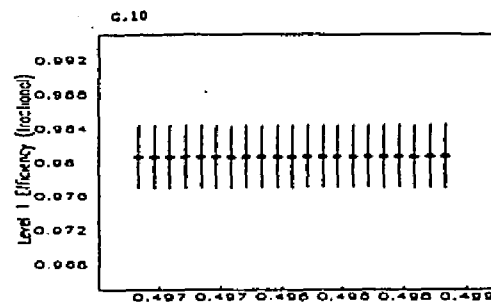
L1 Efficiency Systematic Studies

The L1 efficiency calculation was done as a function of the cut values listed in appendix C. The results of the calculation for the nominal values of the cuts were presented in chapter 8. This appendix presents results, as graphs, for all of the other cut values for the combined 1989 and 1990 samples. Although very similar, results from both QT and FT are presented for completeness. Since different values of the mass and colinearity cuts were applied to this sample, the mass center cut, mass window cut, and colinearity-squared cut were not applied to the sample. Plots of these cut values are included only for completeness and ease of comparison to other appendices of systematic studies. Each plot contains sufficient information for identification of its contents. The figure number appears on the upper left hand corner of each plot and the accompanying caption for each of the figures can be found in the list of figures section at the beginning of this dissertation. As mentioned in the previous appendices, the values and errors are correlated since they correspond to the same samples but with slightly different cut values.

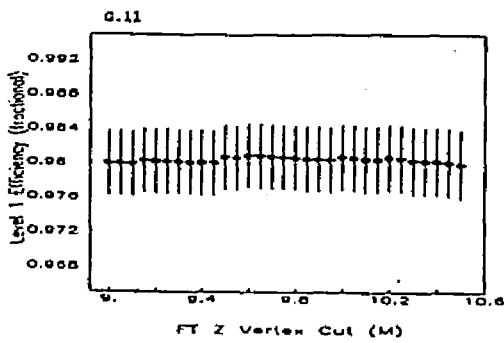




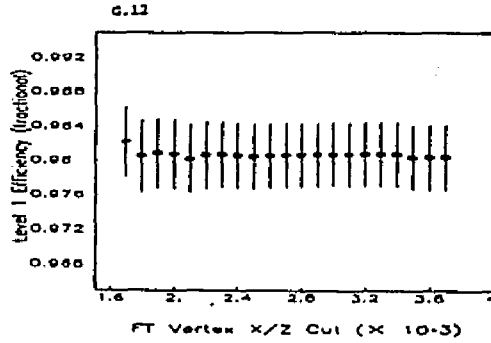
G.9 FT Mass Window Width Cut (GeV/c²) (x 10⁻³)



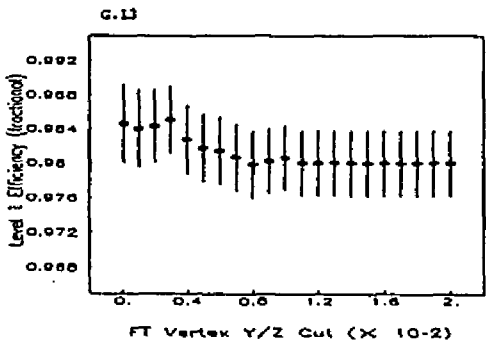
G.10 FT Mass Window Center Cut (GeV/c²)



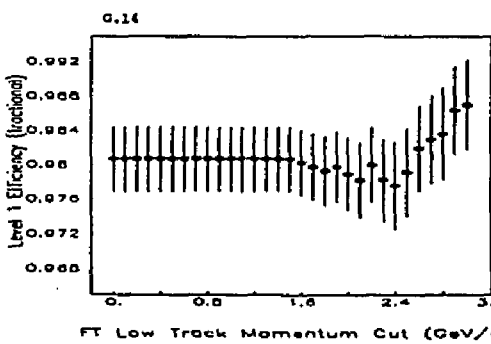
G.11 FT Z Vertex Cut (M)



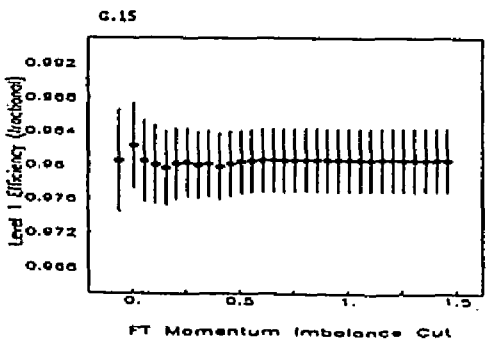
G.12 FT Vertex X/Z Cut (x 10⁻³)



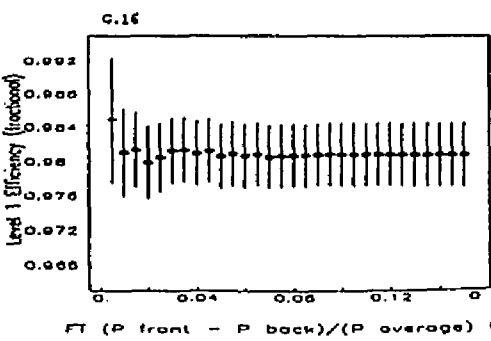
G.13 FT Vertex Y/Z Cut (x 10⁻²)



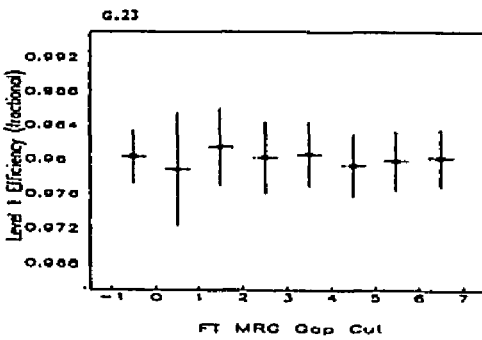
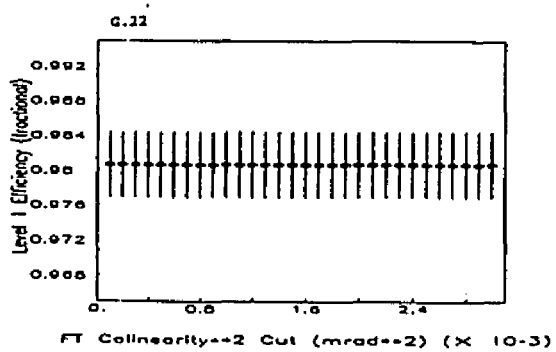
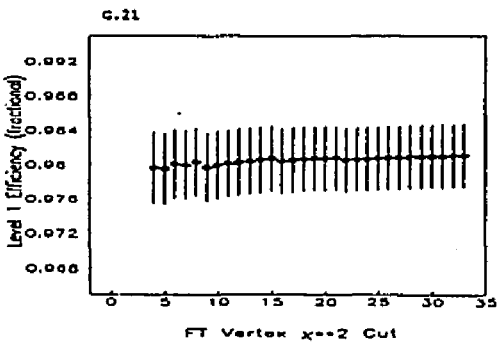
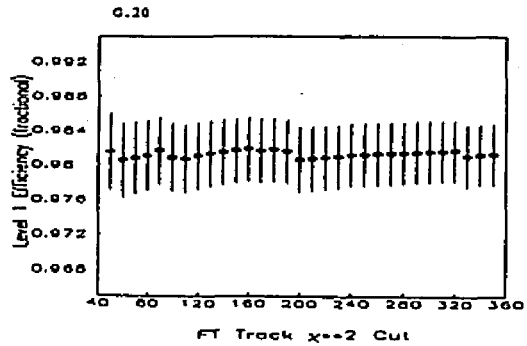
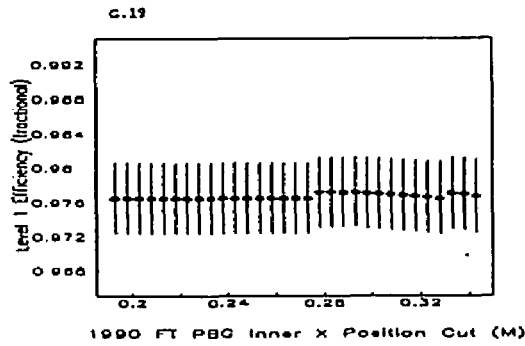
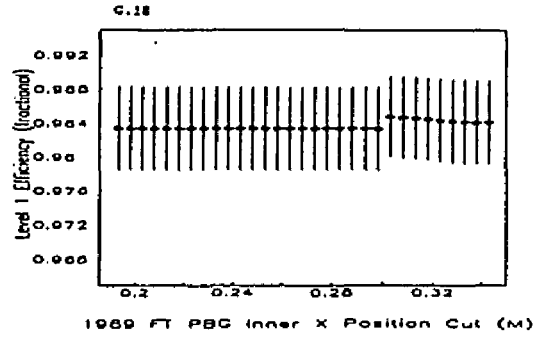
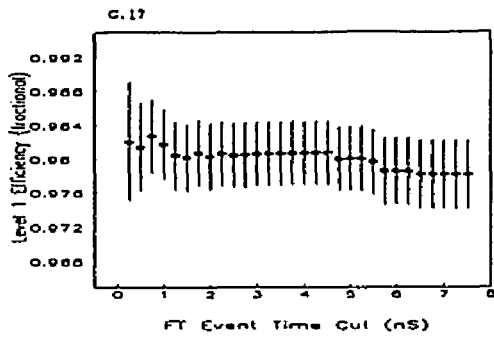
G.14 FT Low Track Momentum Cut (GeV/c)

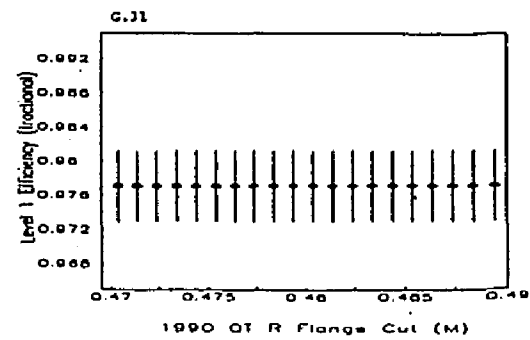
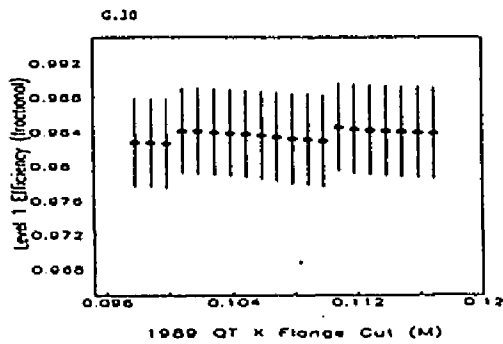
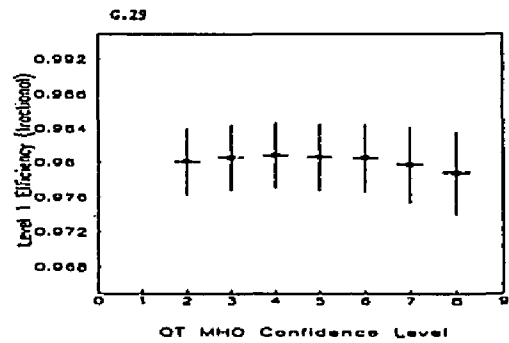
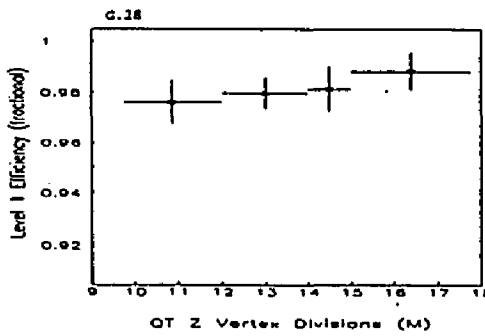
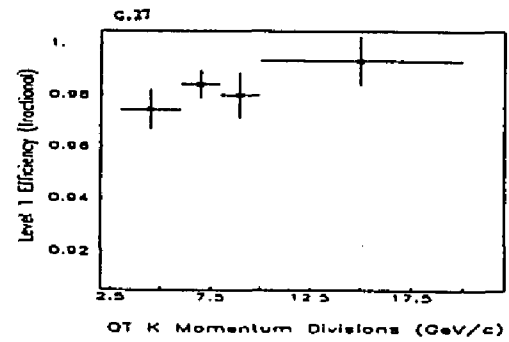
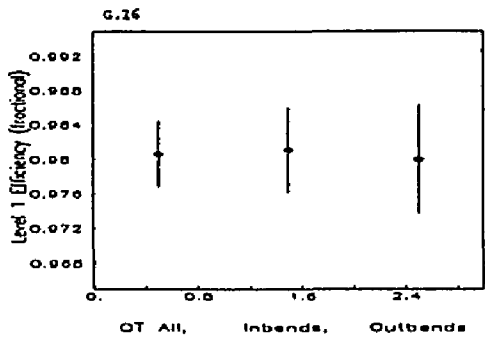
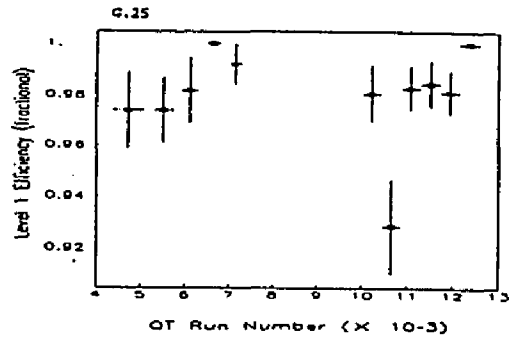
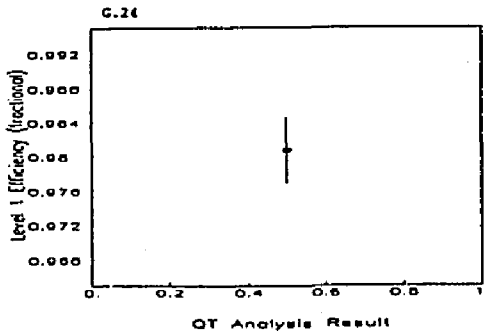


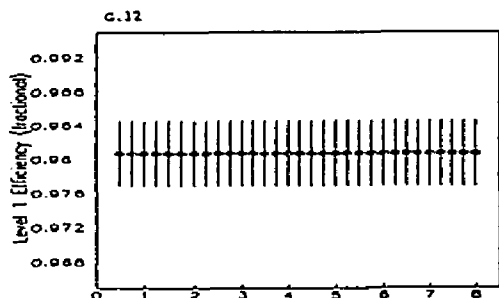
G.15 FT Momentum Imbalance Cut



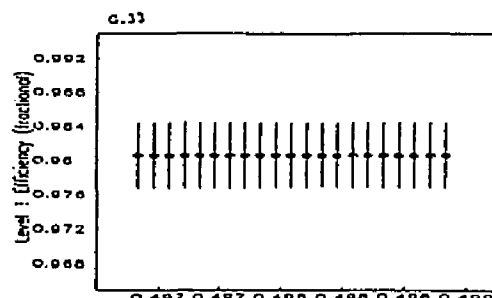
G.16 FT (P front - P back)/(P average) Cut



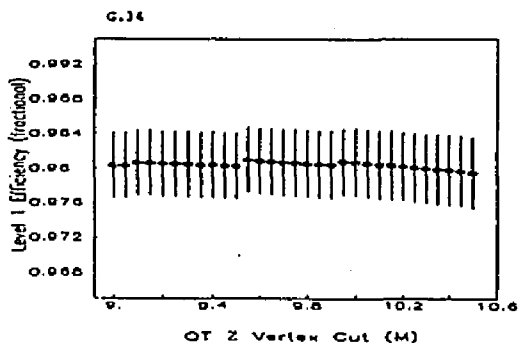




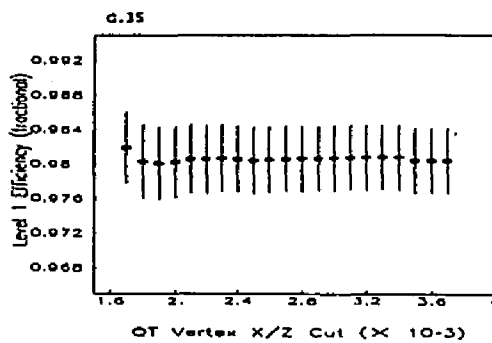
G.32 OT Mass Window Width Cut (GeV/c=2) ($\times 10^{-3}$)



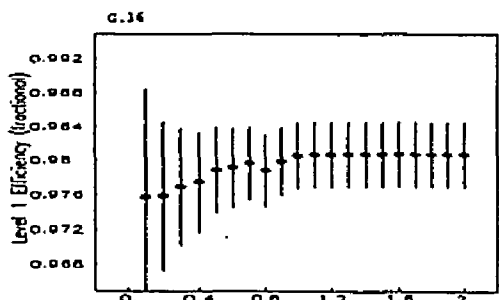
G.33 OT Mass Window Center Cut (GeV/c=2)



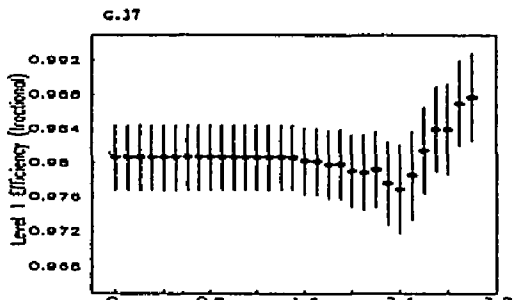
G.34 OT Z Vertex Cut (M)



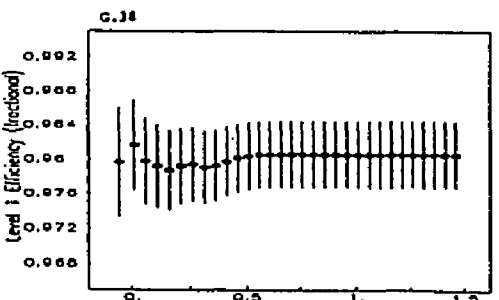
G.35 OT Vertex X/Z Cut ($\times 10^{-3}$)



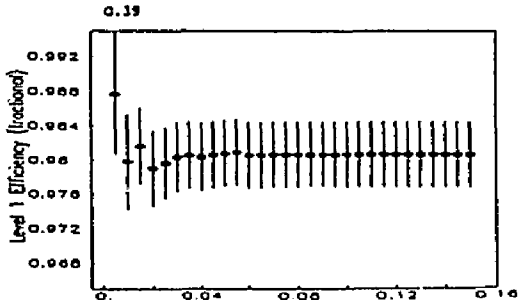
G.36 OT Vertex Y/Z Cut ($\times 10^{-2}$)



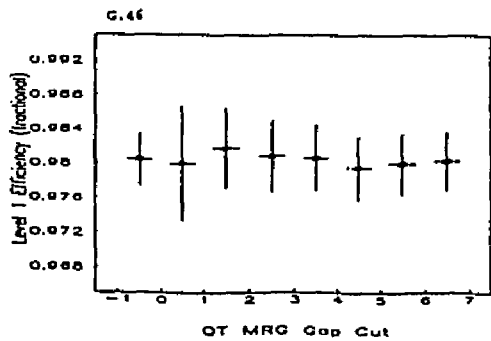
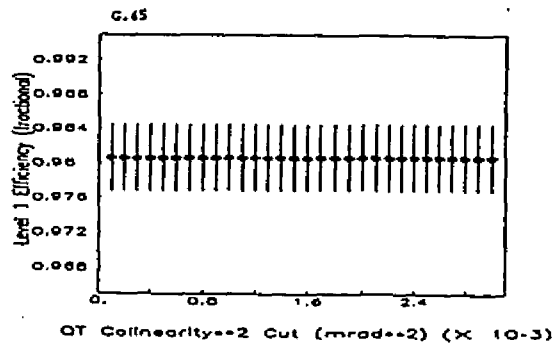
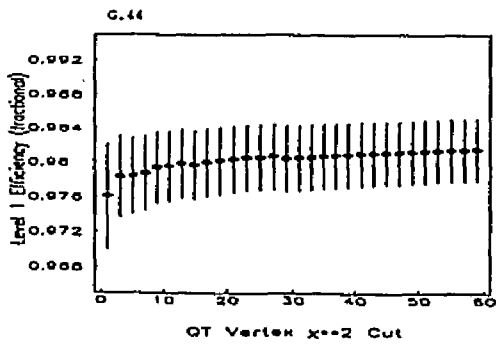
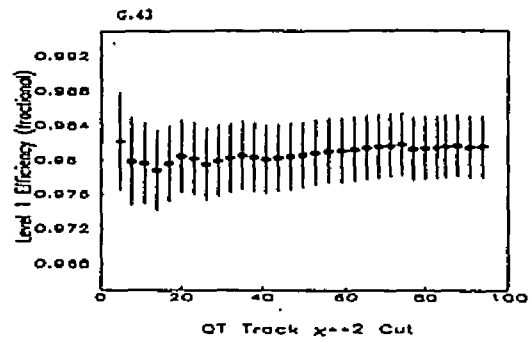
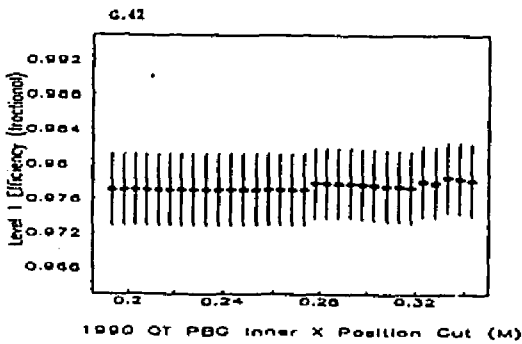
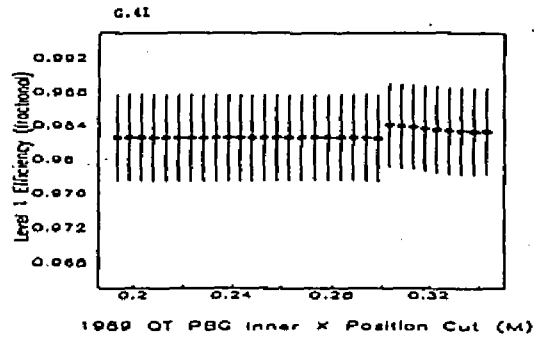
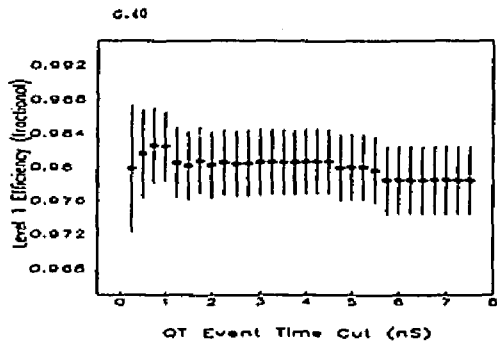
G.37 OT Low Track Momentum Cut (GeV/c)



G.38 OT Momentum Imbalance Cut



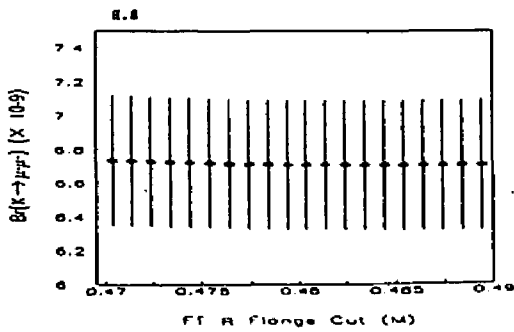
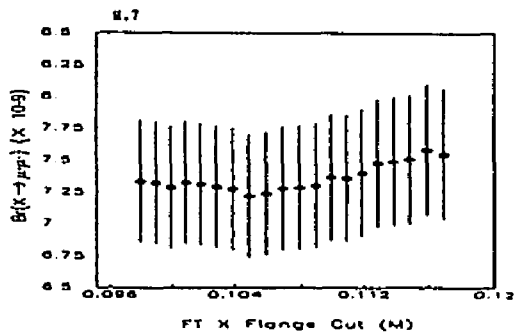
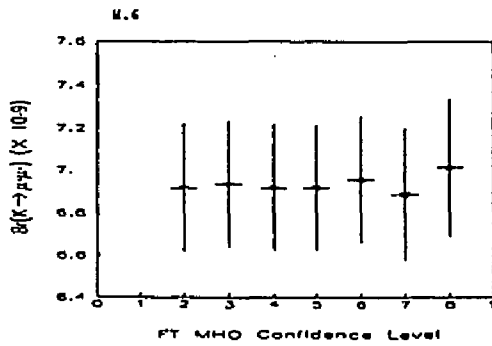
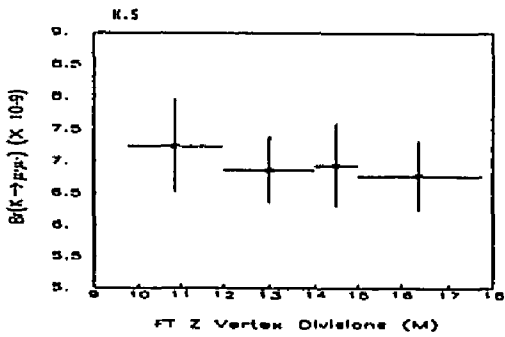
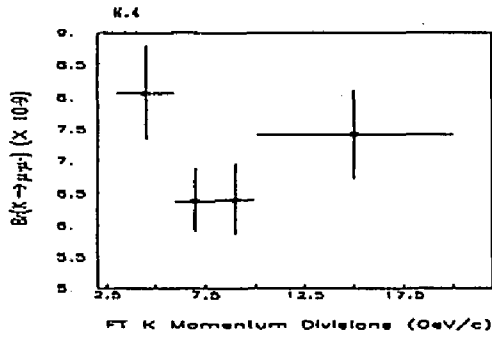
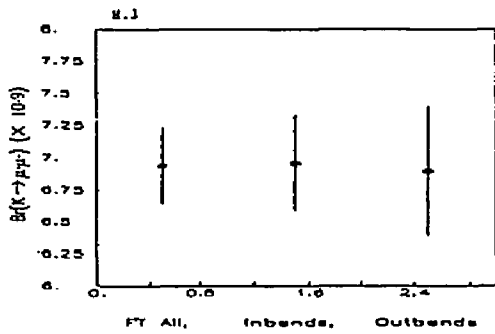
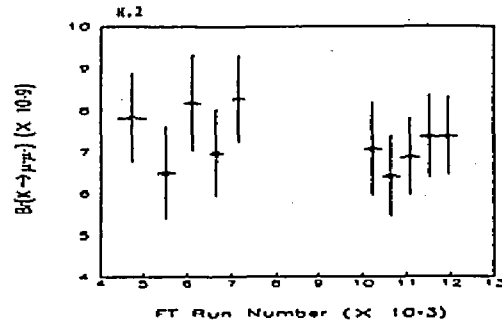
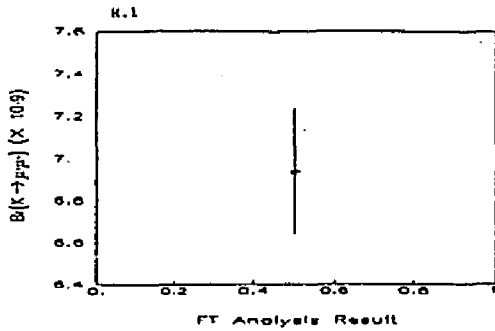
G.39 OT $(P_{front} - P_{back}) / (P_{average})$ Cut

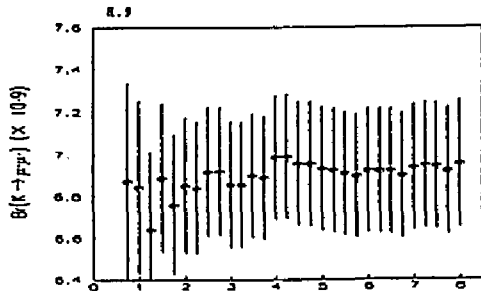


Appendix H

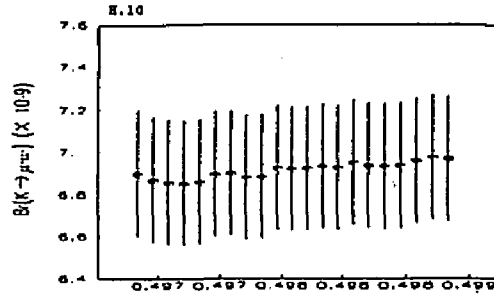
Branching Ratio Systematic Studies

The $K_L^0 \rightarrow \mu^+ \mu^-$ branching ratio was calculated as a function of the cut values listed in appendix C. The results of the calculation for the nominal values of the cuts were presented in chapter 8. This appendix presents results, as graphs, for all of the other cut values for the combined 1989 and 1990 samples. Although similar, results from both QT and FT are presented for completeness. Each plot contains sufficient information for identification of its contents. The figure number appears on the upper left hand corner of each plot and the accompanying caption for each of the figures can be found in the list of figures section at the beginning of this dissertation. The values and errors presented in each plot are correlated. They represent a calculation of the branching ratio from the same data sample but with slightly different cut values as indicated.

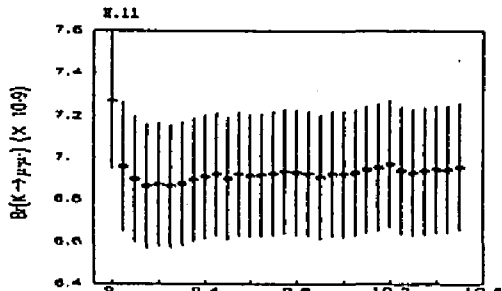




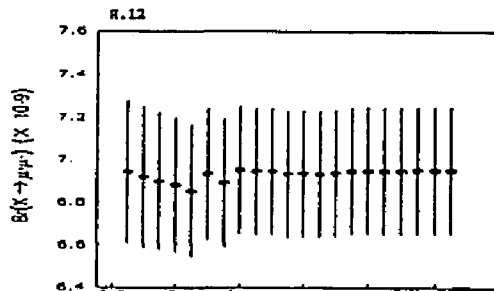
FT Mass Window Width Cut (GeV/c²) (X 10⁻³)



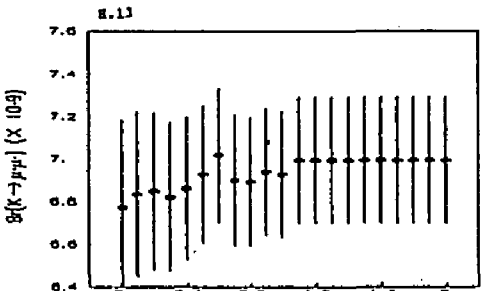
FT Mass Window Center Cut (GeV/c²)



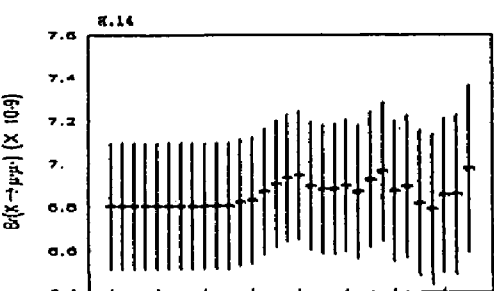
FT Z Vertex Cut (M)



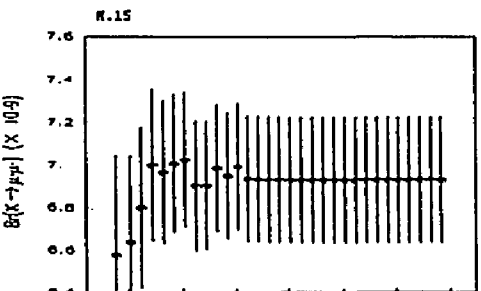
FT Vertex X/Z Cut (X 10⁻³)



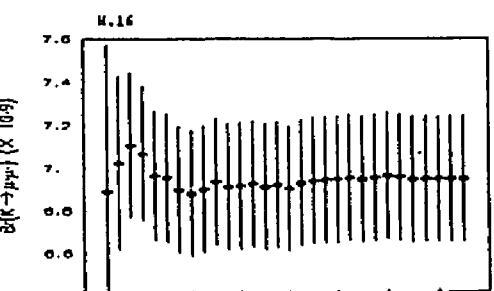
FT Vertex Y/Z Cut (X 10⁻²)



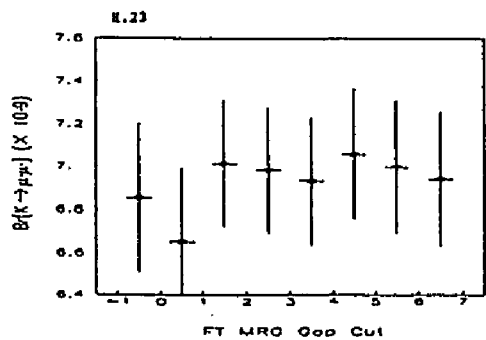
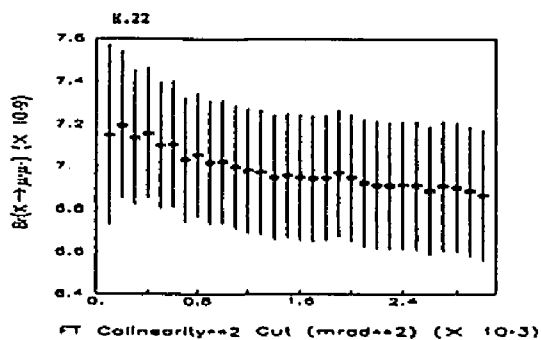
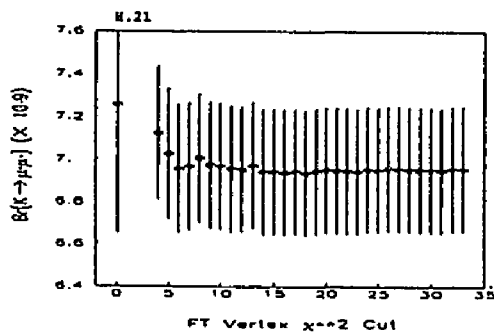
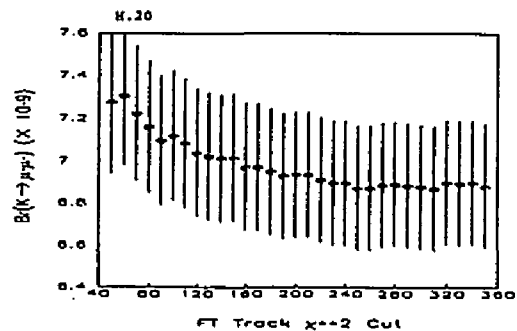
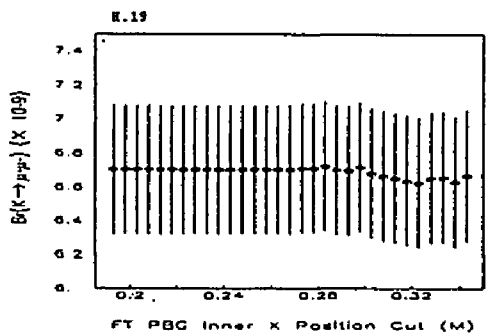
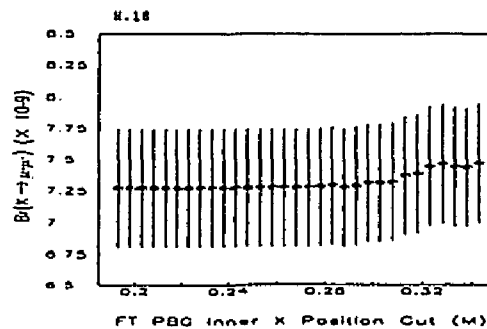
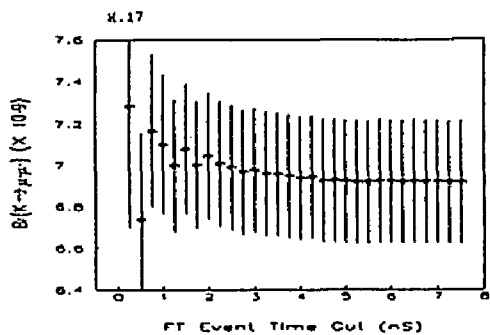
FT Low Track Momentum Cut (GeV/c)

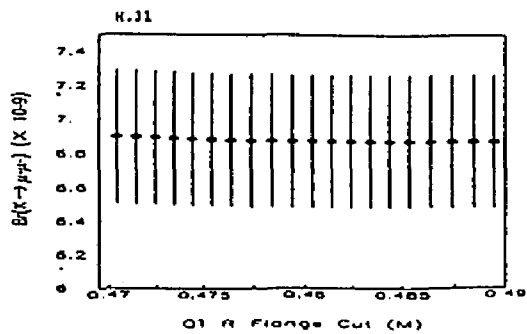
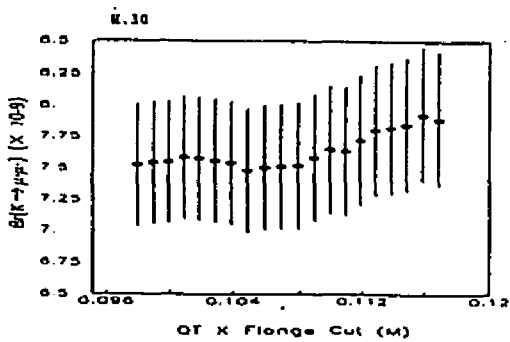
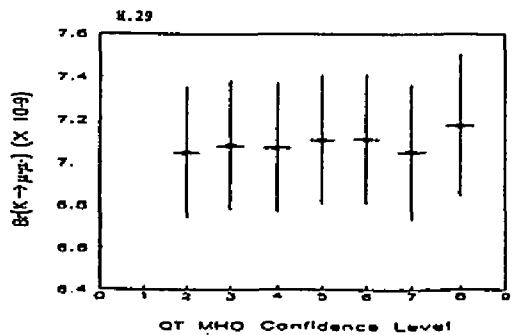
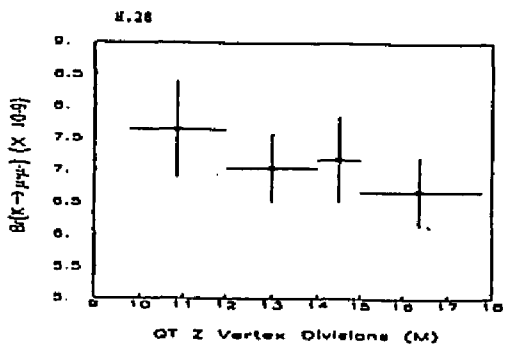
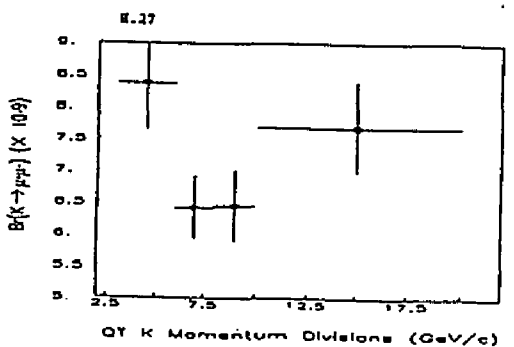
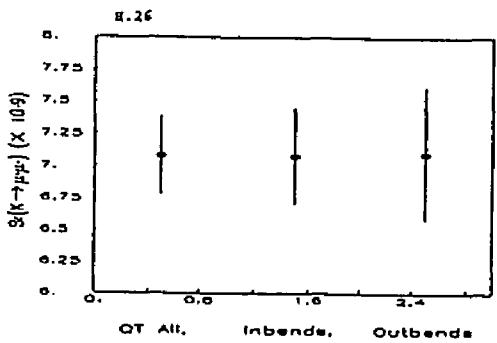
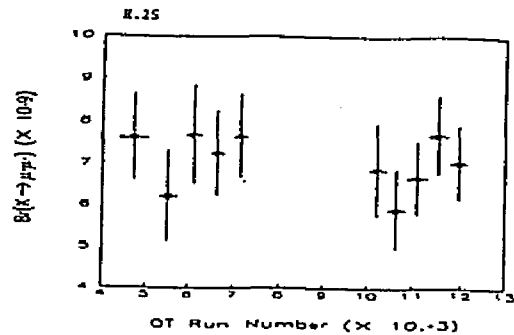
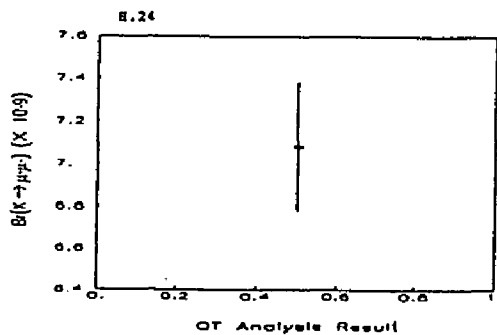


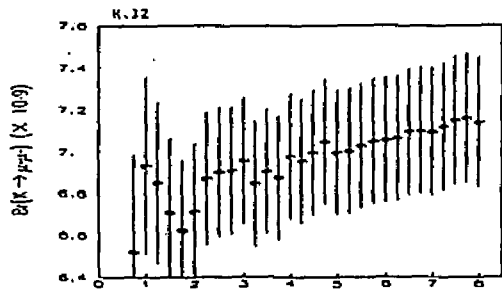
FT Momentum Imbalance Cut



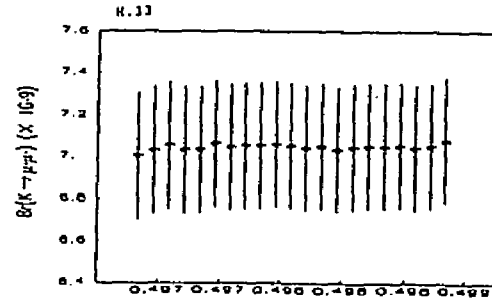
FT (P front - P back)/(P average) Cut



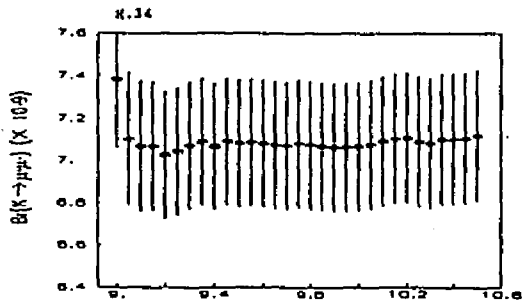




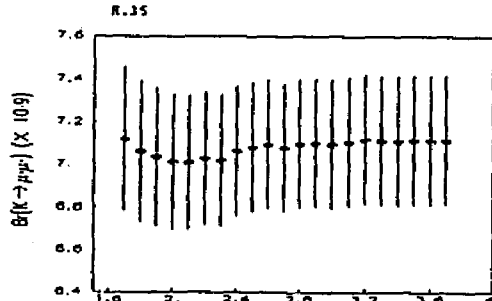
QT Mass Window Width Cut (GeV/c²) (X 10⁻³)



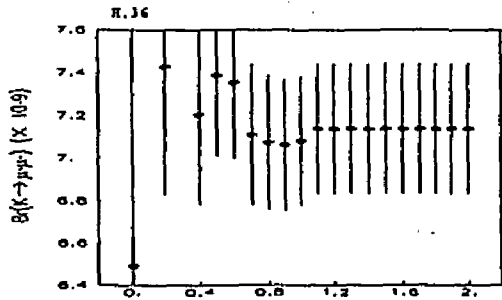
QT Mass Window Center Cut (GeV/c²)



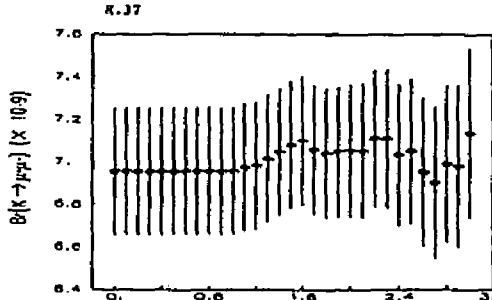
QT Z Vertex Cut (M)



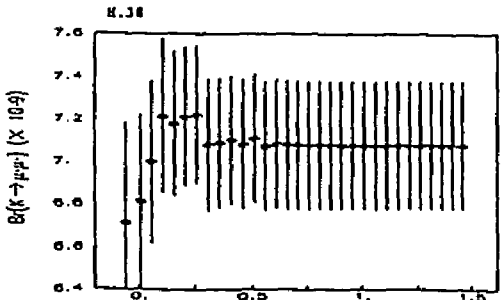
QT Vertex X/Z Cut (X 10⁻³)



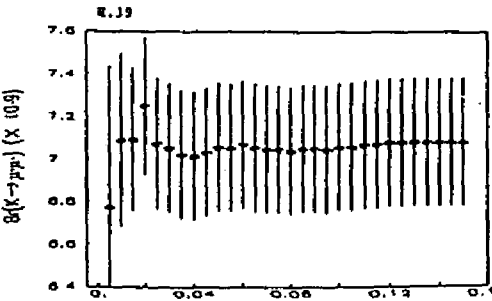
QT Vertex Y/Z Cut (X 10⁻²)



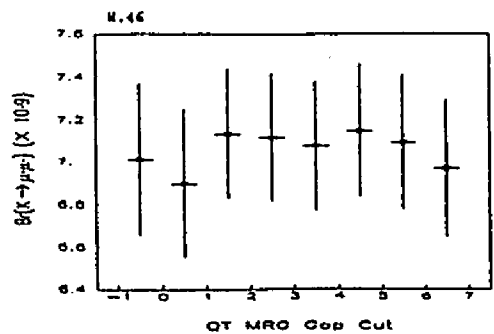
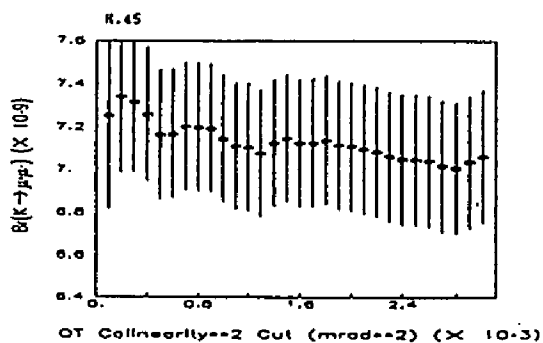
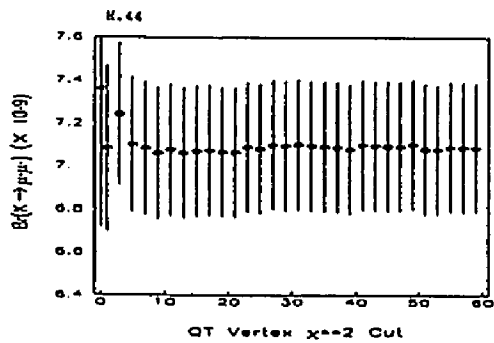
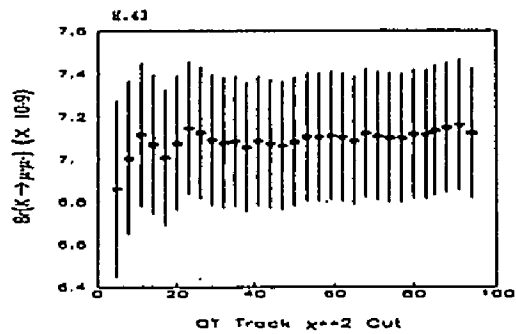
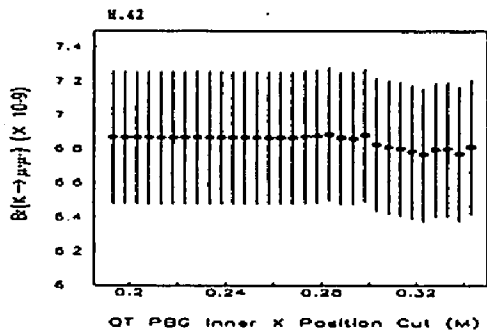
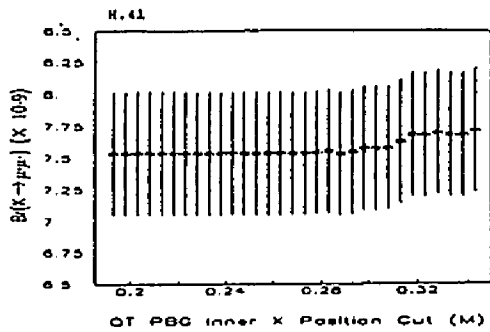
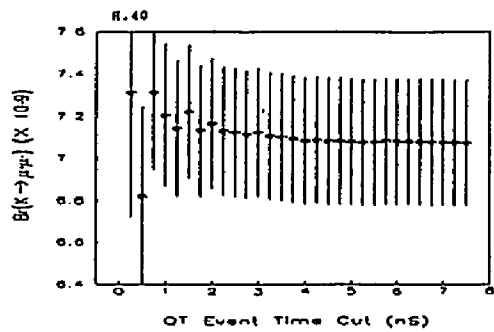
QT Low Track Momentum Cut (GeV/c)



QT Momentum Imbalance Cut



QT (P front - P back)/(P average) Cut



Bibliography

- [1] The BNL AGS E791 Collaboration: A. P. Heinson, J. Horvath, C. Mathiazhagan, W. F. Molzon, *The University of California, Irvine*; K. Arisaka, R. D. Cousins, T. Kaarsberg, J. Konigsberg, J. Kubic, P. Melese, P. Rubin, W. E. Slater, D. L. Wagner, *The University of California, Los Angeles*; G. W. Hart, W. W. Kinnison, D. M. Lee, R. J. McKee, E. C. Milner, G. H. Sanders, H. J. Ziock, *Los Alamos National Laboratory*; P. Knibbe, J. Urheim, *The University of Pennsylvania*; S. Axelrod, K. A. Biery, M. V. Diwan, G. M. Irwin, J. Margulies, D. A. Ouimette, A. Schwartz, Q. Trang, S. G. Wojcicki, *Stanford University*; L. B. Auerbach, J. Belz, P. Buchholz, B. Daniels, C. Guss, V. L. Highland, S. Kettell, W. K. McFarlane, M. Sivertz, *Temple University*; K. Lang, J. Ritchie, A. Yamashita, *The University of Texas at Austin*; M. D. Chapman, M. Eckhause, J. F. Ginkel, P. P. Guss, D. Joyce, A. D. Hancock, J. R. Kane, C. J. Kenney, Y. Kuang, W. F. Vulcan, R. E. Welsh, R. J. Whyley, R. G. Winter, M. T. Witkowski, *The College of William and Mary*.
- [2] C. Mathiazhagan *et al.*, "New Experimental Limits on $K_L^0 \rightarrow \mu e$ and $K_L^0 \rightarrow ee$ Branching Ratios", *Phys. Rev. Lett.* **63** 2181 (1989).
- [3] A. Heinson *et al.*, "Higher Statistics Measurement of the branching ratio for the decay $K_L^0 \rightarrow \mu^+ \mu^-$ ", *Phys. Rev.* **D38** 2914 (1988).
- [4] R. Cousins *et al.*, "Search for the Decays $K_L^0 \rightarrow \mu^\pm e^\mp$ and $K_L^0 \rightarrow e^+ e^-$ ", *Phys. Rev.* **D38** 2914 (1988).
- [5] C. Mathiazhagan *et al.*, "New Experimental Limits on $K_L^0 \rightarrow \mu^\pm e^\mp$ and $K_L^0 \rightarrow e^+ e^-$ Branching Ratios", *Phys. Rev.* **D40** 1712 (1989).
- [6] K. Arisaka *et al.*, "Improved Upper Limit on the Branching Ratio $B(K_L^0 \rightarrow \mu^\pm e^\mp)$ ", *Phys. Rev. Lett.* **70** 1049 (1993).

- [7] K. Arisaka *et al.*, "Improved Upper Limit on the Branching Ratio $B(K_L^0 \rightarrow e^+e^-)$ ", unpublished.
- [8] A. Salam, *Elementary Particle Theory*. (Almquist and Wiksells, 1968).
- [9] S. Weinberg, "A Model of Leptons", *Phys. Rev. Lett.* **19** 1264 (1967).
- [10] S. Glashow, J. Iliopoulos, and L. Miani, "Weak Interactions with Lepton-Hadron Symmetry", *Phys. Rev. D* **2** 1285 (1970).
- [11] J. Christenson, J. Cronin, V. Fitch, and R. Turlay, "Evidence for the 2π Decay of the K_2^0 Meson", *Phys. Rev. Lett.* **13** 138 (1964).
- [12] W. Carithers *et al.*, "Further Observation of the Decay $K_L^0 \rightarrow \mu^+\mu^-$ ", *Phys. Rev. Lett.* **31** 1025 (1973).
- [13] Y. Fukushima *et al.*, "Experimental Measurement of $K_L^0 \rightarrow \mu^+\mu^-$ ", *Phys. Rev. Lett.* **36** 348 (1976).
- [14] M. Shochet *et al.*, "Measurement of the Decay Rate for the Process $K_L^0 \rightarrow \mu^+\mu^-$ ", *Phys. Rev. D* **63** 1965 (1979).
- [15] T. Inagaki *et al.*, "Search for $K_L^0 \rightarrow \mu^\pm e^\mp$ and $K_L^0 \rightarrow e^+e^-$ decays", *Phys. Rev. D* **40** 1712 (1989).
- [16] T. Inagaki *et al.*, "Search for the Rare Decays $K_L^0 \rightarrow \mu^\pm e^\mp$ and $K_L^0 \rightarrow e^+e^-$ ", KEK Preprint 91-84, July 1991.
- [17] K. Arisaka *et al.*, "Improved Measurement of the branching ratio for the decay $K_L^0 \rightarrow \mu^+\mu^-$ ", unpublished.
- [18] G. D. Rochester and C. C. Butler, *Nature* **160** 855 (1947).
- [19] A. Pais, "Some Remarks on the V Particles", *Phys. Rev.* **86** 663 (1952).
- [20] T. D. Lee and C. N. Yang, "Question of Parity Conservation in Weak Interactions", *Phys. Rev.* **104** 254 (1956).
- [21] W. Fry, J. Schneps, and M. Swami, "Evidence for Long-Lived Neutral Unstable Particle", *Phys. Rev.* **103** 1904 (1956).

- [22] K. Lande *et al.*, "Observation of Long-Lived Neutral V Particles", *Phys. Rev.* **103** 1901 (1956).
- [23] C. S. Wu *et al.*, "Experimental Test of Parity Conservation in Beta Decay", *Phys. Rev.* **105** 1413 (1957).
- [24] G. 't Hooft, "Radiative Corrections to Pseudoscalar Meson Decays", *Phys. Lett.* **37B** 195 (1971).
- [25] J. E. Augustin *et al.*, "Discovery of a Narrow Resonance in e^+e^- Annihilation", *Phys. Rev. Lett.* **33** 1406 (1974).
- [26] J. J. Aubert *et al.*, "Experimental Observation of a Heavy Particle J ", *Phys. Rev. Lett.* **33** 1404 (1974).
- [27] S. W. Herb *et al.*, "Observation of a Dimuon Resonance at 9.5 GeV in 400-GeV Proton-Nucleus Collisions", *Phys. Rev. Lett.* **39** 252 (1977).
- [28] M. L. Perl *et al.*, "Evidence for Anomalous Lepton Production in $e^+ - e^-$ Annihilation", *Phys. Rev. Lett.* **35** 1989 (1975).
- [29] C. P. Rubbia, *Proc. 11th Int. Conf. on Neutrino Physics and Astrophysics* (1984).
- [30] E. Commins and P. Bucksbaum, *Weak Interactions of Leptons and Quarks*, (Cambridge University Press, 1983).
- [31] L. B. Okun, *Leptons and Quarks*, (North-Holland, 1982).
- [32] Particle Data Group, "Review of Particle Properties", *Phys. Rev.* **D45** (1992).
- [33] M. Gell-Mann and A. Pais, "Behavior of Neutral Particles under Charge Conjugation", *Phys. Rev.* **97** 1387 (1955).
- [34] D. Perkins, *Introduction to High Energy Physics*, (Addison-Wesley, 1987).
- [35] N. Cabibbo, "Unitary Symmetry and Leptonic Decays", *Phys. Rev. Lett.* **10** 531 (1963).
- [36] M. Kobayashi and T. Maskawa, " CP -Violation in the Renormalizable Theory of Weak Interaction", *Prog. Theor. Phys* **49** 652 (1973).

- [37] L. Sehgal, "Electromagnetic Contribution to the Decays $K_S \rightarrow \bar{l}l$ and $K_L \rightarrow \bar{l}l$ ", *Phys. Rev.* 183 1511 (1969).
- [38] G. Bélanger and C. Geng, "New Range of Mixing Parameters and Rare K Decays", *Phys. Rev.* D43 140 (1990).
- [39] R. Shrock and M. Voloshin, "Bounds on Quark Mixing Angles from the Decay $K_L^0 \rightarrow \mu^+ \mu^-$ ", *Phys. Lett.* 87B 375 (1979).
- [40] L. Bergström, E. Massó, and P. Singer, "Radiative and Muonic Decays of K_L . Implications for Top Mass", *Phys. Lett.* 249B 141 (1990).
- [41] L. Bergström, "Radiative Corrections to Pseudoscalar Meson Decays", *Z. Phys.* C20 135 (1983).
- [42] J. Belz, Ph.D. Thesis, Temple University 1992.
- [43] Figure provided by J. Horvath.
- [44] A. Schwartz, *E791 Target Study*, KL294¹.
- [45] J. Urheim, Ph.D. Thesis, University of Pennsylvania 1990.
- [46] J. Margulies, Ph.D. Thesis, Stanford University 1990
- [47] K. Biery, Ph.D. Thesis, Stanford University 1991.
- [48] R. Cousins, *Poisson Modelling of the E791 Spectrometer Magnets*, KL155.
- [49] J. Ginkle, Ph.D. Thesis, The College of William and Mary 1989.
- [50] P. Rubin, Ph.D. Thesis, UCLA 1989.
- [51] M. Chapman, Ph.D. Thesis, The College of William and Mary 1992.
- [52] J. Konigsberg, Ph.D. Thesis, UCLA 1989.
- [53] C. Kenney, Ph.D. Thesis, The College of William and Mary 1989.
- [54] Logic gates provided by K. Biery and J. Belz.

¹Sources listed as KLnnn are unpublished memos internal to the E791 collaboration. They can be obtained through the SLAC Group G Secretary, SLAC BIN #63, P.O. Box 4349, Stanford, CA 94309.

- [55] P. Buchholz and K. McFarlane, *E791 Level 1 Trigger May Run 1987*, KL135.
- [56] P. Buchholz and K. McFarlane, *E791 Level 1 Trigger Changes for the February Run 1988*, KL140.
- [57] P. Buchholz and K. McFarlane, *E791 Level 1 Trigger Spring Runs 1988 and 1989*, KL208.
- [58] S. Kettell, *L1 Summary for the 1990 Run*, KL359.
- [59] Figure provided by J. Belz.
- [60] R. Cousins, *et al.*, "Fast Parallel Pipelined Readout Architecture for a Completely Flash Digitizing System with Multi-Level Trigger", *Nucl. Inst. Meth.* A277 517 (1989).
- [61] R. Cousins, C. Friedman, P. Melese, *Gray Code TDC.*, KL037.
- [62] R. Cousins, C. Friedman, and P. Mélése, "32-Channel Digital 6-Bit TDC with 2.5 ns Least Count", *IEEE Trans. Nucl. Sci.* 36 650 (1989).
- [63] A. Schwartz and D. Ouimette, *Stanford TDC's* , KL243.
- [64] K. Biery, D. Ouimette, and J. Ritchie, "A Fast Integrating Eight-Bit Bilinear ADC", *IEEE Trans. Nucl. Sci.* 36 646 (1989).
- [65] K. Biery, J. Ritchie, D. Ouimette, *FADC Writeup.*, KL190.
- [66] G. Hart, *Rangefinder Electronics System.*, KL141.
- [67] W. Slater, *Hardware Implementation of Level 2.*, KL127.
- [68] W. Slater, *A Test of the Level 2 Trigger.*, KL150.
- [69] P. Kunz *et al.*, "The 3081/E Processor", SLAC-PUB-3332, April 1984.
- [70] K. Biery, "The Data Acquisition System for BNL AGS Experiment 791", *Proc. Conf. on Computing in High Energy Physics*, Santa Fe NM, April 1990.
- [71] W. Molzon, *Progress Report on Level 3 Trigger Algorithm*, KL051.
- [72] M. Diwan, *Level 3 for Spring 1990*, KL266.

- [73] G. Irwin, *KLUE Offline Manual; Manual for the E791 offline program.*, KL100.
- [74] D. Wagner, *Some Monte Carlo Documentation*, KL173.
- [75] J. Horvath, *Monte Carlo Tuning for the 1990 Data Analysis*, KL354.
- [76] P. Skubic *et al.*, "Neutral-Strange-Particle Production by 300-GeV Protons", *Phys. Rev. D* 18 3115 (1978).
- [77] P. Melese, Ph.D. Thesis, UCLA 1988.
- [78] D. Wagner, *Tuning Pattern Recognition*, KL213.
- [79] D. Wagner, Ph.D. Thesis, UCLA 1990.
- [80] P. Mélése, *Status of Event Fitting*, KL145.
- [81] W. Molzon and S. Imlay, *The QFT Fitting Package and Kinematic Resolutions*, KL237.
- [82] R. Cousins and T. Kaarsberg, *9/89 Release of the FT Track and Event Fitting Package*, KL248.
- [83] J. Belz, *QT Fitter for 1990 Analysis*, KL356.
- [84] R. Cousins, *Miscellaneous 1989 Analysis Notes; Description.*, KL293.
- [85] K. Biery, *Efficiency of the Muon Hodoscope in the 1989 Analysis; Report on efficiency and discussion of changes made.*, KL302.
- [86] A. Heinson *et al.*, "BNL AGS Proposal P871: A New Search for Very Rare K_L Decays", Submitted September 1990.
- [87] J. Urheim and R. Cousins, *Estimate of Contamination from $K_S^0 \rightarrow \pi^+\pi^-$ Decays*, KL229.
- [88] J. Christenson, *et al.*, "Measurement of the Phase and Magnitude of η^\pm " *Phys. Rev. Lett.* 43 1212 (1979).
- [89] N. C. Barford, *Experimental Measurements: Precision, Error and Truth*, (Wiley, 1985).

Vita

The author was born in Sunbury Pennsylvania, October 26 1963. He graduated from Nazareth Area Senior High School in 1981. After a brief period of military service he entered Moravian College. In 1988 he graduated with a B.S in Physics with honors. Following this, he entered the College of William and Mary as a graduate student in the physics department. In 1989 he was awarded a M.S in physics followed by the award of the Ph.D. degree in 1993.